

# **Magnetotelluric study of Howley Basin, Newfoundland**

by

©Tijana Livada

A Thesis submitted to the School of Graduate Studies in partial fulfillment of the  
requirements for the degree of

**MSc Geophysics**

**Department of Earth Sciences**

Memorial University of Newfoundland

**September 2014**

St. John's

Newfoundland and Labrador

# Abstract

The aim of this study is to develop a better understanding of the Howley Basin and its hydrocarbon potential using a magnetotellurics (MT) survey. This sedimentary basin is located in western Newfoundland, and is covered by the Howley formation which is only found in this basin. Very little is known about the basin and its structure. The Rocky Brook formation, which consists of organic rich mudstone that is known for generating hydrocarbons, is found in the adjacent Cormack Basin and is believed to be present in the Howley Basin as well.

The MT method is a passive electromagnetic method that is sensitive to the electrical conductivity structure of the subsurface. The source for MT is completely natural, resulting from the flow of charged particles in the ionosphere (e.g. from solar storms) and from lightning strikes. These cause natural variations in the Earth's magnetic field which in turn result in induced currents in the subsurface.

MT sounding of an 18 km long profile was conducted in August and September 2013, crossing from the Topsail Igneous Complex formation into the Howley formation at about 3 km from the southeast end of the survey and extending to the anticipated location of the boundary between the Howley and Cormack Basins in the northwest. The Howley Basin is characterized by higher conductivities than the surrounding

igneous basement. Strike analysis reveals the basin has a preferred geo-electric orientation of  $9^\circ$  with the deeper structures having a preferred strike of  $33^\circ$ . A range of 2D inversions were performed for both strikes. TM mode only inversion yielded the best results with misfit (least square fit to the observed impedances) of 3.9 for the strike of  $9^\circ$  and 2.4 for the strike orientation of  $33^\circ$ . The MT data suggest a maximum thickness of the basin along the profile of approximately 2 km and that the basin is decreasing in thickness towards its eastern boundary. There are also indications of a conductive feature or features extending beneath the basin, possibly related to faulting through the basin and into the basement or of a step in the base of the basin.

# Acknowledgements

The majority of the funding for this project was provided by NALCOR Energy and the Petroleum Exploration Enhancement Program (PEEP). Partial funding was also provided through a School of Graduate Studies Fellowship to the author.

I cannot express enough my gratitude to those who supported me throughout the entirety of this MSc project. Firstly, I would like to thank Colin Farquharson for providing this project and welcoming me into his team, as well as for his outstanding concerted support and supervision. Also, for their advice and guidance during this study, I would like to express my wholehearted thanks to Charles Hurich, Jessica Spratt whose guidance through data acquisition and later processing was astonishing, as well as Jim Craven's initial introduction to magnetotelluric field methods. Also, further thanks to Jim Craven for providing me with the software needed for this thesis project. Many thanks to POLARIS Consortium as well for use of their instruments.

Finally, I would like to thank my family and friends for all their support, and for always being there for me.

# Table of Contents

<b>Abstract</b>	<b>ii</b>
<b>Acknowledgments</b>	<b>iv</b>
<b>Table of Contents</b>	<b>v</b>
<b>List of Tables</b>	<b>viii</b>
<b>List of Figures</b>	<b>ix</b>
<b>1 Introduction</b>	<b>1</b>
<b>2 Geology of the Howley Basin</b>	<b>8</b>
2.1 Introduction to the geological history . . . . .	8
2.2 Regional Maritimes Basin Geology . . . . .	10
2.3 Formations and Groups . . . . .	10
2.3.1 The Anguille Group . . . . .	13
2.3.2 The North Brook Formation . . . . .	13
2.3.3 The Rocky Brook Formation . . . . .	13
2.3.4 The Humber Fall Formation . . . . .	14
2.3.5 The Howley Formation . . . . .	15
2.4 Geophysical Surveys in the Area . . . . .	15

<b>3</b>	<b>The Magnetotelluric Method</b>	<b>22</b>
3.1	The Source . . . . .	23
3.2	Electrical Properties of Earth materials . . . . .	25
3.3	MT Equations . . . . .	28
3.4	Dimensionality . . . . .	31
3.4.1	1D Earth . . . . .	31
3.4.2	2D Earth . . . . .	32
3.4.3	3D Earth . . . . .	36
3.5	Processing . . . . .	36
3.5.1	Time series to transfer function . . . . .	37
3.5.2	Distortion . . . . .	38
3.5.3	Geo-electric strike: Example from Nechako Basin, BC, Canada	41
3.6	Inversion . . . . .	41
<b>4</b>	<b>Data Acquisition and Processing</b>	<b>45</b>
4.1	Data Acquisition . . . . .	45
4.2	Processing . . . . .	54
4.2.1	Removing erratic data . . . . .	60
<b>5</b>	<b>Decomposition and modelling</b>	<b>67</b>
5.1	1D modelling . . . . .	67
5.2	Strike Angle Analysis . . . . .	71
5.3	2D Inversion . . . . .	83
<b>6</b>	<b>Interpretation and Discussion</b>	<b>96</b>
6.1	Deep Crustal Structures . . . . .	96
6.2	Howley Basin Structures . . . . .	101

<b>7 Conclusion</b>	<b>108</b>
<b>A Unedited .edi files</b>	<b>114</b>
<b>B Edited .edi files</b>	<b>134</b>
<b>C Inversion models</b>	<b>153</b>
<b>D Inversion data</b>	<b>162</b>

# List of Tables

4.1	MT Station Coordinates, coils used $(H_x, H_y, H_z)$ , and dipole spacings $(E_x, E_y)$ . . . . .	51
4.2	Processing files and comments for each site . . . . .	52
5.1	‘Strike1’: Parameters used . . . . .	75
5.2	‘Dcmpmap’: Parameters used . . . . .	77
5.3	‘Dcmp2j’: Parameters used . . . . .	82
5.4	‘Mtrotate’: Parameters used . . . . .	83
5.5	‘J2edi’: Parameters used . . . . .	83
5.6	RMS data misfit values for different models produced by different inversion runs. $\tau$ is the smoothing factor. . . . .	86

# List of Figures

1.1	Geological map of western Newfoundland showing geological terranes, hydrocarbon shows, and well locations [Gov.of.NL, 2000]. . . . .	5
1.2	Geological map of the Deer Lake Basin showing well locations [Gov.of.NL, 2000]. The red rectangle indicates the survey area for this thesis. . . .	6
1.3	A: Late Paleozoic basins of the Maritimes Basin shown in yellow. Contours show depth of the basin in kilometres: CF-Cabot fault, DLB-Deer Lake Basin. B: Retrodeformed map showing inferred positions of the major blocks prior to the Devonian-Carboniferous strike slip [Hibbard and Waldron, 2009]. . . . .	7
2.1	Structural profile of the Deer Lake Basin across the Cabot Fault, including the Cormack and Howley sub-basins. The location of this cross section is indicated in Figure 1.1 [Gov.of.NL, 2000]. . . . .	9
2.2	The Maritimes Basin of Atlantic Canada. Top: Outline showing the extent of the basin. Bottom: Geology of the area [Martin et al., 2008].	11
2.3	Stratigraphic units and their inferred ages in the Deer Lake Basin. [Martin, 2001] . . . . .	12

2.4	Simplified geology of the Deer Lake Basin, indicating distribution of the Rocky Brook Formation and cores/outcrops that have been sampled [Hamblin et al., 1997] The A-A' line corresponds with profile cross section in Figure 2.1. . . . .	17
2.5	Gravity contour map of the Howley Basin from Miller and Wright [1984], with the same UTM coordinates as used in this thesis. (a) Geological map of the area; (b) Bouguer gravity anomaly with contour intervals of 2.5 mGal; (c) Regional trend surface for fifth order polynomial with contour intervals of 2.5 mGal; (d) Residual gravity found by subtracting trend values from Bouguer anomaly data with contours of 2.5 mGal. Red square outlines this project's study area. Blue line highlights the location of the profile in Figure 2.7. This project's profile is approximated by the green line. . . . .	18
2.6	Modelled cross-section (location outlined in Figure 2.6 by a blue line) using Bouguer anomaly and observed magnetic anomaly by Miller and Wright [1984]. Legend is the same as in Figure 2.6 a. . . . .	19
2.7	Residual magnetic anomaly map of the Deer Lake Basin (Government of Newfoundland and Labrador). Study area is outlined by the yellow rectangle. The discontinuity in the map is a result of using two data sets to create the map, regional dataset and more recent Deer Lake dataset. . . . .	20
2.8	Migrated seismic reflection section of Lithoprobe onshore Vibroseis profiles across the island of Newfoundland, plotted 1:1 with an assumed velocity of 6000 m/s. Deer Lake basin is located in the top left of the section [Van der Velden et al., 2004]. . . . .	21

3.1	Power spectrum illustrating 1/f characteristics of the Earth’s magnetic field. Short period signals are produced by interaction in the Earth-ionosphere waveguide, and long period signals are generated by solar wind-magnetosphere interaction. Insert emphasizes the reduced signal in the dead-band around 1 Hz [Simpson and Bahr, 2005]. . . . .	24
3.2	The magnetosphere [Viljanen, 2012]. . . . .	25
3.3	Typical ranges of conductivities of Earth materials [Nabighian, 1987] (this is a standard conductivity table found in many text books). . .	26
3.4	A simple 2D model consisting of two abutting quarter spaces with different conductivities $\sigma_1$ and $\sigma_2$ meeting at a vertical contact. The $x$ -direction is the strike direction for this example [Weidelt and Chave, 2012]. . . . .	33
3.5	Galvanic effect for a conductive (left) and a resistive (right) inhomogeneity. Charges build up on the surface of the object causing a secondary electric field ( $E_s$ - dashed lines), which is weaker but still adds up vectorially to the primary field ( $E_p$ , direction of the red arrow), resulting in static shift (top left and top right). After Miensopust [2010].	39
3.6	Results from decomposition analysis of the Nechako Basin, BC, dataset by Spratt and Craven (2011), showing the preferred geo-electric strike direction for each site using period bands of 1-10s and 10-100s. Arrows in the bottom two panels show the strike direction with a 90° ambiguity. The colours in the top two panels indicate the maximum phase difference between TM and TE modes [Spratt and Craven, 2011].	42

4.1	MT profile across the Howley Basin (green dashed line). The MT profile followed a planned seismic profile. The specific locations of the MT stations were determined by accessibility, ground conditions, and locations of infrastructure. Note the power line (thin dashed black line) that follows the MT profile eastwards and to the west of Grand Lake/Sandy Lake (figure by professor Chuck Hurich). . . . .	46
4.2	Typical instrument layout for each station . . . . .	48
4.3	Photographs of the instruments used . . . . .	49
4.4	Station locations. Geological map with stations plotted (UTM coordinates, zone 21). Blue dots are AMT stations while green dots are for combined AMT and BBMT stations. . . . .	53
4.5	Left: Placing a coil at the station HW107; Right: Brook between stations HW138 and HW139. . . . .	55
4.6	A portion of the time series for $E_x, E_y, H_x, H_y$ recorded for station HW135. . . . .	56
4.7	Window screen shot of SSMT 2000: Robust Processing from Phoenix Geophysics. Outlined by green squares are the steps taken and numbered in the order in which they were performed. . . . .	57
4.8	Window screen shot of the table to be filled in Step 1 in Figure 4.7. Here information for an individual site is entered. . . . .	58
4.9	Window screen shot of the table for Step 3 in Figure 4.7. Here an individual site is referenced to the remote reference site file in order to carry out the remote reference processing. . . . .	59
4.10	Observed apparent resistivity and phase curves for site HW135 before (left) and after (right) editing. The red curve corresponds to the TE (XY) component and the green to the TM (YX) component. . . . .	60

4.11	Observed apparent resistivity and phase curve for site HW135 (left) and the editing window for 650 Hz (right). Righthand side panels show how many times the particular frequency was sampled and the value measured. . . . .	61
4.12	Observed apparent resistivity and phase curve for site HW135 (left) and editing window for 49 Hz (right). Righthand side panel shows how many times the particular frequency was sampled and the value measured. . . . .	61
4.13	Observed apparent resistivity and phase curves for site HW135 before editing in WinGLink. The red circles correspond to the TE (XY) component and the blue squares to the TM (YX) component. Curves are the best fit for apparent resistivity that are later used for the Occam inversion. Azimuth of 0° indicates good data . . . . .	62
4.14	Observed apparent resistivity and phase curves for HW135 after editing in WinGLink. . . . .	63
4.15	Pseudo section of apparent resistivity vs. period along the survey profile for AMT and BBMT soundings combined. . . . .	64
4.16	Pseudo section of phase vs. period along the survey profile. . . . .	65
4.17	Sounding curves for two of the BBMT stations, HW140 and HW134.	66

5.1	Left: The TM apparent resistivity and phase curves for HW135 (symbols observed data and curves predicted data) from 1-D Occam inversion. Right: The resistivity vs. depth model (pink) produced by the 1D Occam inversion of the apparent resistivity and phase data for HW135 performed in WinGLink. The green line is the result of a Marquardt inversion which predicts an 8-layer Earth model. The blue line is the Bostick smooth fitted model. The Bostick inversion shows maximum imaging depth around 2 km, and the maximum depth of the Occam and multilayer inversion can in general be set arbitrarily in the inversion parameters. . . . .	69
5.2	2D images made from stitching together the 1D Occam inversion models for TE and TM modes. Vertical bars show the 1D Occam inversion for each location and the approximate depth to which the sounding penetrates. The background colours are the software's interpolations based on connecting the features of the vertical bars. . . . .	70
5.3	Occam layered inversion results for stations HW103 and HW113 (same colour-coding as in Figure 5.1) with a clear decrease in average resistivity at station HW113 above about 1 km that is not present for HW103, suggesting the basin's eastern edge is located somewhere in-between these stations. . . . .	71
5.4	Depth penetration estimates from the 1D inversions. These are the same as in Figure 5.2, just without the interpolated background. . . .	72

5.5	Maps showing the preferred geo-electric strike direction at each site for decade period bands for the AMT soundings. The colour scale illustrates the maximum phase difference between the TM and TE mode phases. Stations missing the square indicate the phase difference to be greater than 30°, which means the data is 2D or 3D and not necessarily of poor quality. (grey areas are lake coverage . . . . .	74
5.6	Maps showing the preferred geo-electric strike direction at each site for decade bands for the BBMT soundings. The colour scale illustrates the maximum phase difference between the TM and TE mode phases. Stations missing the square indicate the phase difference to be greater than 30°, which means the data is 2D or 3D and not of poor quality.	76
5.7	RMS misfits for preferred strike calculations for each station over the whole period range for data recalculated at a geo-electric strike of 9°. Blue represents where the data are fit well by this strike direction, red indicates the strike does not fit the data at all. AMT soundings range between 0.0001 s and about 1 s, BBMT soundings range from about 1s to 10000 s. East portion of the profile has low RMS mist values. .	79
5.8	RMS misfits for each station over the whole period range for data recalculated at a geo-electric strike of 33°. Blue represents where the data are fit well by this strike direction, red indicates the strike does not fit the data at all. AMT soundings range between 0.0001 s and about 1 s, BBMT soundings range from about 1 s to 10000s. This strike has the lowest RMS misfit values for BBMT. . . . .	80

5.9	RMS misfits for each station over the whole period range for data recalculated at a geo-electric strike of $85^\circ$ . Blue represents where the data are fit well by this strike direction, red indicates the strike does not fit the data at all. AMT soundings range between 0.0001 s and about 1 s, BBMT soundings range from about 1 s to 10000 s. . . . .	81
5.10	The mesh used for the 2D inversions is represented by the grid in the above two panels. Top: Mesh used for the whole section; Bottom: Zoom in to the top 4 km of the mesh. . . . .	84
5.11	The constructed resistivity models calculated in Table 5.6. Larger images are included in Appendix C. . . . .	87
5.12	The constructed resistivity models calculated in Table 5.6, top 4 km. Larger images are included in Appendix C . . . . .	88
5.13	The constructed model for TM mode only inversions with $\tau = 3$ for both strike directions. Top: Conductivity cross section of the full 2D model for data rotated to a strike of $9^\circ$ ; Middle: Conductivity cross section of the full 2D model for data rotated to a strike of $33^\circ$ ; Bottom: Comparison of RMS data misfit values for strikes $9^\circ$ and $33^\circ$ for each station. The RMS values, with a few exceptions, follow each other for both strikes with a value around 2. The exceptions are stations HW126-HW131, which might be due to nearby power lines or the data are 3D in this area. The distance between HW103 and HW141 is 18 km. . . . .	89

5.14	Zoom in to the top 4 km of the models shown in Figure 5.13. Top: Cross section produced by using data rotated to 9°; Bottom: Cross section produced by using data rotated to 33°. It can be seen in both models that the more conductive basin is thickening towards the Northwest towards the Cabot fault, where its maximum thickness reaches about 1.5-2 km. . . . .	90
5.15	Graph showing apparent resistivity (top) and phase (bottom) vs. period for the observed (blue circles) and calculated (blue line) data for TM mode, strike 33°, site HW135. The calculated data matches the observed data well, resulting in low RMS misfit value of 1.288 (for this site). . . . .	92
5.16	The constructed models for TM mode only and $\tau = 5$ . Top: Conductivity cross section of the full 2D model for data rotated to a strike of 9°; Middle: Conductivity cross section of the full 2D model for data rotated to a strike of 33°; Bottom: Comparison of RMS data misfit values for strike 9° and 33° for each station. . . . .	93
5.17	Zoom in to the top 4 km of the models shown in Figure 5.16. Top: Cross section produced by using data rotated to 9°; Bottom: Cross section produced by using data rotated to 33°. It can be seen in both models that the more conductive basin is thickening towards the Northwest towards the Cabot fault, where its maximum thickness reaches about 2 km. . . . .	94
6.1	2D inversion results for TM mode only, $\tau = 3$ , and a strike of 9° with (a) two stations closest to the power lines omitted, (b) three closest omitted, and (c) six closest stations omitted from the inversion. . . .	98

6.2	2D inversion results for TM mode only, $\tau = 5$ , and a strike of $33^\circ$ with (a) two stations closest to the power lines omitted, (b) three closest omitted, and (c) six closest stations omitted from the inversion. . . .	99
6.3	Bouguer anomaly map (a coloured version of Figure 2.5b produced in Oasis Montaj [Miller and Wright, 1984]), with the MT stations indicated by the coloured dots. The black dots indicate the location of the gravity measurements. . . . .	100
6.4	Zoom ins to the top 4 km of the models shown in Figure 6.1: TM mode only, $\tau=3$ , and a strike of $9^\circ$ . (a)-(c) the two, three and six soundings closest to the power line are omitted from the inversion. . . . .	102
6.5	Zoom ins to the top 4 km of the models shown in Figure 6.2: TM mode only, $\tau=5$ , and a strike of $33^\circ$ . (a)-(c) the two, three and six soundings closest to the power line are omitted from the inversion. . . . .	103
6.6	Proposed Howley Basin models based on the MT data and inversions. Left: Inversion used for generating model and proposed structure of the basin using $9^\circ$ for geo-electric orientation. Right: Inversion used for generating model and proposed structure of the basin using $33^\circ$ for geo-electric orientation. . . . .	104
6.7	Structural setting of a negative flower structure. The possible location of the Howley Basin within such a structure is outlined by the red square (image modified from Wikipedia: Strike-slip tectonics). . . . .	106

# Chapter 1

## Introduction

The magnetotelluric (MT) method is a passive electromagnetic method that is sensitive to the electric resistivity structure of the subsurface. The method makes use of the Earth's natural electromagnetic fields. The method is attractive because of its low cost and minimal environmental damage. This thesis is concerned with an 18 km MT profile across the Howley Basin in western Newfoundland.

The Howley Basin is located in western Newfoundland, Canada, just north-east of the town of Deer Lake (Figure 1.1 and Figure 1.2). It is an onshore basin, and is often referred to as a sub-basin of the Deer Lake Basin. Relatively little work has been done on the Howley Basin and so not much is known about it.

The Deer Lake Basin, which is a successor basin generated by post collisional processes after the main Acadian compressional mountain building episode, represents one of several areas of Lower Carboniferous rocks in western Newfoundland belonging to the northeast margin of the Maritimes Basin [Hamblin et al., 1997]. The Maritimes Basin was produced by post orogenic extensional processes in the mid to late

Devonian, and was further deformed along the Cabot Fault by strike-slip movement during the Carboniferous (Figure 1.3) [Langdon, 1993]. The same fault runs through the Deer Lake Basin dividing it into two lateral sub basins: the Cormack and Howley Basins. Almost all of the rocks in the Deer Lake Basin are Carboniferous rocks that formed coeval with motion on the Cabot fault.

It has been assumed that the Cormack and Howley sub-basins are partly symmetrical, and hence filled with the same sediments from the local surrounding region. However, the Howley formation is only found in its namesake basin and, without further knowledge on deeper lying stratigraphy, what lies beneath the Howley formation in this sub-basin remains unknown [Langdon, 1993]. The government of Newfoundland and Labrador through the Petroleum Exploration Enhancement Program (PEEP) is funding a project to further understand the nature of the Howley Basin, including its structure, stratigraphic fill and thicknesses. This is because there is an interest in re-evaluating the petroleum potential of the region. The MT survey described in this thesis was one component of this project.

On the west side of the Cabot fault, the Cormack Basin is the site of seven old exploration wells drilled in the early 1900's [Gov.of.NL, 2000]. Mill's 1 rig was destroyed due to a gas blow out, and two of Claybar wells had significant gas shows. Several modern exploration wells were drilled in the Cormack Basin by Deer Lake Oil and Gas. Rocky Brook formation shales are proven to be organic rich and have the potential to be a source rock, while North Brook is a good reservoir rock. However, the Howley formation, only present in the Howley Basin, also could act as a possible reservoir [Gov.of.NL, 2000].

The MT method has been used for hydrocarbon exploration in many cases. It was a very significant tool in the Soviet Union during the 1970's. It has primarily been used as a supplementary method to seismic, or in places where seismic acquisition proved difficult, e.g. in areas that are heavily forested, or areas with a volcanic overburden opaque to seismic overlying a sedimentary basin. An excellent example of the later case is the Nechako Basin in British Columbia [Spratt and Craven, 2011]. Another advantage of the MT method over seismics in hydrocarbon exploration is the depth to which it can image the subsurface. Howley Basin however, was anticipated to be 2-5 km deep, depths to which seismic can clearly propagate. Also, an opaque overburden is not present. Nevertheless, the terrain is really swampy, and for that reason, along with the cost, minimal environmental impact, and sensitivity to conductivity of the subsurface, MT was chosen as a complimentary method to seismic and gravity for this project.

This thesis is divided into five chapters, namely 'Geology of the Howley Basin', 'Theory of the Magnetotelluric method', 'Data Acquisition and Processing', 'Imaging and Decomposition Analysis', and 'Interpretation and Discussion'. The first two chapters provide background information and theory for the remainder of the thesis. Chapter 2 covers the geological history of western Newfoundland and tectonic processes involved in its formation. Chapter 3 summarizes the theory of the MT method including the source, the properties measured, assumptions, dimensionality, data acquisition and processing. Chapter 4 covers data acquisition for the Howley Basin survey, introducing the field information and methods from terrain to equipment used. This is then followed by my initial processing approach. Chapter 5 describes 1D imaging of the subsurface, and decomposition analysis. This chapter also describes the 2D inversions that were done on the data, and presents the 2D subsurface models that were

constructed. Finally, Chapter 6 presents my interpretation of the MT data.

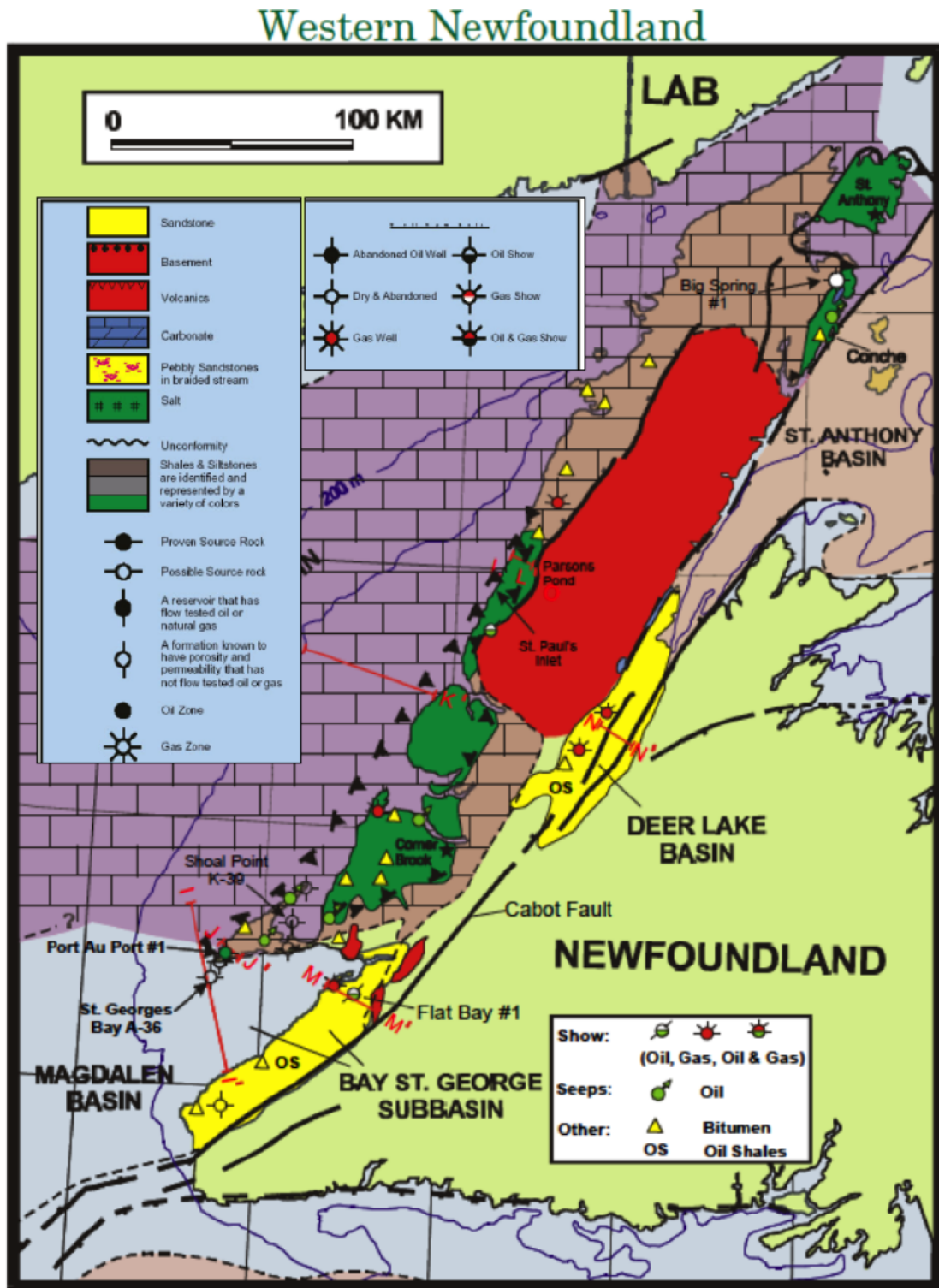


Figure 1.1: Geological map of western Newfoundland showing geological terranes, hydrocarbon shows, and well locations [Gov.of.NL, 2000].

## Deer Lake Basin

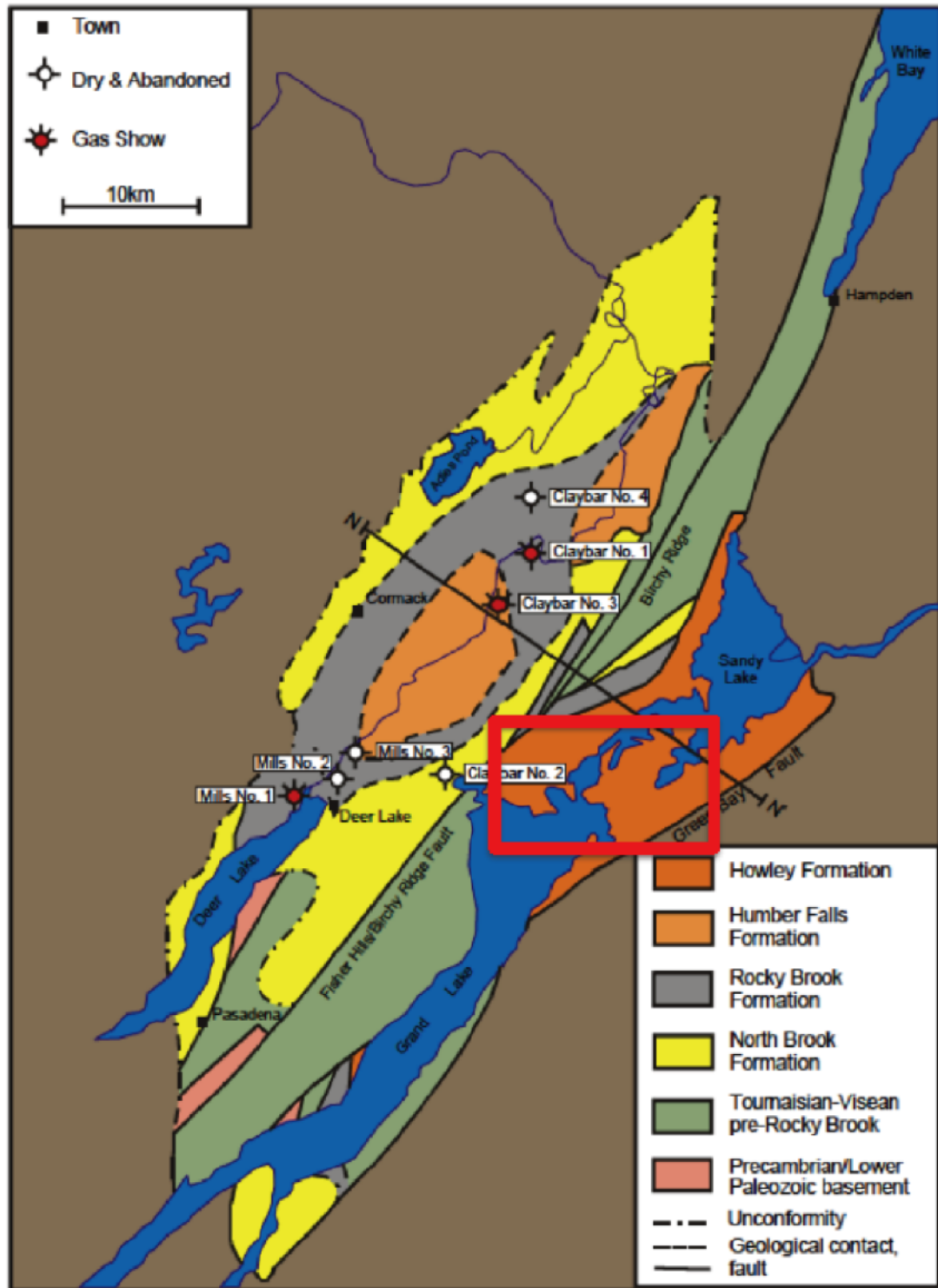


Figure 1.2: Geological map of the Deer Lake Basin showing well locations [Gov.of.NL, 2000]. The red rectangle indicates the survey area for this thesis.

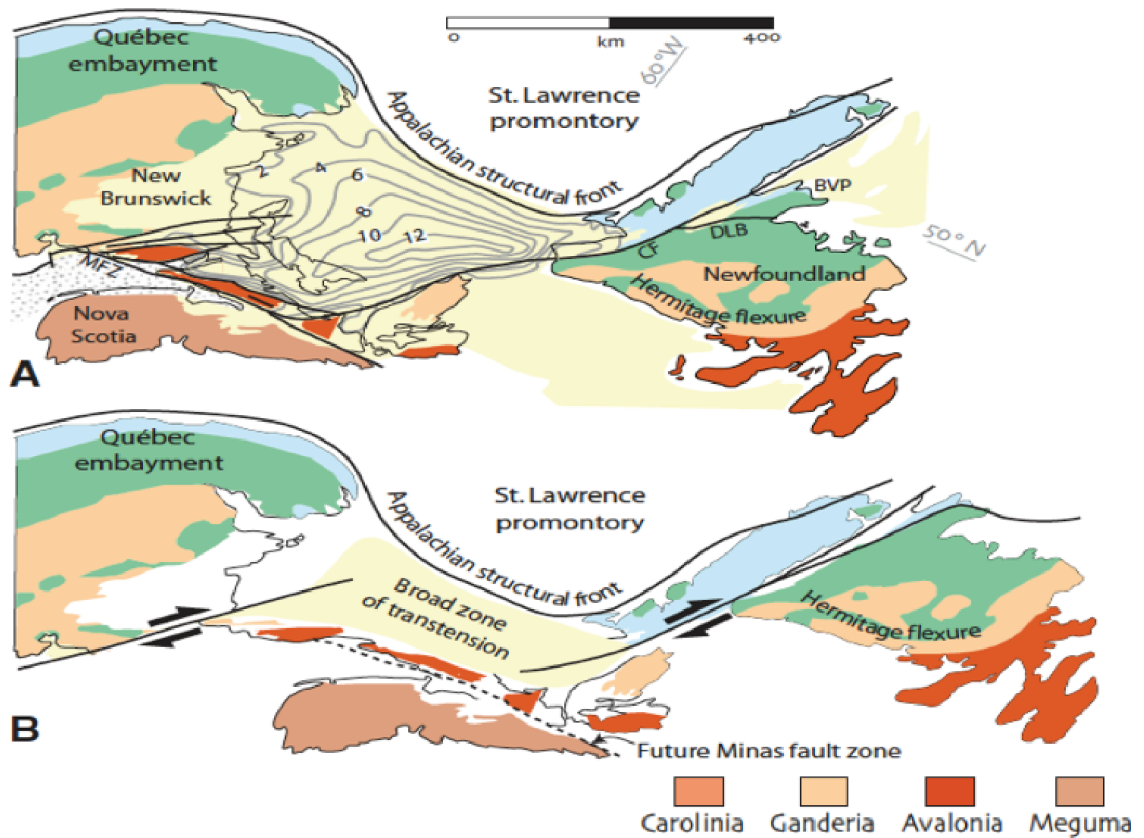


Figure 1.3: A: Late Paleozoic basins of the Maritimes Basin shown in yellow. Contours show depth of the basin in kilometres: CF-Cabot fault, DLB-Deer Lake Basin. B: Retrodeformed map showing inferred positions of the major blocks prior to the Devonian-Carboniferous strike slip [Hibbard and Waldron, 2009].

# Chapter 2

## Geology of the Howley Basin

### 2.1 Introduction to the geological history

The geology of the Howley Basin itself is largely unknown. No wells deeper than a few hundred metres have been drilled in the Howley Basin, however gravity and magnetic surveys were done over the area in the 1980's by Miller and Wright (1984). More is known about the general structure and lithology of the Cormack sub-basin and of the Deer Lake Basin as a whole. The development of the Deer Lake basin began in the Late Devonian-Early Carboniferous with deposition of two megasequences: the Anguille group (Tournaisian) and the Deer Lake group (Visean)[Martin, 2001]. It is thought that the normal faulting on the southeast margin created a land-locked half graben with an internal draining system which received several kilometres of the North Brook/Rocky Brook formation (see Figure 2.1) [Hamblin et al., 1997]. The Deer Lake Basin contains predominately non-marine sediments including alluvial fan deposits, braided and meandering river deposits, lacustrine and swamp deposits, all of which were laid down in a strike slip structural setting. Subsequent normal faulting led to deposition of the Humber Falls and Howley Formations [Langdon, 1993]. Later,

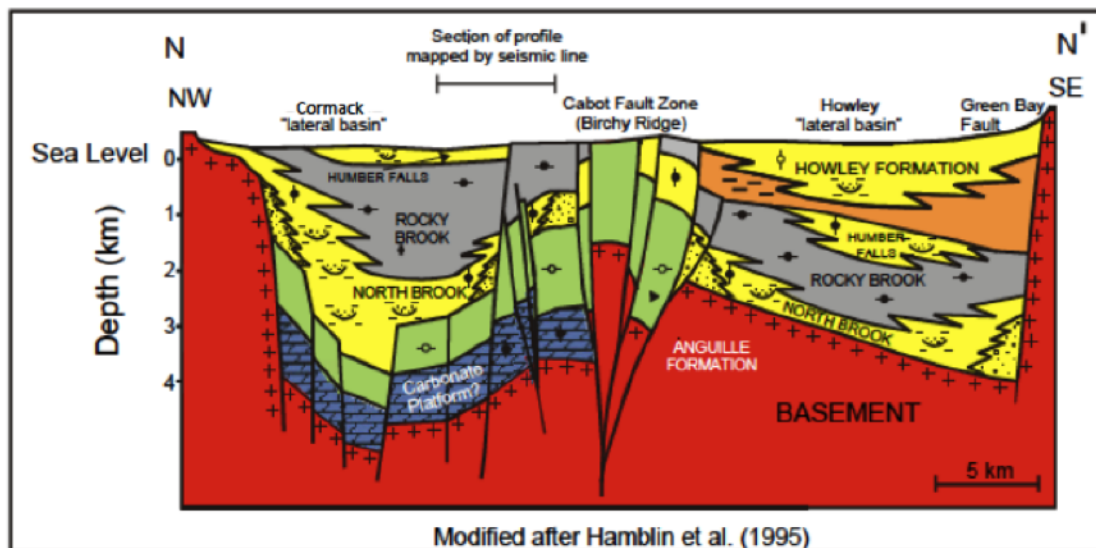


Figure 2.1: Structural profile of the Deer Lake Basin across the Cabot Fault, including the Cormack and Howley sub-basins. The location of this cross section is indicated in Figure 1.1 [Gov.of.NL, 2000].

transpressional shear created a 3-4 km deep, narrow central-uplifted flower structure complex along the Cabot Fault. This flower structure subdivided the basin into two parts: the Howley and Cormack lateral sub basins [Hamblin et al., 1997].

The cross-section shown in Figure 2.1 is based on studies and well cores done over the Cormack Basin; the Howley Basin interpretation is speculative based on the assumption of its symmetry to the Cormack Basin, and on gravity and magnetic surveys. Additionally, formations in the Howley sub-basin are based on the geological map of the Deer Lake Basin west of the Cabot fault.

## 2.2 Regional Maritimes Basin Geology

The west coast of Newfoundland lies within the northeast Canadian Appalachians which have been affected by multiple orogenic events. The earliest sedimentary sequence is a Late Proterozoic - Early Cambrian siliciclastic rift sequence deposited while the Iapetus Ocean formed [Cooper et al., 2001]. From Greenland to Texas a eastward sloping continental margin was deposited, followed by a basal clastic sequence and a series of upward shoaling carbonate cycles deposited throughout the middle Cambrian to early Ordovician.

The Howley Basin is part of the northern extension of the Maritimes Basin. The Maritimes Basin of Atlantic Canada (outlined in Figure 2.2) was tectonically active during the final assembly of Pangea from the Mid-Devonian to the Early Permian following terrane accretion and ocean closure. This was followed by a prolonged period of convergence that post-dated the collision of Gondwana and Laurasia [Martin et al., 2008]. The basin fill was laid down in suites of periodically connected fault-bounded depocenters, which could be associated with strike-slip faults. The basin fills are largely continental but include one open-marine interval with evaporite accumulation (Mississippian), as well as restricted-marine intervals reflecting progressive loss of oceanic connection. Basinal architecture testifies to rapid subsidence against a backdrop of glacioeustatic influence in a paleoequatorial setting [Martin et al., 2008].

## 2.3 Formations and Groups

The Deer Lake Basin rests unconformably on Grenvillian basement which forms the western border of the Early Palaeozoic Appalachian plate [Irving and Strong, 1984]. The basement is directly tied by early Cambrian volcanics and sediments across the

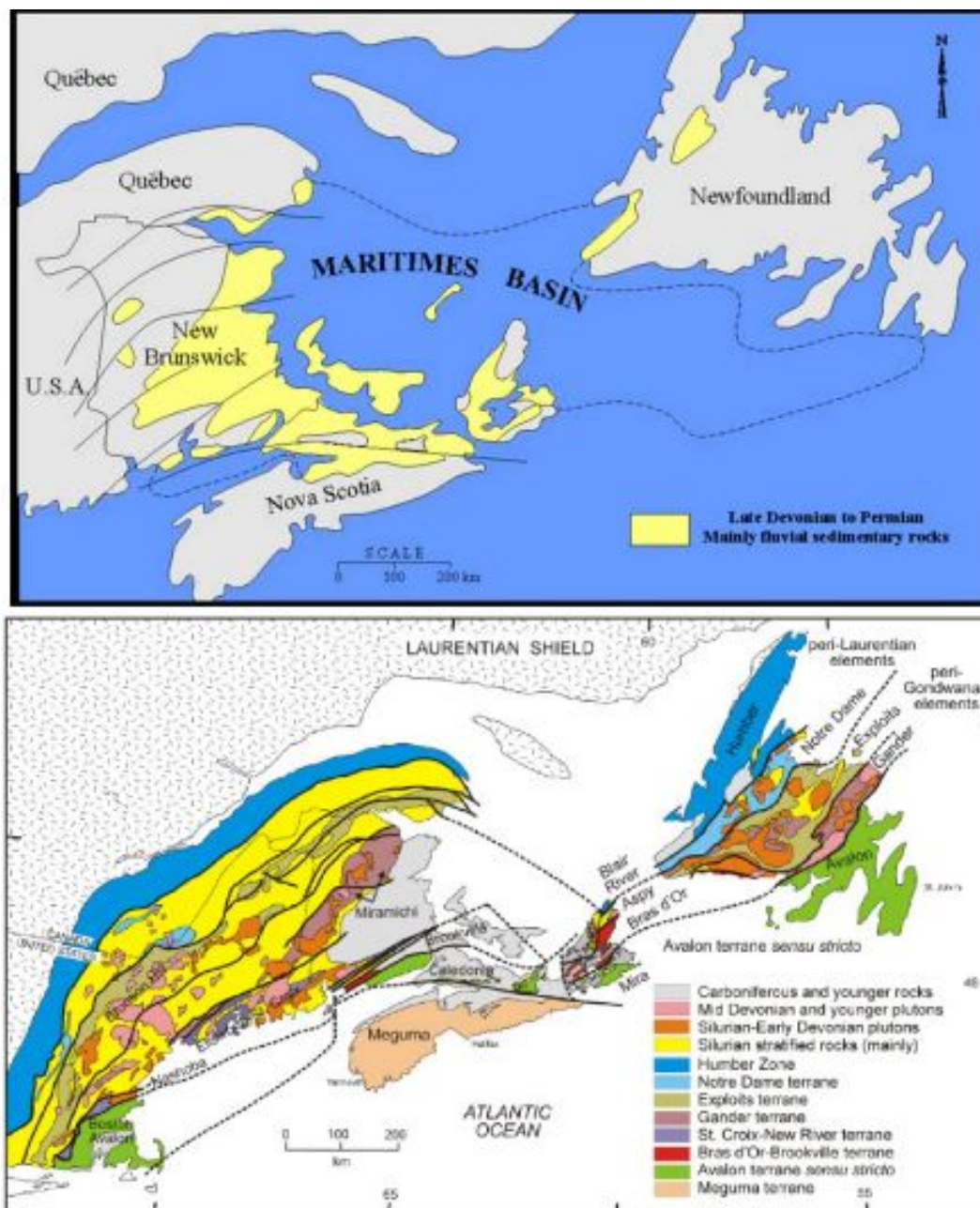


Figure 2.2: The Maritimes Basin of Atlantic Canada. Top: Outline showing the extent of the basin. Bottom: Geology of the area [Martin et al., 2008].

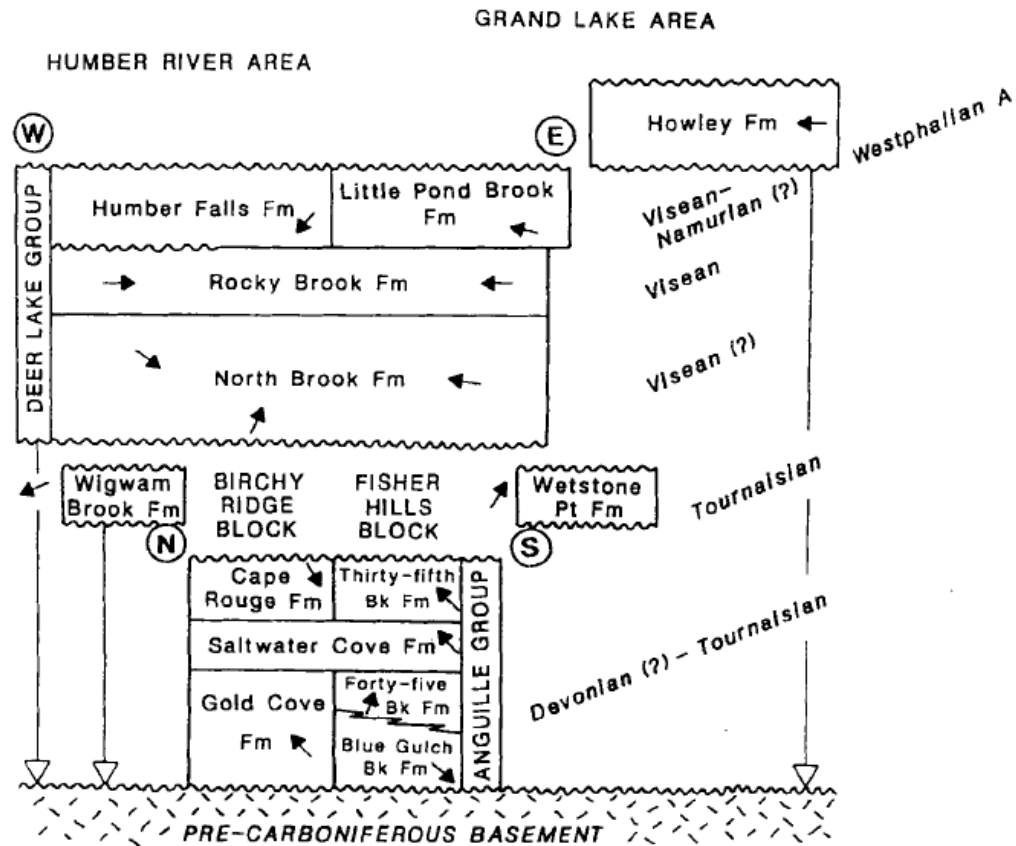


Figure 2.3: Stratigraphic units and their inferred ages in the Deer Lake Basin. [Martin, 2001]

Strait of Belle Isle to the Grenville Province of the mainland [Irving and Strong, 1984]. The Basin sediments have been subdivided into the Anguille, North Brook, Rocky Brook, Humber Falls and Howley formations [Hamblin et al., 1997]. Earlier exploration of the Cormack Basin has suggested Rocky Brook shales to have oil and gas generative capacity, and the sandstones of the North Brook to have good reservoir quality potential [Gov.of.NL, 2000]. Stratigraphic units and their inferred ages in the Deer Lake basin show onlapping relations and unconformities onto the basement (Figure 2.3) [Martin, 2001].

### **2.3.1 The Anguille Group**

The development of the Deer Lake Basin began in Late Devonian - Early Carboniferous, leading to Anguille deposition. Inclusion of Anguille Group lithologies as clasts in the later Tournaisian strata supports the concept of Late Tournaisian - Viséan relief and exposure of inverted, fault-bounded Anguille Group rocks [Hamblin et al., 1997]. The flower structures of the Anguille Group are portrayed as forming peninsulas in the Rocky Brook paleolake. There is no evidence that the Anguille group is present in the Howley sub-basin, and even if it is, being compact sandstone, MT would probably not be able to distinguish it from underlying igneous basement.

### **2.3.2 The North Brook Formation**

The North Brook Formation is the lowermost formation of the Deer Lake Group consisting of mainly red to grey conglomerates, siltstone, sandstone, and minor limestone. It is suggested that the formation has a thickness of 1200 m in the Cormack Basin, with thickness increasing southwards, and is interpreted as fluvial and alluvial fan deposits [Hamblin et al., 1997].

### **2.3.3 The Rocky Brook Formation**

The Rocky Brook Formation overlies the North Brook Formation. Its maximum thickness is estimated to be 550 m in the Cormack Basin, with its lower member consisting of red calcareous siltstone, grey to green siltstones and dolomitic limestone, and its upper member dominated by grey, green and black mudstones and siltstone [Irving and Strong, 1984]. Its deposition occurred in predominantly shallow, alkaline lacustrine and minor fluvial environments. It is fossil rich, and includes fish, ostracods and

plants. Oil shales and organic rich mudstones are characteristics of the Lower and Upper grey beds [Hamblin et al., 1997]. Samples from cores and outcrops have suggested excellent thermally immature potential source rock. Source rock intervals are commonly thin but can be very rich (up to 15 percent TOC). Type I organic derived matter containing algae *Botryococcus*, strong predominance of saturate over aromatic hydrocarbons and low pristane/phytane ratio are some of the features that the Rocky Brook Formation possesses. These features are common to other petroliferous Lower Carboniferous units in the Maritimes Basin of Atlantic Canada such as the Moncton Subbasin in New Brunswick, Cape Breton Island, and Conche in Newfoundland [Hamblin et al., 1997]. The origin of the bitumen in the Howley sub basin is more uncertain. In this area, east of the Cabot Fault, with the Howley formation overlaying it, the Rocky Brook rocks are buried deeper, making the Howley Basin potentially more hydrocarbon prone. Some general geological work has been done over the Deer Lake Basin targeting the Rocky Brook Formation (Figure 2.4) [Hamblin et al., 1997]. If present in the Howley Basin, the Rocky Brook Formation rocks are expected to have higher than normal electrical conductivities because of shale rich sediments.

### **2.3.4 The Humber Fall Formation**

Overlying the Rocky Brook formation is the Humber Falls formation. It is interpreted as an alluvial-fan to fluvial deposit, consisting of grey to reddish conglomerates and arkosic sandstone, as well as red to grey siltstones and mudstones [Irving and Strong, 1984]. Estimated thickness in the Cormack Basin, and also the speculated thickness in the Howley Basin, is 250 m [Hamblin et al., 1997] [Irving and Strong, 1984].

### 2.3.5 The Howley Formation

The Howley formation is lowermost Carboniferous in age, and it is interpreted to be a fluvial system in which high sinuosity channels were located on a well vegetated, but poorly drained alluvial plain [Hyde, 1979]. It is only found on the east side of the Cabot fault, where it is the most exposed formation. In the area where the MT data were acquired, the Howley Formation is the only one that has been mapped.

## 2.4 Geophysical Surveys in the Area

Gravity results published by Miller and Wright [1984] are included in this section as Figure 2.5. All images are spatially correlated with the geological map of the area shown in Figure 2.5(a). The study area discussed in this thesis is located in the south-east portion of these maps (outlined by the red square). The Bouguer anomaly (Figure 2.5b) shows a pronounced east-west low across this project's study area with a rapid increase to the south in the middle of the area. The gravity residual after removal of a regional trend (Figure 2.5c) shows the sharp rise along a SW-NE line that follows the hypothesized eastern edge of the Howley Basin and a localized low in the centre of this project's study area [Miller and Wright, 1984]. Additionally, a magnetic study was done by Miller and Wright [1984] in the area, and so the depth of the source of the magnetic anomaly is a good estimate of the thickness of the Howley Basin sediments. The gravity modelling based upon the density information suggested that 1.5 km of sediments is present in the Howley Basin. This thickness also agrees with the depth to the top of the magnetic feature, the anomalous high in the middle of the basin (Figure 2.6) [Miller and Wright, 1984].

The study by Hamblin et al. [1997], which used more recent magnetic data (Figure

2.7), interpreted Howley Basin to have an eastward dipping half-graben shape, with sediments thickening towards the eastern hinge zone (as seen in Figure 2.1). That study suggests that the sub-basin basin is 3-4 km deep. These results are quite different to those of Miller and Wright [1984], and hence more data or different types of surveys are needed to test the two interpretations.

No seismic reflection surveys have been shot in the immediate area of the MT survey, however, there is a more regional seismic dataset which Lithoprobe collected in 1989 [Van der Velden et al., 2004]. That seismic survey targeted deep crustal structures of the Newfoundland Appalachians, and therefore as the acquisition parameters were chosen to see deep structures, the shallower imaging was of poor quality and hindered the identification of major structural elements at shallower depths [Van der Velden et al., 2004]. Later, in 2004, the seismic reflection profiles were reprocessed (Figure 2.8) [Van der Velden et al., 2004]. Because of the large scale data, the Deer Lake Basin is only a small portion of the seismic section, viewed in the top west side of the profile (as a yellow lens), and as such the resolution is not good enough to distinguish between different sedimentary units in the basin, and even the basement of the basin is defined only approximately.

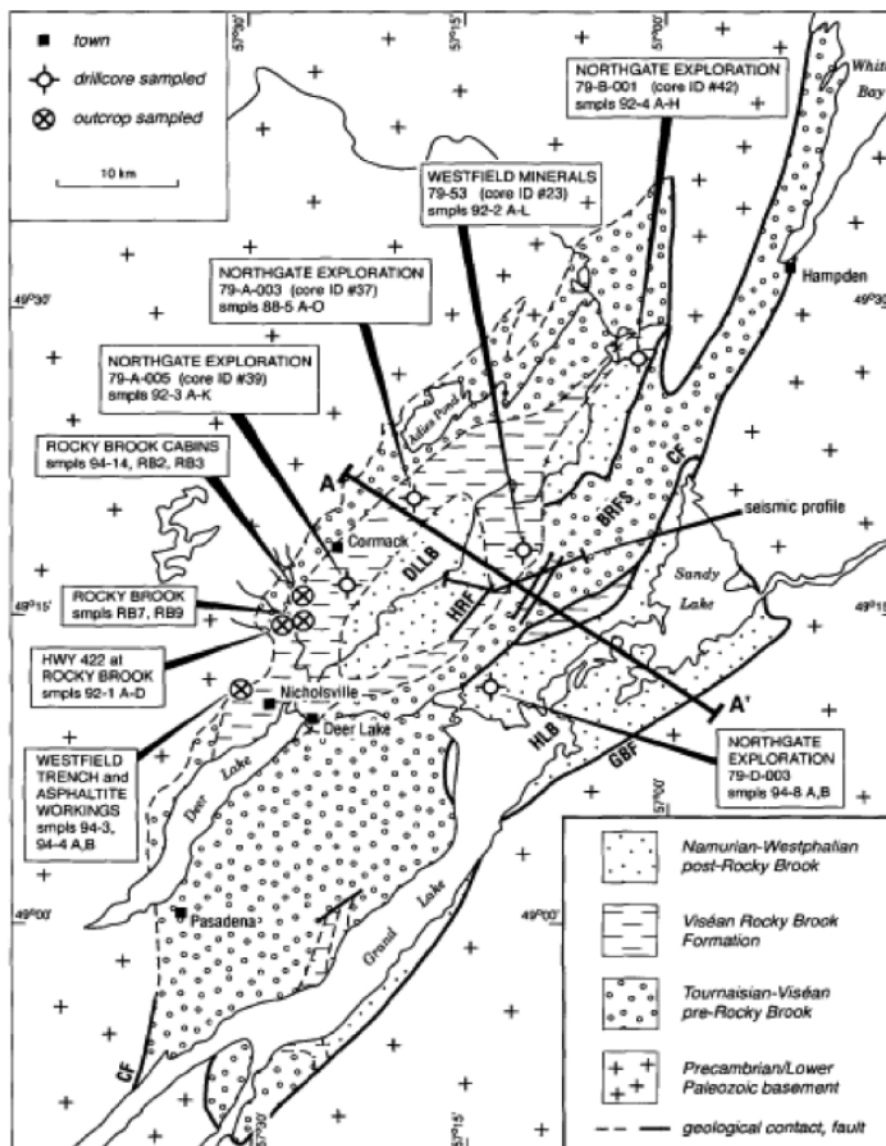


Figure 2.4: Simplified geology of the Deer Lake Basin, indicating distribution of the Rocky Brook Formation and cores/outcrops that have been sampled [Hamblin et al., 1997] The A-A' line corresponds with profile cross section in Figure 2.1.

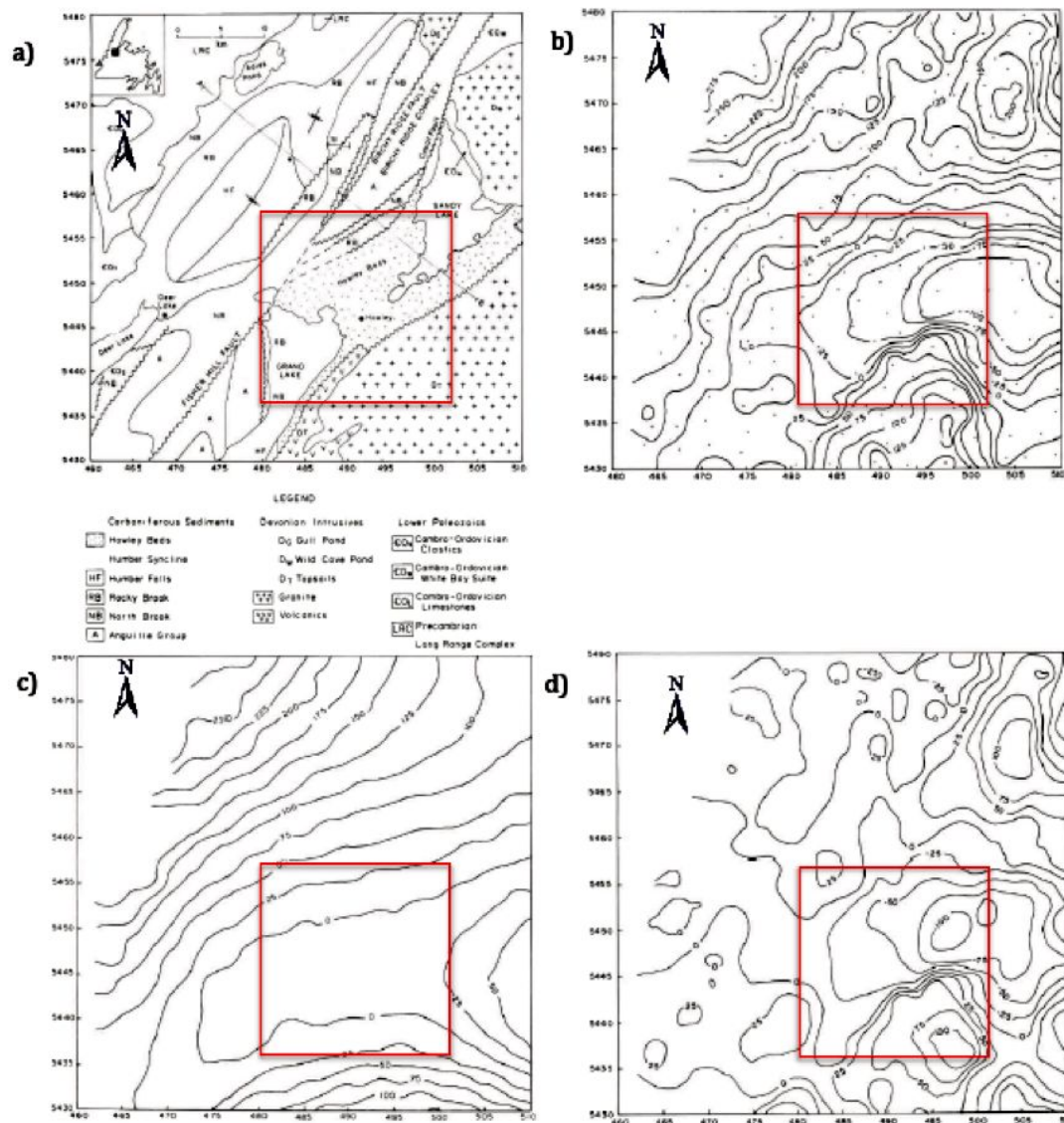


Figure 2.5: Gravity contour map of the Howley Basin from Miller and Wright [1984], with the same UTM coordinates as used in this thesis. (a) Geological map of the area; (b) Bouguer gravity anomaly with contour intervals of 2.5 mGal; (c) Regional trend surface for fifth order polynomial with contour intervals of 2.5 mGal; (d) Residual gravity found by subtracting trend values from Bouguer anomaly data with contours of 2.5 mGal. Red square outlines this project's study area. Blue line highlights the location of the profile in Figure 2.7. This project's profile is approximated by the green line.

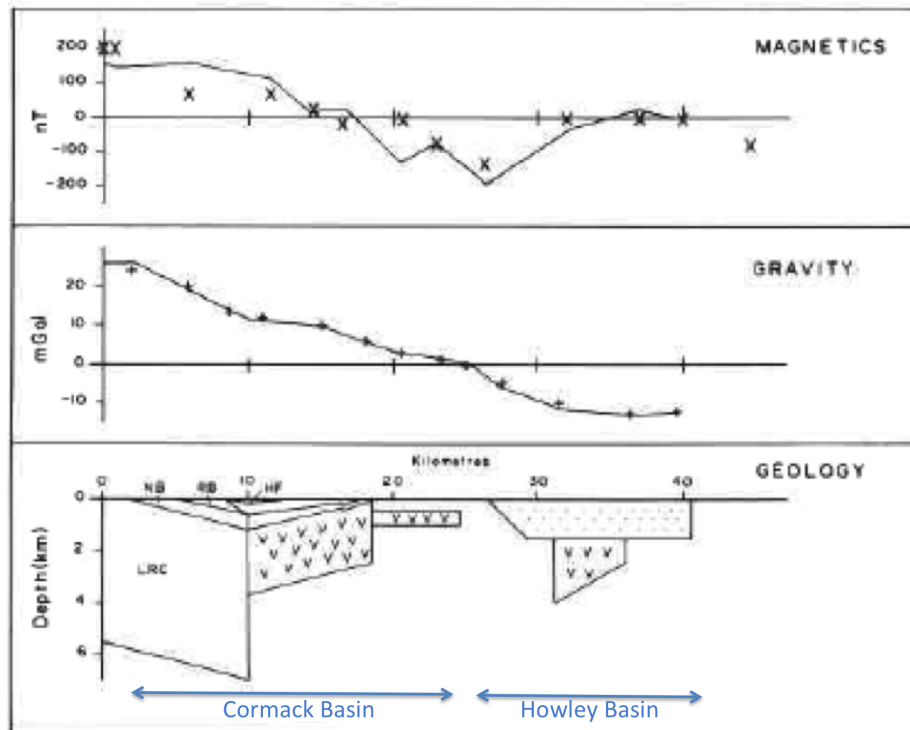


Figure 2.6: Modelled cross-section (location outlined in Figure 2.6 by a blue line) using Bouguer anomaly and observed magnetic anomaly by Miller and Wright [1984]. Legend is the same as in Figure 2.6 a.

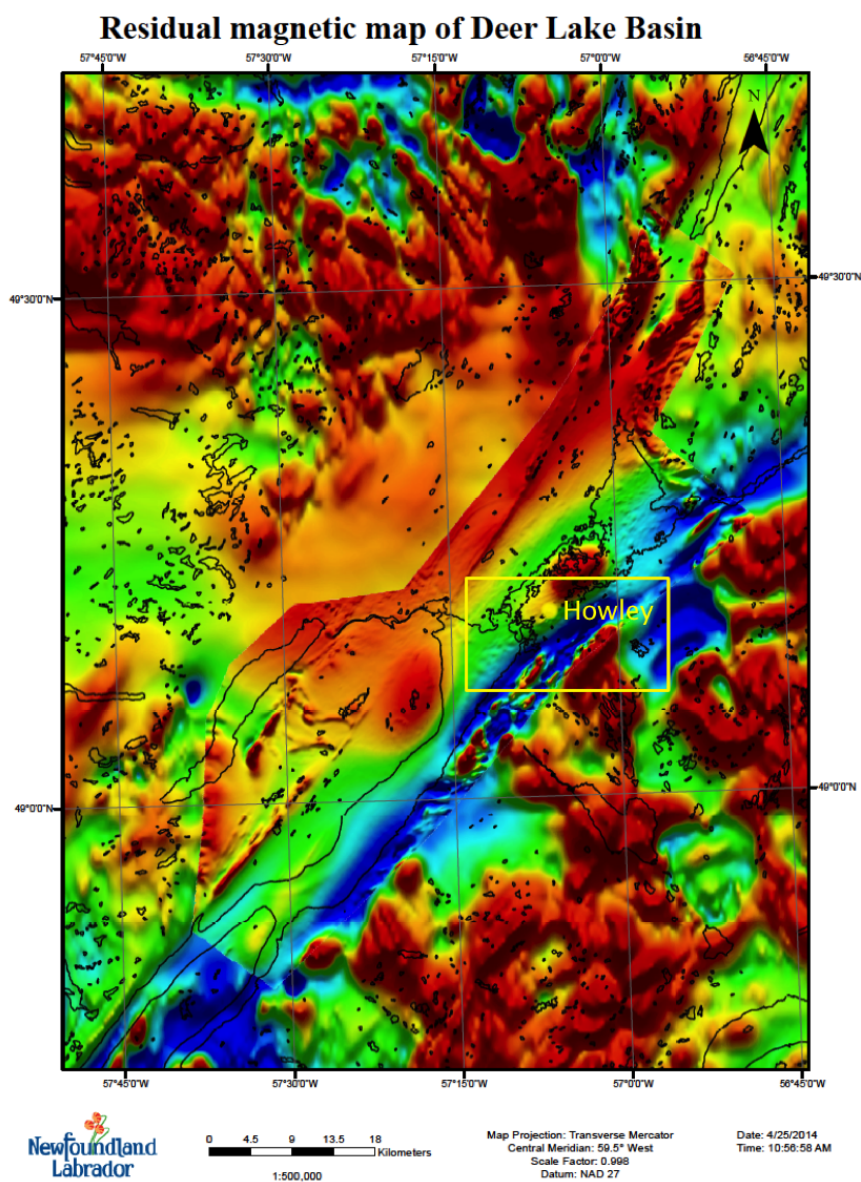


Figure 2.7: Residual magnetic anomaly map of the Deer Lake Basin (Government of Newfoundland and Labrador). Study area is outlined by the yellow rectangle. The discontinuity in the map is a result of using two data sets to create the map, regional dataset and more recent Deer Lake dataset.

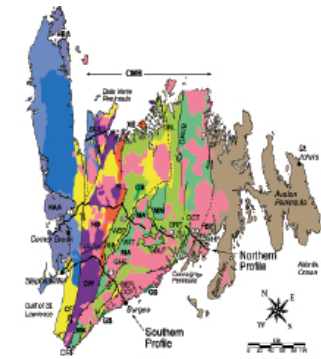


Figure 1: Tectonic provinces and basins of Newfoundland after Collins et al. (1993). See text for details on location of tectonic provinces and basins.

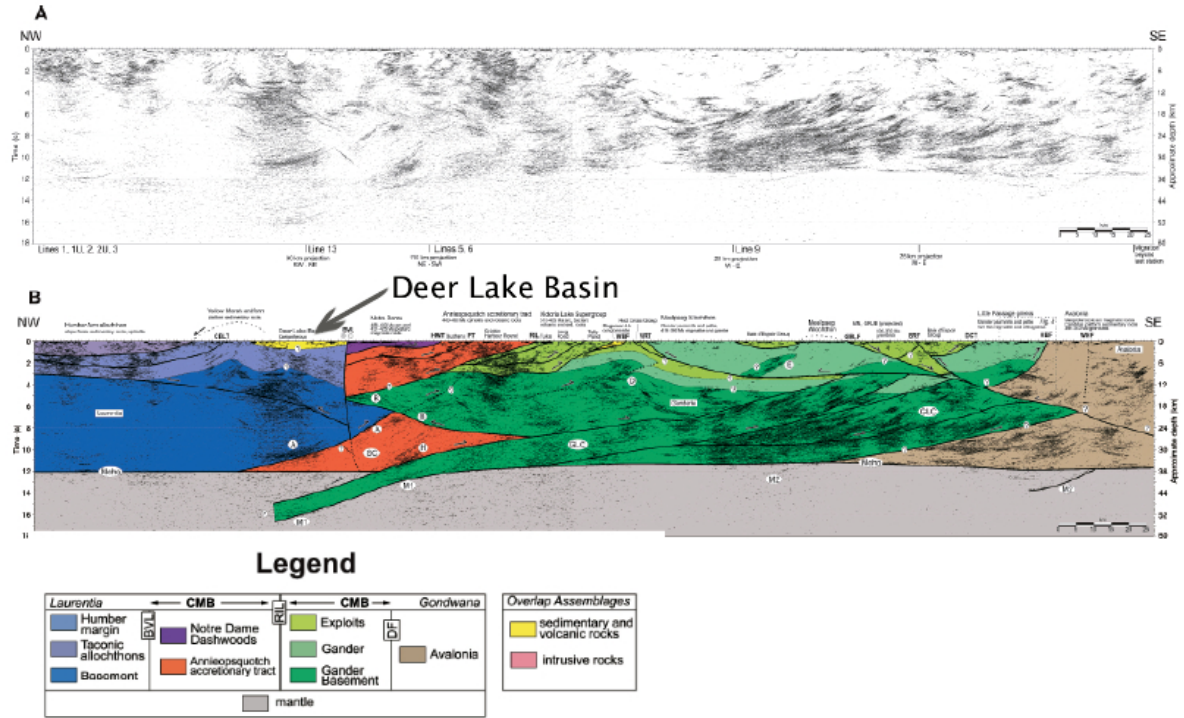
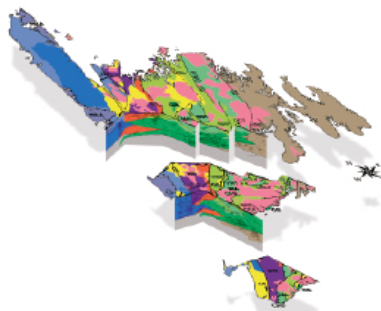


Figure 2.8: Migrated seismic reflection section of Lithoprobe onshore Vibroseis profiles across the island of Newfoundland, plotted 1:1 with an assumed velocity of 6000 m/s. Deer Lake basin is located in the top left of the section [Van der Velden et al., 2004].

# Chapter 3

## The Magnetotelluric Method

The magnetotelluric (subsequently referred to as MT) method is a geophysical method that uses natural electromagnetic signals to image the subsurface resistivity structure [Xiao and Unsworth, 2006]. It is a remote sensing technique that has the ability to image the Earth's electrical resistivity structure from depths of a few 100 metres to several 100's of kilometres. The MT method was chosen for this project in order to determine the depth to basement within the Howley basin.

In hydrocarbon exploration, MT is used in preference to traditional seismic methods in areas such as those including high velocity carbonates, shallow volcanics, over-thrust belts, salt structures and other such features that cause seismic methods problems. This is not the case with the Howley Basin. However MT was used as a supplementary method to compliment seismic and other geophysical studies in the area. MT has a lower spatial resolution than seismic reflection, but is less expensive and has lower environmental impact [Xiao and Unsworth, 2006].

### 3.1 The Source

Magnetotelluric fields result from the flow of charged particles in the ionosphere, such as lightning and solar energy, causing natural variations in the Earth's magnetic field, that induce electric currents in the Earth's subsurface [Kearey and Brooks, 1991]. There are many sources of these naturally occurring time variations of the magnetic field. Sources for electromagnetic fields with frequencies higher than 1 Hz (or periods shorter than 1s) are caused by meteorological activities such as lightning discharges. These signals are known as 'sferic'. While local lightning discharges might saturate amplitudes, the signals from the widely distributed equatorial regions that propagate around the world within a waveguide bounded by the ionosphere and the Earth's surface are highly significant [Simpson and Bahr, 2005]. These signals propagate as Transverse Electric (TE), Transverse Magnetic (TM) or Transverse Electric and Magnetic modes (discussed later). Interaction between the solar plasma wind and the geomagnetic field, and the solar radiation ionizing effects on the upper atmosphere, produce electromagnetic field with frequencies lower than 1 Hz (periods longer than 1s) (Figure 3.1) [Simpson and Bahr, 2005]. It is these low amplitude fluctuations of external origin that MT sounding seeks to exploit as opposed to the magnetic field generated in the Earth's outer core [Simpson and Bahr, 2005]. The power spectrum of the naturally occurring time variations in the Earth's field (which is shown in Figure 3.1) also illustrates the reduced signal power in the so called 'dead band' around 1 Hz. In MT soundings this is manifested by reduced data quality [Simpson and Bahr, 2005].

Plasma contains high-energy positive and negative particles, and although it is electrically neutral, because the number of positive and negative charges are equal, it contains free electric charge that makes it electrically conductive. Plasma responds strongly to the electromagnetic field and gives rise to electric currents in near Earth

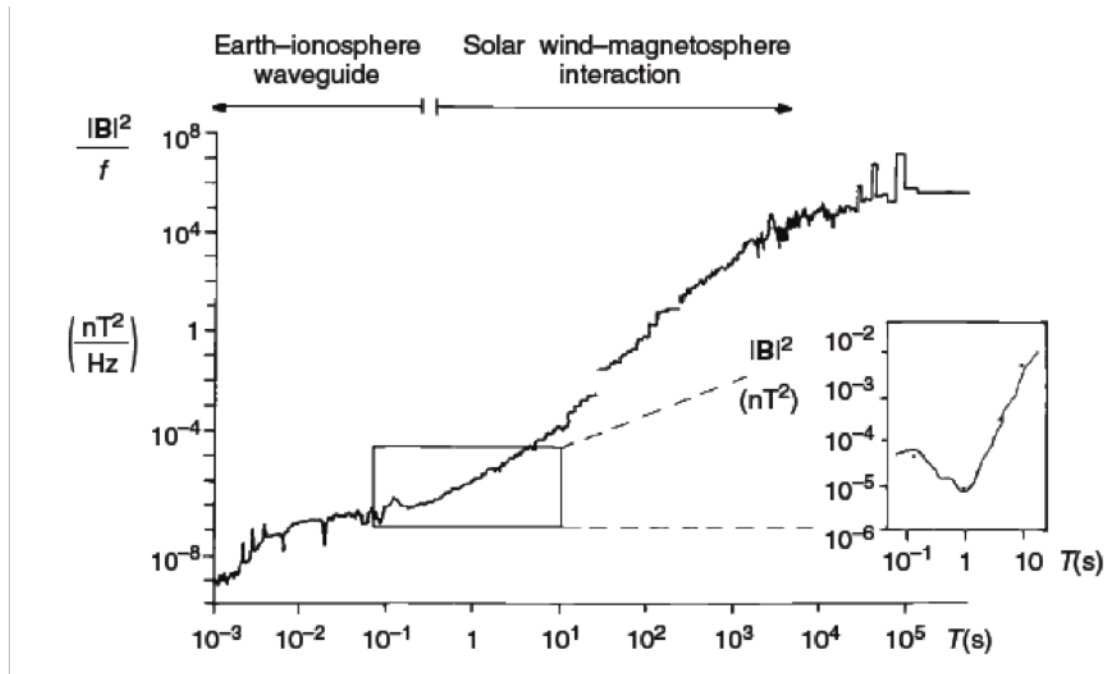


Figure 3.1: Power spectrum illustrating  $1/f$  characteristics of the Earth’s magnetic field. Short period signals are produced by interaction in the Earth-ionosphere waveguide, and long period signals are generated by solar wind-magnetosphere interaction. Insert emphasizes the reduced signal in the dead-band around 1 Hz [Simpson and Bahr, 2005].

space [Viljanen, 2012]. Earth has a strong internal field that can be approximated by a dipole field with an axis tilted  $11^\circ$  from the rotation axis. However, forced by solar winds, the dipole field is modified (Figure 3.2) by compression on the sunward (day) side and elongation on the night side. This is the reason why the waveguide between surface and ionosphere during the day is approximately 60 km wide, and 90 km wide at night [Simpson and Bahr, 2005].

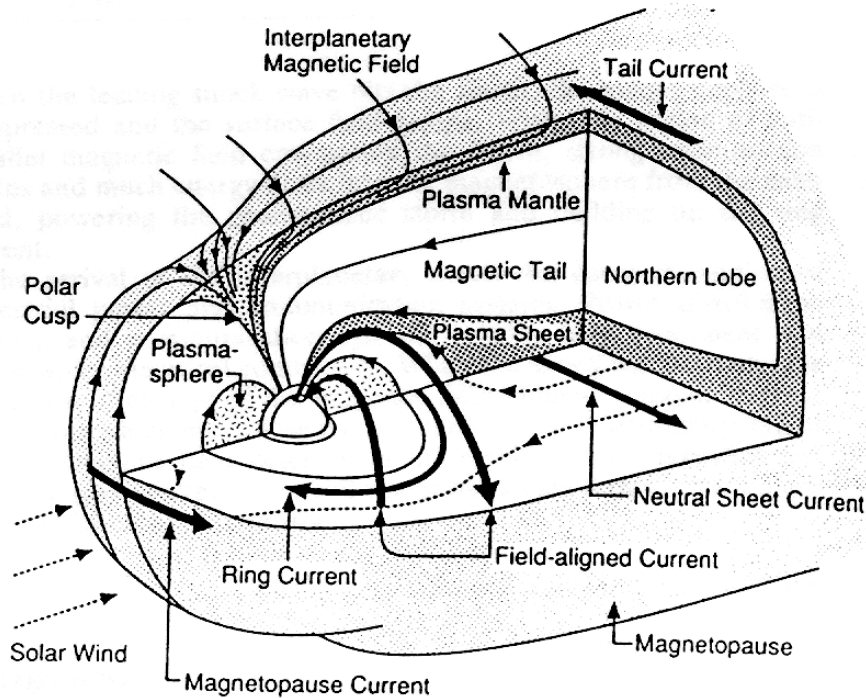


Figure 3.2: The magnetosphere [Viljanen, 2012].

## 3.2 Electrical Properties of Earth materials

The MT method is a geophysical technique that detects variations in the electrical resistivity structure of the subsurface. Resistivity is measured in Ohm-metres ( $\Omega m$ ), and its inverse, electrical conductivity, is measured in Siemens/metre ( $S/m$ ). The resistivity structure can be correlated to geological units to provide a subsurface image or map of the Earth. In the first few kilometres of the subsurface, resistivity is highly dependent on fluid content and its salinity, pore volume porosity, and conductive mineral content. The general correlation between resistivity and material is shown by Figure 3.3. Resistivity can be lowered by an increase of salinity or fluid volume, and presence of clay minerals (in shale and other mudstones), graphitic carbon, and metallic mineralization. Fault zones can be moderately conductive due to greater mineralization along them [Rodriguez and Sampson, 2010].

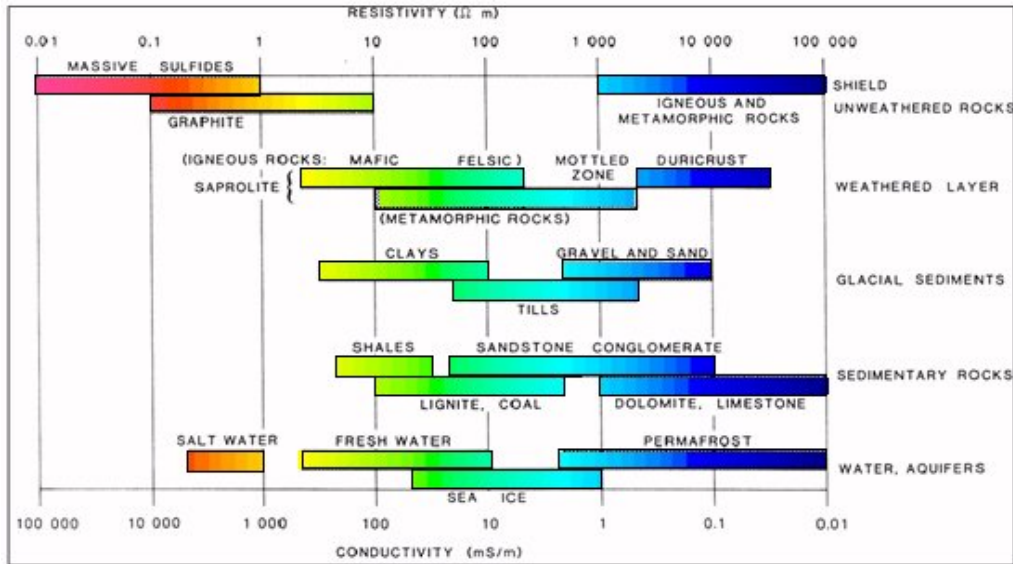


Figure 3.3: Typical ranges of conductivities of Earth materials [Nabighian, 1987] (this is a standard conductivity table found in many text books).

Electric conductivity measures the ability of a material to conduct electric current. As mentioned above it is dependant on minerals as well as the rock types and it is influenced by its overall environment: wetness/dryness, temperature, the connectivity of the minerals. Conductivity  $\sigma$  relates the electric conduction current density  $\mathbf{j}_f$  and the electric field  $\mathbf{E}$  by Ohm's Law:

$$\mathbf{j}_f = \sigma \mathbf{E}. \quad (3.1)$$

The ability to become polarized by an external electric field, and hence reduce the total electric field inside a medium, is called permittivity  $\epsilon$ . This relates the electric field  $\mathbf{E}$  to electrical displacement  $\mathbf{D}$ :

$$\mathbf{D} = \epsilon \mathbf{E}. \quad (3.2)$$

The total electric current density  $\mathbf{j}$  is given by the sum of the current density (the

diffusion part) and the displacement current:

$$\mathbf{j} = \sigma \mathbf{E} + \frac{\partial \mathbf{D}}{\partial t}. \quad (3.3)$$

The process becomes purely diffusive if the displacement current is negligibly small compared to the conduction currents [Miensopust, 2010]. Combining equations 3.3 with the frequency-period relationship  $T = 2\pi/\omega$ , gives the limits on the assumption of negligible displacement current [Miensopust, 2010]:

$$\sigma \mathbf{E} \gg \frac{\partial \mathbf{D}}{\partial t} \Rightarrow 1 \gg \frac{\frac{\partial \mathbf{D}}{\partial t}}{\sigma \mathbf{E}} = \frac{\varepsilon \frac{\partial \mathbf{E}}{\partial t}}{\sigma \mathbf{E}} \simeq \frac{\varepsilon}{\sigma T}. \quad (3.4)$$

Hence, the displacement current term becomes small enough to be neglected, only if the following is true [Miensopust, 2010]:

$$T \gg \frac{\varepsilon}{\sigma}. \quad (3.5)$$

For MT surveys with common periods ranging between  $10^{-5}s$  to  $10^5s$  equation 3.5 is valid for almost all MT data. The minimum conductivity value amongst rocks (about  $10^{-6}S/m$ ) and maximum electric permittivity value makes the displacement currents comparable with conductivity currents if the period of interest is about  $10^{-4}s$  or less. However, it is more likely one would be dealing with materials with larger conductivity and hence the period at which displacement currents are not negligible would be smaller than  $10^{-5}s$ , which is not recorded by MT [Miensopust, 2010]. In conclusion, in MT studies the displacement current can be neglected and the induction in the Earth can be treated as a pure diffusion process (called the quasi static approximation).

Materials also have a magnetic permeability value  $\mu$  which quantifies the ability of a material to be magnetized when a magnetic field is applied. It is also a factor that relates the magnetic intensity  $\mathbf{B}$  to the magnetic induction  $\mathbf{H}$ :

$$\mathbf{H} = \frac{1}{\mu} \mathbf{B}. \quad (3.6)$$

Generally, Earth's materials have magnetic permeabilities close to that of free space (vacuum), excluding rocks with high iron content. The presence of iron rich ferrimagnetic minerals, such as magnetite, can affect the apparent resistivity reading of a MT survey [Miensoopust, 2010]. However, we can generally assume:

$$\mu = \mu_0. \quad (3.7)$$

### 3.3 MT Equations

One measures and relates the time-varying oscillations of the natural electric and magnetic fields; the response curve, amplitude, and phase lag are calculated from perpendicular electric ( $E_x$ ) and magnetic ( $H_y$ ) fields (x and y are the two horizontal, mutually perpendicular co-ordinate directions) [Spratt and Craven, 2011]. So, as a result, the apparent resistivity of the subsurface is then represented by [Xiao and Unsworth, 2006]:

$$\rho_{xy} = \frac{1}{2\pi f \mu_0} \left| \frac{\mathbf{E}_x}{\mathbf{H}_y} \right|^2 \quad (3.8)$$

where  $f$  is the frequency and  $\mu_0$  is the permeability of free space. The depth of penetration in the Earth is controlled by the skin depth ( $\delta$ ) phenomena, defined by [Xiao and Unsworth, 2006]:

$$\delta = \sqrt{\frac{2}{\omega\mu\sigma}}, \quad (3.9)$$

where  $\rho$  is the resistivity of the Earth.

Equation (3.9) indicates that the depth of the penetration decreases as the electromagnetic signal frequency increases. The electrical resistivity of the subsurface commonly ranges from 0.1 to 10 000  $\Omega m$  (Figure 3.3), and the frequencies used in MT span from 1000 to 0.0001 Hz giving skin depths from less than 100 m to hundreds of kilometres. In data processing and interpretation, multiple frequencies are used to determine variation with depth of the electrical resistivity.

The behaviour of electromagnetic fields at any frequency is described by Maxwell's equations [Simpson and Bahr, 2005]:

$$\nabla \times \mathbf{E} = -\frac{\partial \mathbf{B}}{\partial t} \quad (3.10)$$

$$\nabla \times \mathbf{H} = \mathbf{j}_f \quad (3.11)$$

$$\nabla \cdot \mathbf{B} = 0 \quad (3.12)$$

$$\nabla \cdot \mathbf{D} = \eta_f \quad (3.13)$$

where, as mentioned previously,  $E$  is the electric field,  $B$  is the magnetic induction,  $H$  is the magnetic intensity,  $j_f$  is conduction current density,  $D$  is the electric displacement and  $\eta_f$  is free charge density.

For the purpose of the MT technique, one can assume that at mid latitudes (such as Newfoundland) the measured fields are due to large scale uniform, horizontal sheets

of current far away in the ionosphere or lightning strikes at equatorial latitudes. The fields from such sources can be considered to be plane waves, i.e., waves with a planar wave front across which the fields are constant. Also, because of the dramatic contrast in physical properties between air and the ground, the plane waves can be thought of as impinging on the Earth's surface at normal incidence [Simpson and Bahr, 2005]. The mathematical equations for a plane wave propagating in the vertical z-direction are:

$$\mathbf{E} = \mathbf{E}_0 e^{i(\omega t - kz)} \quad (3.14)$$

$$\mathbf{H} = \mathbf{H}_0 e^{i(\omega t - kz)} \quad (3.15)$$

with amplitudes at the origin of  $E_0$  and  $H_0$ , angular frequency  $\omega$  (period  $T = 2\pi/\omega$ ), and wavelength  $\lambda = 2\pi/k$  ( $k$  is a wavenumber), and  $i$  is  $\sqrt{-1}$ .

The plane wave assumption is fundamental to the MT technique because it the wavenumber not to vary and thus can be neglected. The impedance tensor calculated from the orthogonal electric and magnetic fields at any given site should then be self-similar regardless of when the fields are recorded [Simpson and Bahr, 2005].

The impedance tensor  $Z$  is a complex-valued, frequency dependent tensor that describes the relationship between the orthogonal horizontal ( $E_x, E_y$ ) and magnetic field components ( $\mathbf{H}_x, H_y$  or  $\mathbf{B}_x/\mu_0, \mathbf{B}_y/\mu_0$ ):

$$\mathbf{E} = Z \frac{\mathbf{B}}{\mu_0} \text{ or } \begin{pmatrix} \mathbf{E}_x \\ \mathbf{E}_y \end{pmatrix} = \begin{pmatrix} \mathbf{Z}_{xx} & \mathbf{Z}_{xy} \\ \mathbf{Z}_{yx} & \mathbf{Z}_{yy} \end{pmatrix} \begin{pmatrix} \frac{\mathbf{B}_x}{\mu_0} \\ \frac{\mathbf{B}_y}{\mu_0} \end{pmatrix}. \quad (3.16)$$

The tensor  $\mathbf{Z}$  is complex, containing real and imaginary parts, meaning not only a

magnitude for each element but a phase as well [Miensopust, 2010].

## 3.4 Dimensionality

MT signatures can be 1D, 2D, or 3D. 1D analysis assumes that the conductivity varies only with depth, while 2D assumes that it varies with depth and one horizontal direction (usually perpendicular to an electric strike, with the signature being unchanged along the strike), and 3D assumes the response to come from three dimensional structures that vary in both horizontal directions as well as with depth.

### 3.4.1 1D Earth

1D is the simple situation that assumes conductivity  $\sigma$  varies only with depth. Such a conductivity variation can be approximated as a stack of uniform layers. In this case, the impedance tensor is simplified as the diagonal components equal zero ( $\mathbf{Z}_{xx} = \mathbf{Z}_{yy} = 0$ ), and since lateral conductivity variation is not present the off-diagonal components have the same amplitude but different signs ( $\mathbf{Z}_{xy} = -\mathbf{Z}_{yx}$ ) [Miensopust, 2010].

$$\begin{pmatrix} \mathbf{E}_x \\ \mathbf{E}_y \end{pmatrix} = \begin{pmatrix} 0 & \mathbf{Z}_{xy} \\ -\mathbf{Z}_{xy} & 0 \end{pmatrix} \begin{pmatrix} \frac{\mathbf{B}_x}{\mu_0} \\ \frac{\mathbf{B}_y}{\mu_0} \end{pmatrix}. \quad (3.17)$$

From equation 3.17 one can simply determine the elements of the impedance tensor as:

$$\mathbf{E}_x = \mathbf{Z}_{xy} \cdot \frac{\mathbf{B}_y}{\mu_0} \Rightarrow \frac{\mathbf{E}_x}{\frac{\mathbf{B}_y}{\mu_0}} = \mathbf{Z}_{xy} \implies \mathbf{Z}_{xy} = \mu_0 \frac{\mathbf{E}_x}{\mathbf{B}_y} = -\mu_0 \frac{\mathbf{E}_y}{\mathbf{B}_x}. \quad (3.18)$$

Finally, the apparent resistivity  $\rho_a$ , and the impedance phase  $\phi$  are given by:

$$\rho_a = \frac{1}{\mu_0 \omega} |\mathbf{Z}|^2 \quad (3.19)$$

$$\phi = \tan^{-1} \left( \frac{\text{Im}\mathbf{Z}}{\text{Re}\mathbf{Z}} \right). \quad (3.20)$$

In the case of an isotropic, homogenous half-space,  $\rho_a$  is equal to the actual resistivity value of the half-space [Miensoopust, 2010]. A MT phase angle can be defined as the phase shift between  $E_x$  and  $H_y$  [Xiao and Unsworth, 2006].

### 3.4.2 2D Earth

2D models are characterized by a strike direction along which the conductivity structure is constant [Weidelt and Chave, 2012]. Conservation of current is the physical principle governing induction at a discontinuity in geological structure such as a contact (Figure 3.4), and since current flow across a boundary must be conserved, the change in conductivity means there is a discontinuity in electric field normal to the discontinuity [Simpson and Bahr, 2005]. The MT response would be distinct on either side of the contact and far from it, and its characteristics would be different for the electric field polarized across strike and along strike (Figure 3.4) [Weidelt and Chave, 2012].

In a 2D Earth, the apparent resistivities and phase lag are different along strike than perpendicular to strike [Spratt and Craven, 2011]. For the strike in the x-direction,  $\mathbf{E}_x$ ,  $\mathbf{H}_y$ , and  $\mathbf{H}_z$  comprise the transverse electric (TE) mode, and  $\mathbf{H}_x$ ,  $\mathbf{E}_y$ , and  $\mathbf{E}_z$  comprise the transverse magnetic (TM) mode [Xiao and Unsworth, 2006]. These two modes are independent of each other.

For a 2D model, equations (3.10) and (3.11) decompose into two distinct modes. For

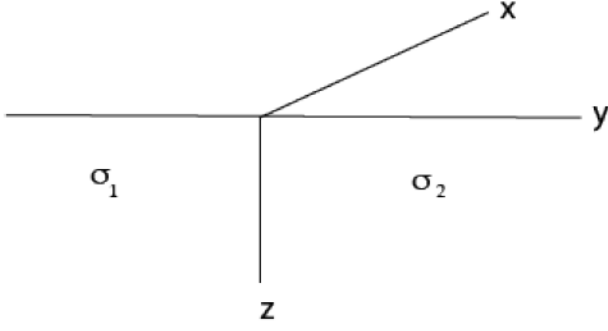


Figure 3.4: A simple 2D model consisting of two abutting quarter spaces with different conductivities  $\sigma_1$  and  $\sigma_2$  meeting at a vertical contact. The  $x$ -direction is the strike direction for this example [Weidelt and Chave, 2012].

the E-polarization or TE mode ( $\mathbf{E}$  points in strike direction, and  $\mathbf{B}$  lies in the plane orthogonal to strike), equations (3.10) and (3.11) reduce to the following in component form:

$$\partial_z \mathbf{E}_x = -i\omega \mathbf{B}_y \quad (3.21)$$

$$-\partial_y \mathbf{E}_x = -i\omega \mathbf{B}_z \quad (3.22)$$

$$\partial_y \mathbf{B}_y - \partial_z \mathbf{B}_z = \mu_0(\sigma \mathbf{E}_x + \mathbf{J}_x) \quad (3.23)$$

and for B-polarization or TM mode ( $\mathbf{B}$  points in strike direction, and  $\mathbf{E}$  lies in the plane orthogonal to strike):

$$\partial_z \mathbf{B}_x = \mu_0(\sigma \mathbf{E}_y + \mathbf{J}_y) \quad (3.24)$$

$$-\partial_y \mathbf{B}_x = \mu_0(\sigma \mathbf{E}_z + \mathbf{J}_z) \quad (3.25)$$

$$\partial_y \mathbf{E}_z - \partial_z \mathbf{E}_y = -i\omega \mathbf{B}_x. \quad (3.26)$$

Determining the strike direction of MT data is often done by a technique that separates the effect of regional-scale and small-scale structures in the data, called tensor

decomposition [Xiao and Unsworth, 2006]. As described later, a mathematical decomposition analysis of directionality is used to determine the dimensionality of a real data-set, to determine the preferred geo-electric strike direction consistent with the data, and to examine the data for effects of galvanic distortion [Spratt and Craven, 2011]. The galvanic effect is a frequency independent response of the Earth to electric fields which can distort MT impedance tensors [Simpson and Bahr, 2005].

For a 2D model the impedance tensor is simplified from equation (3.16) as the diagonal elements are zero when the coordinate system is aligned with the geoelectric strike, and the off-diagonal elements ( $\mathbf{Z}_{xy}$  and  $\mathbf{Z}_{yx}$ ) represent the two modes:

$$\mathbf{Z}_{2D} = \begin{pmatrix} 0 & \mathbf{Z}_{xy}(\omega) \\ \mathbf{Z}_{yx}(\omega) & 0 \end{pmatrix} = \begin{pmatrix} 0 & \mathbf{Z}_{TM}(\omega) \\ \mathbf{Z}_{TE}(\omega) & 0 \end{pmatrix} \quad (3.27)$$

In order to invert and process data as 2D, one must assess to what extent the data can be considered 2D. If the data are 2D, then the electric strike should be consistent throughout the survey area. If the strike is not consistent then the structure is 3D, and problems can arise when using 2D inversions to interpret such data [Qibin et al., 2011]. 2D interpretation of the data may be appropriate for a limited number of sites and over a limited period band. As the Howley Basin is an elongated structure, it was expected that the regional-scale electrical structures would have a strike parallel to that of the surface geological features, and hence that the data can be treated as 2D. When a 3D body is parallel to the regional 2D strike, the TE mode is affected by galvanic and inductive elongated effects, whereas the TM mode is affected mainly by galvanic effects, making it suitable for 2D interpretation [Ledo, 2004].

In this project, the frequencies are grouped into decades, and the best strike is deter-

mined for each decade for each station. The direction of the strike plays an important role because, for the decades and stations for which the phase difference is greater than  $10^\circ$  between TE and TM modes, this is an indication that the Earth cannot be considered 1-D. The simplest dimensionality estimator available is calculating the error when data is fit to a particular strike. The Groom-Bailey decomposition involves a formal least square fit to the observed impedance (or more correctly to linear combinations of the observed impedance). It has been shown that for RMS values of misfit greater than two, the data might be highly contaminated (noisy) or 3D [Spratt and Craven, 2011]. If a whole data-set has a large error, different period ranges can be used to interpret the data for different depth ranges (short periods for shallower depths, and longer periods for deeper). Having a basin sitting on top of a possible igneous complex as in the Howley Basin case, it is possible that more than one strike may be appropriate: one for the basin sediments and one for the basement.

An alternative method (not covered in this project) to evaluate the dimensionality of regional electrical structure is to use skewness (S) which was introduced by Swift in 1967. This parameter is used to assess whether the electrical structure is 2D. Skewness is given by [Qibin et al., 2011]:

$$S = \frac{|\mathbf{Z}_{xx} + \mathbf{Z}_{yy}|}{|\mathbf{Z}_{xy} - \mathbf{Z}_{yx}|} \quad (3.28)$$

where  $\mathbf{Z}_{xx}$ ,  $\mathbf{Z}_{yy}$ ,  $\mathbf{Z}_{xy}$ ,  $\mathbf{Z}_{yx}$  are the impedance tensor elements. Bahr [1991] introduced phase sensitive skewness  $\eta$  which considers distortion in impedance tensors [Qibin et al., 2011]:

$$\eta = \frac{\sqrt{2|Re\mathbf{Z}_{xx} \cdot Im\mathbf{Z}_{yx} - Re\mathbf{Z}_{yy} \cdot Im\mathbf{Z}_{xy} + Re\mathbf{Z}_{xy} \cdot Im\mathbf{Z}_{yy} - Re\mathbf{Z}_{yx} \cdot Im\mathbf{Z}_{xx}|}}{|\mathbf{Z}_{xy} - \mathbf{Z}_{yx}|} \quad (3.29)$$

Values of  $\eta$  over 0.3 are considered as an indication of 3D effects, while those under 0.3 could be treated as 2D. The zero value is an ideal 1D or 2D electrical structure [Qibin et al., 2011].

### 3.4.3 3D Earth

The response of a 3D is much more complicated, as the MT signatures vary in both lateral directions and with depth. In this case, decoupling into TE and TM modes is no longer possible, and the diagonal elements of the impedance tensor do not approach zero for any orientation of the x and y axes. The impedance tensor is full with four complex elements for each frequency [Miensopust, 2010].

## 3.5 Processing

MT data are recorded as time series of the components of the electric and magnetic fields. A number of processing steps are typically performed in order to arrive at impedances for a range of frequencies at each site. The processing steps performed on the Howley Basin data are briefly described in the following section.

### 3.5.1 Time series to transfer function

Three steps are involved in time series to transfer functions processing: Preconditioning of the data, conversion from time series to initial estimates of impedances in the frequency domain, and estimation of the transfer function [Miensopust, 2010]. Data reduction is then achieved by stacking data falling within particular spectral bands and from different time segments [Simpson and Bahr, 2005].

Preconditioning removes severe noise or outliers and reduces the effects of trends, such as those caused by electrode drift, and notch filtering to remove narrow band noise, such as power lines. This also includes the splitting of the time series into segments of smaller lengths (the more the better). Time segments, also called windows (commonly the Hamming window function is used), are converted to the frequency domain using the Fourier transform [Miensopust, 2010]. The basic segmenting of the data involves multiplication by a rectangular window, whereas multiplication by smoother window (Hamming) reduces effects of spectral leakage. By applying a trend remover and anti alias filter (which must be applied prior to either analog to digital conversion or digital resampling, and definitely prior Fourier transformation), one can omit all the frequencies above the Nyquist Frequency [Simpson and Bahr, 2005]. The equipment used for this survey stores time series of signals at three different sampling rates, the lowest rates are acquired continuously (150 Hz) and the higher rates go up to 2400 Hz.

As a result of the processing described above, the electric and magnetic fields recorded in time series are converted into four components of the impedance tensor, varying with frequency, and often subsequently converted into apparent resistivity and phase for x-y and y-x modes. The x-y and y-x modes, x being N-S direction, and y E-W direction for this thesis. Moreover, if short period and broad band (AMT and BBMT)

data are available for the same site, they are merged to produce a single response per site in the frequency domain.

### 3.5.2 Distortion

Distortion is caused by all the small scale near-surface conductivity inhomogeneities that cannot be resolved within the conductivity model, but still affect the MT response [Miensopust, 2010]. There are two major effects of distortion: galvanic and inductive effects. The galvanic effect (electric), also referred to as current deflection, current leakage or current channelling, is caused by primary electric fields ( $E_p$ ) that produce build up electrical charges where conductivity variations occur. These boundary charges cause a secondary field ( $E_s$ ) that has an enhancing effect at the ends of a conductive inhomogeneity, and a reducing effect along the sides and over the inhomogeneity, where it is antiparallel to the primary field ( $E_p$ ). The opposite applies for a more resistive inhomogeneity (Figure 3.5). Thus, in MT soundings, the apparent resistivity is shifted upwards above a resistive body, and downwards over a conductive body. The upward or downward shift is static, i.e. a constant shift on log-log apparent resistivity plots. It affects the electric field as well as the magnetic field [Miensopust, 2010].

Galvanic distortion of the magnetic field is caused by the secondary magnetic field associated with anomalous current flow caused by electric charge accumulation. However, the effect of the magnetic field distortion on the impedance response diminishes with decreasing frequency so it can be assumed negligible in MT. The inductive magnetic distortion is frequency dependant, involves a phase response, and cannot be properly separated from the regional MT response by phase-based methods (such

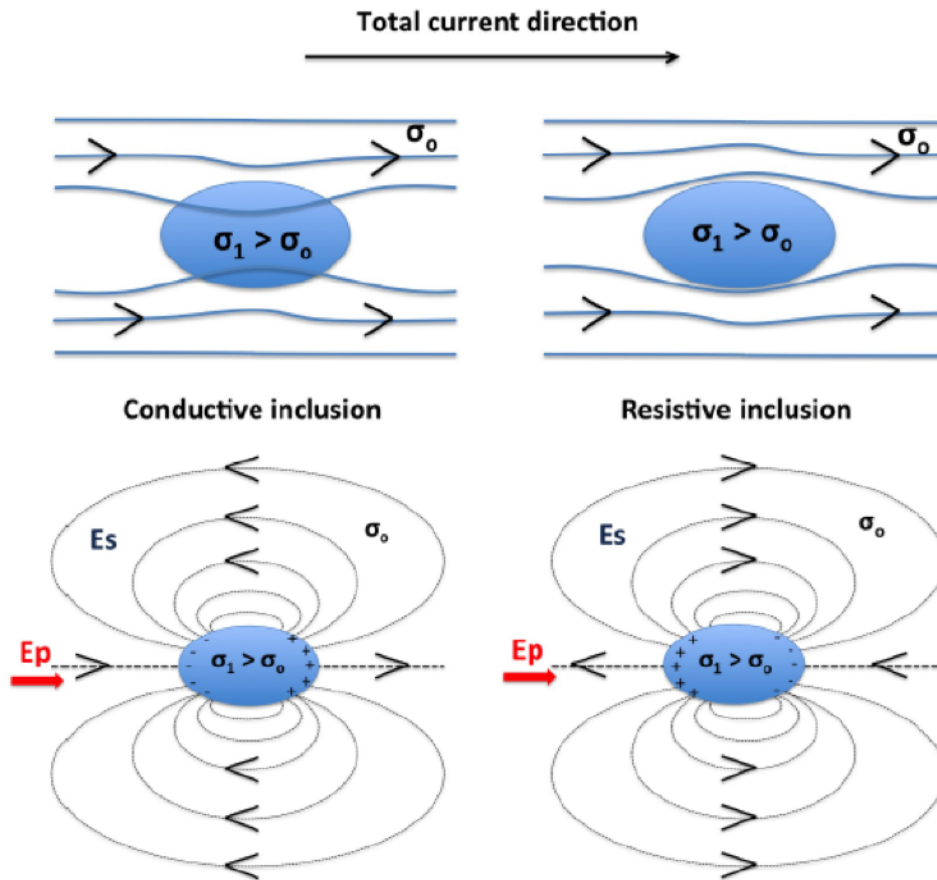


Figure 3.5: Galvanic effect for a conductive (left) and a resistive (right) inhomogeneity. Charges build up on the surface of the object causing a secondary electric field ( $E_s$  - dashed lines), which is weaker but still adds up vectorially to the primary field ( $E_p$ , direction of the red arrow), resulting in static shift (top left and top right). After Miensopust [2010].

as Groom-Bailey or phase tensor). It also tends to increase with frequency as the inductive response of heterogeneities increases [Miensopust, 2010].

Understanding the directionality and dimensionality of the data is essential to accurate interpretation of the MT data. Groom and Bailey [1989] suggested that the determination of geo-electric strike and frequency-independent telluric distortion must be done by fitting a model on a frequency-by-frequency and site-by-site basis independently [McNeice and Jones, 2001]. From these results, a minimum RMS value is sought to determine the most appropriate strike direction. However, strike direction still remains one of the poorest resolved of the parameters recovered during decomposition based on the rotation of the impedance tensor. Increased noise leads to increased statistical uncertainties in the parameters fitted to the observed impedance data using least-square methodology [McNeice and Jones, 2001].

In the Groom and Bailey method, the parts of galvanic distortion that are determinable are shear, twist, and induction by regional strike and regional impedance. The twist tensor rotates the regional electric field clockwise by an angle  $\tan^{-1}(t)$  where  $t$  is the determined twist. The shear tensor develops anisotropy on an axis which bisects the regional principle axis, and it rotates vectors on the x-axis clockwise, and those on the y-axis counter clockwise [McNeice and Jones, 2001].

In this project, distortion is dealt with by using the ‘dcmp2j’ code of Alan Jones (personal communication) to shift two curves of TE and TM modes to match and overlap at the highest frequencies.

### 3.5.3 Geo-electric strike: Example from Nechako Basin, BC, Canada

Here, an example by Spratt and Craven [2011], which presents results from decomposition analysis showing the preferred geo-electric strike direction for a survey in the Nechako Basin of BC, is considered (Figure 3.6). Spratt and Craven applied single- and multi-site Groom-Bailey decompositions, and concluded that the data were independent of the measurement coordinate system for periods shorter than 0.1 s (that is the data are 1D as the phase difference is low). The maximum phase differences between TE and TM modes were observed between 1-100 s, and the data were strongly dependent on the geo-electric strike angle at these periods. Furthermore the general orientation of the western data was about  $5 - 10^\circ$ , the central portion of the survey had moderate amounts of phase shift (blue squares) indicating the data to be 1D at those sites, but towards the east the preferred strike orientation was  $35^\circ$  with high misfit values indicating the subsurface to be 3D. It is stated that those changes are evidence for preserved resistivity structure of strain directions as a result of different tectonic pulses.

## 3.6 Inversion

2D inversion is justified if the RMS is low and distortion is not extreme (shear angle is  $< 45^\circ$ ), and then one can proceed with non-biased inversion modelling. Inversion is the process of automatically constructing an Earth model that reproduces the observed data-set [Simpson and Bahr, 2005]. As electromagnetic energy propagates diffusively through the Earth, MT data do not provide good resolution of the subsurface and the inverse problem is non-unique, i.e. there are many models that could adequately reproduce the data. Many MT inversion schemes are founded on the philosophy of

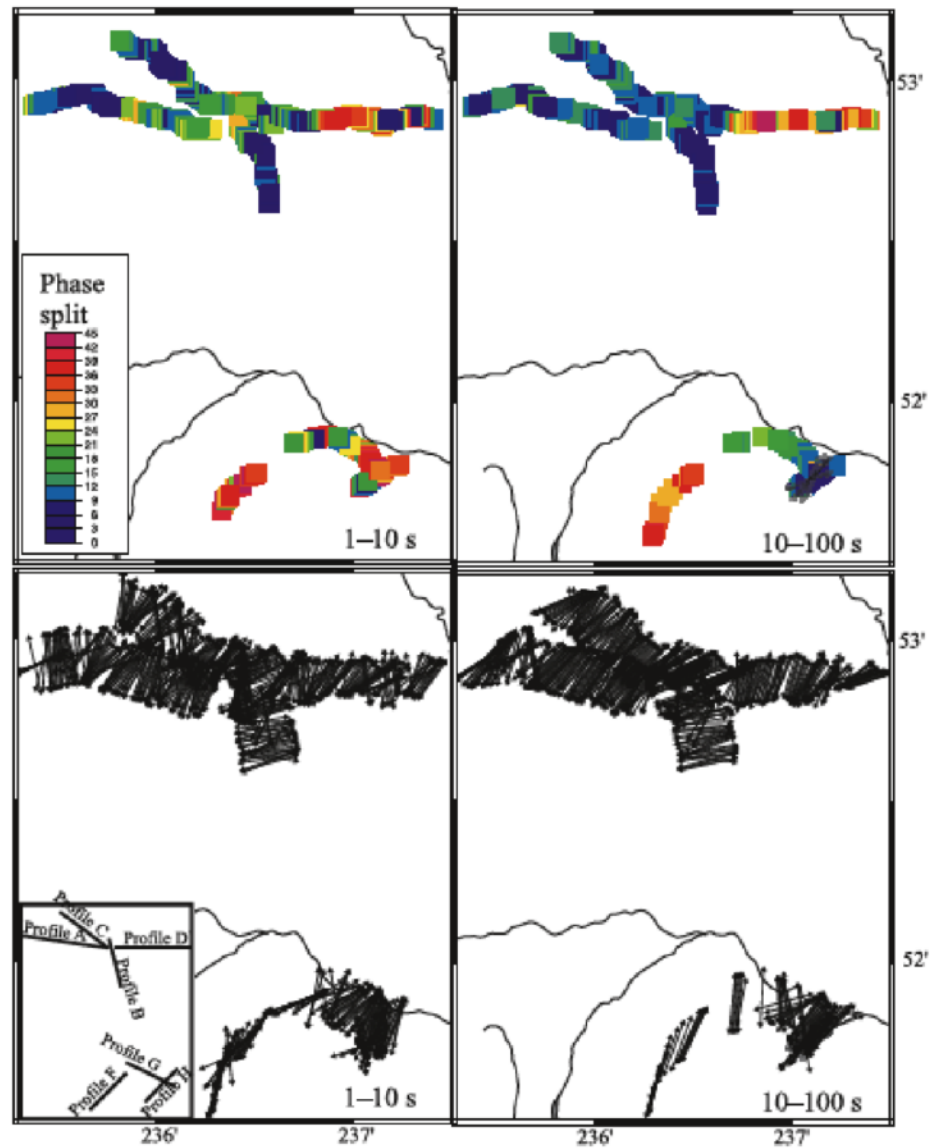


Figure 3.6: Results from decomposition analysis of the Nechako Basin, BC, dataset by Spratt and Craven (2011), showing the preferred geo-electric strike direction for each site using period bands of 1-10s and 10-100s. Arrows in the bottom two panels show the strike direction with a  $90^\circ$  ambiguity. The colours in the top two panels indicate the maximum phase difference between TM and TE modes [Spratt and Craven, 2011].

minimizing model complexity in addition to fitting experimental data rather than fitting the data as closely as possible, which can result in rough, unrealistic models. The smoothest model that fits the data to within an accepted data misfit is usually chosen [Simpson and Bahr, 2005]. This produces models that are blurred images of the Earth's subsurface but which are unlikely to contain misleading artefacts.

The usual approach to solving a nonlinear inverse problem is to approximate the forward function with its first order Taylor expansion about some reference model. A solution to the linearized inversion is then computed and taken as the new model, with this process then being repeated [Rodi and Mackie, 2001]. Convergence minimizes an objective function over the space of models, and produces the optimal solution of the nonlinear inverse problem. The 2D nonlinear conjugate gradients (NLCG) algorithm developed by Rodi and Mackie (2001) is used in this project.

The NLCG algorithm is superior in the sense that instead of involving generation of a full Jacobian matrix and complete solution of a linearized inverse problem at each iteration of the inversion, it uses an efficient, implicit means of calculating the effect of the Jacobian matrix and combines the iterative solution of the system of equations and of the nonlinear inverse into a single iterative procedure [Rodi and Mackie, 2001]. The forward modelling relationship is:

$$\mathbf{d} = F(\mathbf{m}) + \mathbf{e} \quad (3.30)$$

where  $\mathbf{d}$  is the vector of synthesized data (either the log apparent resistivity amplitude or phase for a particular polarization - TE or TM),  $\mathbf{m}$  is the model vector (vector of log resistivities in the cells in the model),  $\mathbf{e}$  is the vector of measurement noise, and  $F$  is the forward modelling function. The inverse problem is solved by finding the model

that minimizes the objective function  $\Psi$  [Rodi and Mackie, 2001]:

$$\Psi(\mathbf{m}) = (\mathbf{d} - F(\mathbf{m}))^T V^{-1} (\mathbf{d} - F(\mathbf{m})) + \lambda \mathbf{m}^T \mathbf{L}^T \mathbf{L} \mathbf{m} \quad (3.31)$$

where  $\lambda$  is the regularization parameter,  $V$  is a positive-definite matrix which plays the role of the variance of the error vector  $\mathbf{e}$ , and  $\mathbf{L}$  is a simple second order-difference operator matrix such that when the grid of model blocks is uniform  $\mathbf{L}\mathbf{m}$  approximates the Laplacian of  $\log \rho$ . A more in-depth explanation of the algorithm is available in Rodi and Mackie's paper [Rodi and Mackie, 2001].

# Chapter 4

## Data Acquisition and Processing

### 4.1 Data Acquisition

40 magnetotelluric soundings were collected during the last week of August and the first two weeks of September, 2013, along an 18 km profile across the Howley Basin. The profile extends from approximately 7 km southeast of Howley, following the abandoned rail track through the town of Howley, towards Deer Lake in the north west (Figure 4.1). The data were collected by three graduate students, including myself, Patric Belliveau and Angela Carter, under the supervision of Jessica Spratt, an independent MT consultant.

All the data were collected using Phoenix equipment from the POLARIS consortium. Prior to the survey, equipment was tested and calibrated by Jessica Spratt. Data for both the audio magnetotelluric (AMT) frequency range and broadband magnetotelluric (BBMT) frequency range were collected. AMT usually records data over a period range of 0.0001 s to 0.1 s, and BBMT from 0.001 s to 1000 s. The AMT

### August/September 2013 MT Program –Howley Basin

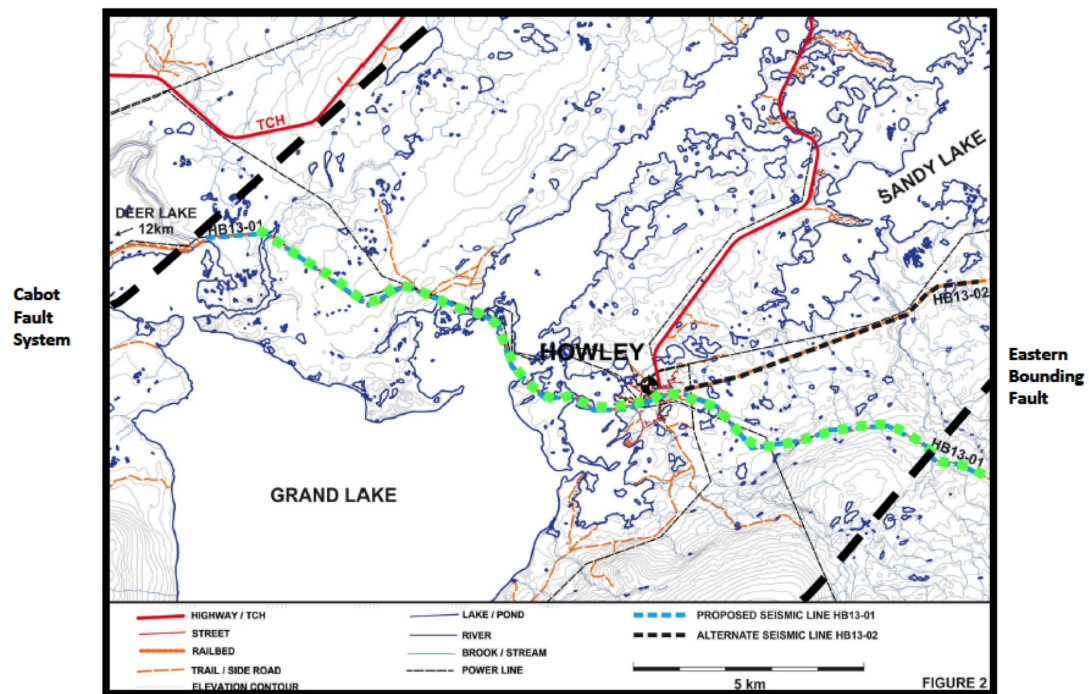


Figure 4.1: MT profile across the Howley Basin (green dashed line). The MT profile followed a planned seismic profile. The specific locations of the MT stations were determined by accessibility, ground conditions, and locations of infrastructure. Note the power line (thin dashed black line) that follows the MT profile eastwards and to the west of Grand Lake/Sandy Lake (figure by professor Chuck Hurich).

recordings were done over a couple of hours and the BBMT recordings overnight. The data collection sites were spaced at approximately 500 m intervals. BBMT measurements were made at every fourth site. One BBMT site was recorded overnight, and 4 AMT sites during daytime, thus about 2 km of the profile were covered per day.

A remote site was installed approximately 3 km to the south of the profile. The purpose for this site was to remove any bias effects of all noise recorded that is not coherent between the survey and the remote station, such as the noise from vehicles passing near the survey. The remote reference site was installed at a particularly quiet place on the shores of Grand Lake.

Horizontal electric fields (x and y directions) were recorded using pot electrodes for BBMT and steel rods for AMT. For this survey, the pairs of electrodes were aligned in North-South (x) and East-West (y) directions. Different electrodes were used because the BBMT recordings were obtained over much longer periods of time and using steel electrodes would result in charge being built up on the electrodes thus giving a false reading. The electrode dipoles were 50 m long for AMT and 100 m long for BBMT, terrain conditions permitting. The horizontal components of the magnetic field were measured using Phoenix induction coils, AMTC-30 for AMT, about 82 cm long, providing magnetic data at frequencies between 10 000 Hz and 1 Hz, and MTC-50H for BBMT, 144 cm in length, providing data at frequencies up to 1000 Hz and down to 0.00002 Hz. The electrodes and coils were connected to an MT unit and powered by a 34 Ah battery (Figure 4.2 and Figure 4.3). Frequencies sampled were from 0.0001 to 10000 Hz using single station recordings of the horizontal components of the electric and magnetic fields. 25 AMT sites had a vertical magnetic coil installed and 3 BBMT sites.

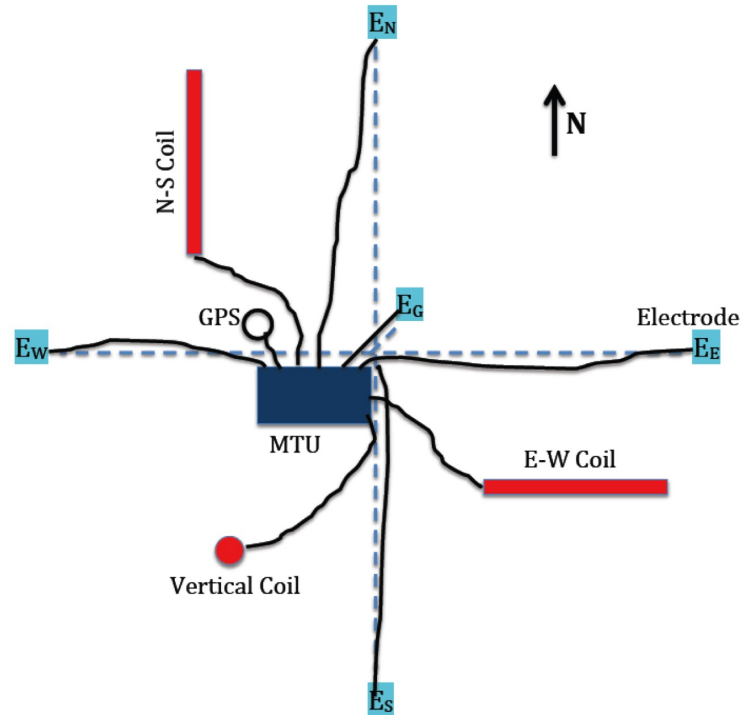


Figure 4.2: Typical instrument layout for each station

Table 4.1 lists the locations of the 40 MT sites, including the remote site, and Table 4.2 lists the processing files and comments for each station. Longitude and latitude are in degrees referenced to the WSG84 datum. The azimuth for all soundings was  $0^\circ$ . Coil numbers ( $H_x$ ,  $H_y$ , and  $H_z$ ) are included in Table 4.1 as this information was necessary for calibration. The distances, in metres, between electrode pairs are also listed. The tables are followed by a map (Figure 4.4) indicating the position of each station. Stations were named HW103-HW120 and HW124-HW141 starting from the southeast towards the northwest, with the exception of HW120 which was recorded further from the road and power line in order to replace the sounding for HW131

**Electrodes:**

$E_N$  - North Electrode

$E_S$  - South Electrode

$E_E$  - East Electrode

$E_W$  - West Electrode

$E_G$  - Ground Electrode

(Two types of electrodes are shown: Pots were used for BBMT, and steel rods for AMT)

**MTU**

Magnetotelluric  
Unit

**Coils:**

N-S Cable is attached to the  
south end

E-W: Cable is attached to  
the west end

Vertical

(Smaller coiled shown were  
used for AMT, and longer  
for BBMT)



Figure 4.3: Photographs of the instruments used

that was right under the power line. Additionally, three sites were installed HW001-HW003 on the road a few kilometres northeast from Howley. However, as these were the first sites to record, some mistakes were made and therefore only HW001 (closest to the profile) is included in the data-set and the data from the other two stations are omitted.

Table 4.1: MT Station Coordinates, coils used ( $H_x, H_y, H_z$ ), and dipole spacings ( $E_x, E_y$ )

Insatal. Date	Site name	File name	Box	Lat	Long	Hx	Hy	Hz	Ex	Ey
Aug 28, 2013	HWa000	1496828A	1496	49.14949	57.14178	1143	1142		86.1	84.8
Aug 28, 2013	HWa001	1495828A	1495	49.17167	57.09091	1428	1149	1141	71.8	67.1
Aug 29, 2013	HWb001	1495828B	1495	49.17167	57.09091	1826	1488		71.8	67.1
Aug 29, 2013	HWa004	1497829A	1497	49.18063	57.0527	1327	1144	1326	50	50
Aug 29, 2013	HWa003	1498829A	1498	49.17883	57.05972	1147	1148		50	50
Aug 29, 2013	HWa002	1495829A	1495	49.17816	57.06494	1328	1149	1141	94	100.9
Aug 30, 2013	HWa104 fail	1498830A	1498	49.15807	57.03147	1141	1328	1149	50	50
Aug 31, 2013	HWa105	1495831A	1495	49.16083	57.0388	1327	1145		52.4	50
Aug 31, 2013	HWa103	1498831A	1498	49.15533	57.02834	1326	1141	1147	64.9	65.6
Aug 31, 2013	HWa104	1497831A	1497	49.15813	57.03306	1328	1144	1149	50	52.4
Aug 31, 2013	HWa106	1497831B	1497	49.16153	57.04515	1148	1328	1146	50	50
Aug 31, 2013	HWa108	1495831B	1495	49.16063	57.06192	1145	1144	1327	50	50
Sept 1, 2013	HWb103	1498831B	1498	49.15533	57.02834	1401	1826		64.9	65.6
Sept 1, 2013	HWa109	1498901A	1498	49.15827	57.06738	1149	1148	1144	50	50
Sept 1, 2013	HWa110	1495901A	1495	49.15808	57.15808	1327	1328		50	50
Sept 2, 2013	HWb107	1497901A	1497	49.15999	57.05208	1401	1488		94.2	79.9
Sept 2, 2013	HWa112	1495902A	1495	49.15825	57.08651	1148	1327	1141	50	51.9
Sept 2, 2013	HWa107	1497902A	1497	49.15999	57.05208	1326	1145		94.2	79.9
Sept 2, 2013	HWa113	1498902A	1498	46.16221	57.09106	1146	1328		50	50
Sept 2, 2013	HWa114	1495902B	1495	49.16569	57.09533	1147	1327	1326	52.4	50
Sept 3, 2013	HWb111	1497902B	1497	49.15723	57.08253	1401	1488		83.6	83.7
Sept 3, 2013	HWa111	1497903A	1497	49.15723	57.08253	1146	1328	1327	83.6	83.7
Sept 3, 2013	HWa115	1497903B	1497	49.16798	57.09895	1328	1327	1146	97.8	89.3
Sept 3, 2013	HWa116	1498903A	1498	49.16861	57.10777	1148	1141	1326	50	50
Sept 5, 2013	HWb115	1497903C	1497	49.16798	57.09895	1488	1401		97.8	89.3
Sept 3, 2013	HWa117	1495903A	1495	49.16556	57.12383	1144	1147	1149	50	50
Sept 3, 2013	HWa119	1498903B	1498	49.16775	57.14022	1148	1141	1326	41.5	46.5
Sept 5, 2013	HWa141	1498905A	1498	49.19909	57.2542	1326	1327	1148	50	48.65
Sept 5, 2013	HWa140	1497905A	1497	49.20046	57.24667	1141	1149		89.2	95.7
Sept 5, 2013	HWa139	1495905A	1495	49.20076	57.23914	1146	1145		52.4	50
Sept 5, 2013	HWa137	1498905B	1498	49.19593	57.22464	1148	1326		50	52.4
Sept 6, 2013	HWb140	1497905B	1497	49.20046	57.24667	1401	1488		89.2	95.7
Sept 6, 2013	HWa135	1498906A	1498	49.19044	57.21286	1146	1326		50	50
Sept 6, 2013	HWa136	1495906A	1495	49.19290	57.21789	1145	1328	1148	50	50
Sept 6, 2013	HWa138	1497906A	1497	49.19929	57.23135	1327	1147	1149	80.6	46
Sept 6, 2013	HWa133	1498906B	1498	49.18697	57.20042	1326	1146	1145	50	50
Sept 7, 2013	HWb138	1497906B	1497	49.19929	57.23135	1401	1402	1488	80.6	46
Sept 7, 2013	HWa132	1495907A	1495	49.18923	57.19435	1328	1148	1141	50	50
Sept 7, 2013	HWa131	1498907A	1498	49.18921	57.18809	1326	1145	1146	50	50
Sept 7, 2013	HWa134	1497907A	1497	49.18629	57.20588	1147	1149	1327	83.8	99.9
Sept 7, 2013	HWa128	1498907B	1498	49.18435	57.16869	1146	1141		50	50
Sept 7, 2013	HWa130	1495907B	1495	49.1871	57.18285	1145	1148		50	47.3
Sept 8, 2013	HWa127	1498908A	1498	49.18099	57.16323	1149	1327	1147	50	50
Sept 8, 2013	HWa120	1495908A	1495	49.19086	57.18442	1148	1145	1326	50	50
Sept 9, 2013	HWb129	1495908C	1495	49.18402	57.17757	1401	1826		89.5	94.3
Sept 9, 2013	HWa134	1497908B	1497	49.18629	57.20588	1488	1402		83.8	99.9
Sept 9, 2013	HWa129	1495909A	1495	49.18402	57.17757	1146	1144		89.5	94.3
Sept 9, 2013	HWa126	1497909A	1497	49.17789	57.16063	1326	1141	1148	46.2	53
Sept 9, 2013	HWa125	1498909A	1489	49.17041	57.15662	1149	1145	1327	85	87
Sept 9, 2013	HWa124	1497909B	1497	49.16751	57.14697	1328	1147	1148	52.4	50
Sept 11, 2013	HWb125	1498909B	1489	49.17041	57.15662	1401	1402	1826	85	87
Sept 11, 2013	HWa118	1495911A	1495	49.16566	57.13411	1327	1145	1149	78	43.7
Sept 12, 2013	HWb118	1495911B	1495	49.16566	57.13411	1402	1826	1401	78	43.7

Table 4.2: Processing files and comments for each site

Insatal. Date	Site name	File name	Processing ref site	Comment
Aug 28, 2013	HWa000	1496828A	Local	
Aug 28, 2013	HWa001	1495828A	1496828A	
Aug 29, 2013	HWb001	1495828B	1496828B	
Aug 29, 2013	HWa004	1497829A	1496829A	Off the wrong path
Aug 29, 2013	HWa003	1498829A	1496829A	Bad weather, coils were flooded
Aug 29, 2013	HWa002	1495829A	1496829A	Battery never connector to the unit properly
Aug 30, 2013	HWa104 fail	1498830A	1496830A	Hx and Hy coil connection to unit mixed up
Aug 31,2013	HWa105	1495831A	1496831A	
Aug 31,2013	HWa103	1498831A	1496831A	
Aug 31,2013	HWa104	1497831A	1496831A	
Aug 31,2013	HWa106	1497831B	1496831A	
Aug 31,2013	HWa108	1495831B	1496831A	
Sept 1, 2013	HWb103	1498831B	1496831B	
Sept 1, 2013	HWa109	1498901A	1496901A	
Sept 1, 2013	HWa110	1495901A	1496901A	
Sept 2, 2013	HWb107	1497901A	Local	
Sept 2, 2013	HWa112	1495902A	1496902A	
Sept 2, 2013	HWa107	1497902A	1497902A	
Sept 2, 2013	HWa113	1498902A	1497902A	
Sept 2, 2013	HWa114	1495902B	1497902A	
Sept 3, 2013	HWb111	1497902B	1496902B	
Sept 3, 2013	HWa111	1497903A	1496903A	
Sept 3, 2013	HWa115	1497903B	1496903A	
Sept 3, 2013	HWa116	1498903A	1496903A	
Sept 5, 2013	HWb115	1497903C	1496903B	
Sept 3, 2013	HWa117	1495903A	1496903A	
Sept 3, 2013	HWa119	1498903B	1496903A	
Sept 5, 2013	HWa141	1498905A	1496905A	Next to the dam
Sept 5, 2013	HWa140	1497905A	1496905A	
Sept 5, 2013	HWa139	1495905A	1496905A	
Sept 5, 2013	HWa137	1498905B	1496905A	
Sept 6, 2013	HWb140	1497905B	1496905B	
Sept 6, 2013	HWa135	1498906A	1496906A	
Sept 6, 2013	HWa136	1495906A	1496906A	
Sept 6, 2013	HWa138	1497906A	1496906A	
Sept 6, 2013	HWa133	1498906B	1496906A	
Sept 7, 2013	HWb138	1497906B	1496906B	
Sept 7, 2013	HWa132	1495907A	1496907A	
Sept 7, 2013	HWa131	1498907A	1496907A	Right under power line
Sept 7, 2013	HWa134	1497907A	1496907A	Very close to power line
Sept 7, 2013	HWa128	1498907B	1496907A	Very close to power line
Sept 7, 2013	HWa130	1495907B	1496907A	Very close to power line
Sept 8, 2013	HWa127	1498908A	1495908A	Very close to power line
Sept 8, 2013	HWa120	1495908A	1498908A	Installed to replace HW131
Sept 9, 2013	HWb129	1495908C	1496908B	Very close to power line
Sept 9, 2013	HWa134	1497908B	1496908B	
Sept 9, 2013	HWa129	1495909A	1496909A	Very close to power line
Sept 9, 2013	HWa126	1497909A	1496909A	Very close to power line
Sept 9, 2013	HWa125	1498909A	1496909A	
Sept 9, 2013	HWa124	1497909B	1496909A	
Sept 11, 2013	HWb125	1498909B	1496909B	
Sept 11, 2013	HWa118	1495911A	1496910A	
Sept 12, 2013	HWb118	1495911B	1496911B	

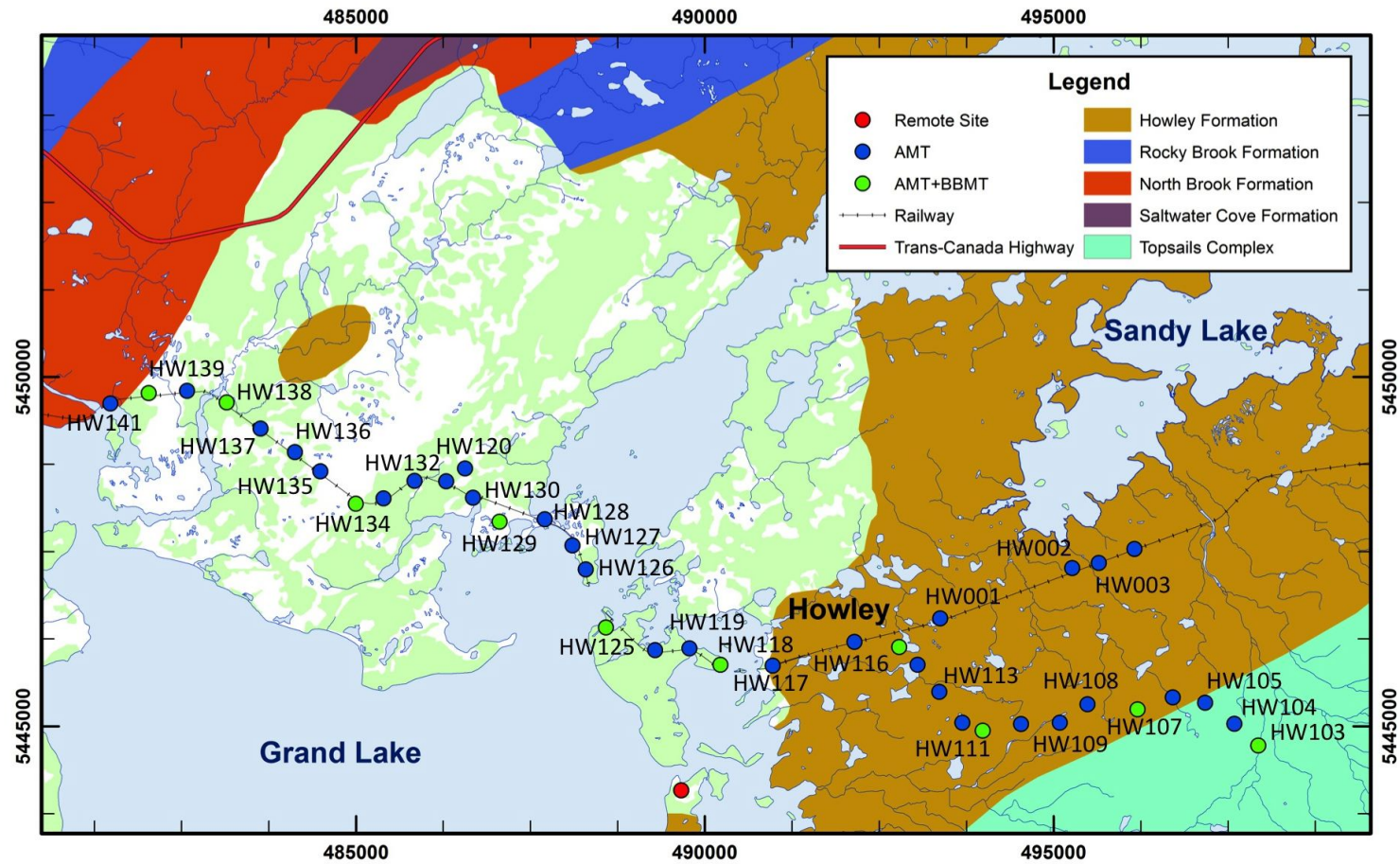


Figure 4.4: Station locations. Geological map with stations plotted (UTM coordinates, zone 21). Blue dots are AMT stations while green dots are for combined AMT and BBMT stations.

The ground conditions and ground cover changed greatly after the easternmost part of the line (after stations HW107/HW108) (Figure 4.5). Stations HW103-HW108 were set in thick bush, while other stations were in more mossy and swampy conditions. This is considered to be one of the indications that the boundary between the Topsoil igneous rocks and the Howley Basin is located close to HW107/HW108.

In general, the data are of medium quality. Sources of noise were plentiful. As the survey was conducted along a dirt road often used by locals, vehicles were one source of noise. The southeast part of the survey experienced less noise, however approaching the town of Howley the amount of noise increased. A dam apparently used for hydroelectric generation is located at the northwest end of the line, and stations close by it (HW141 - HW138) were strongly influenced by it. Additionally, power lines run from the dam and approximately follow the survey line as far southeast as the causeway. This influenced the readings significantly, especially for stations HW125-HW131 when the power lines were crossing or running parallel to the dirt road. In the northwest part, performing the survey in swampy conditions was also challenging, for example, the buried coils were flooded at a couple of sites after rain.

## 4.2 Processing

In order to explain the steps taken in processing and editing the data to obtain the sounding curves for each station, an example of a single sounding, HW135, will be used. The other sounding curves are included in Appendix A (unedited) and Appendix B (edited).



Figure 4.5: Left: Placing a coil at the station HW107; Right: Brook between stations HW138 and HW139.

The data were recorded as time series of  $E_x$ ,  $E_y$ ,  $H_x$ ,  $H_y$ . A time slice for HW135 is given in Figure 4.6.

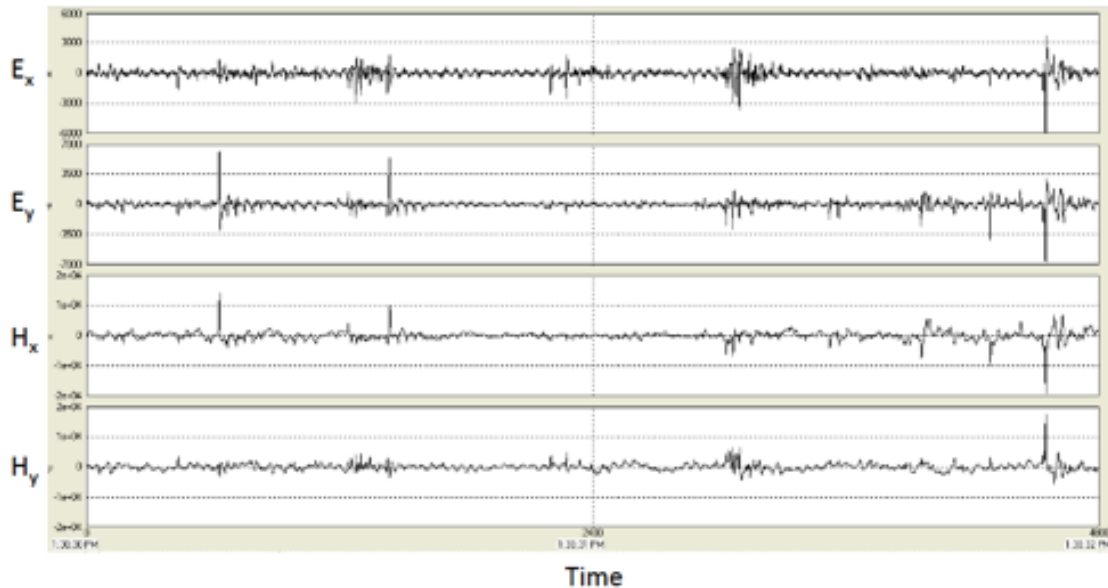


Figure 4.6: A portion of the time series for  $E_x$ ,  $E_y$ ,  $H_x$ ,  $H_y$  recorded for station HW135.

The initial processing of the data was done using the program SSMT 2000: Robust Processing from Phoenix Geophysics (Figure 4.7). In this software, Step 1 (indicated by the green square in Figure 4.7) is to enter the coils and the MT unit used for the sounding (this information is used for calibration), as well as dipole distances, declination and the name of a station (Figure 4.8). Next, the recorded time-series were converted to the frequency domain via a Fourier Transform (Step 2 in Figure 4.7) and then processed to determine the impedance tensor, from which apparent resistivity and phase can be calculated. Step 3 involves referencing the sounding to the remote reference site recording (Figure 4.9), and finally performing the remote reference processing (Step 4). The processing technique using robust remote reference is described by Method 6 in Jones et al. [1989].

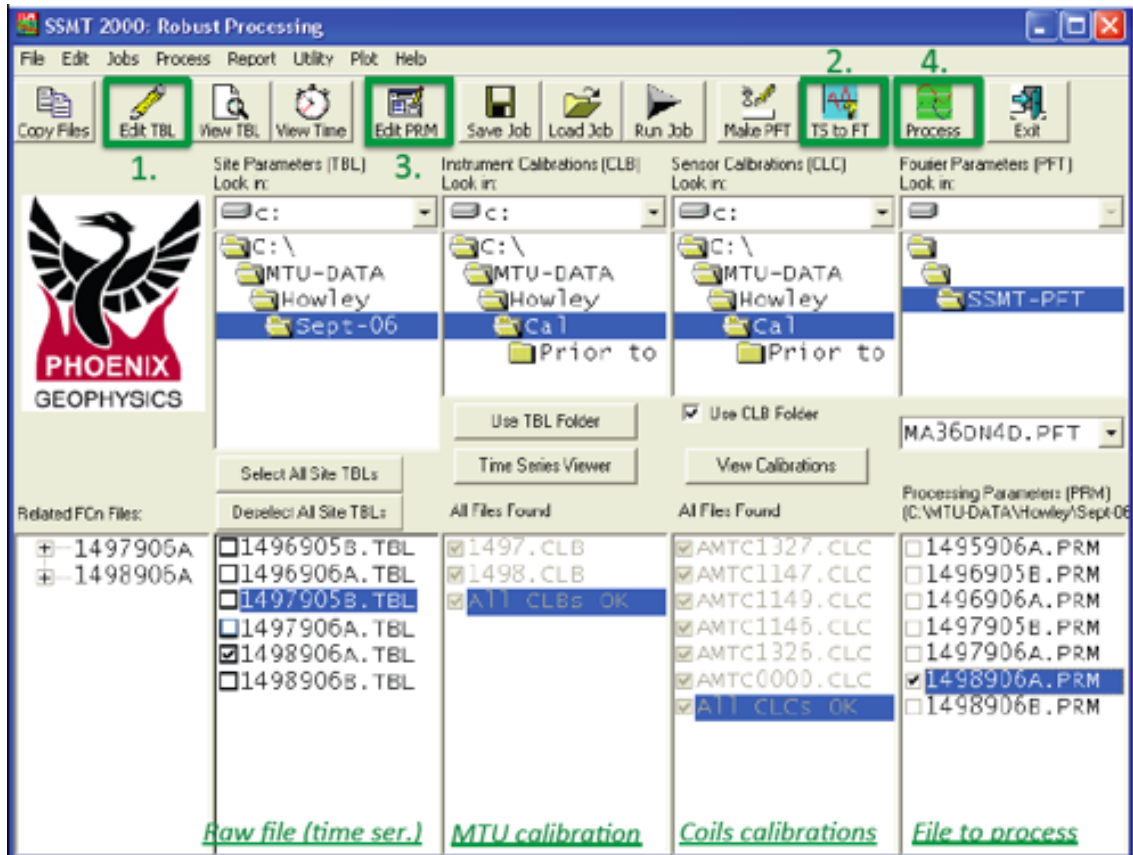


Figure 4.7: Window screen shot of SSMT 2000: Robust Processing from Phoenix Geophysics. Outlined by green squares are the steps taken and numbered in the order in which they were performed.

The processing described above yielded apparent resistivity and phase response curves in the period range from 0.0001 to 1 s for AMT and 1 to 1000 s for BBMT. At locations where both AMT and BBMT data were collected the response curves were merged together to generate one file. Rotation of the impedance tensor (described in the next chapter) allows for decoupling into TE and TM modes.

**1.**

**TBL Multi-table Editing**

Table Names: 1498906A.TBL

Client: MUN

Survey: HOW

Permitter:

Layout By:

Site Name: **Hwa135** **Name the site**

Latitude: 49:11.426, N

Longitude: 057:12.770, W

Elevation (m): 110

North Reference: 3 - Magnetic North

Declination: **22.7** **Change the declination**

Ex Azimuth: 0

Ex [N-S] (m): **50**

Ey [E-W] (m): **50** **Enter the distance measured between dipoles**

Hx Azimuth: 0

Hx Serial #: **AMTC1146**

Hy Serial #: **AMTC1326**

Hz Serial #: **AMTC0000** **Enter which coils were used in order to calibrate**

Ex kOhms: 1.345

Ex AC mV: 36.96821

Ex DC mV: -0.00745

Ey kOhms: 0.696

Ey AC mV: 9.46597

Ey DC mV: 0.01818

Instrument File Name: 1498906A

Do not correct layout errors using this Editor! Instead, type the information as written on the Layout Sheet, click Save All, and then choose Layout Errors from the Edit menu.

Toggle Fields

Save All

Close

Figure 4.8: Window screen shot of the table to be filled in Step 1 in Figure 4.7. Here information for an individual site is entered.

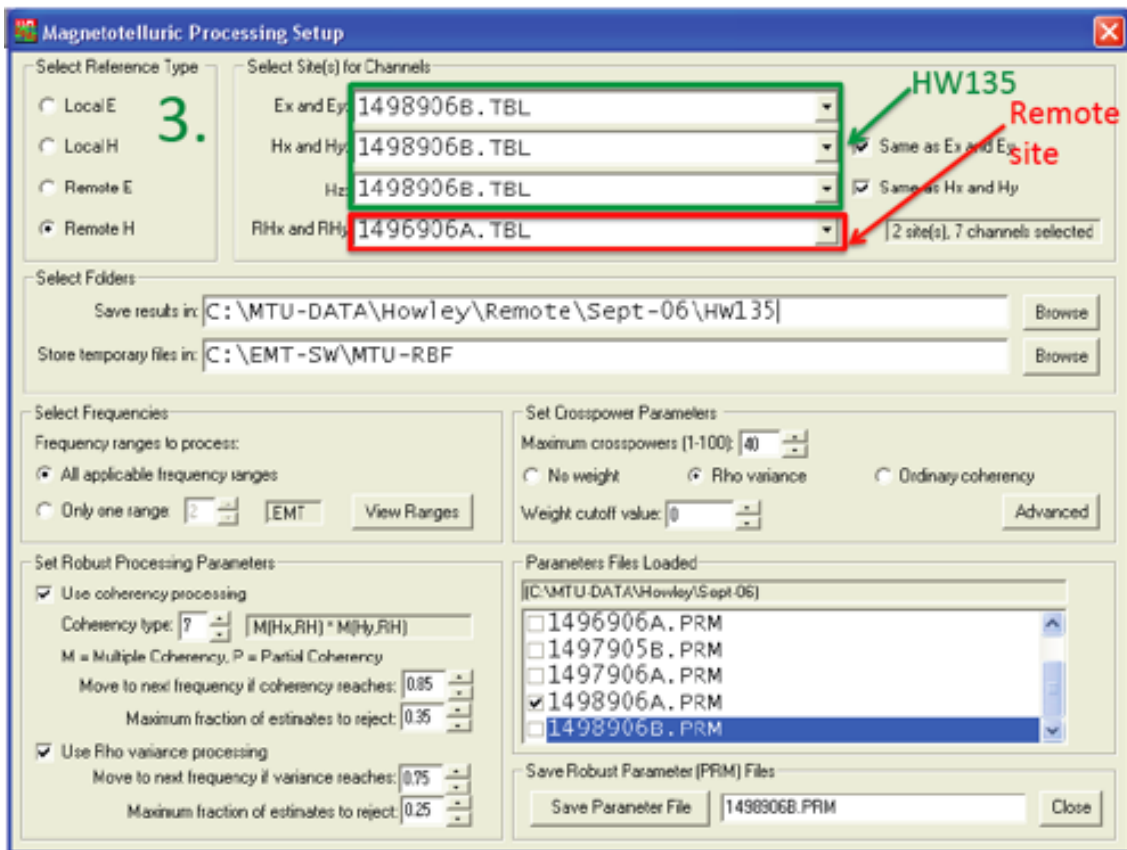


Figure 4.9: Window screen shot of the table for Step 3 in Figure 4.7. Here an individual site is referenced to the remote reference site file in order to carry out the remote reference processing.

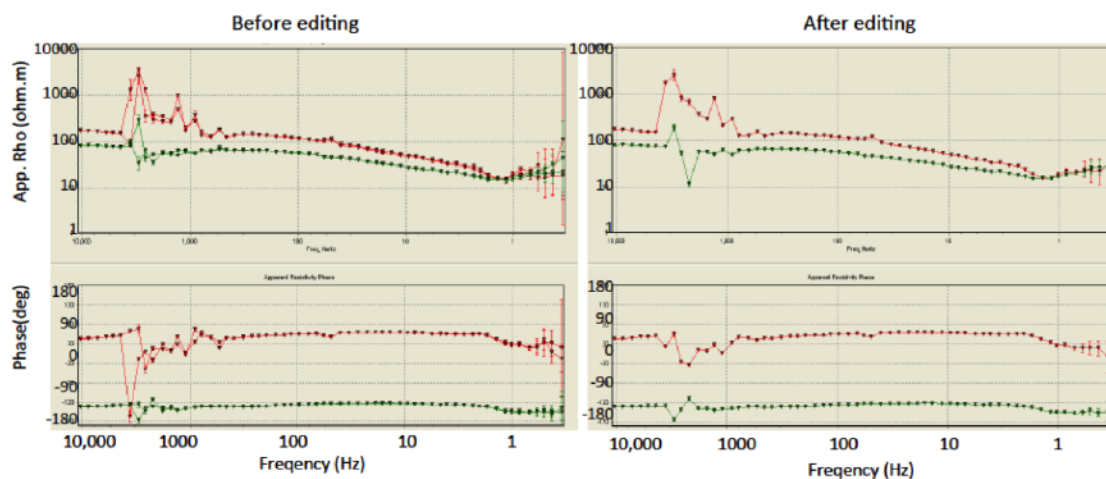


Figure 4.10: Observed apparent resistivity and phase curves for site HW135 before (left) and after (right) editing. The red curve corresponds to the TE (XY) component and the green to the TM (YX) component.

#### 4.2.1 Removing erratic data

The data were next edited and cleaned using the program MTeditor to remove obvious noise effects. The apparent resistivity and phase curves for site HW135 before and after editing are shown in Figure 4.10. The red triangles correspond to the TE (XY or north-south) component and the green to the TM (YX or east-west) component. Examples for the same sounding for the particular frequencies of 650 Hz and 49 Hz are shown in Figures 4.11 and 4.12 respectively. One can go through each individual frequency and see how many times it had been sampled and the value measured (right panels in Figures 4.11 and 4.12). The big outliers are switched off, so the average values represent the value of most of the measurements.

Once the data from all sites were edited, they were imported into WinGLink, a software package available from Schlumberger. Figure 4.13 shows the view of the sounding curves for site HW135 in WinGLink. The TE and TM modes are then individually

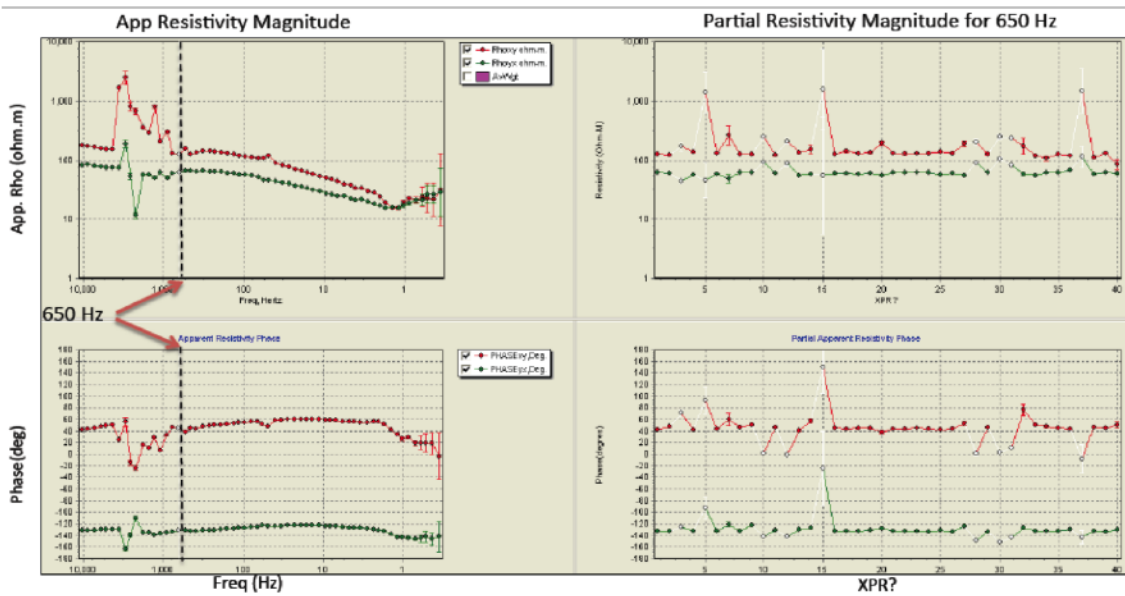


Figure 4.11: Observed apparent resistivity and phase curve for site HW135 (left) and the editing window for 650 Hz (right). Righthand side panels show how many times the particular frequency was sampled and the value measured.

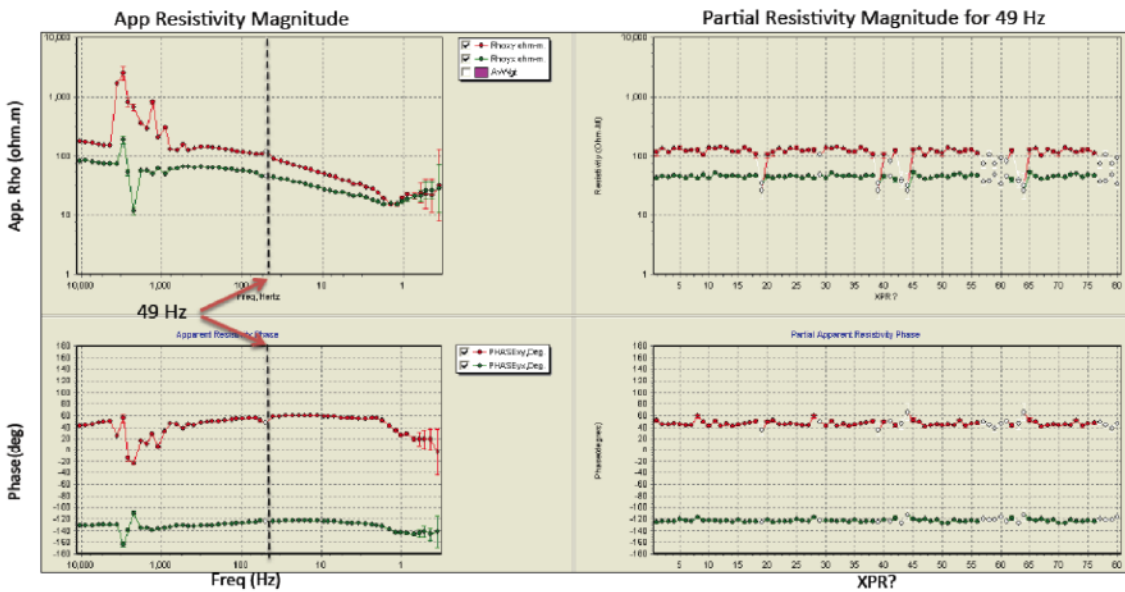


Figure 4.12: Observed apparent resistivity and phase curve for site HW135 (left) and editing window for 49 Hz (right). Righthand side panel shows how many times the particular frequency was sampled and the value measured.

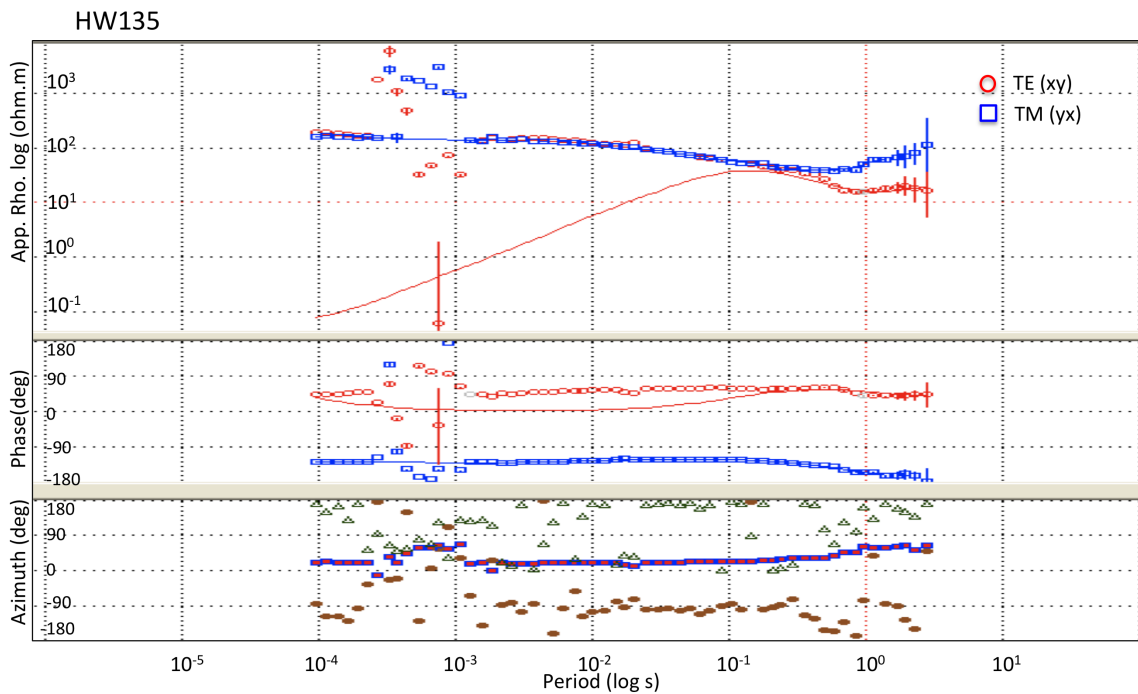


Figure 4.13: Observed apparent resistivity and phase curves for site HW135 before editing in WinGLink. The red circles correspond to the TE (XY) component and the blue squares to the TM (YX) component. Curves are the best fit for apparent resistivity that are later used for the Occam inversion. Azimuth of  $0^\circ$  indicates good data

further edited, removing the readings with large error bars (Figure 4.14) and corrected for static shift by shifting the curves to overlap at the highest frequencies. A significant part of the data editing done in the study involved removal of frequencies in the dead bend  $10^3$  Hz.

From the edited curves, a pseudo-section of apparent resistivity varying with frequency for each mode can be produced (Figure 4.15), as well as the pseudo section for phase varying with frequency (Figure 4.16). For frequencies at which the phase

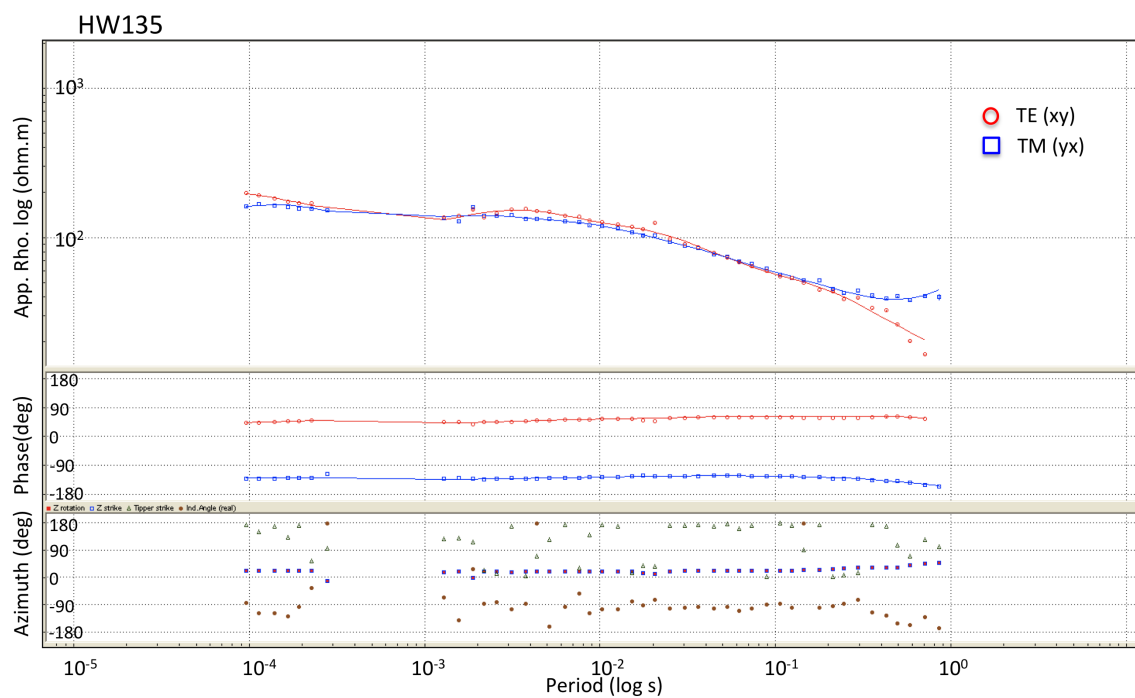


Figure 4.14: Observed apparent resistivity and phase curves for HW135 after editing in WinGLink.

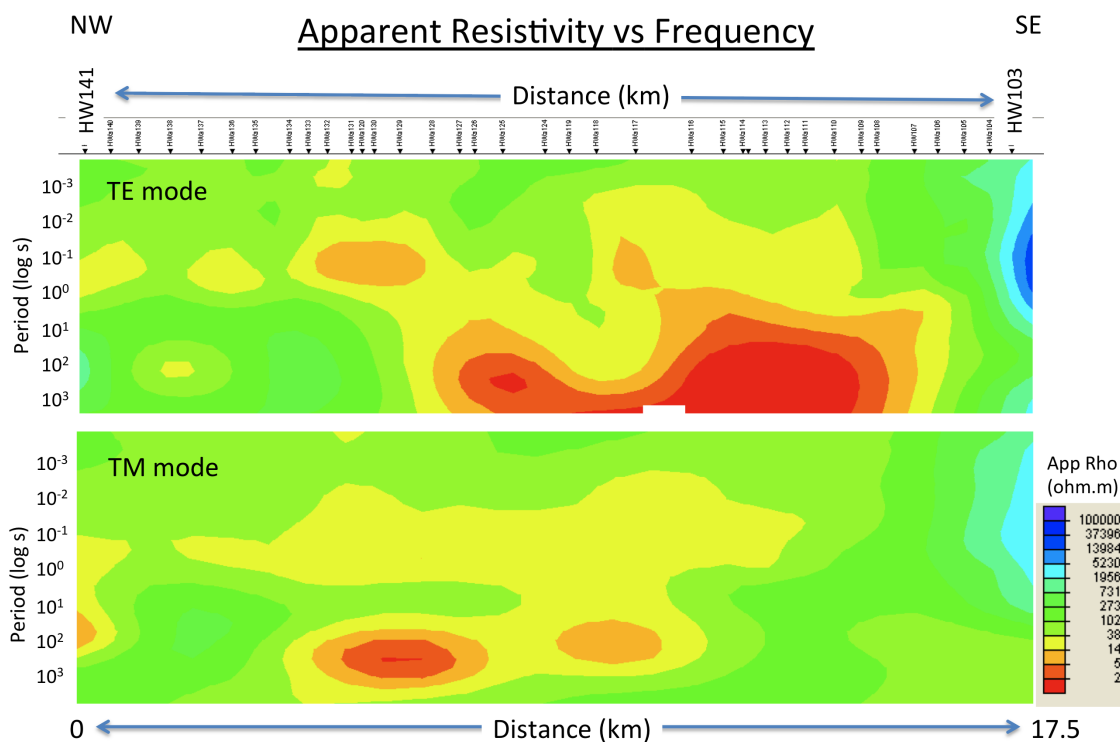


Figure 4.15: Pseudo section of apparent resistivity vs. period along the survey profile for AMT and BBMT soundings combined.

difference between TE and TM modes is less than  $10^\circ$ , the data can be considered 1D and independent of geo-electric strike. However, where this value is exceeded the data is closer to 2D or maybe even 3D.

Most of the other sounding curves experience a similar pattern (Appendix A and B) with TE and TM modes overlapping at higher frequencies, which is characteristic of a 1D environment. At the lower frequencies they curve up and separate, which is characteristic of 2D or 3D structures. The apparent resistivities also tend to increase at the lower frequencies (Figure 4.17); this is assumed to correspond to the increase in resistivity when moving from the basin sediments into the igneous basement.

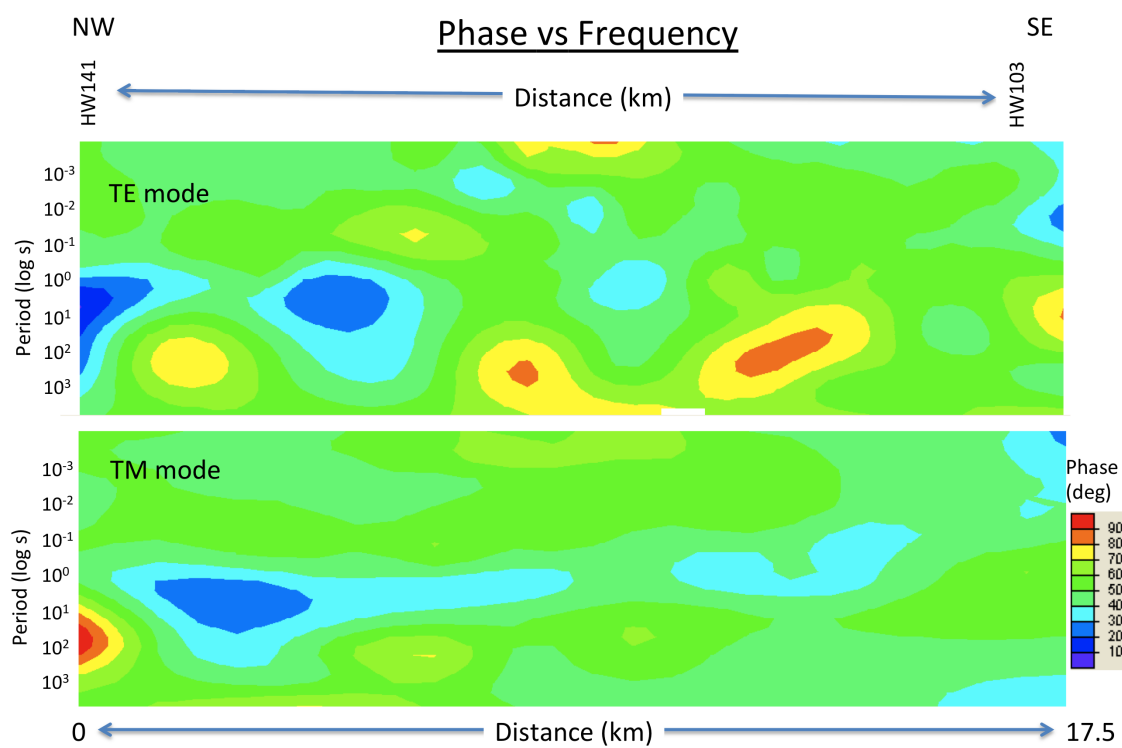


Figure 4.16: Pseudo section of phase vs. period along the survey profile.

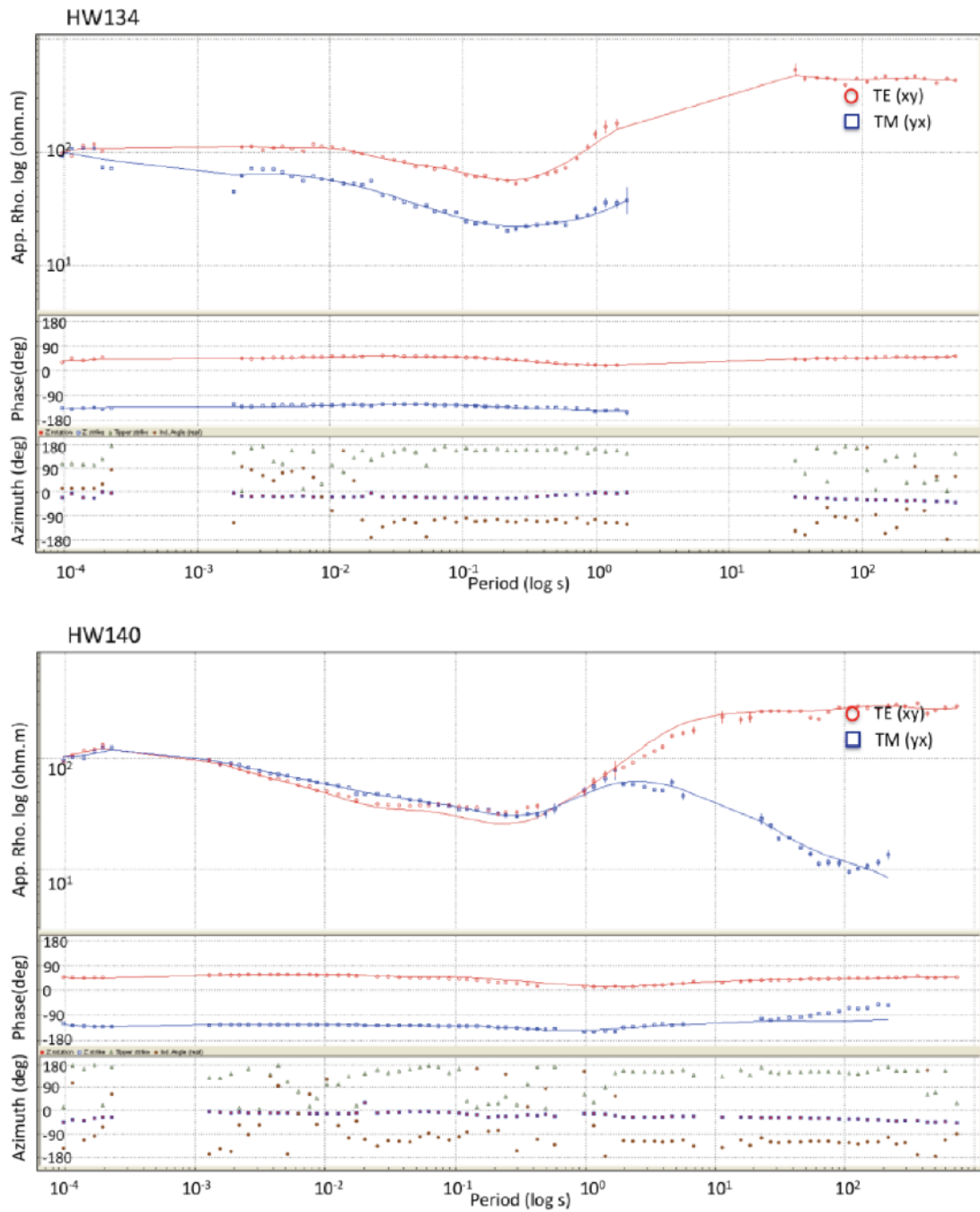


Figure 4.17: Sounding curves for two of the BBMT stations, HW140 and HW134.

# Chapter 5

## Decomposition and modelling

In this chapter the data are first modelled using 1D Earth modelling, when appropriate. For period ranges for which there is a phase difference of less than  $10^\circ$ , one can consider the data to be 1D for the depth ranges corresponding to the period range. Then geo-electric strike analysis to determine preferred strike direction for the data set will be described. Finally 2D inversions of the data based on the preferred directions are described.

### 5.1 1D modelling

Before carrying out geo-electric strike analysis, one can proceed with 1D modelling and inversion. In this case, TE and TM modes (in terms of the measurement coordinate system) are treated individually, each having a resistivity model fit to their curves. Here Occam inversion in WinGLink was used. Occam inversion (the pink curve in Figure 5.1 for site HW135) fits the apparent resistivity curve as a function of depth using a 45 layer Earth model. The green line is the Marquardt layered model with only 8 layers used for modelling. An example is displayed in Figure 5.1 show-

ing the results for site HW135 for the TM mode. In this model, one can see that the sounding images the subsurface to approximately 2000 m, and has an average resistivity of roughly  $100 \Omega m$ , which is representative of the resistivity of sedimentary rocks. This suggests that this sounding does not reach the basement.

After this procedure has been applied to each site, the 1D resistivity models can be stitched together to form a 2D image using the WinGLink Profile Section (Figure 5.2). One can choose from which fitted curve to generate the 2D image. Here the Occam layered inversion was used. The vertical bars in Figure 5.2 show the Occam inversion result for each location and the skin depth they penetrate to, while the colouring in between is an interpolation done by the software between each station. Not much can be concluded from the 1D inversions as quite different images are produced for the two modes. It is important to remember when looking at Figure 5.2 that 1D inversions are only applicable to a limited number of sites, and therefore this is only an initial interpretation. However, one feature that is present in both modes is the generally more conductive layer that is present in the first 2 km depth of the central and western sections of the profile. In the eastern part of both profiles, this conductive feature starts between stations HW107 and HW108. For example, an average apparent resistivity at HW103 is around  $10^3 \Omega m$  for all the depths. At HW113 the resistivity is approximately 10-100  $\Omega m$  above about 1 km and approximately  $10^3 \Omega m$  below (Figure 5.3). Potentially this represents the more conductive sedimentary basin lying on top of more resistive igneous basement. Nevertheless, a 2-D treatment is necessary given the difference between the modes.

The 1D inversions also reveal approximate information about the estimated depth penetration of the data for each site (Figure 5.4). This was calculated by the software

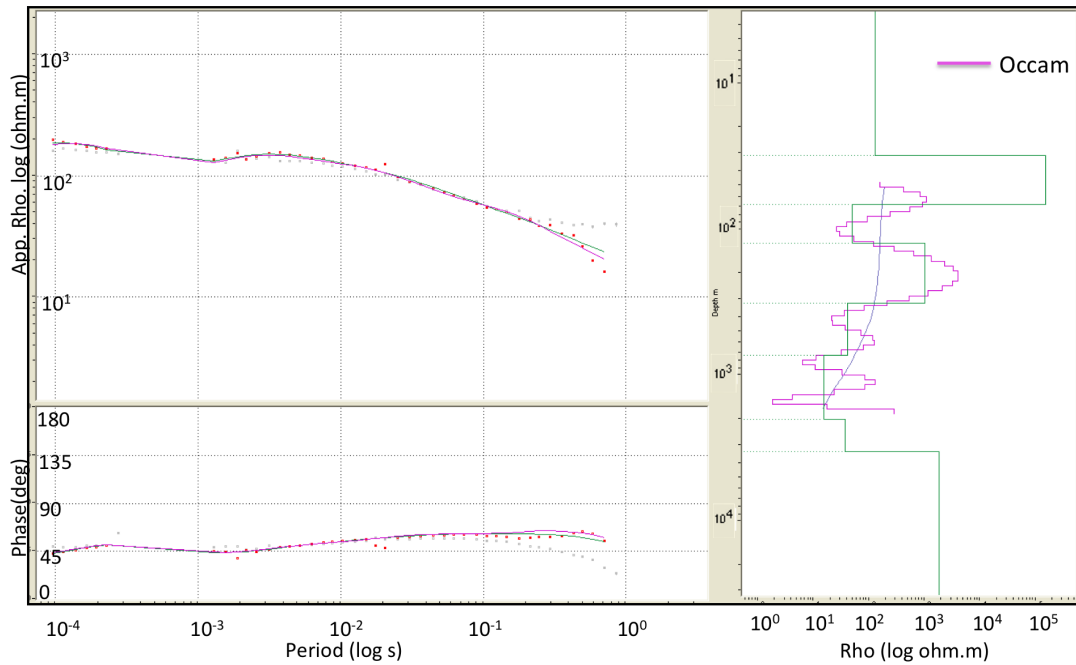


Figure 5.1: Left: The TM apparent resistivity and phase curves for HW135 (symbols observed data and curves predicted data) from 1-D Occam inversion. Right: The resistivity vs. depth model (pink) produced by the 1D Occam inversion of the apparent resistivity and phase data for HW135 performed in WinGLink. The green line is the result of a Marquardt inversion which predicts an 8-layer Earth model. The blue line is the Bostick smooth fitted model. The Bostick inversion shows maximum imaging depth around 2 km, and the maximum depth of the Occam and multilayer inversion can in general be set arbitrarily in the inversion parameters.

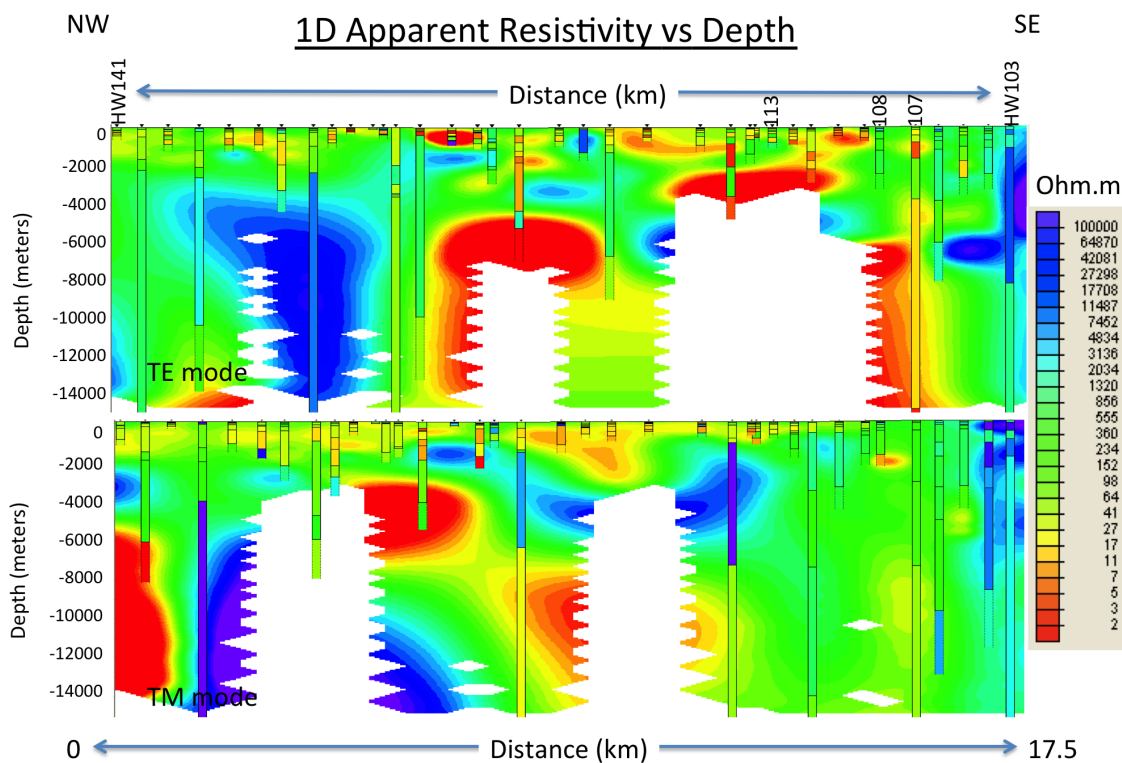


Figure 5.2: 2D images made from stitching together the 1D Occam inversion models for TE and TM modes. Vertical bars show the 1D Occam inversion for each location and the approximate depth to which the sounding penetrates. The background colours are the software's interpolations based on connecting the features of the vertical bars.

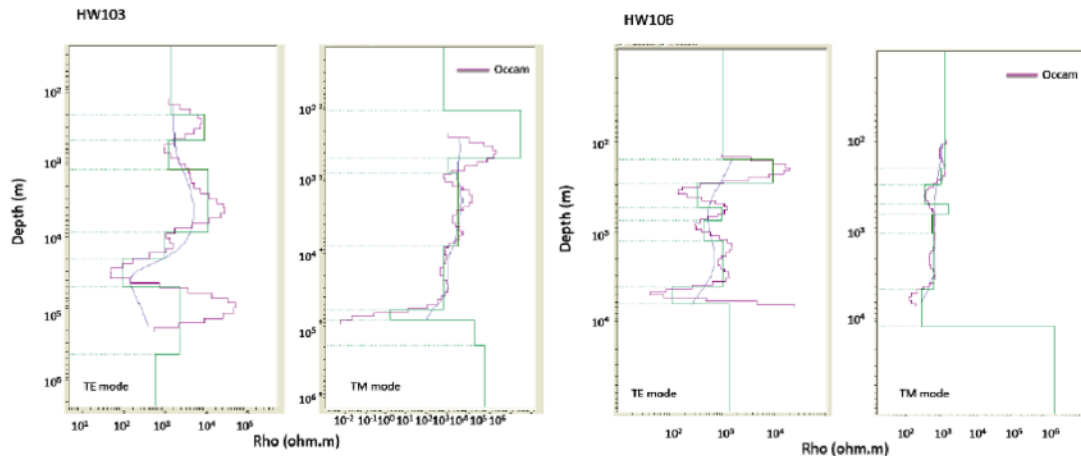


Figure 5.3: Occam layered inversion results for stations HW103 and HW113 (same colour-coding as in Figure 5.1) with a clear decrease in average resistivity at station HW113 above about 1 km that is not present for HW103, suggesting the basin's eastern edge is located somewhere in-between these stations.

using the conductivity values and skin depth equation (equation 3.9). Some of the soundings do not see very deep, but there are a number that do. In general, it is the AMT+BBMT soundings that see deeper, but also some of the AMT soundings over the eastern edge of the profile where the subsurface is more resistive see to depths of multiple kilometres.

## 5.2 Strike Angle Analysis

If the assumption of a purely 2D Earth were true and absence of noise, the error to fitted strike (RMS) value should be zero (see Section 3.5.2). Instrumental and environmental sources of noise can result in a non-zero value for a 2D Earth. However, in general, the RMS should not exceed a value of 2 if the Earth is 2D [Chave, 2012]. The RMS threshold of 2 depends critically on the error estimates used in the analysis properly reflecting the true level of stochastic errors on the observed impedances (the fact that the 3.5% error underestimates the true errors leads to the large misfits noted

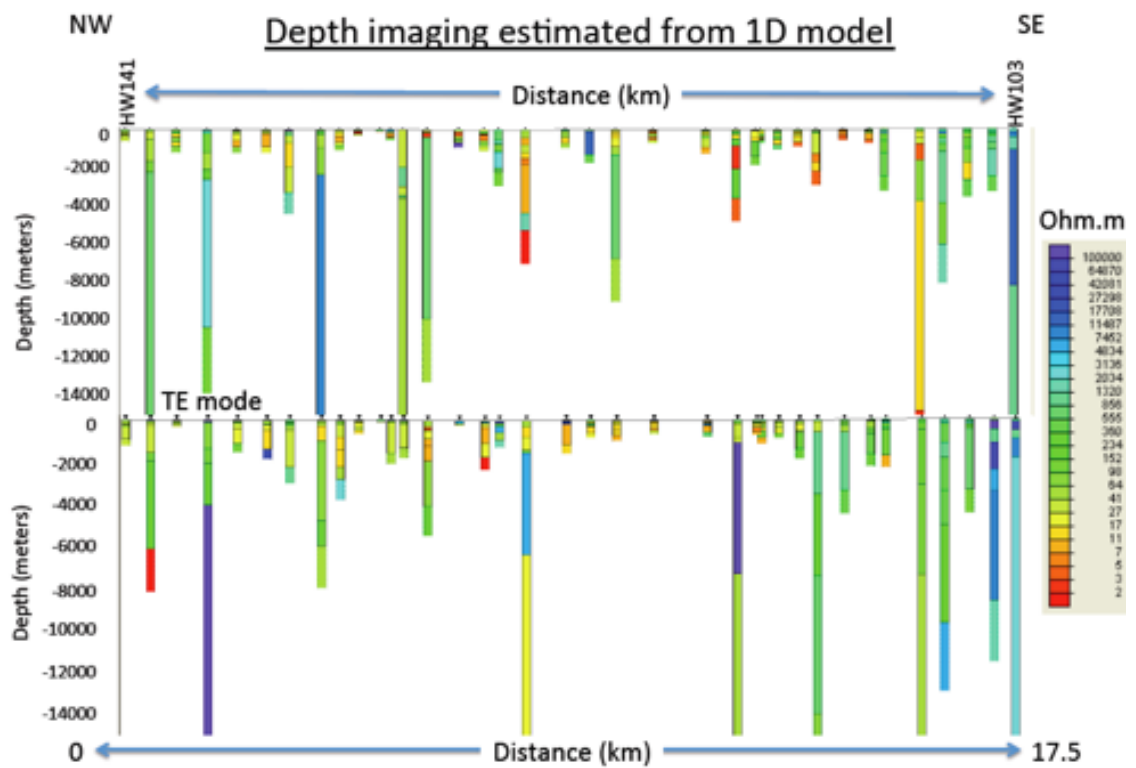


Figure 5.4: Depth penetration estimates from the 1D inversions. These are the same as in Figure 5.2, just without the interpolated background.

in the AMT deadband). Ideally, a model can be generated along a profile at one strike angle for all periods, but in most cases, due to the complexity of the subsurface, this angle changes with period ranges and hence with depth.

The program ‘strike1’ from Alan Jones (personal communication, October 2013), which uses the decomposition method described by McNeice and Jones [2001], was used to perform strike direction analysis on the Howley Basin data. Further, the program ‘dcmpmap’ was run to plot the calculated strike directions on the map. It is important to note that the data edited in MT Editor were used, not the data that were used for 1D modelling that was additionally edited in WinGLink as well, where noisy frequencies were eliminated. ‘Strike1’ and ‘dcmpmap’ were performed on all the frequencies. The parameters used for these programs are listed in Tables 5.1 and 5.2.

For the purpose of this project, the frequencies were divided into decades and the decomposition and strike analysis applied to each decade individually. The results for the AMT sites are shown in Figure 5.5 and those for lower frequencies of the BBMT sites in Figure 5.6. The orientations of the arrows represent the most preferred strike direction for a particular frequency band, and the colour of the squares indicates the phase difference between TE and TM modes, TE mode still having N-S orientation, and TM S-W orientation. Where the phase difference is less than  $10^\circ$ , one can consider the data for that station at that frequency band to be 1D and strike direction is not important. Where the phase difference is greater, the orientations of the arrows indicate the best-fitting geo-electric strike.

As seen in Figure 5.5, for the period band of 0.001-0.01 s half of the stations are 1D (blue squares), and for the others 2D (or 3D) with a general strike direction varying

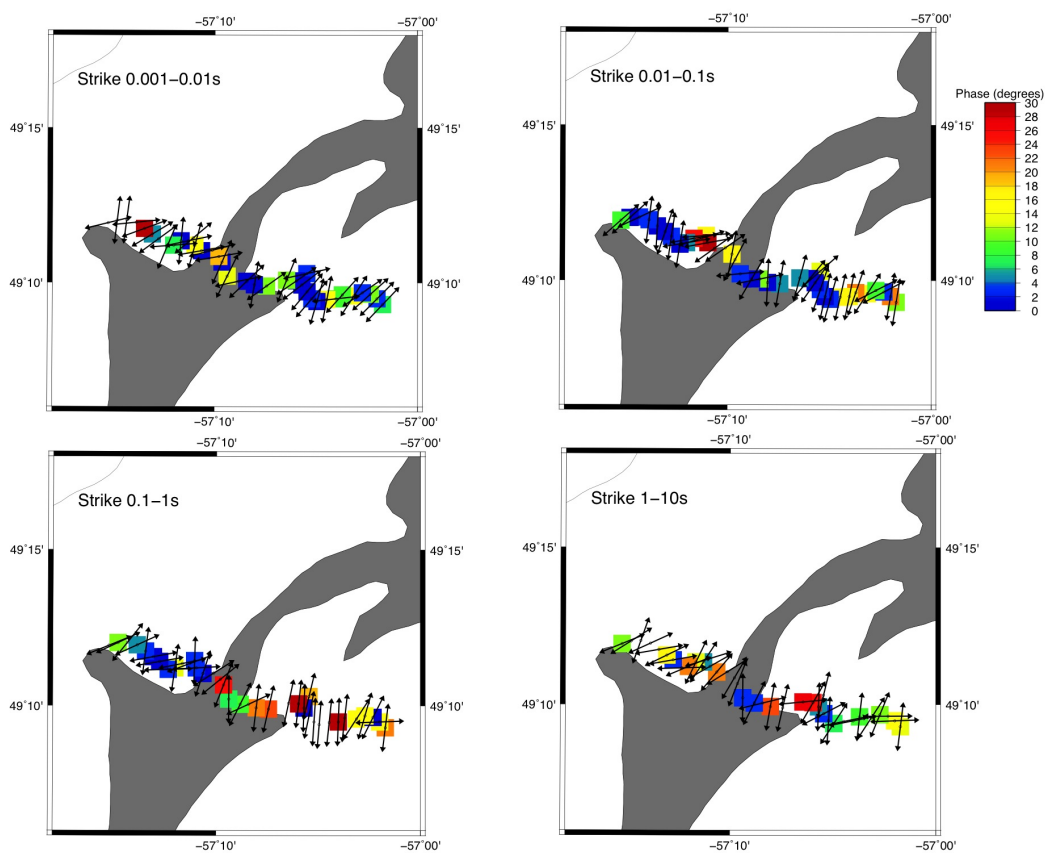


Figure 5.5: Maps showing the preferred geo-electric strike direction at each site for decade period bands for the AMT soundings. The colour scale illustrates the maximum phase difference between the TM and TE mode phases. Stations missing the square indicate the phase difference to be greater than  $30^\circ$ , which means the data is 2D or 3D and not necessarily of poor quality. (grey areas are lake coverage)

Table 5.1: ‘Strike1’: Parameters used

Command	Parameter	Notes
Print level	0	Higher if you want to see more output information
Quite mode	F	(False)
Expert mode	N	
Site list	HWa103.dat	This is an example for site HWa103.dat
Impedance relative error	3.5	RMS misfit values are slightly higher therefore higher error floor is used
Minimum/Minimum period	def	Default
Bandwidth	1	This forces single decade period to one strike (0.1 to calculate for each frequency individually, 8 forces all 8 bands (the whole data) to a single strike direction)
Overlap	def	
Change bounds	y	Yes
Lower strike	-10000	Allows maximum strike variation, later this changes to a preferred strike orientation
Upper strike	10000	Later this changes to a preferred strike orientation, limiting the data to a single strike orientation
Shear etc	def	Use default for sheet and twist values
Stac	N	No, for the first runs

between  $9^\circ$ ,  $45^\circ$ , or  $85^\circ$ . The period band 0.01-0.1 s is quite different, with most stations being 1D with the exception of the southeast corner with a strike of  $9^\circ$ , and the central part with a strike of around  $85^\circ$ . Periods 0.1-1 s are mostly 1D in the northwest third just to the west of the causeway of the profile, with greater phase differences in the southeast section with preferred strikes of  $9^\circ$ . Periods 1-10 s are predominately 2D or 3D, with some of the more repetitive strikes being between  $9^\circ$ ,  $33^\circ$ , or  $85^\circ$ .

Unlike the AMT data, the long period BBMT data seem to have a more consistent strike suggesting that deeper structures have a predominately preferred geo-electric

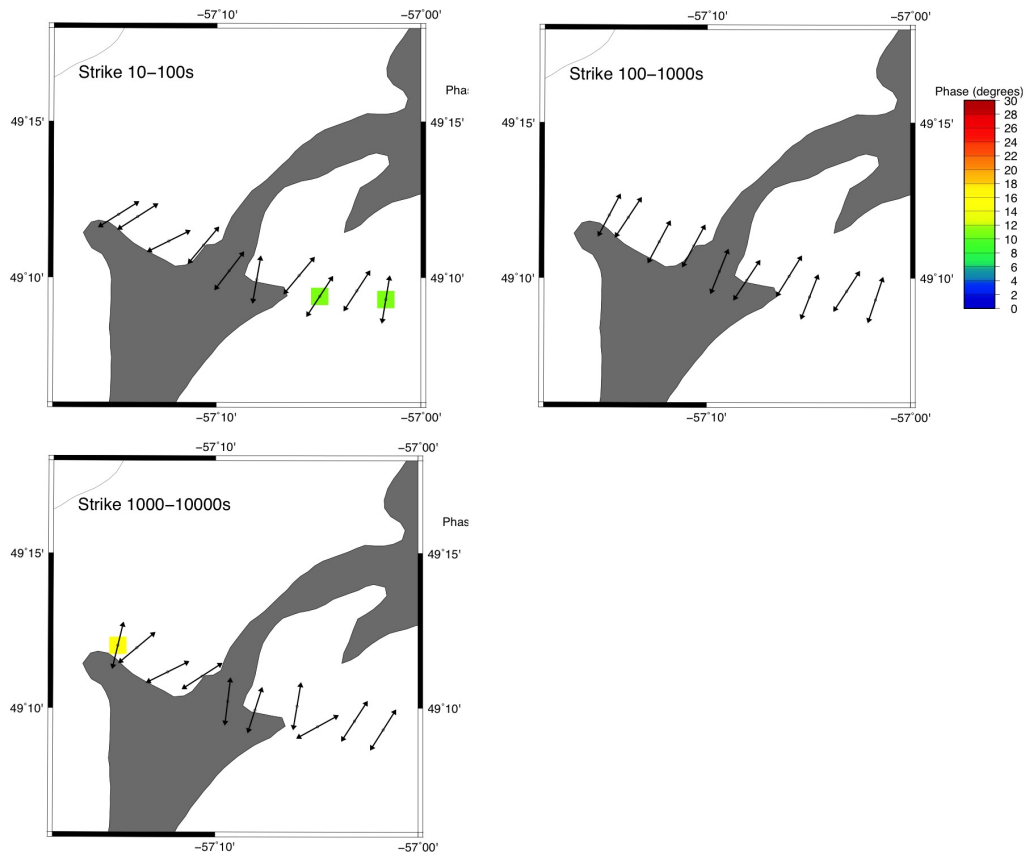


Figure 5.6: Maps showing the preferred geo-electric strike direction at each site for decade bands for the BBMT soundings. The colour scale illustrates the maximum phase difference between the TM and TE mode phases. Stations missing the square indicate the phase difference to be greater than  $30^\circ$ , which means the data is 2D or 3D and not of poor quality.

Table 5.2: ‘Dcmpmap’: Parameters used

<b>Command</b>	<b>Parameter</b>	<b>Notes</b>
Print level	0	
Execute GMT commands	T	True
Select parameters	1113	Options are listed, in this project 1113 was used, 1000 means to plot maximum within a range, 1 to plot the regional azimuth and 13 to plot the phase difference
Scale arrow	N	
Maximum phase difference	30	If phase difference is higher than 30 than the phase difference will not be plotted (Figures 5.5 and 5.6)
Nibblet-Bostick depth	F	
Multiple periods	F	False, display single period range for each map
Enter colour palette file	def	
Geo/hydro	T	True, plot geological and geographical information available
Min period	0.001	Later it changes to 0.01, 0.1 and so on to 1000 to plot each single decade period band
Max period	0.01	Later it changes to 0.1, 1 and so on to 10000
Site labelled	F	
Text header	Strike 0.001-0.01s	This is the header for the map produced with these periods

strike of  $33^\circ$  (Figure 5.6). This value is almost parallel to the Cabot fault at the western edge of the Howley Basin and the Green Bay fault at the eastern edge.

To assess how well the data can be fit with a 2D Earth, the three most dominant strike directions were chosen:  $9^\circ$ ,  $33^\circ$ , and  $85^\circ$ , and ‘strike1’ run again. This time, instead of using lower and upper strike bounds of -10000 and 10000, the data were forced to fit each of the chosen strike directions in turn by setting lower and upper strike bounds to  $9^\circ/9^\circ$ ,  $33^\circ/33^\circ$ , and  $85^\circ/85^\circ$ . Also, the bandwidth command was changed to 8, which

enables one to look at each frequency individually instead of decade bands achieved with command 1. This procedure gave the misfit of the data to each particular strike, i.e., the RMS values. Values below 2 are considered to indicate that the data match the strike (if the data is 1D, strike orientation should not make a difference on the misfit value), and above 5 as the data not matching the strike at all. The results are plotted against frequency for each station for the three chosen strikes in Figures 5.7 to 5.9. The geo-electric strike of  $9^\circ$  gives the best fits to the data for the AMT periods, however  $33^\circ$  yields better results for the deeper, i.e. longer period BBMT soundings. The strike of  $85^\circ$  gave the worst results of the three strikes tested and thus was eliminated from further investigation. All of the strikes experience poor data along the dead bend.

Ideally, a model would be generated along a profile at one strike angle for all periods. However, in reality the subsurface is often complex and this angle can change with depth, as is the case for the Howley Basin data-set with  $9^\circ$  being more appropriate for the AMT periods and  $33^\circ$  for the longer period BBMT data. The profile therefore needs to be looked at at two different strike angles,  $9^\circ$  corresponding more to shallower (top 2-3 km, the basin) structures, and  $33^\circ$  corresponding to deeper (down to 15 km, basement) orientation. In some cases, mostly the central part of the profile, no strike angle can be found that fits the data with a reasonable RMS value (i.e.,  $<2$ ). This could be due to noise caused from the nearby power lines, or it could suggest that the subsurface at these soundings may not be accurately represented with a 2D model, but is 3D. Also, the east end of the profile remained mostly blue ( $\text{RMS} < 2$ ) over most frequencies for all three strikes, indicating that this data has no preference for a particular strike, and thus it is 1D. However, it is interesting to note that the strike of the deeper structure (i.e., the longer period BBMT data) is parallel to the Cabot fault.

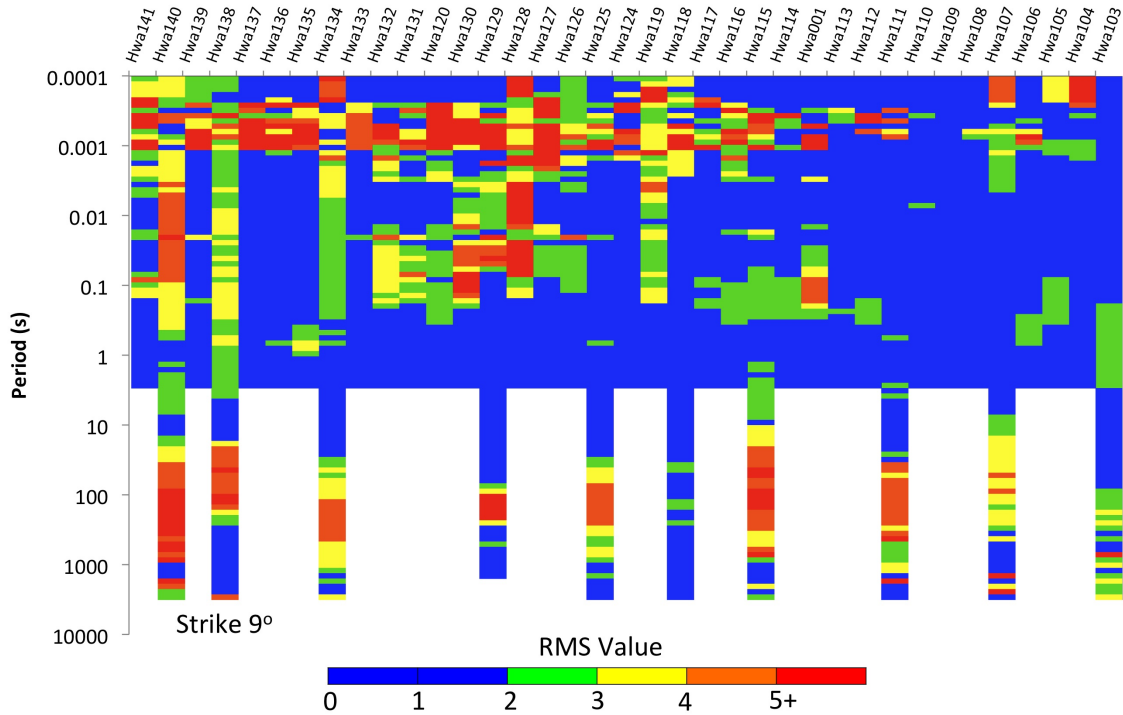


Figure 5.7: RMS misfits for preferred strike calculations for each station over the whole period range for data recalculated at a geo-electric strike of  $9^\circ$ . Blue represents where the data are fit well by this strike direction, red indicates the strike does not fit the data at all. AMT soundings range between 0.0001 s and about 1 s, BBMT soundings range from about 1s to 10000 s. East portion of the profile has low RMS mist values.

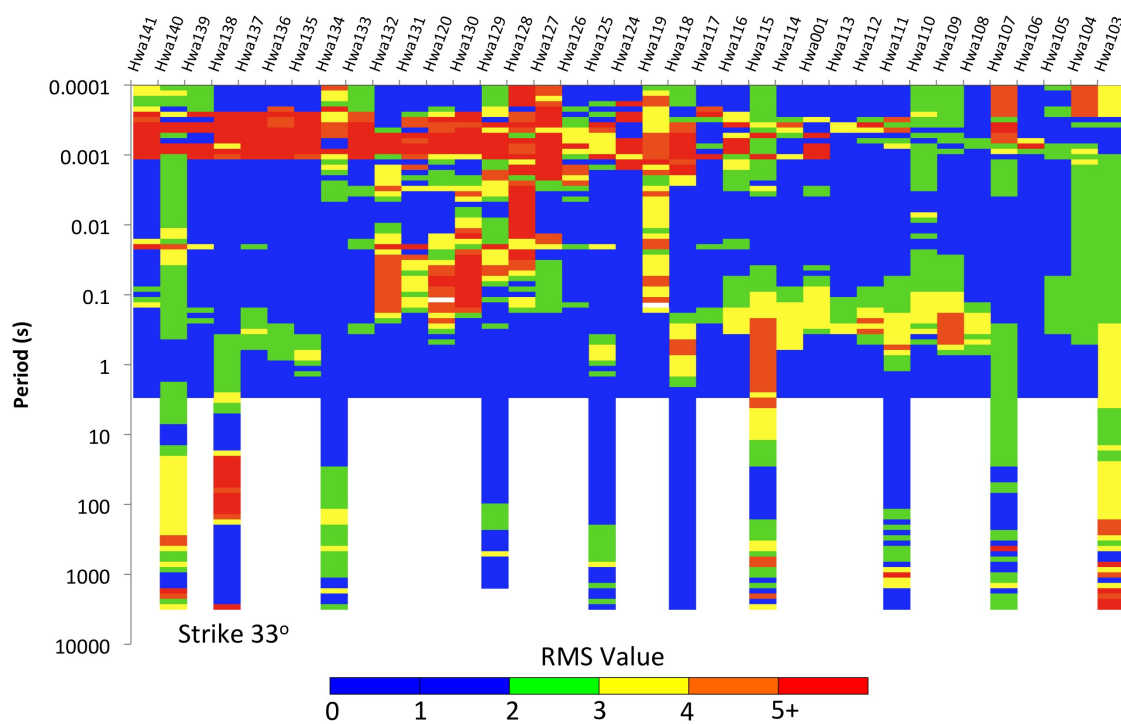


Figure 5.8: RMS misfits for each station over the whole period range for data recalculated at a geo-electric strike of  $33^\circ$ . Blue represents where the data are fit well by this strike direction, red indicates the strike does not fit the data at all. AMT soundings range between 0.0001 s and about 1 s, BBMT soundings range from about 1 s to 10000s. This strike has the lowest RMS misfit values for BBMT.

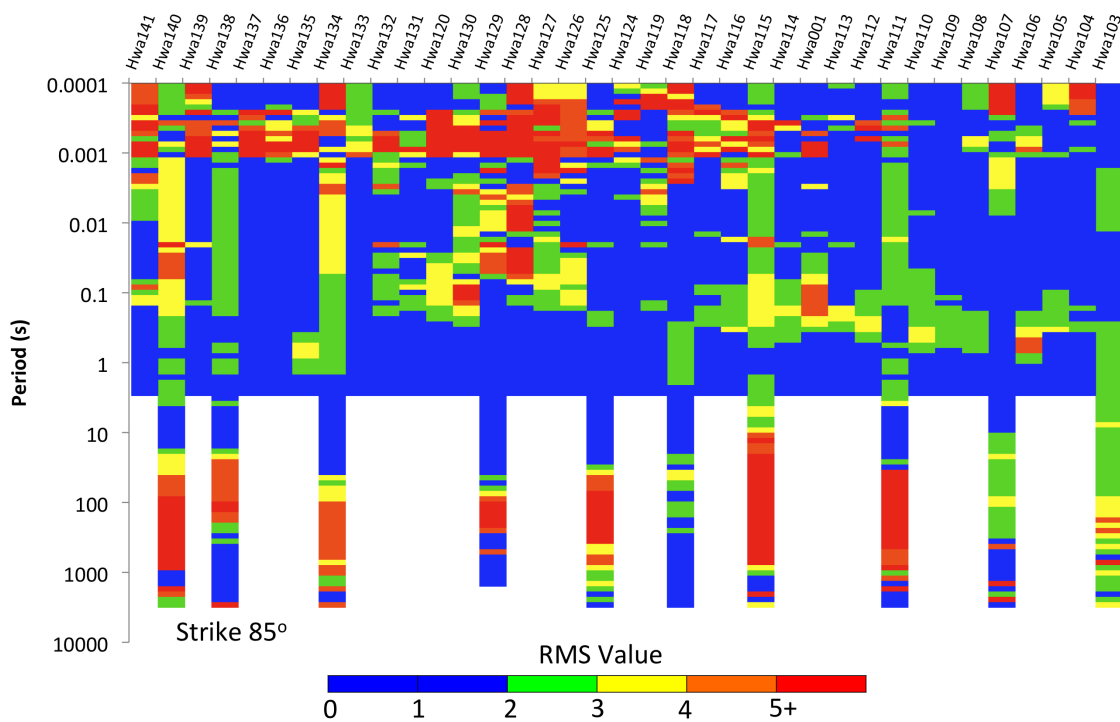


Figure 5.9: RMS misfits for each station over the whole period range for data recalculated at a geo-electric strike of  $85^\circ$ . Blue represents where the data are fit well by this strike direction, red indicates the strike does not fit the data at all. AMT soundings range between 0.0001 s and about 1 s, BBMT soundings range from about 1 s to 10000 s.

With two geo-electric strike directions selected, ‘strike1’ was run again, with bandwidth equaling 8 and the strike angle limited to either 9° or 33°, but this time selecting ‘Yes’ for statistics. The steps taken for distortion removal were as follows using program ‘dcmp2j’ (Table 5.3):

Table 5.3: ‘Dcmp2j’: Parameters used

<b>Command</b>	<b>Parameter</b>	<b>Notes</b>
Print level	0	
Station name (no extension)	HWa103	e.g.
Correct for anisotropy	T	
Correct for errors	T	
Give period range	1,5	Explanation below

Commands given above are an example for HW103, as the first 5 entries range from 0.445-0.469 s. One scrolls up to the highest frequencies to make sure that the first few entries have similar apparent resistivity values. This step corrects for anisotropy by shifting the two apparent resistivity curves to match at the highest frequencies. The first and second numbers represent from which period to start and to which period to take an average.

This outputs the file, e.g., ‘HWa103g.dat’, but does not produce the transfer function data. This file has been corrected for anisotropy, but not yet corrected for strike orientation. The data has to be rotated separately, and then the two files merged together using the procedure described by Tables 5.4 and 5.5.

The steps described above (dcmp2j, mtrotate, and j2edi) were repeated for each station for both of the azimuth angles. The EDI files were saved with a file name extension indicating the corresponding azimuth (HW103g\_9.edi or HW103g\_33.edi)

Table 5.4: 'Mtrotate': Parameters used

Print level	0	
File name	HWa103.dat	e.g.
Is this GB file	F	
Azimuth to rotate	9	or 33
		this outputs HWa103r.dat file

Table 5.5: 'J2edi': Parameters used

Print level	0	
Data file name	HWa103g.dat	e.g.
Give tf name	HWa103r.dat	e.g.
		this outputs HWa103g.edi file

and imported into WinGLink.

### 5.3 2D Inversion

Having been rotated to preferred strikes and corrected for distortion, the two data sets (for strike  $9^\circ$  and  $33^\circ$ ) were imported into WinGLink as two separate projects, each according to its strike. The sounding curves were edited again to remove very noisy data and data with large error bars. Also, the data for which the RMS for fitting the preferred strike direction was high were omitted.

A mesh was then created for a 2D inversion (Figure 5.10). The number of cells was 95 in the horizontal direction, having two or three cells between each station (150 - 250 m spacing), and the number of cells in the vertical direction was 104 cells, with first four kilometres of the subsurface having much finer mesh (at the spacing of 50 - 75 m) than the deeper section (about 750 m).

Inversions were performed using the 2D code in WinGLink (developed by Rodi and Mackie [2001] with the following settings:

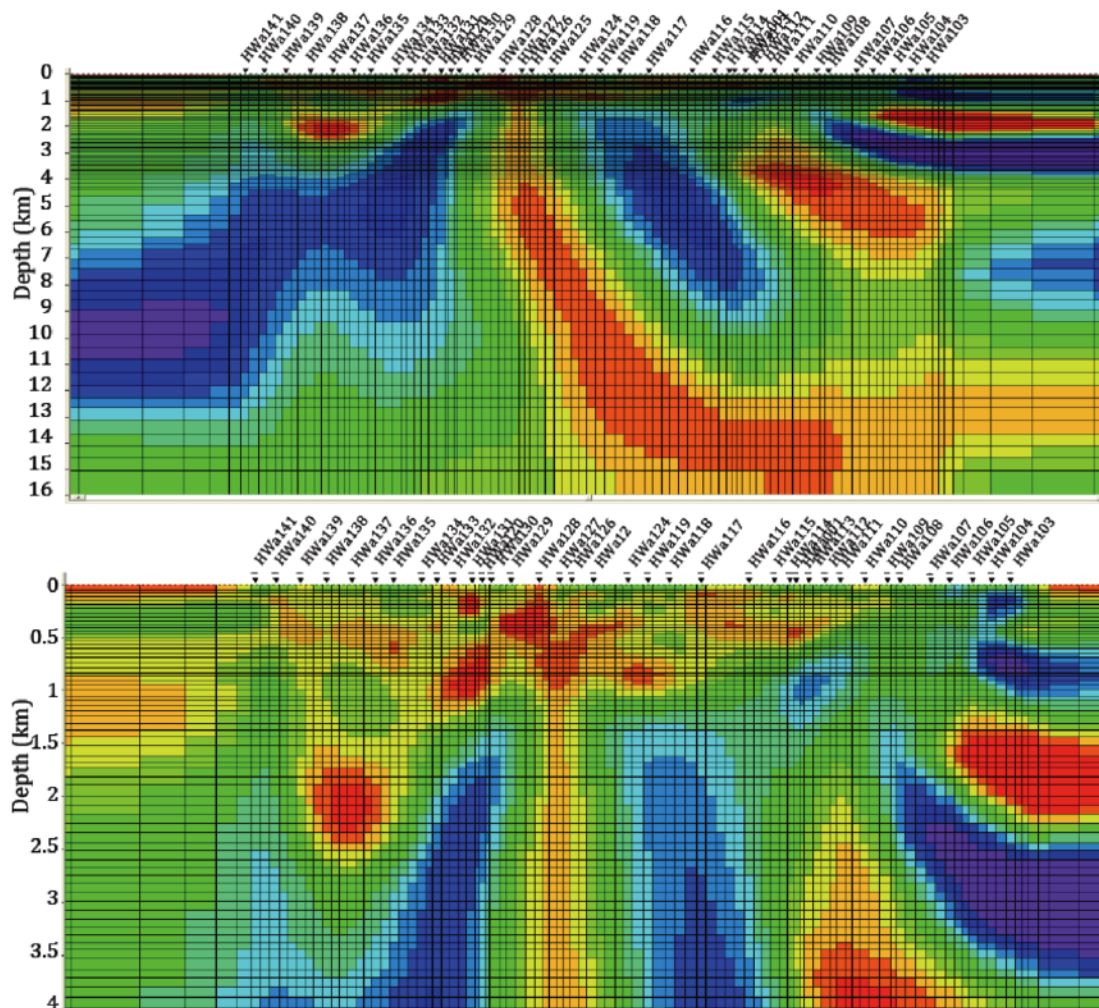


Figure 5.10: The mesh used for the 2D inversions is represented by the grid in the above two panels. Top: Mesh used for the whole section; Bottom: Zoom in to the top 4 km of the mesh.

- Minimum frequency TM/TE: 0.001 Hz
- TE/TM number of decades: 8
- Selected: Use station data
- Unselected: use smoothed curves
- Smooth Inversion:
  - Solve for the smoothest model
  - Uniform Laplacian operator
  - Minimize integral of Laplacian\*2
- Tau smoothing parameter: This value was altered between 3 and 5 for different runs
- Error Floor:7% (5% was selected originally, but data errors for majority of measurements exceeded the error floor, and so increasing the floor decreased RMS misfit, even though there might not be an actual improvement in the data fit and resistivity model)
- Data error: default (if the top layer varies significantly from station to station phase error can be made smaller and resistivity error higher, so the data is automatically corrected for a static shift).

Tau parameter controls the degree of smoothing for the amplitudes in the region of overlap. Increasing tau leads to greater overlap smoothing. The smoothing parameter should be capable of adapting to various bit error rate estimates.

Table 5.6 gives the RMS data misfit values for the models constructed by the various inversion runs for different combinations of modes and smoothing parameters. The

Table 5.6: RMS data misfit values for different models produced by different inversion runs.  $\tau$  is the smoothing factor.

	TE+TM	TE+TM	TE	TE	TM	TM
	$\tau = 5$	$\tau = 3$	$\tau = 5$	$\tau = 3$	$\tau = 5$	$\tau = 3$
Strike 9	5.0758	4.6694	4.5517	4.6156	3.9334	3.9281
Strike 33	5.0519	4.8313	4.9521	4.8605	2.3697	2.6879

models that yielded the best results for the two strike directions used the TM mode only with  $\tau = 5$  for the geo-electric orientation of  $33^\circ$ , and using the TM mode only with  $\tau = 3$  for a strike  $9^\circ$ . This not to say the TE+TM mode is inferior, as it provides complimentary, but not identical, information on an underlying 2-D resistivity structure. The TE mode provides higher resolution of the integrated conductance of deep conductive features than the TM mode, and therefore excluding the TE mode would decrease the resolution and with it RMS value. However, it is true that the TE mode response is more susceptible than the TM mode to distortion by 3-D conductive features of finite length. Figure 5.11 and 5.12 are constructed of models from Table 5.6 along 18 km long profile, Figure 5.11 are full depth cross sections and 5.12 top 4 km. All of the models experience a deep vertical conductor in the middle of the section, with TE+TM and TM modes sharing similar resistivity model. TE mode models are quite different, especially around that vertical conductor, possibly indicating the 3-D structure in that area. Hence, the further interpretation is preferred on the TM modes, which also have the lowest RMS misfit values. The models for the TM mode only with  $\tau = 3$  for both strike directions are shown in Figure 5.13. Figure 5.14 shows zoomed in images of the top 4 km of these two models.

The TM mode yielded the lowest RMS values, especially for strike  $33^\circ$ . In general terms, 2.6879 (for TM mode,  $\tau=3$ ) is not the most desired result; preferably this value would be below 2. However it is one of the lowest calculated for the Howley

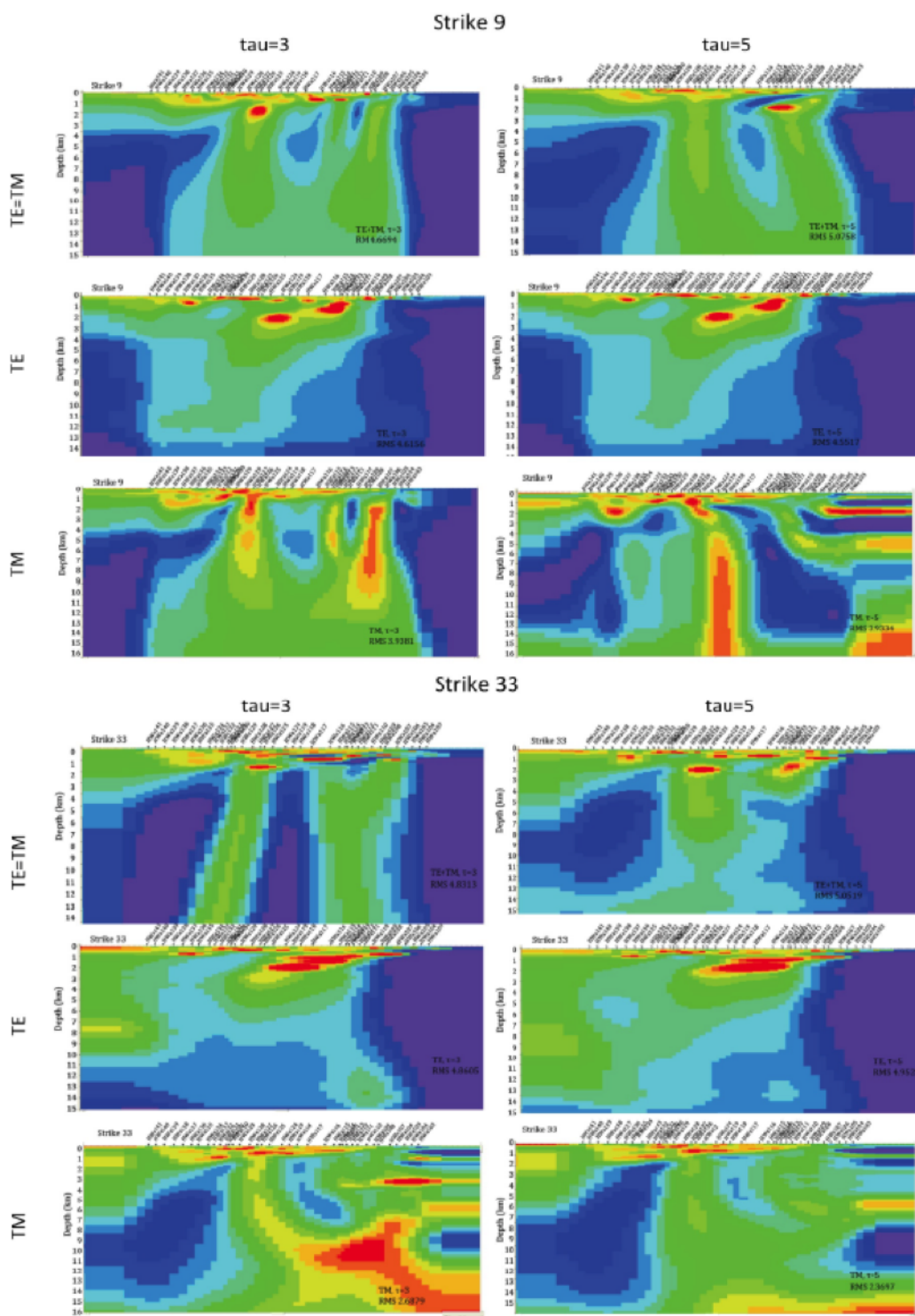


Figure 5.11: The constructed resistivity models calculated in Table 5.6. Larger images are included in Appendix C.

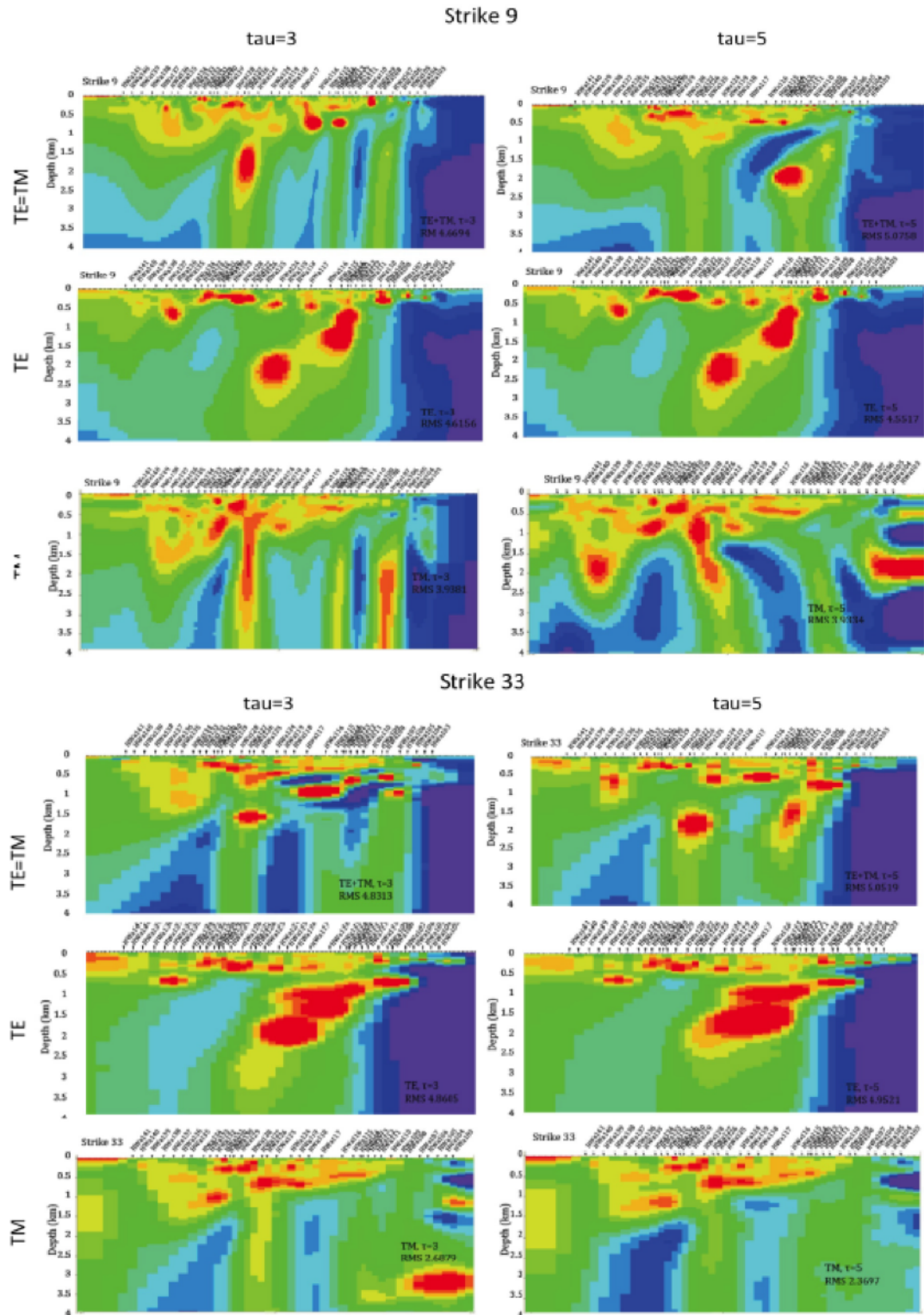


Figure 5.12: The constructed resistivity models calculated in Table 5.6, top 4 km. Larger images are included in Appendix C

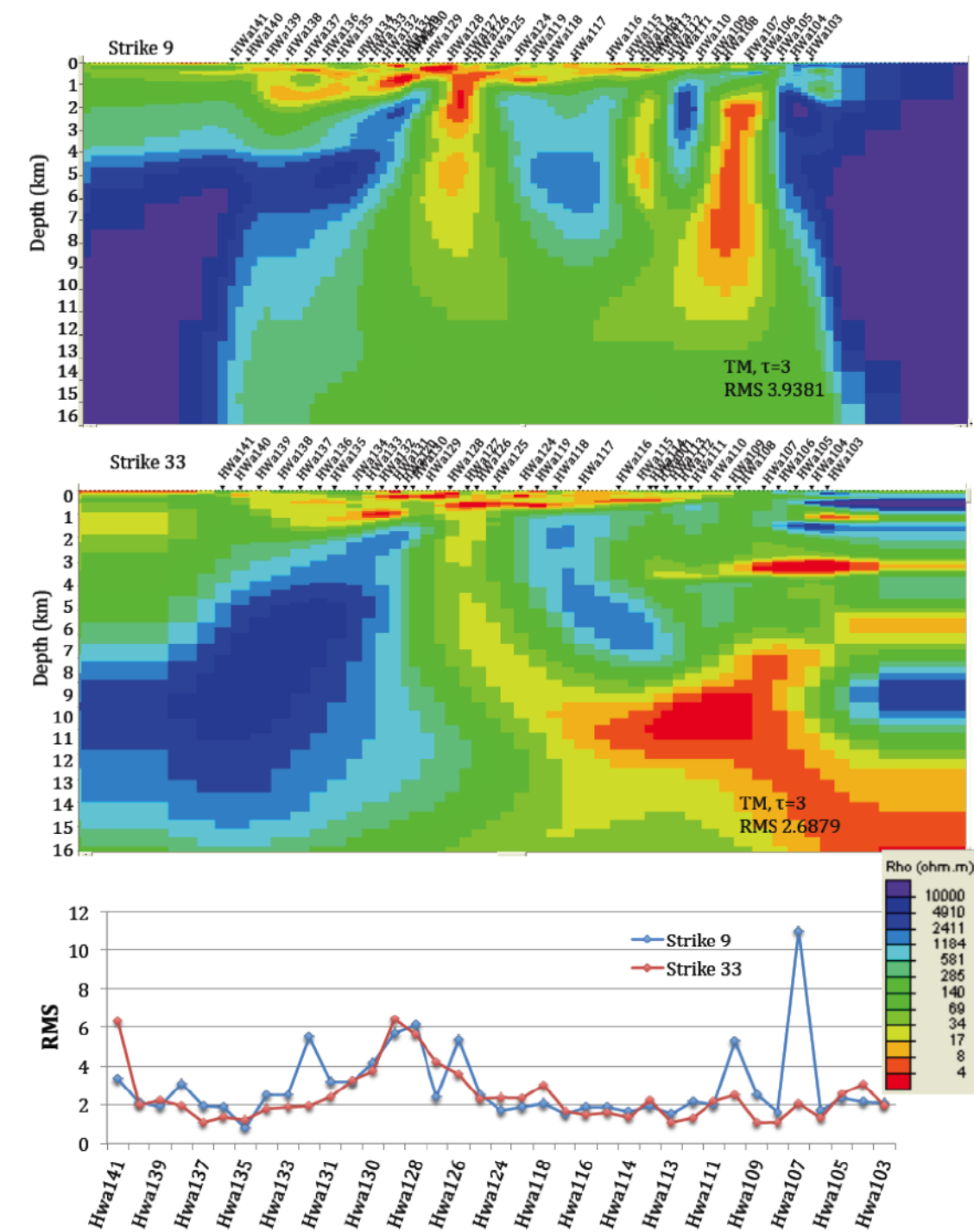


Figure 5.13: The constructed model for TM mode only inversions with  $\tau = 3$  for both strike directions. Top: Conductivity cross section of the full 2D model for data rotated to a strike of  $9^\circ$ ; Middle: Conductivity cross section of the full 2D model for data rotated to a strike of  $33^\circ$ ; Bottom: Comparison of RMS data misfit values for strikes  $9^\circ$  and  $33^\circ$  for each station. The RMS values, with a few exceptions, follow each other for both strikes with a value around 2. The exceptions are stations HW126-HW131, which might be due to nearby power lines or the data are 3D in this area. The distance between HW103 and HW141 is 18 km.

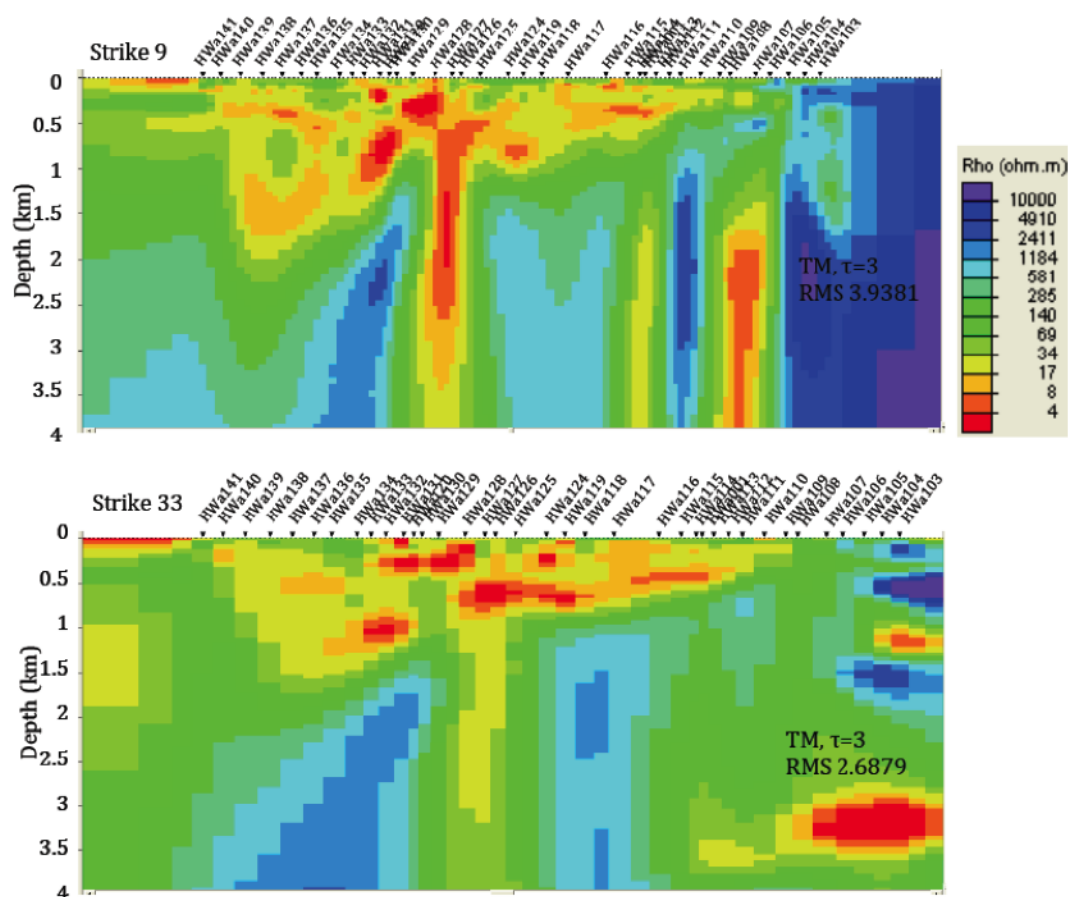


Figure 5.14: Zoom in to the top 4 km of the models shown in Figure 5.13. Top: Cross section produced by using data rotated to  $9^\circ$ ; Bottom: Cross section produced by using data rotated to  $33^\circ$ . It can be seen in both models that the more conductive basin is thickening towards the Northwest towards the Cabot fault, where its maximum thickness reaches about 1.5-2 km.

Basin data. An example of the fit of the calculated sounding curves to the observed curves for this inversion (for site HW135) is shown in Figure 5.15. The calculated data are close to the observed data over the whole period range, and is thus considered a good fit to the data.

In the conductivity models for both strikes, one can observe that the maximum depth of the conductive feature (assumed to consist of the sediments in the basin) reaches about 2 km at the northwest end of the profile (Figure 5.13 and Figure 5.14). Further, towards the eastern end of the profile the depth of the conductive feature is decreasing, i.e. getting shallower, and it pinches out at the surface between stations HW107 and HW108. In the central part of the profile, the models for both strikes have a deeper, vertical, and more conductive feature. This could simply be due to poor quality data in this area (very close to power lines) or a structural feature such as a fault, causing an increase in conductivity. This feature will be investigated in more depth later.

The models constructed for the TM mode only inversion and  $\tau = 5$  for  $9^\circ$  and  $33^\circ$  strikes are shown in Figure 5.16 and Figure 5.17. When comparing the RMS data misfit values for both sets of rotated data (Figure 5.16) there is again a preference for  $33^\circ$ . However, the shape and depth of the basin do not change much between the two models, leading to a conclusion that the RMS values are more strongly influenced by the basement, as the  $33^\circ$  orientation was preferred by the longer periods. Also, for both models, RMS values experience an increase between HW126-HW131, most likely caused by noise or perhaps 3D effects.

Models for both calculated strikes are similar, with a conductive basin layer on top

## HW135, TM mode

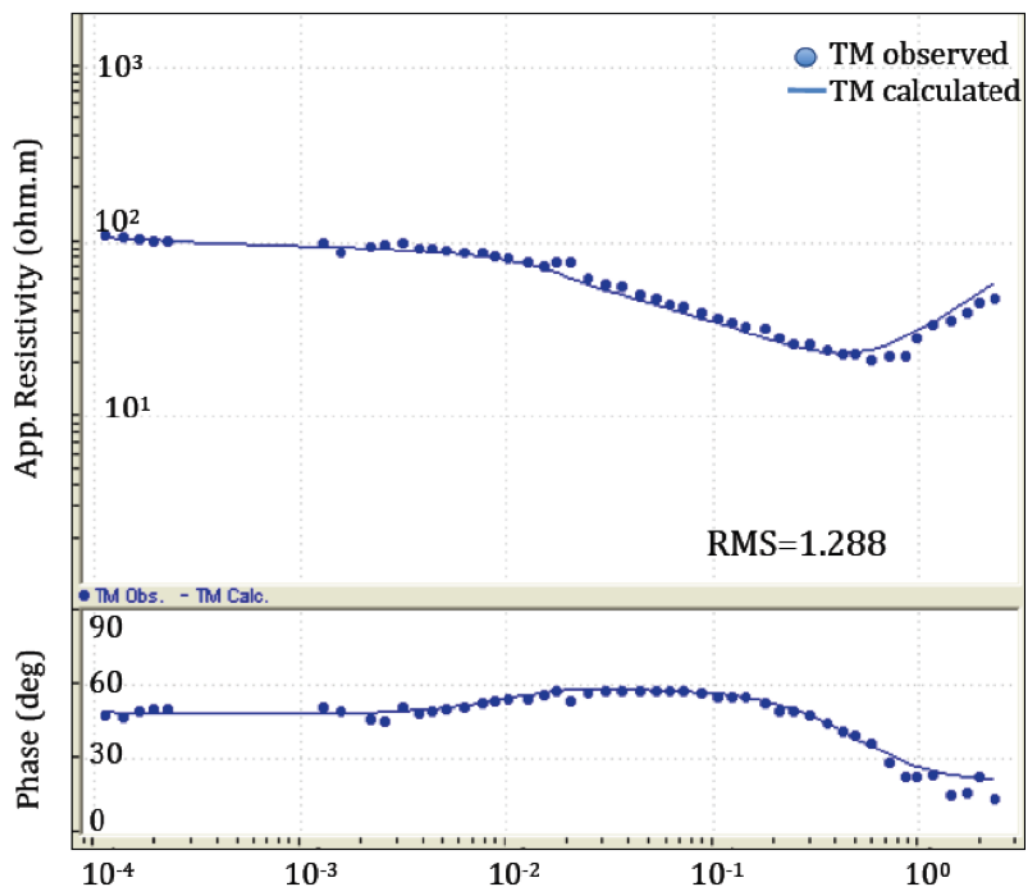


Figure 5.15: Graph showing apparent resistivity (top) and phase (bottom) vs. period for the observed (blue circles) and calculated (blue line) data for TM mode, strike  $33^\circ$ , site HW135. The calculated data matches the observed data well, resulting in low RMS misfit value of 1.288 (for this site).

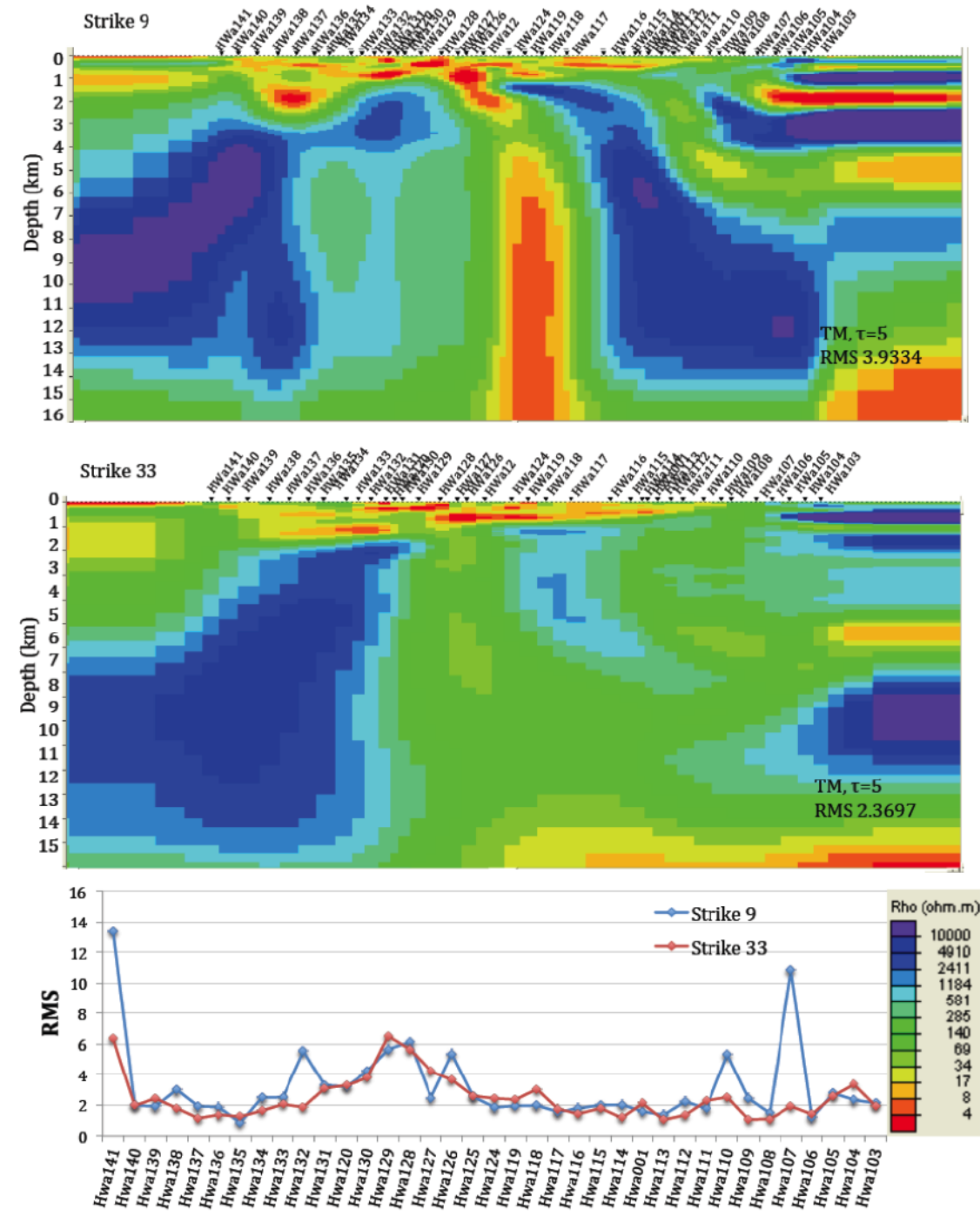


Figure 5.16: The constructed models for TM mode only and  $\tau = 5$ . Top: Conductivity cross section of the full 2D model for data rotated to a strike of  $9^\circ$ ; Middle: Conductivity cross section of the full 2D model for data rotated to a strike of  $33^\circ$ ; Bottom: Comparison of RMS data misfit values for strike  $9^\circ$  and  $33^\circ$  for each station.

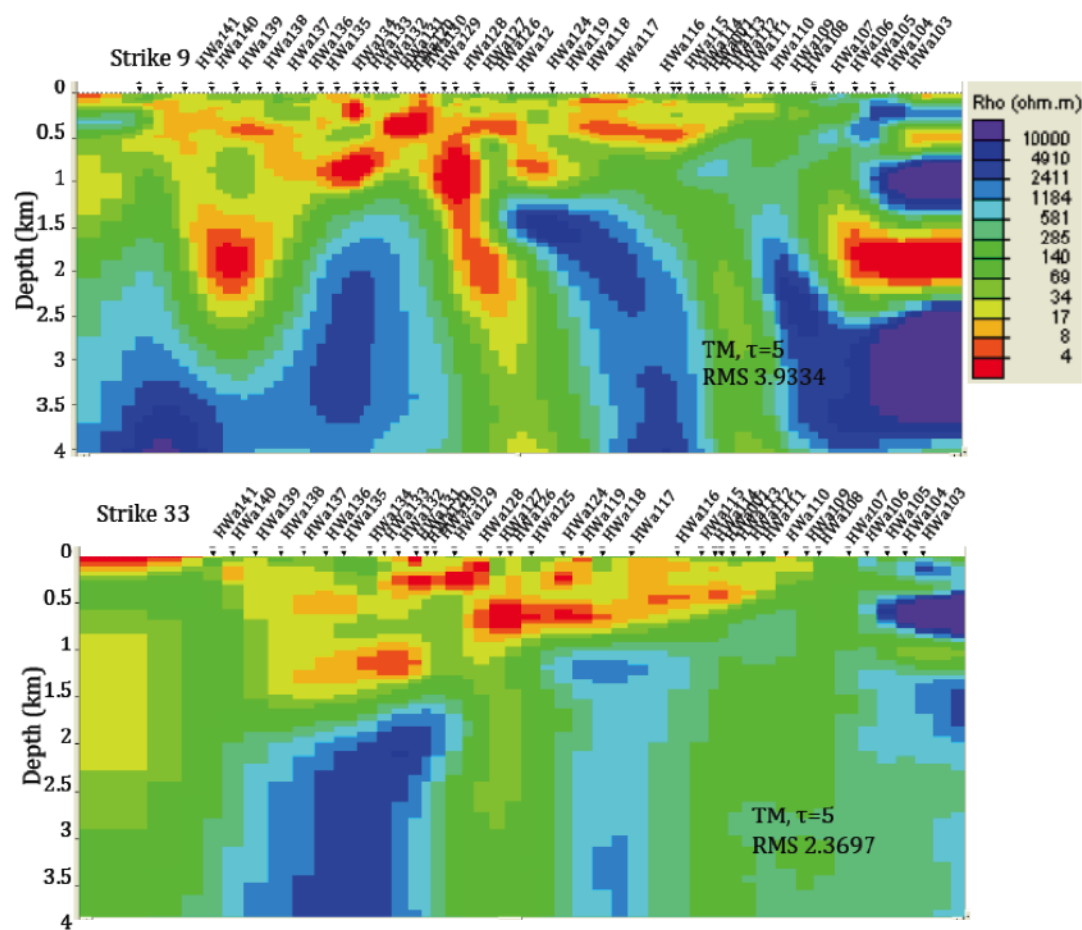


Figure 5.17: Zoom in to the top 4 km of the models shown in Figure 5.16. Top: Cross section produced by using data rotated to  $9^\circ$ ; Bottom: Cross section produced by using data rotated to  $33^\circ$ . It can be seen in both models that the more conductive basin is thickening towards the Northwest towards the Cabot fault, where its maximum thickness reaches about 2 km.

of the more resistive basement just as for the results for  $\tau = 3$ . The conductive layer pinches out at the east end of the profile, and reaches its maximum depth of about 2 km in the western end of the profile towards the Cabot fault. All the models also display a deep vertical feature between sites HW125-HW130. Overall, the shallower conductive structure is consistent in all the models, while the deeper basement varies with the exception of the vertical conductive feature in the central portion of the profile that is repeated in some form or other in all the models.

# Chapter 6

## Interpretation and Discussion

This chapter discusses some of the major features observed in the inversion models from Chapter 5, and the results are compared to other available information for the area. Finally, a geological interpretation of the Basin's modelled resistivity structures is discussed.

### 6.1 Deep Crustal Structures

The structure expected was a conductive top layer (the basin) with resistive basement underlying it. This is, in general, the structure seen in the inverted models. However, in most of the models from Chapter 5, a deep almost vertical conductor is observed in the middle of the profile. This feature aligns with the stations with the highest RMS values (Figures 5.11, 5.12, 5.14, 5.15), which were also the stations that were located in very close proximity to the power lines (HW126-HW131). In order to be sure the feature is real, and not an artifact of the noise, inversions were re-run with stations most affected by the power lines omitted. The inversions were re-run for TM mode data only, using  $\tau=3$  for a strike of  $9^\circ$  and  $\tau=5$  for  $33^\circ$ , as these produced the lowest RMS data misfits for the two strike directions out of the previous suite of inversions.

Successively more and more noisy stations were omitted. Figure 6.1 shows the results for a strike of  $9^\circ$  and Figure 6.2 shows the results for a strike of  $33^\circ$ . Eliminating two, three and then six stations for  $9^\circ$  had no influence on the deeper structures (Figure 6.1). As the longer periods tend to have a preferred strike orientation of  $33^\circ$  and this strike yielded overall a better RMS value, Figure 6.2 is instead looked at more closely. The vertical conductive feature in the middle of the section shifts slightly in position as more and more stations are omitted, but it is present to some extent in all inversions. Moreover, the basement conductor is clearly visible in TE apparent resistivity and phase pseudo section (low apparent resistivity and high phases at long periods - Figure 4.16, at longer periods at sites near HW127). This observation further provides strong support for the feature being real and not a spurious feature arising in the inversion.

The Bouguer gravity anomaly data for the area exhibits a significant decrease in the vicinity of stations HW125-HW131 (Figure 6.3, produced in Oasis Montaj, a coloured image of Figure 2.5b by Miller and Wright [1984] ), the stations under which the vertical conductive feature exists. The largest drop in the gravity anomaly occurs around station HW125, exactly where the conductive top layer thickens to the west. This could indicate a sudden offset and thickening of sediments in the basin, and the deep vertical conductive feature could be this off-setting fault. This interpretation agrees with the assumption that the Howley Basin is a part of a negative flower structure. The existence of this gravity low goes some way to corroborating the presence of the deep conductive feature. Also, the gravity anomaly extends to the east, roughly in the direction of  $85^\circ$ , which was one of the preferred strike orientations for the central portion of the profile (HW126-HW134) for mid period ranges. Since the anomaly continues pass the Green Bay fault to the east, it is possible that the signature is

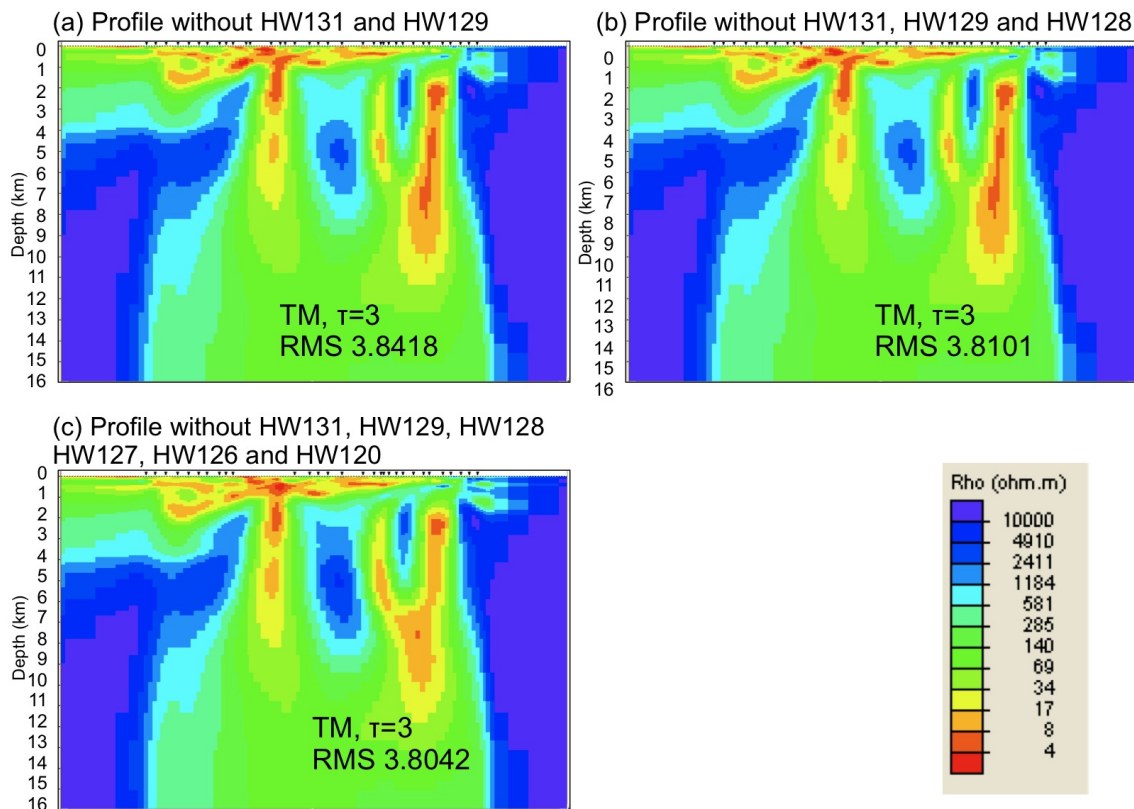


Figure 6.1: 2D inversion results for TM mode only,  $\tau = 3$ , and a strike of  $9^\circ$  with (a) two stations closest to the power lines omitted, (b) three closest omitted, and (c) six closest stations omitted from the inversion.

caused by basement rocks, and suggests that the basement is Topsail Igneous Complex. However, the gravity readings are sparsely spaced and the swampy conditions in the basin are not the most amenable for acquiring accurate densely spaced gravity readings. The intriguing magnetic anomaly within the basin (seen in Figure 2.7) is located just north of the profile, but potentially could be a result of the faulting within the basin.

Other deep structures are variable from model to model, and not in shape, thus are not further discussed, as the prime interest lays in the shallower basin. There is some indication in the models of a significant vertical feature at the eastern end of the

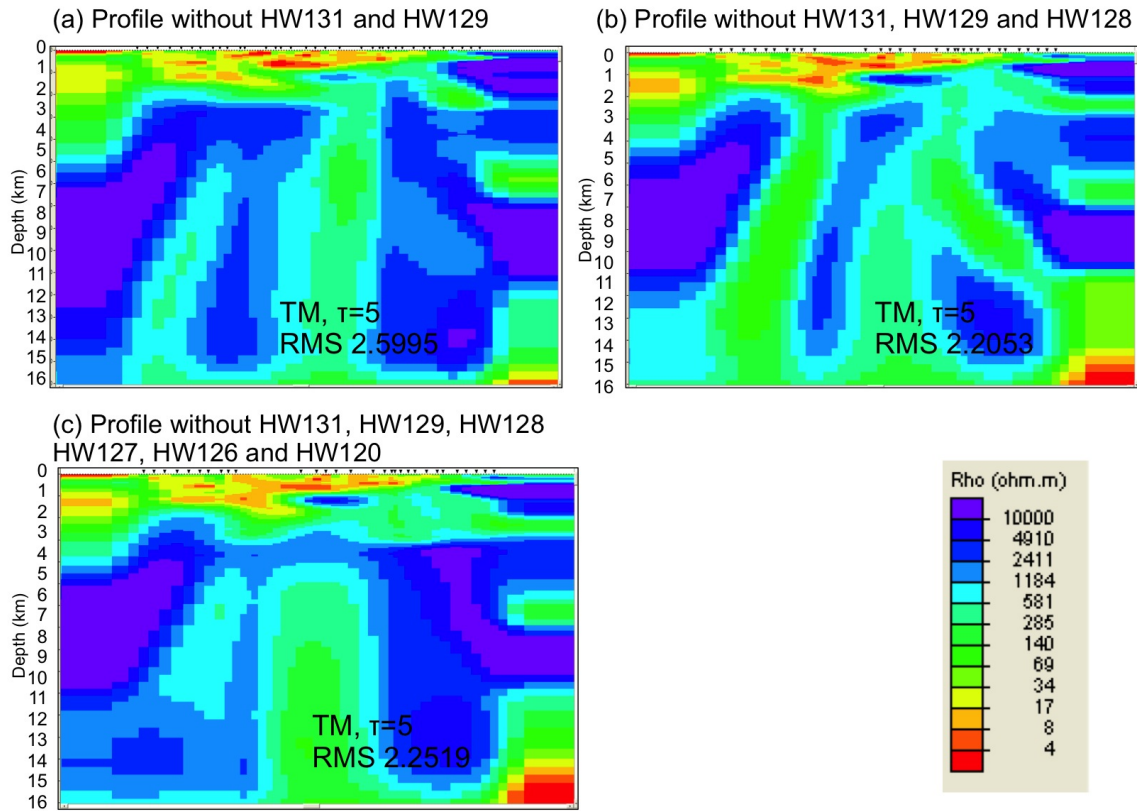


Figure 6.2: 2D inversion results for TM mode only,  $\tau = 5$ , and a strike of  $33^\circ$  with (a) two stations closest to the power lines omitted, (b) three closest omitted, and (c) six closest stations omitted from the inversion.

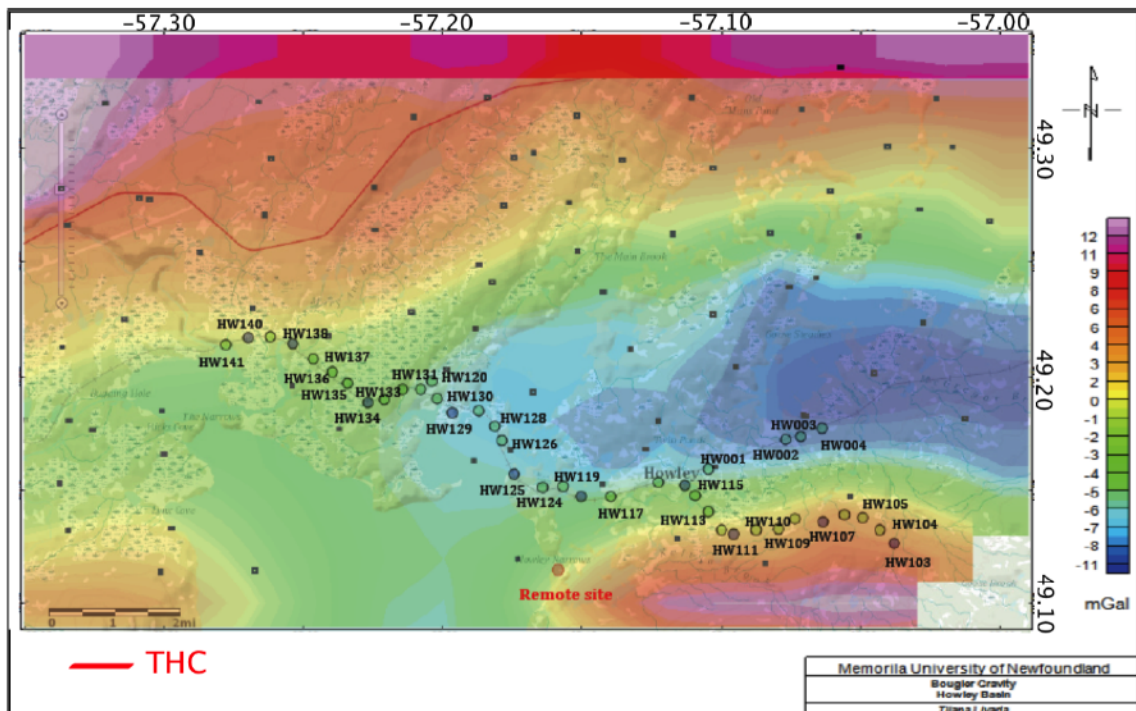


Figure 6.3: Bouguer anomaly map (a coloured version of Figure 2.5b produced in Oasis Montaj [Miller and Wright, 1984]), with the MT stations indicated by the coloured dots. The black dots indicate the location of the gravity measurements.

profile that could correspond to the Green Bay fault (the eastern bounding fault of the Howley Basin; see Figure 2.1) cutting down deep into the subsurface, but there is no indication of 4 km of sediments on the eastern end of the Basin as previously interpreted by Hamblin et al. [1997].

## 6.2 Howley Basin Structures

For more in-depth analysis of the Basin and its structure, the 2D conductivity models are zoomed in to the top 4 km (Figure 6.4 and Figure 6.5). Similar to Figures 6.1 and 6.2, Figures 6.4 and 6.5 investigate the influence of the potentially noisy soundings close to the power line. Figure 6.4 shows the results for strike of  $9^\circ$  and Figure 6.5 for a strike of  $33^\circ$ . Neither of the two strikes' inversions differ much as more and more stations are omitted, even more so than for the deeper parts of the models. All the models reveal that the basin is deepening towards the Cabot fault. Also, there is a deepening of the basin in the middle part of the profile around stations HW125-HW131. In the  $9^\circ$  strike models (Figure 6.4) this deepening coincides with the top of the deep vertical conductor. This deepening could again indicate the presence of a structural fault reaching the bottom of the basin.

For further interpretation, geological units assumed are as the ones from the neighbouring Cormack Basin. The lower most unit in the Howley Basin is the North Brook formation, which is the most compact and made up of conglomerates and sandstones, making it more resistive. Characteristic electric resistivity for this unit is about  $200 \Omega m$ . Next is the Rocky Brook formation, which is more shale rich and thus expected to be more conductive. The approximated average resistivity for this formation is about  $25 \Omega m$ . The Humber Fall Formation overlays the Rocky Brook formation. It is

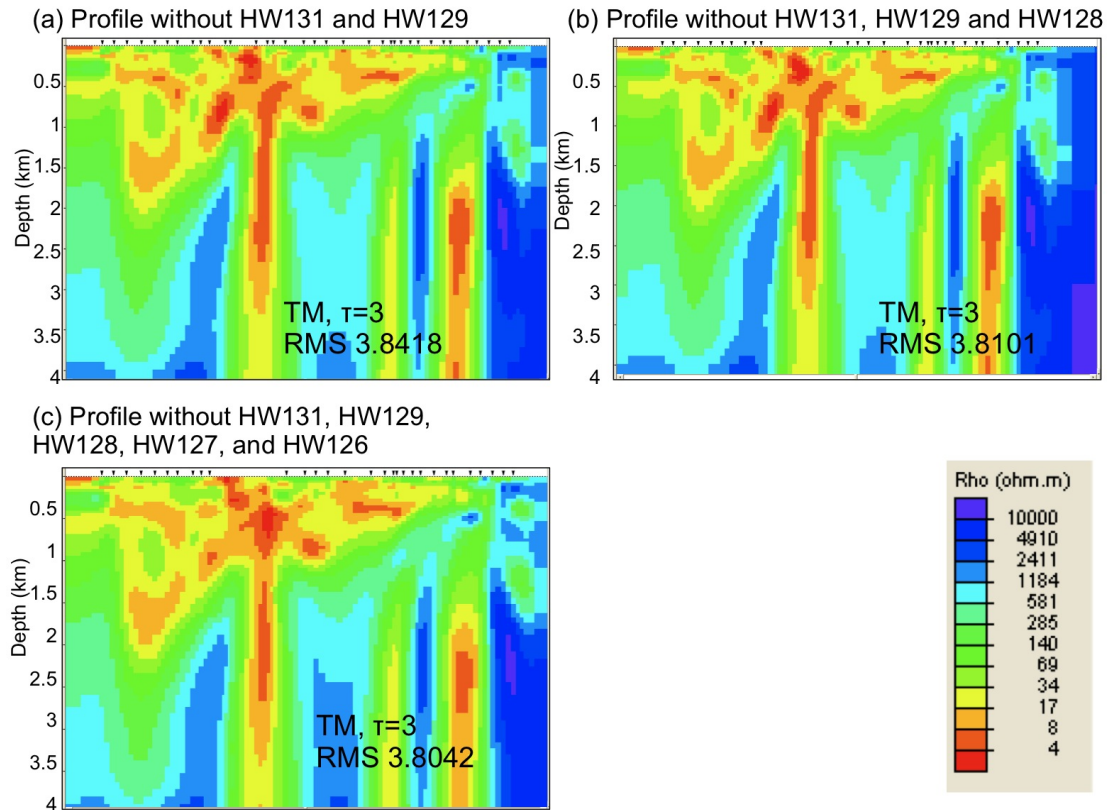


Figure 6.4: Zoom ins to the top 4 km of the models shown in Figure 6.1: TM mode only,  $\tau=3$ , and a strike of  $9^\circ$ . (a)-(c) the two, three and six soundings closest to the power line are omitted from the inversion.

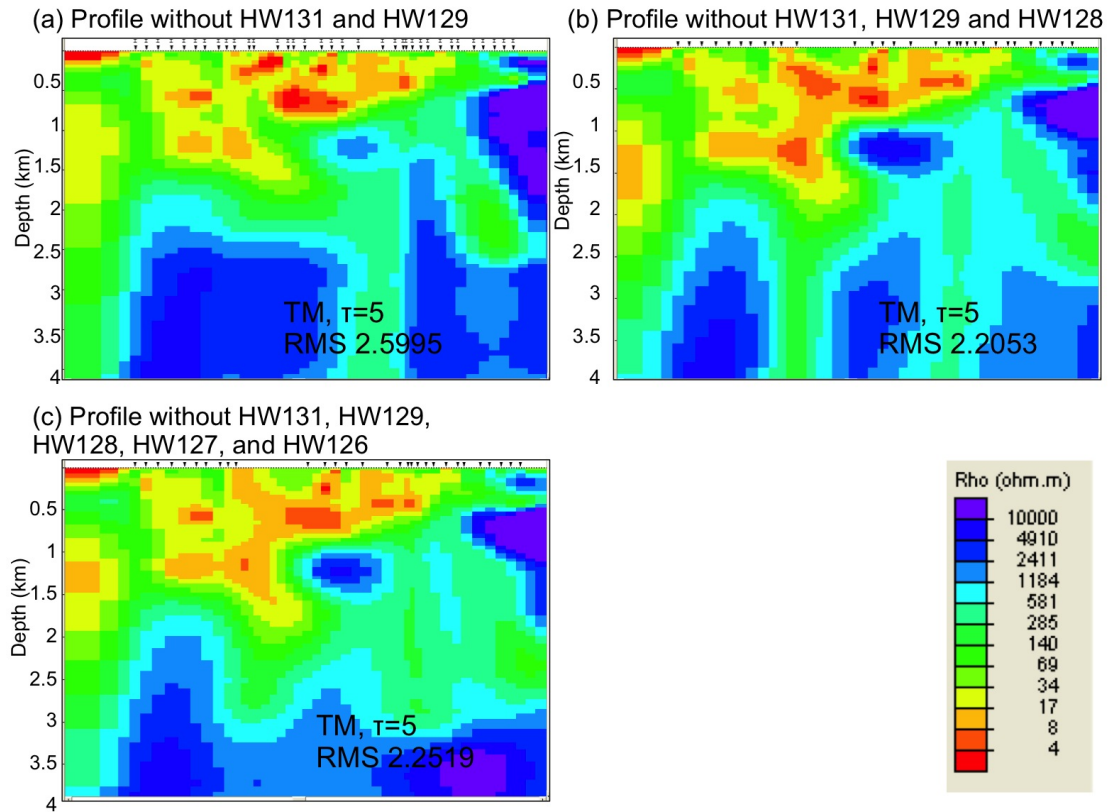


Figure 6.5: Zoom ins to the top 4 km of the models shown in Figure 6.2: TM mode only,  $\tau=5$ , and a strike of  $33^\circ$ . (a)-(c) the two, three and six soundings closest to the power line are omitted from the inversion.

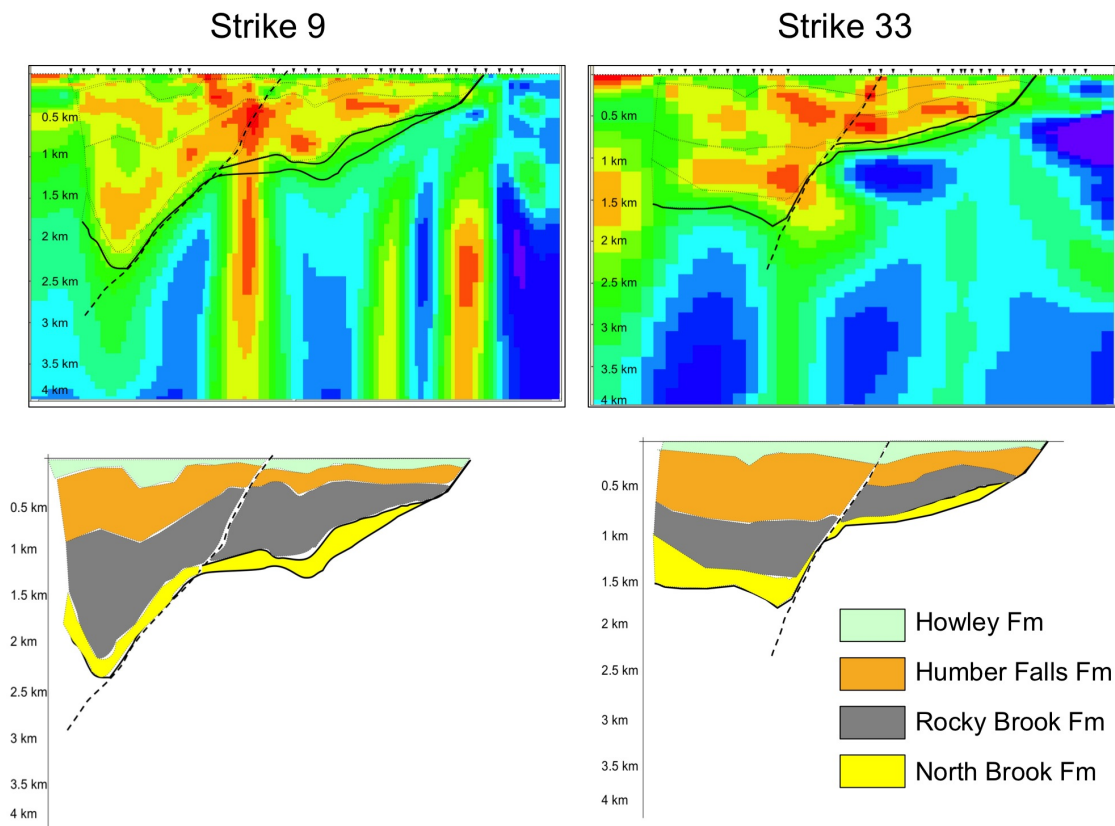


Figure 6.6: Proposed Howley Basin models based on the MT data and inversions. Left: Inversion used for generating model and proposed structure of the basin using  $9^\circ$  for geo-electric orientation. Right: Inversion used for generating model and proposed structure of the basin using  $33^\circ$  for geo-electric orientation.

interpreted as an alluvial fan deposit and therefore finer grained and expected to have higher conductivity. The MT method does not provide the best resolution, so the distinction between these two units is difficult and the contact between only speculated along some points of higher resistivity. The Howley formation is a poorly drained fluvial system. and the poorly sorted sediments tend to be less conductive, hence the Howley formation was picked as the top more resistive layer with an average resistivity of  $150 \Omega m$  (Figure 6.6).

Two basin structure models are proposed (Figure 6.6). In both models, the most obvious feature is the general wedge-shaped basin going from about 2 km in the west

to 0 km in the east (assuming all the basin sedimentary rocks are more conductive than the basement rocks). The layering within the basin is remarkably similar between the two interpretations and is consistent with the four formations that are believed to be found in the basin: the North Brook, Rocky Brook, Humber Falls, and Howley Formations. Because of the limited resolution of the MT data, it is hard to define structures within the sedimentary rocks of the basin, but layering appears not to be simple with horizontal bedding, but could indicate possible folding. Halfway along the profile, a vertical conductor is present in both the models, and it is interpreted as a possible steep basin deepening due to a fault within a negative flower structure (Figure 6.7). On the other hand, the Cabot fault at the moment is interpreted as a compressional, positive flower structure, but with the Deer Lake Basin's complex geological history it is possible that the basin was initially an extensional negative flower structure, and later inverted. This could mean that the Howley Formation was most likely deposited during the negative flower structure period. However, it is important to note that the data in this central part of the profile were affected by power line noise, and so it is possible, although unlikely, that the steep and/or deep conductor is an artefact. The major difference between the two interpretations is the estimated basin depth. Using the geo-electric strike of  $9^\circ$ , the Howley Basin appears to have a maximum depth of just a bit more than 2 km, while using the strike orientation of  $33^\circ$  the maximum depth is significantly less at more like 1.5 km. However, in both interpretations the Rocky Brook Formation, which is the hydrocarbon prone formation, is the thickest of all, ranging in thickness from 0.5 - 1.5 km.

In both scenarios shown in Figure 6.6, the basin is much shallower than expected based on the previous work done on the Basin although consistent with the geophysics-based

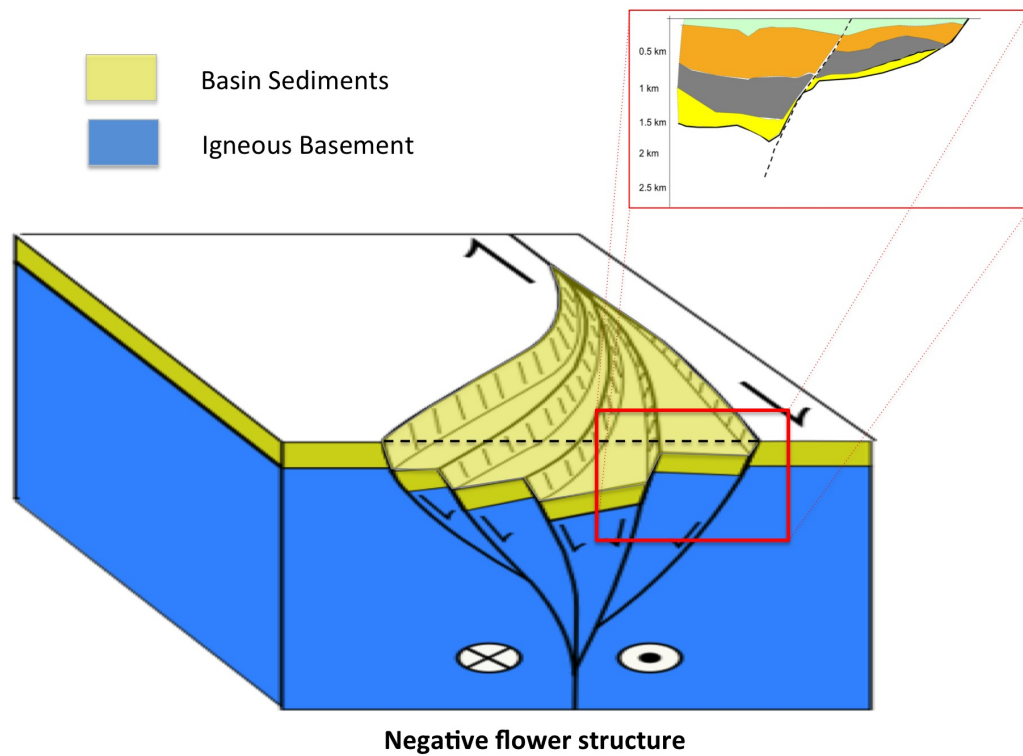


Figure 6.7: Structural setting of a negative flower structure. The possible location of the Howley Basin within such a structure is outlined by the red square (image modified from Wikipedia: Strike-slip tectonics).

interpretation of Miller and Wright [1984] (Figure 2.6). In addition, if the interpretation using the electrical orientation of  $33^\circ$  is considered, the Rocky Brook formation is not deep enough for generation of hydrocarbons. Nevertheless, slices of the Anguille group caught up in the Cabot fault system show cleavage indicating that they had once been at higher P-T than the oil window (personal communication with Dr. Tomas Calon and Linden Ernst). The Deer Lake group rocks are apparently significantly lower P-T, but their present thickness does not necessarily record the depth of burial because of the basin inversion, and maybe the Deer Lake group did make it to the oil window. However, for better understanding and affirmation of the interpreted models, they should be compared to the interpretations from seismic and gravity data that are being acquired in the area.

The interpretation of the units' thicknesses and distribution is not interlay reliable, and the MT method lacks the precision, however the general shape of the basin is genuine. It is also valid to assume that the enhanced conductivity below HW130 is a narrow highly conductive fault zone, and that its conductance has 'smeared' outwards by the regularization in the interpretation.

# Chapter 7

## Conclusion

The Howley Basin is located in western Newfoundland. It is located just east of the Cabot fault and is often referred to as a sub-basin of the Deer Lake Basin. The Cormack sub-basin, located on the west side of the Cabot fault, consists of three main geological units: the North Brook formation (conglomerates and sandstone), Rocky Brook formation (organic rich shale), and Humber Falls formation (sandstone). The same units may occur in the Howley Basin with the addition of the Howley formation. Hypothetically, the presence of the Howley formation means that the Rocky Brook formation is buried deeper in the Howley Basin and hence has been subjected to more favourable conditions for hydrocarbon production.

An MT survey comprising 40 stations, along an 18 km long profile, was conducted in August and September 2013, crossing from the Topsail igneous formation in the east to approximately the Cabot fault in the west.

The preferred geo-electric strike orientation for higher frequencies (shallower subsurface) was  $9^\circ$ , while for lower frequencies (deeper soundings) was  $33^\circ$ , which is almost

parallel to the Cabot fault.

The data were rotated to these two orientations, and 2-D inversions were performed. To evaluate the inversion models, Root Mean Square (RMS) data misfit values were calculated. For both strike directions, the TM mode only yielded better results, using a smoothing factor  $\tau$  of 3 for strike  $9^\circ$ , and  $\tau$  of 5 for  $33^\circ$ .

The inversion models of the resistivity profile (one for each of the preferred strike orientations,  $9^\circ$  and  $33^\circ$ , see Figure 6.6) indicate the basin to be deepening westward, towards the Cabot fault, reaching its maximum depth of about 2 km just to the east of the fault. The most conductive unit in the basin was interpreted to be the shale rich Rocky Brook formation. Given the depth of the basin suggested by the MT results, the Howley Basin is probably not any more hydrocarbon prospective than the neighbouring Cormack Basin.

# Bibliography

A. D. Chave. *Chapter 6: Distortion of magnetotelluric data: its identification and removal*. Cambridge University Press, 1st edition, 2012.

M. Cooper, J. Weissenberer, I. Knight, D. Hostad, D. Gillespie, H. Williams, E. Burden, J. Porter-Chaudhry, D. Rae, and E. Clark. Basin evolution in western Newfoundland: New insight from hydrocarbon exploration. *Technical report, PanCanadian Petroleum, Newfoundland Geological Survey, Hunt Oil, Memorial University and Mobil Oil.*, 2001.

Gov.of.NL. Sedimentary basin and hydrocarbon potential of Newfoundland and Labrador. Technical report, Government of Newfoundland and Labrador Dept. of Mines and Energy, 2000.

A.P. Hamblin, M.G. Flower, J. Utting, G.S. Lanngdon, and D Hawkins. Stratigraphy, palynology and source rock potential of lacustrine deposits of the lower Carboniferous (Visean) Rocky Brook Formation, Deer Lake subbasin, Newfoundland. *Bulletin of Canadian Petroleum Geology*, 45(1):25–53, 1997.

J. Hibbard and J.W. Waldron. Truncation and translation of Appalachian promontories: Mid - palaeozoic strike-slip tectonics and basin initiation. *Geological Society of America*, 37(6):487–490, June 2009.

- R.S. Hyde. Geology of Carboniferous strata in portions of the Deer Lake Basin, western Newfoundland. *Mineral Development Division, Department of Mines and Energy, Government of Nfld and Labrador*, 1979.
- E. Irving and D.F. Strong. Palaeomagnetism of the Early Carboniferous Deer Lake Group, western Newfoundland: No evidence for mid-Carboniferous displacement of “Acadia”. *Earth and Planetary Science Letters*, 69:379–390, 1984.
- A. Jones, A. Chaves, G. Egbert, D. Auld, and K.Barh. A comparison of technique for magnetotelluric response function estimation. *Journal of Geophysical Research*, 94:14210–14213, 1989.
- P. Kearey and M. Brooks. *An Introduction to Geophysical Exploration*. Blackwell Science, 2nd edition, 1991.
- G.S. Langdon. A study of the petroleum potential and regional petroleum prospectivity of the Deer Lake Group and Howley Formation on permits 93-103 and 93-104, Deer Lake Basin. Master’s thesis, Memorial University of Newfoundland, 1993.
- J. Ledo. 2-D versus 3-D magnetotelluric data interpretation. *Surveys in Geophysics*, 27:111–148, 2004.
- C. Martin. Canada’s unexplored lands: Deer lake basin case study. *Oil Gas Journal*, 99(52), 2001.
- R. Martin, N. Culshaw, M.C. Rygel, and V. Pascucci. *Sedimentary Basins of the World, Chapter 6: The Maritimes Basin of Atlantic Canada: Basin Creation and Destruction in the Collisional Zone of Pangea*, volume 8. 2008.
- G.W. McNeice and A.G. Jones. Multisite, multifrequency tensor decomposition of magnetotelluric data. *Geophysics*, 66, 2001.

- M.P. Miensopust. *Multidimensional Magnetotellurics: A 2D Study and a 3D Approach to Simultaneously Invert for Resistivity Structure and Distortion Parameters*. PhD thesis, NUI Galway, 2010.
- H.G. Miller and J.A. Wright. Gravity and magnetic interpretation of the Deer Lake Basin, Newfoundland. *Canadian Journal of Earth Science*, 21:10–18, 1984.
- M.N. Nabighian, editor. *Electromagnetic Methods in Applied Geophysics*, volume 1 of *Investigations in Geophysics no.3*. Society of Exploration Geophysicists, 1987.
- X. Qibin, C. Xinping, L. Guanghe, X. Xingwang, and Z. Baolin. Application of 2d magnetotelluric methods in a geological complex area, Xinjiang, China. *Journal of Applied Geophysics*, 75:19–30, 2011.
- W. Rodi and R.L. Mackie. Nonlinear conjugate gradients algorithm for 2-d magnetotelluric inversion. *Geophysics*, 66(1):174–187, February 2001.
- B. D. Rodriguez and J. A. Sampson. Magnetotelluric survey to characterize the Sunnyside porphyry copper system in the Patagonia mountains, Arizona. *USGS*, 2010.
- F. Simpson and K. Bahr. *Practical Magnetotellurics*. Press Syndicate of the University of Cambridge, 1st edition, 2005.
- J. Spratt and J. Craven. Near-surface and crustal-scale images of the Nechako Basin, British Columbia, Canada, from magnetotelluric investigation. *Canadian Journal of Earth Sciences*, 48:987–999, 2011.
- A. J. Van der Velden, C.R. Van Staal, and F. A. Cook. Crustal structure, fossil subductoin, and the tectonic evolution of the Newfoundland Appalachians: Evidence

from a reprocessed seismic reflection survey. *GSA Bulletin*, 116(11/12):1485–1498, Nov/Dec 2004.

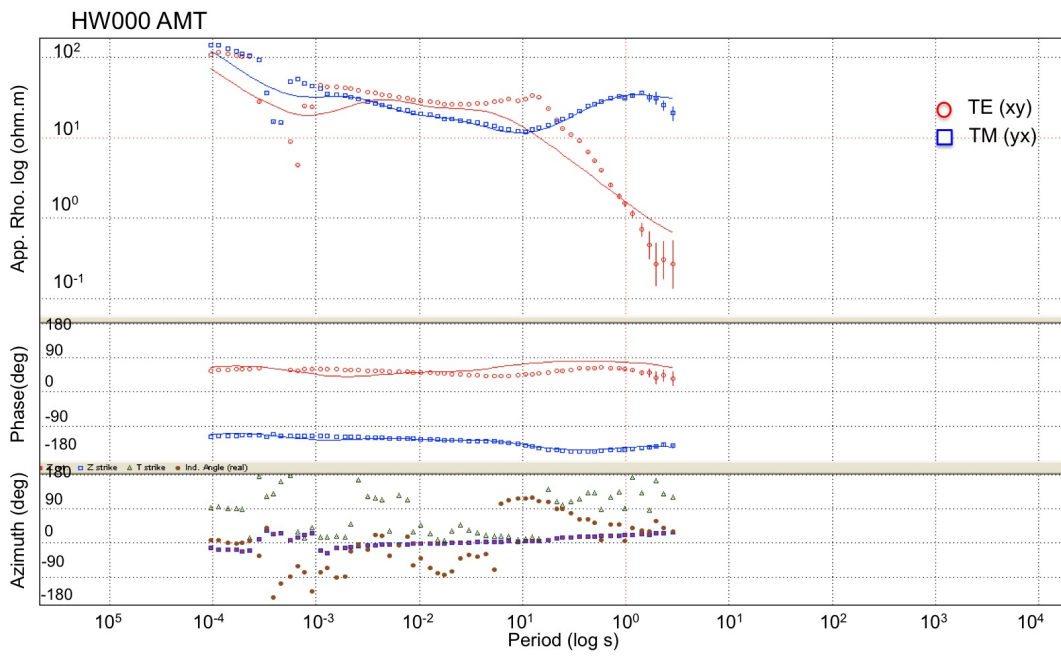
Ari Viljanen. *Chapter 3B: Description of the magnetospheric/ionospheric sources (The Magnetotelluric Method Theory and practice)*. Cambridge University Press, 1st edition, 2012.

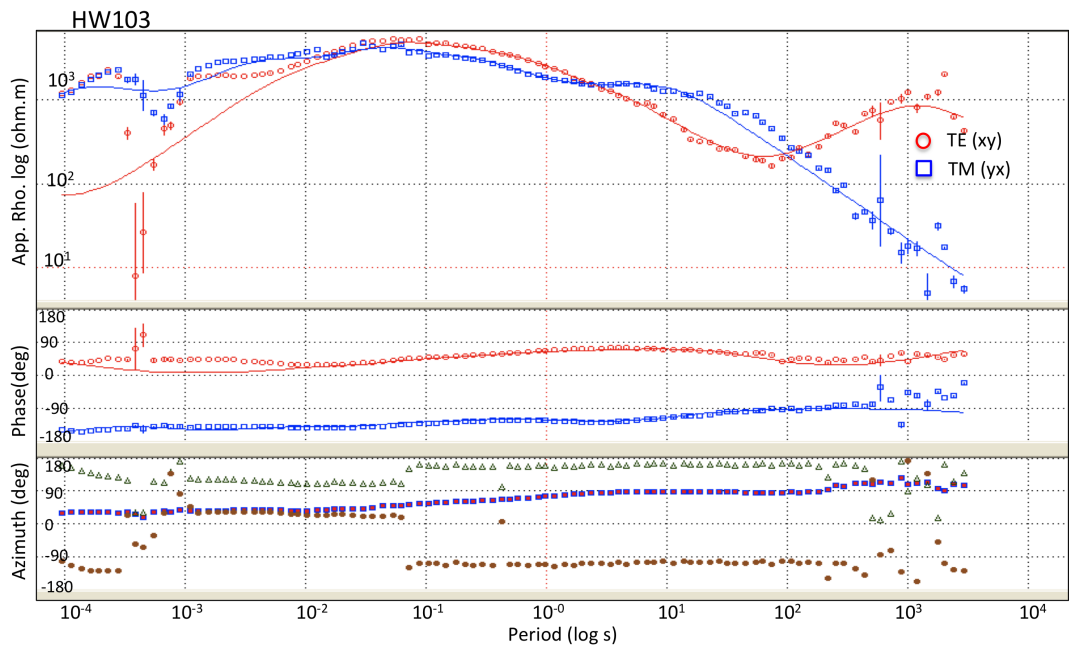
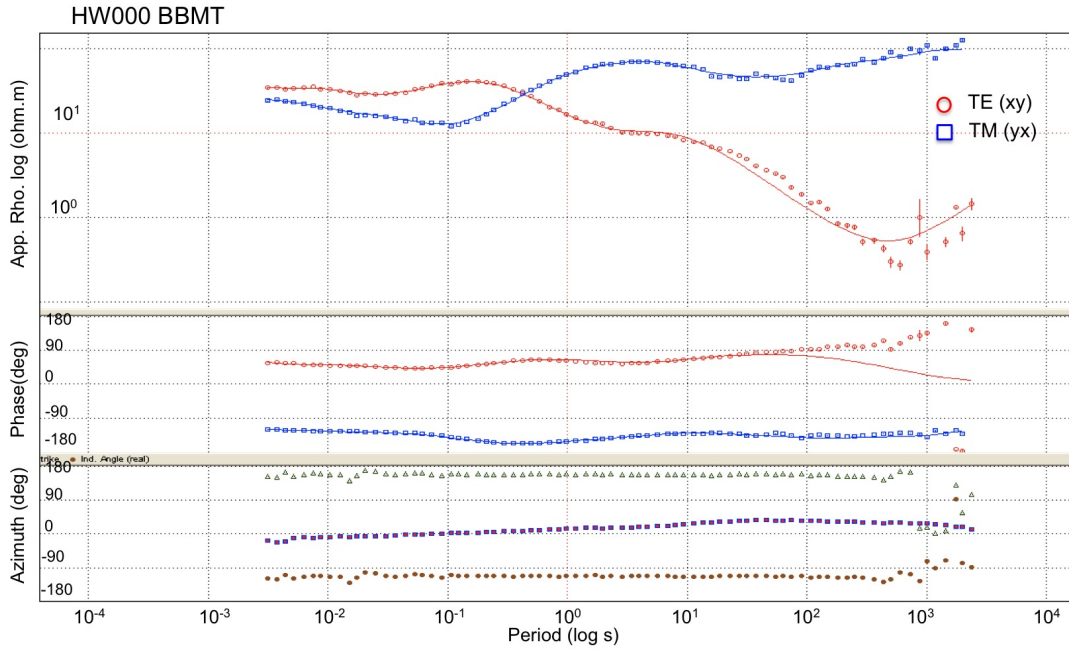
Peter Weidelt and A. D. Chave. *Chapter 2: The theoretical basis for electromagnetic induction (The Magnetotelluric Method Theory and practice)*. Cambridge University Press, 1st edition, 2012.

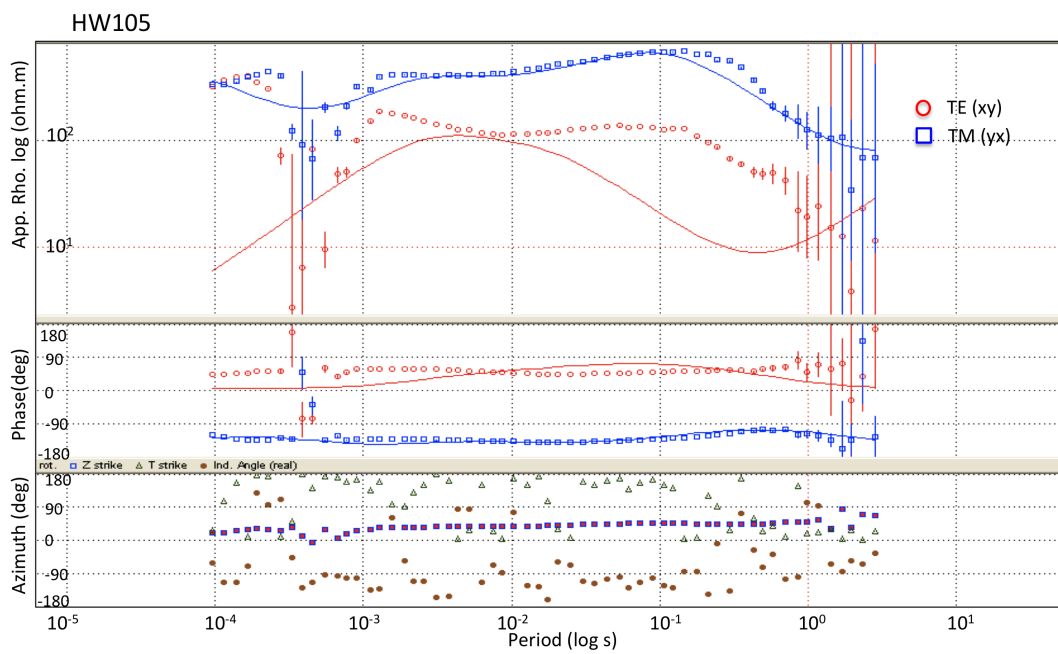
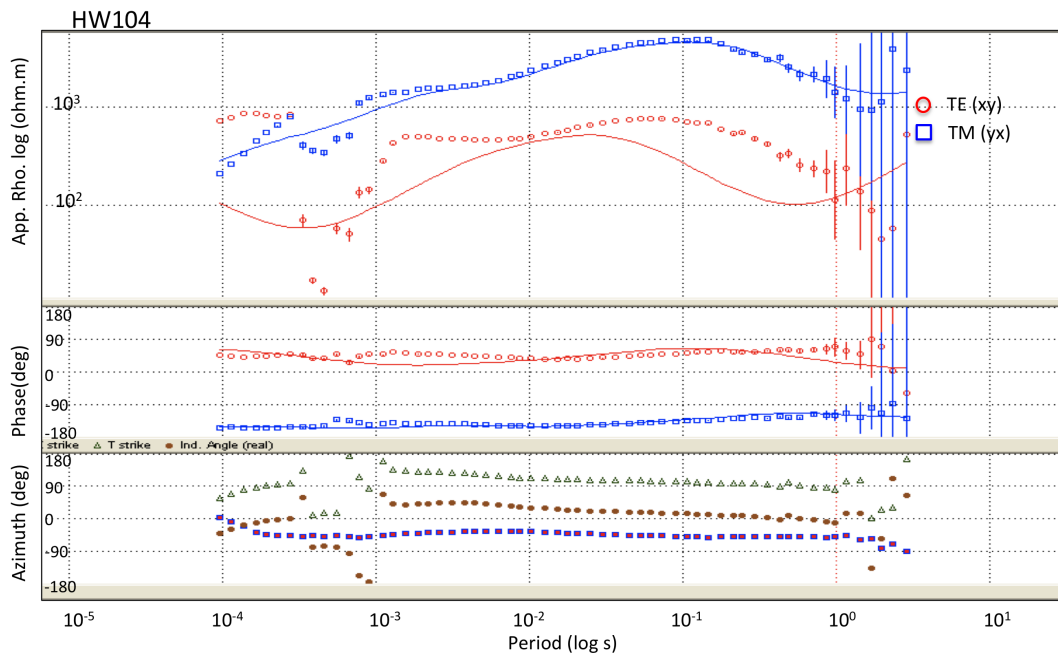
W. Xiao and M. Unsworth. Structural imaging in the Rocky Mountain foothills (Alberta) using magnetotelluric exploration. *AAPG Bulletin*, 90(3):321–333, 2006.

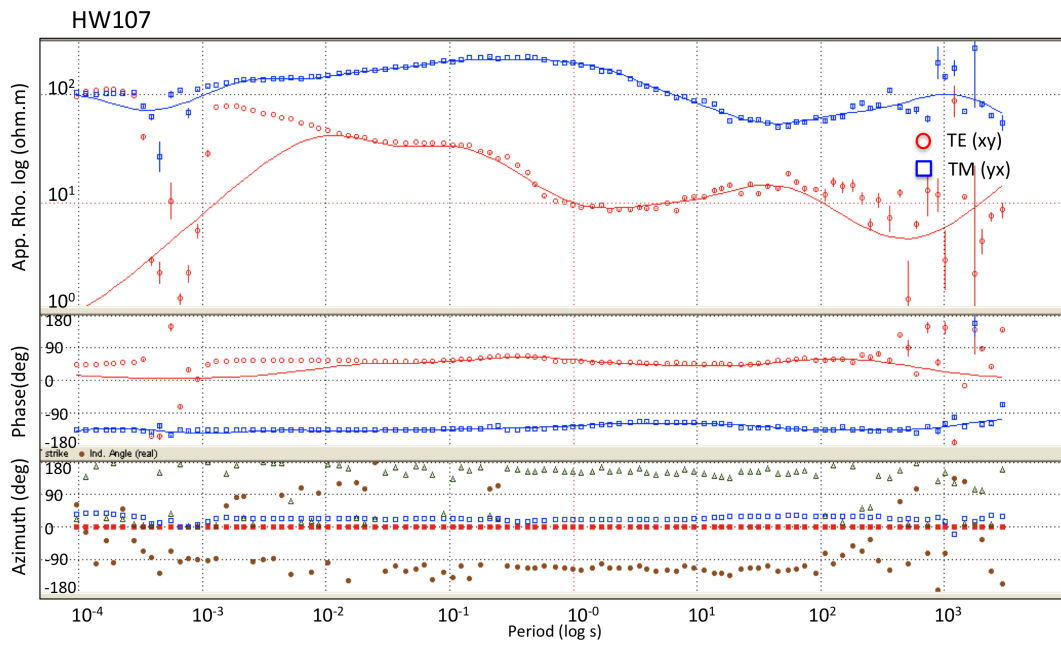
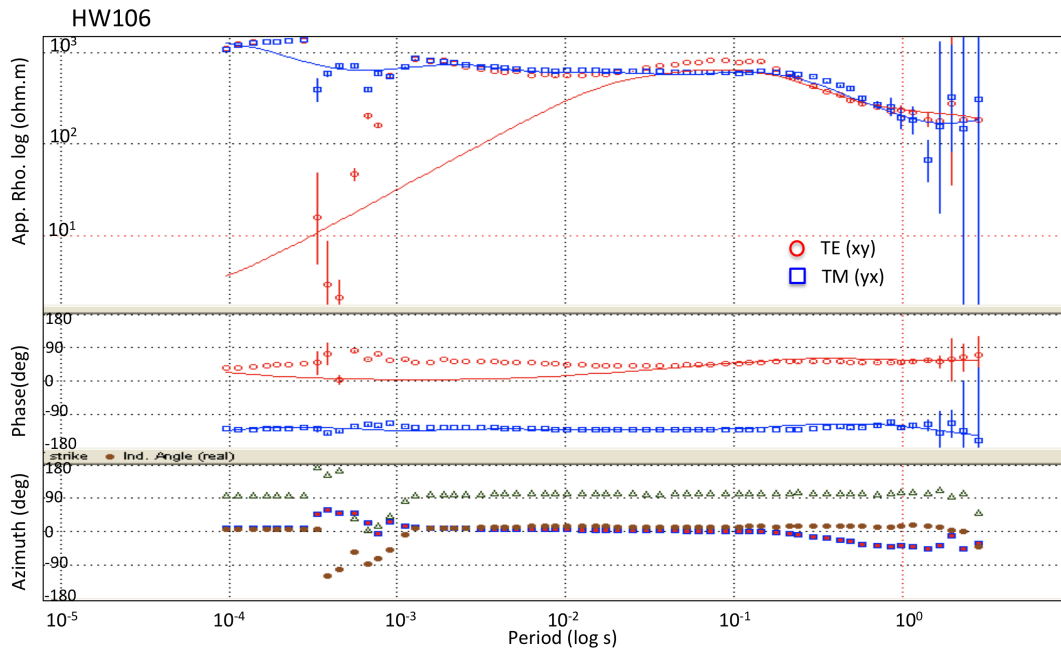
# Appendix A

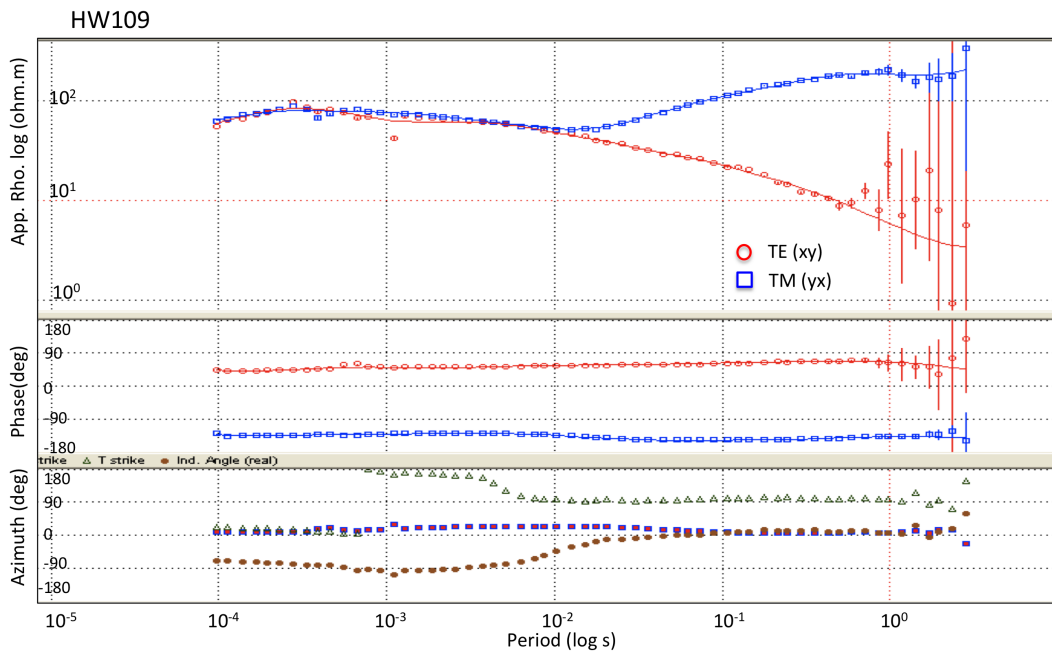
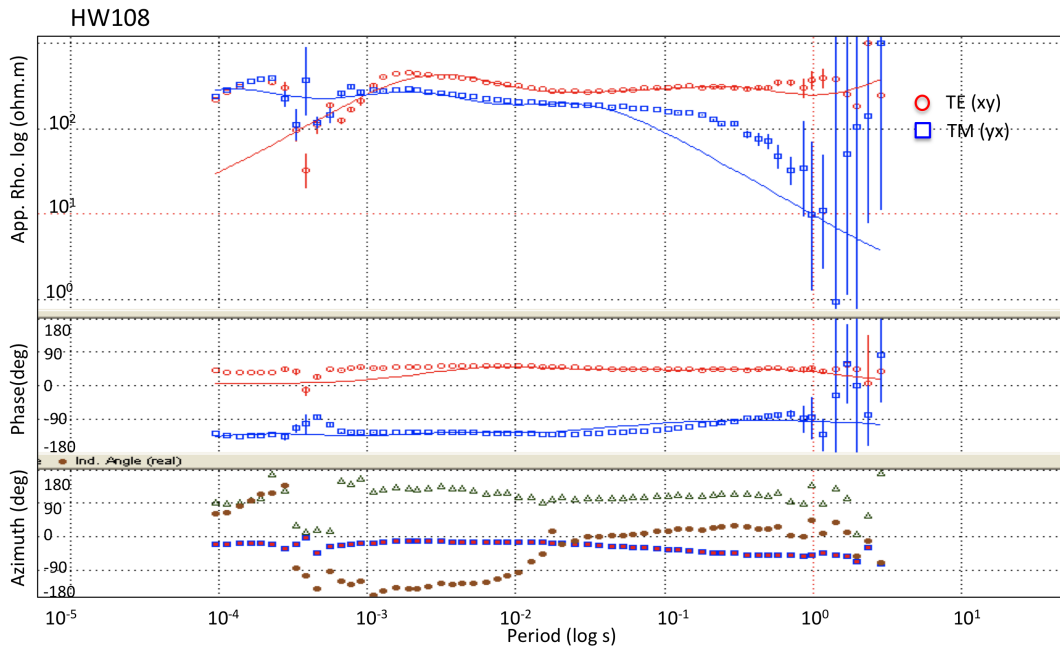
## Unedited .edi files

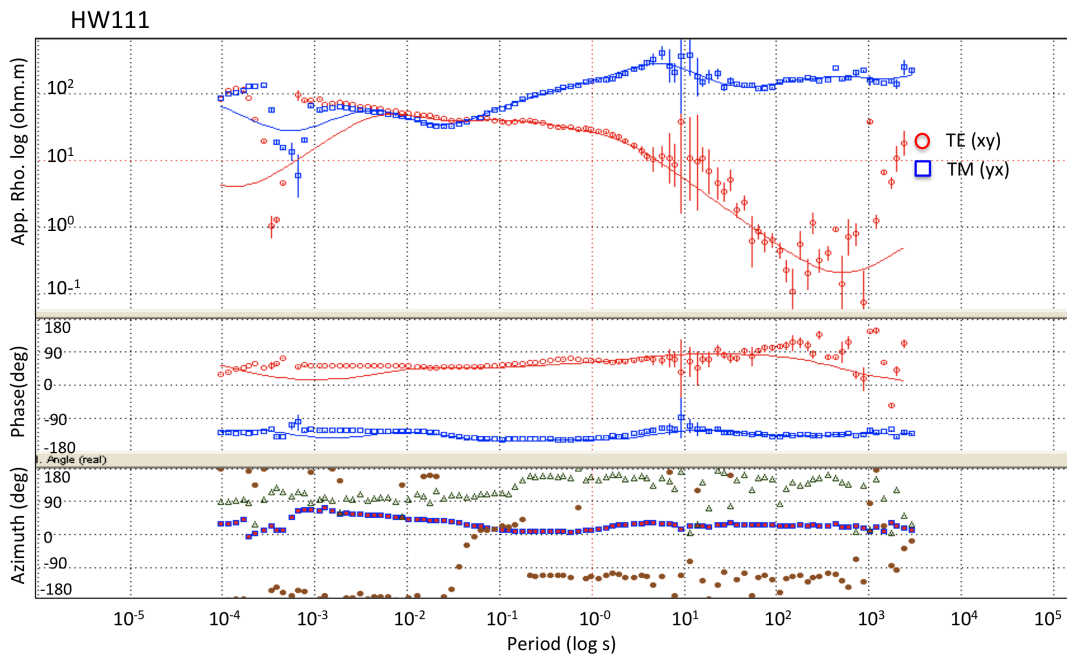
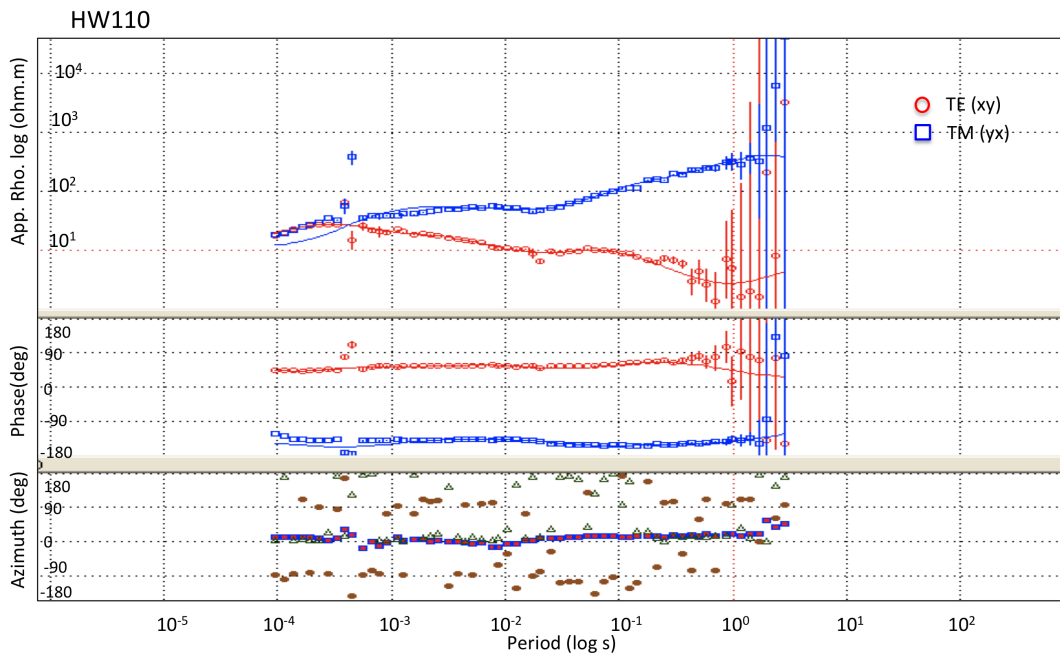


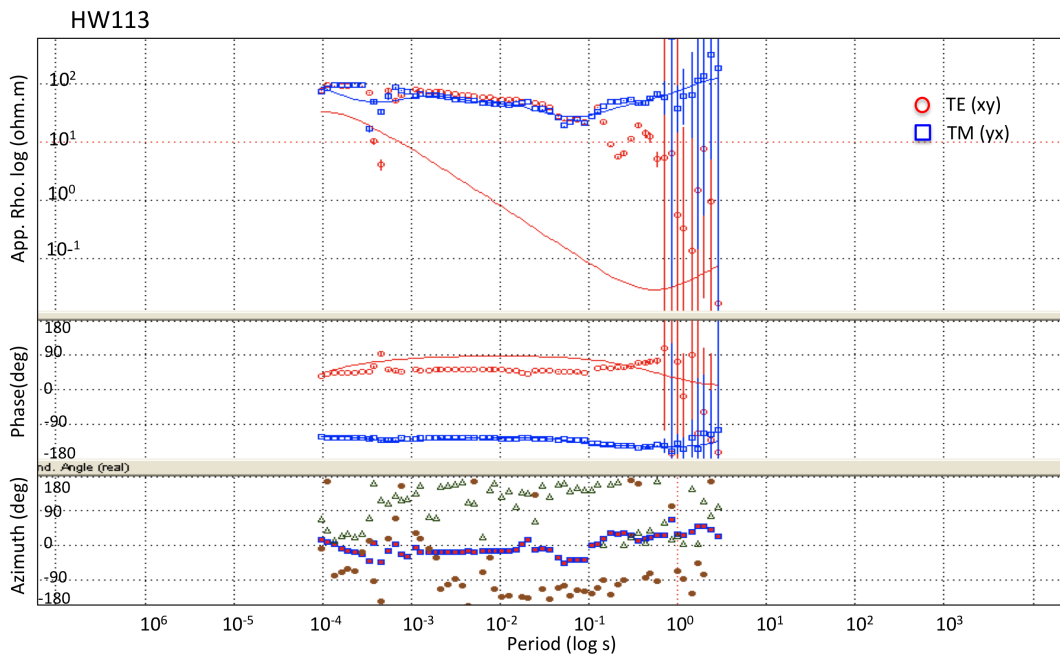
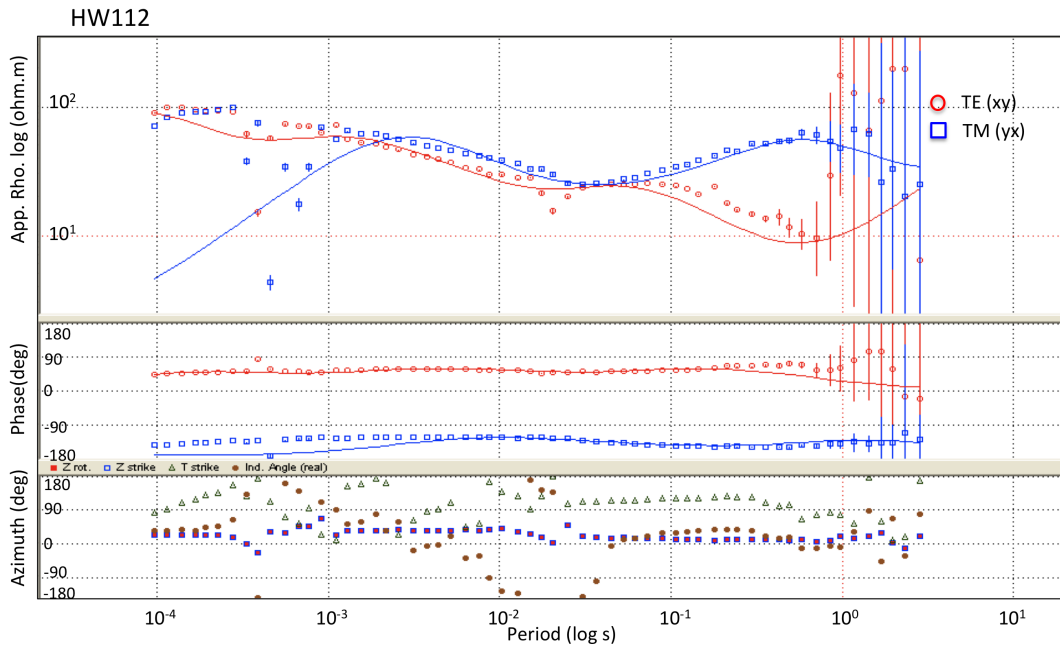


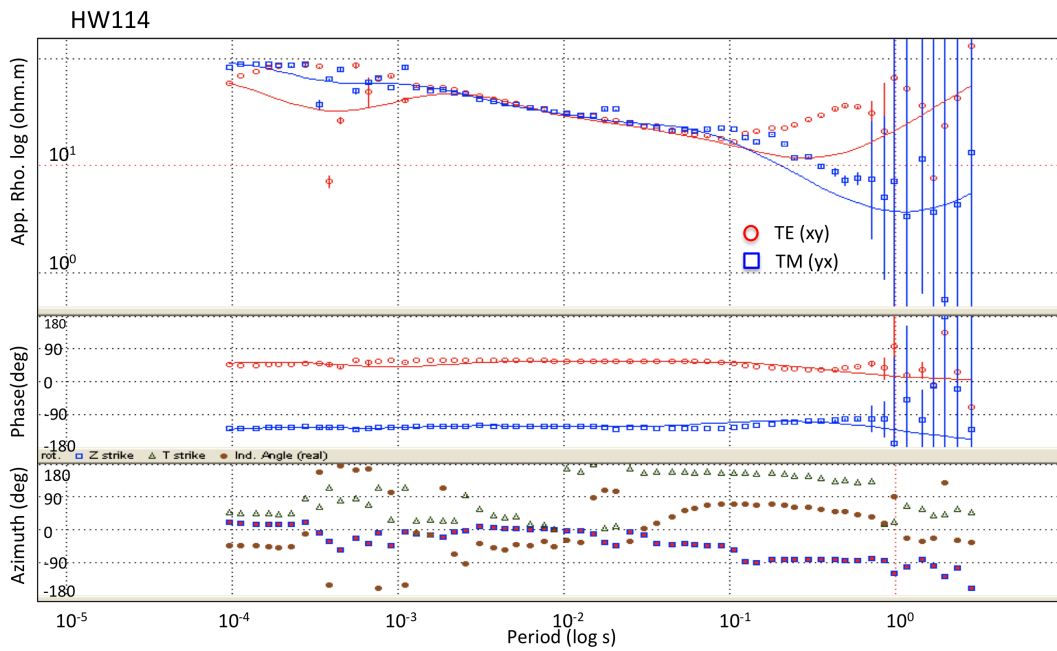
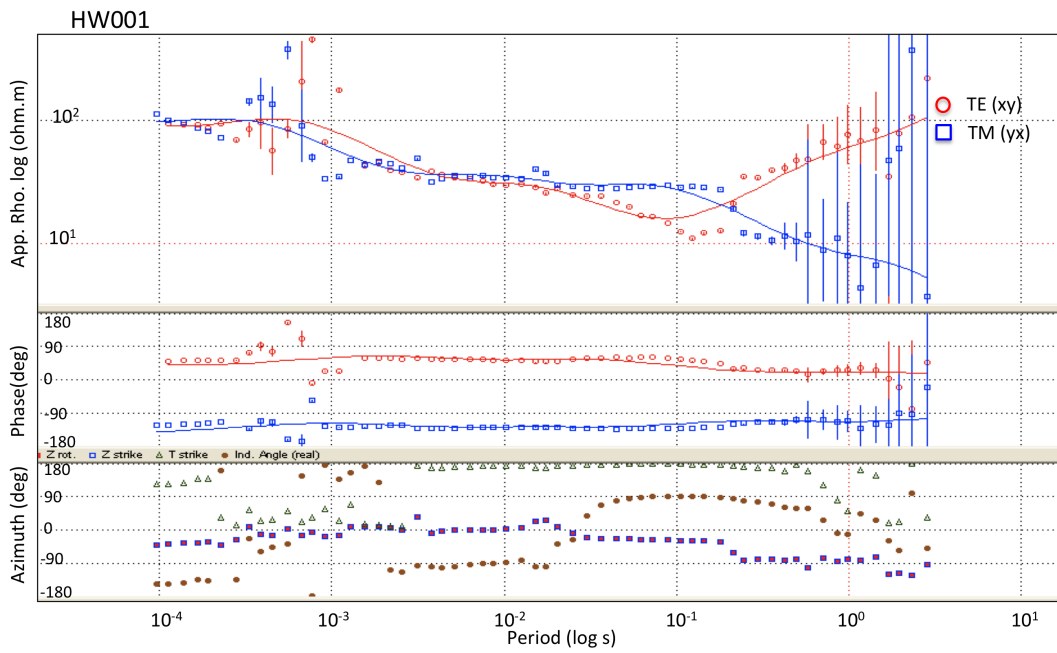


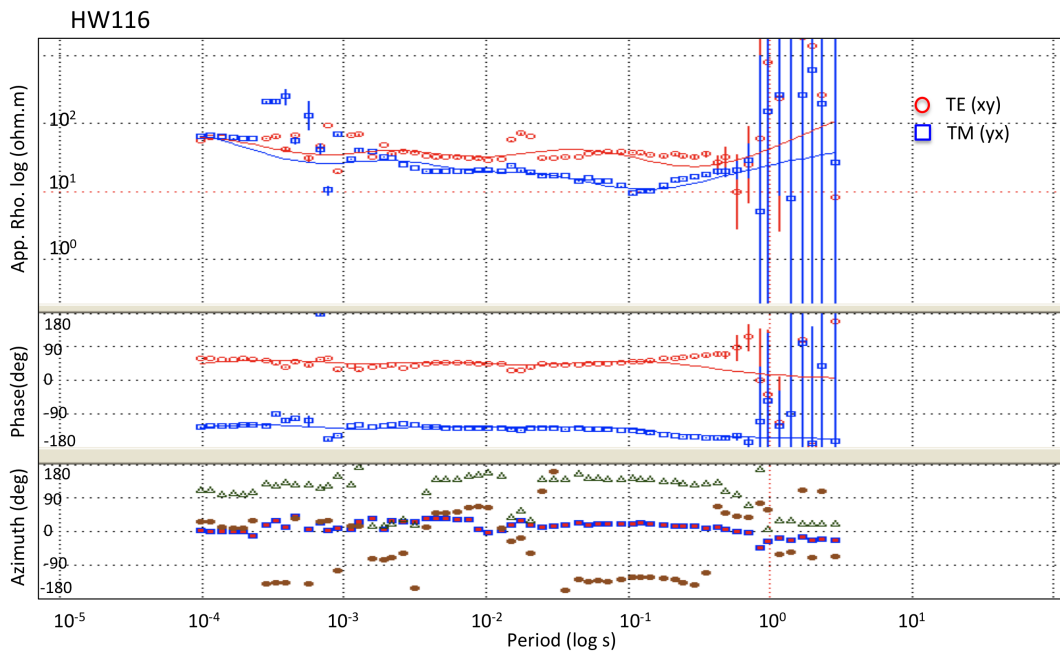
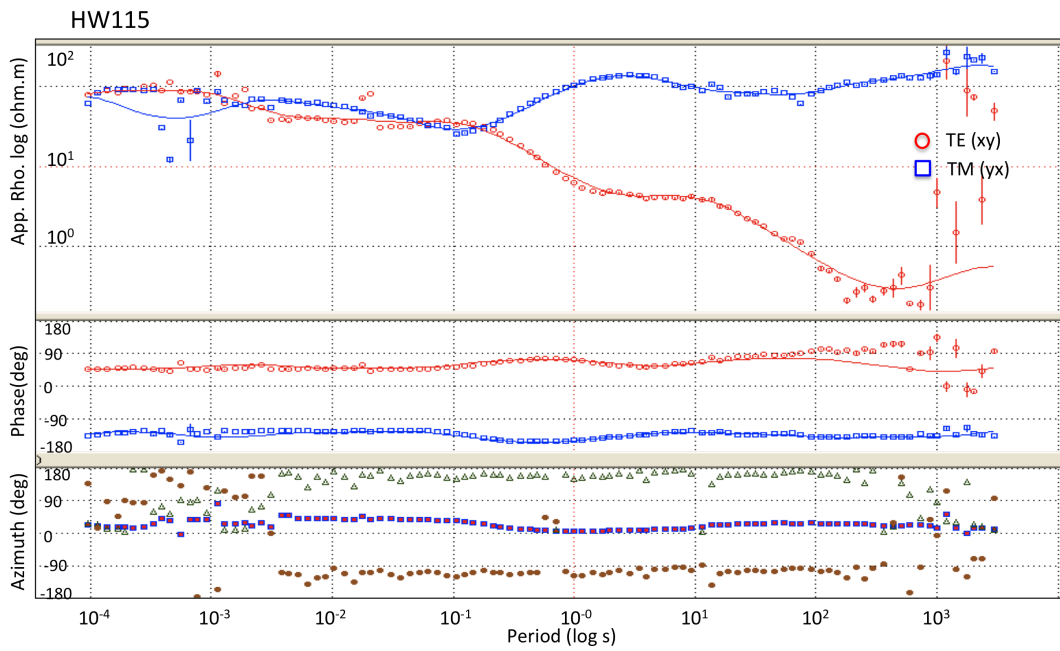


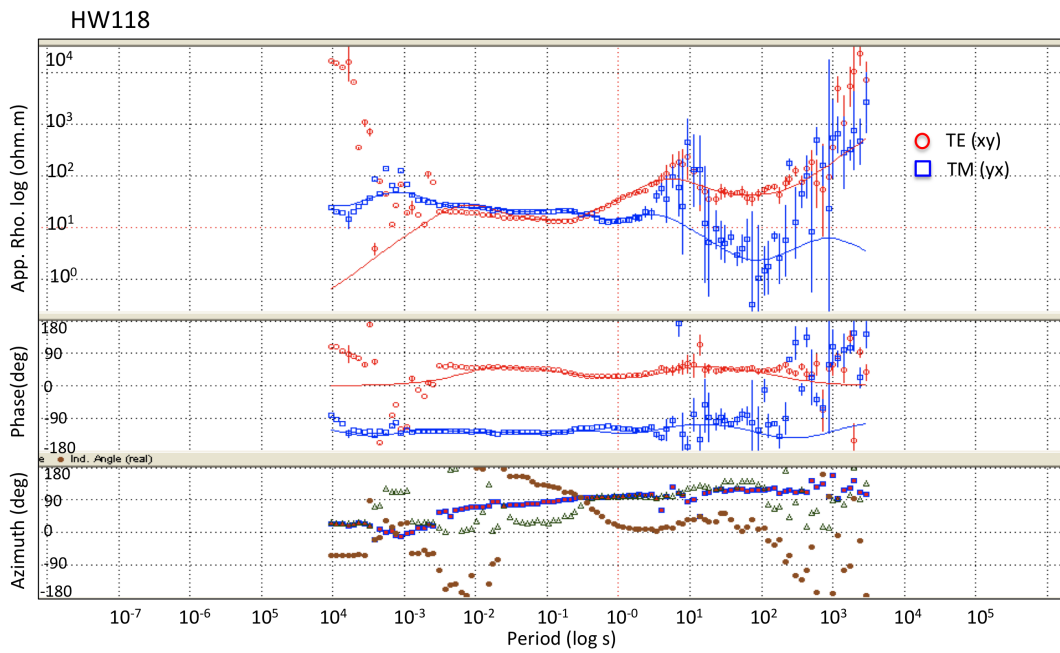
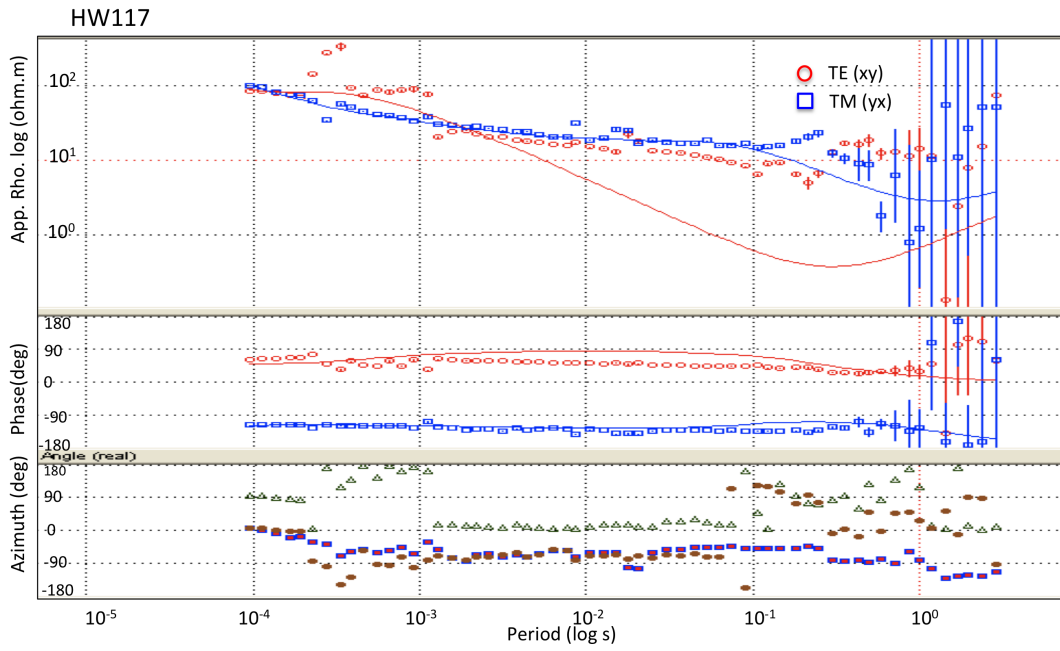


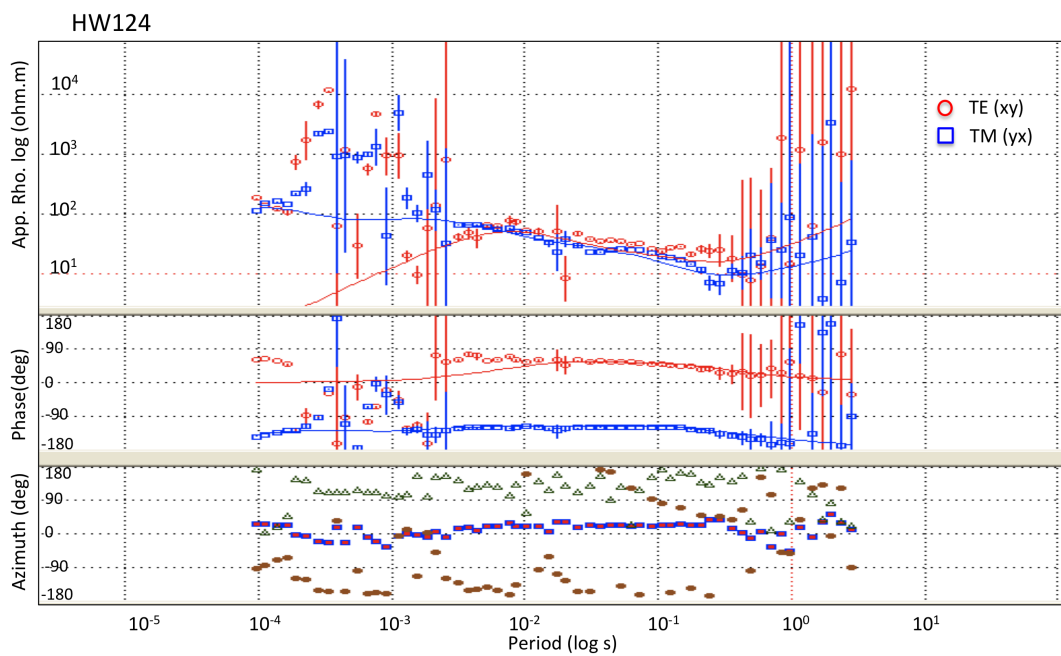
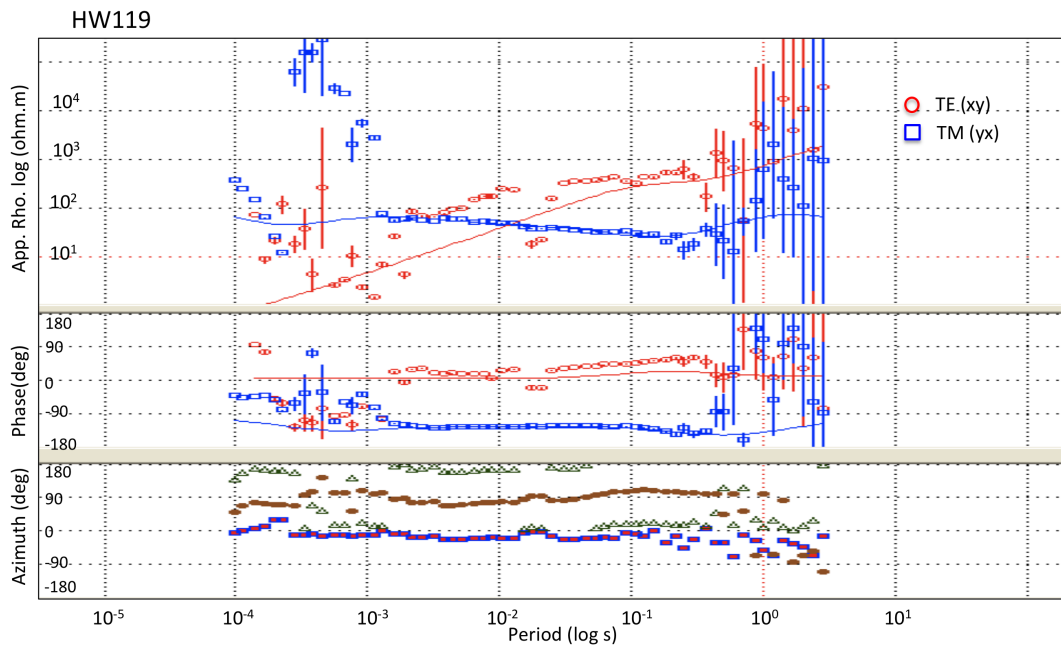


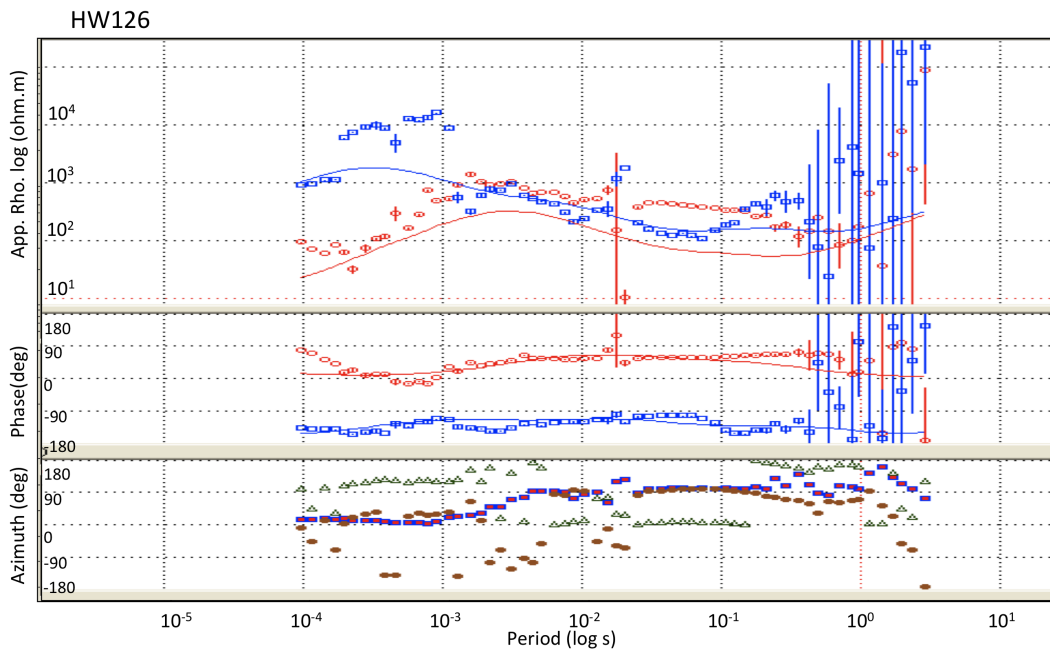
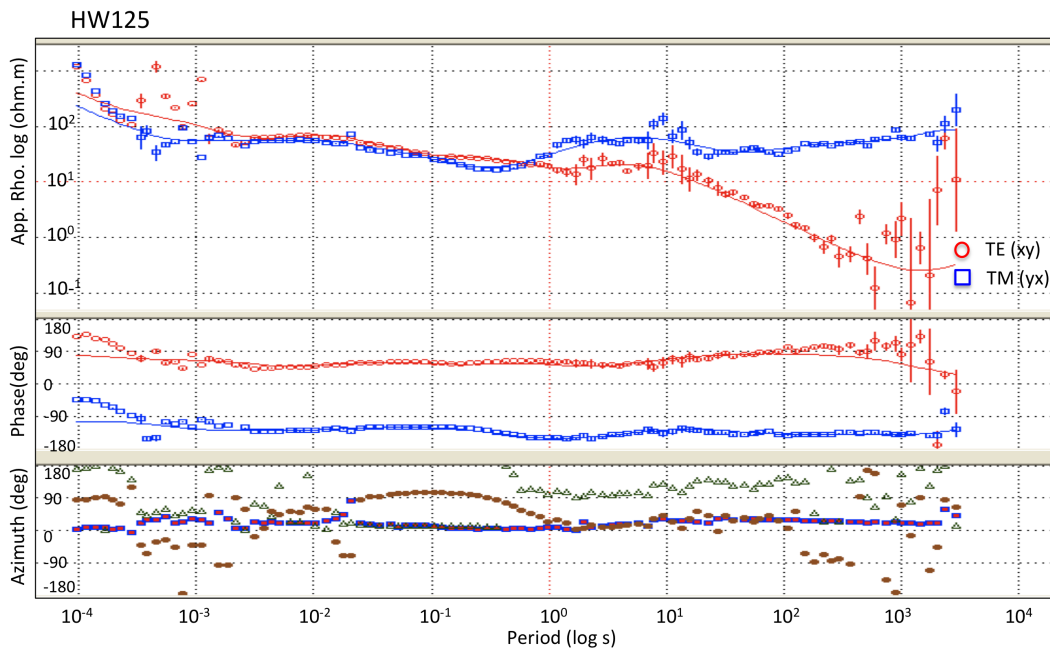


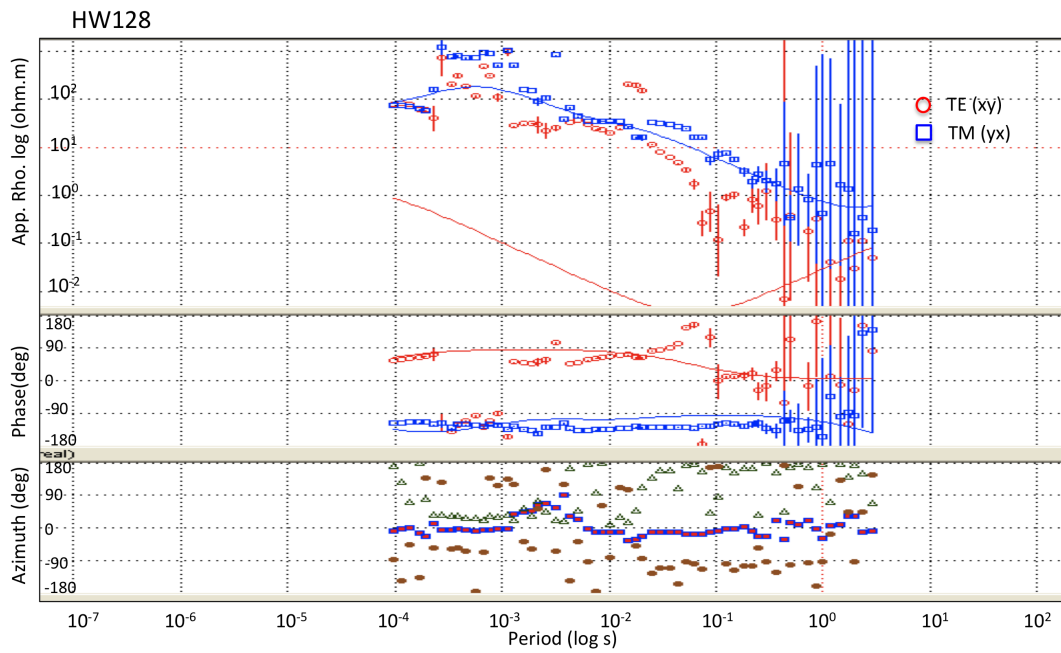
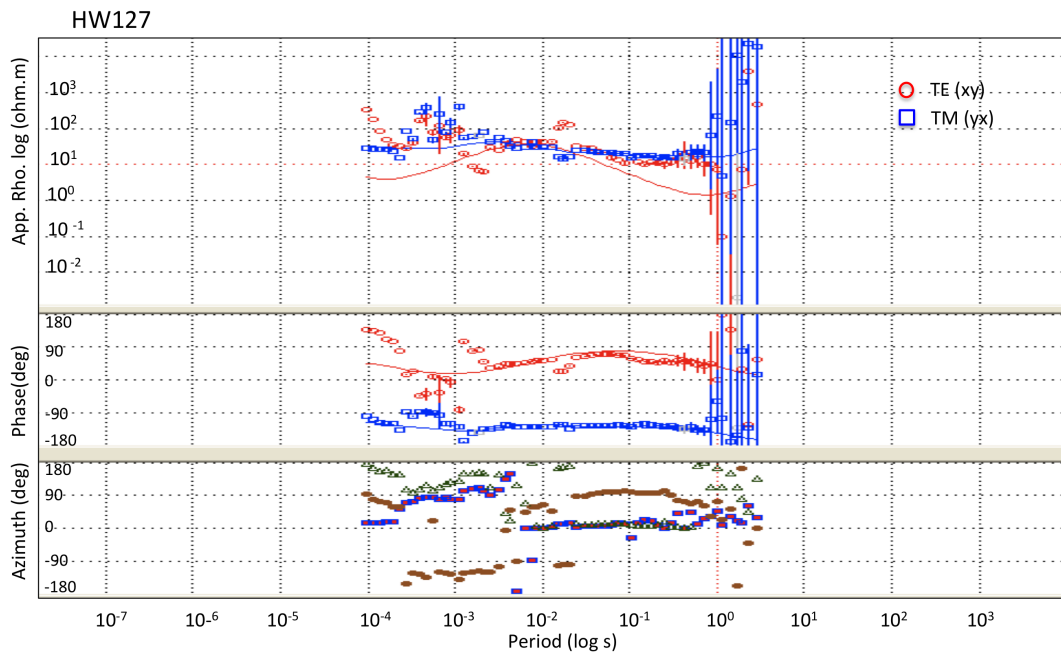


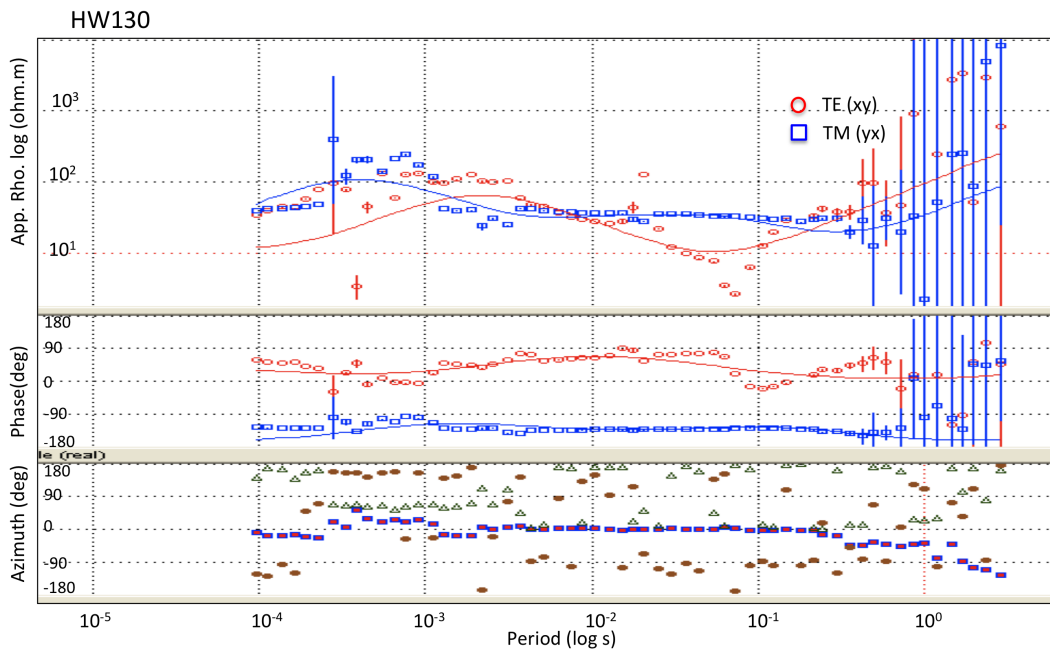
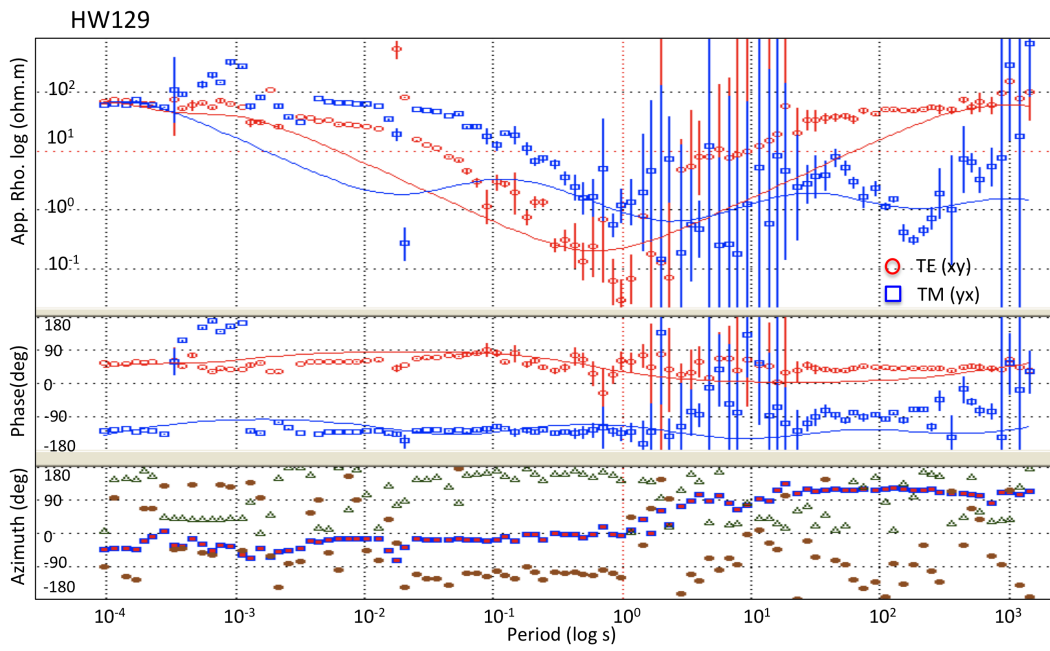


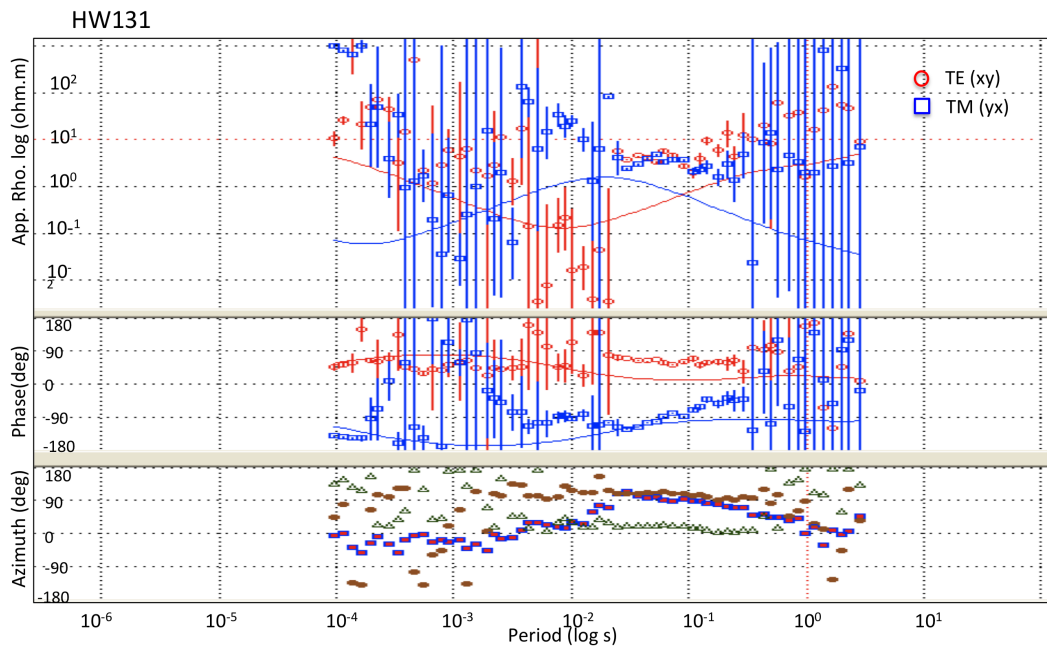
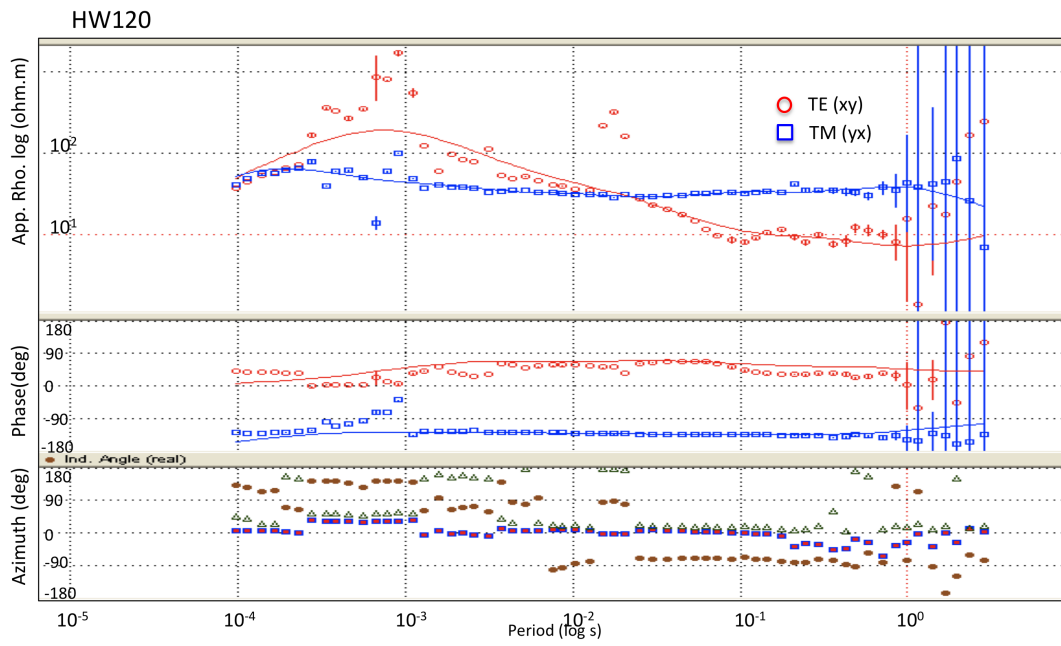


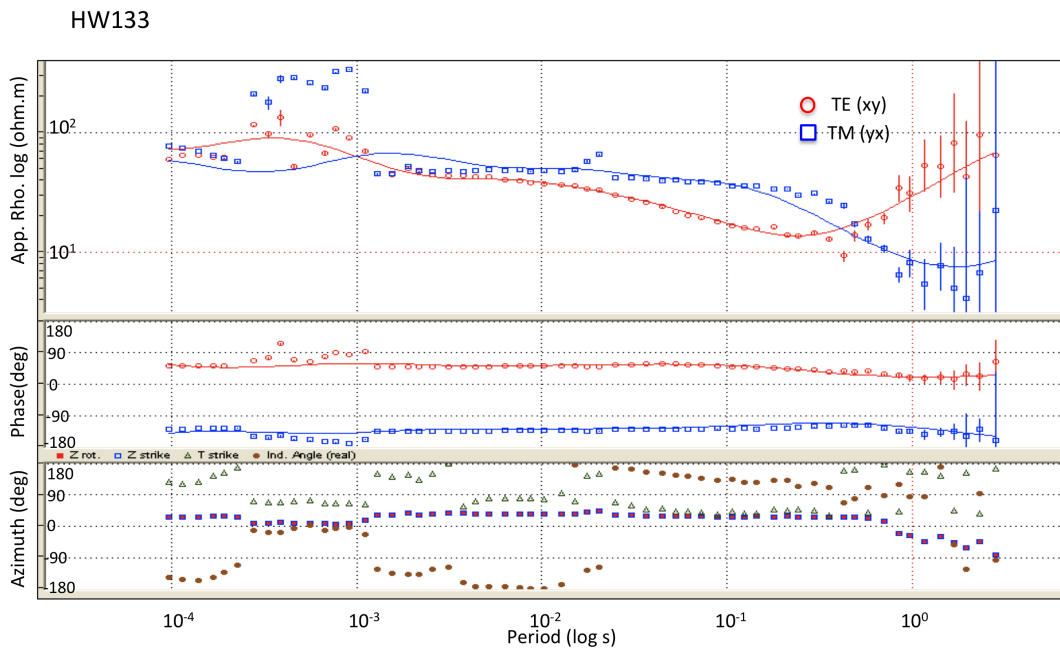
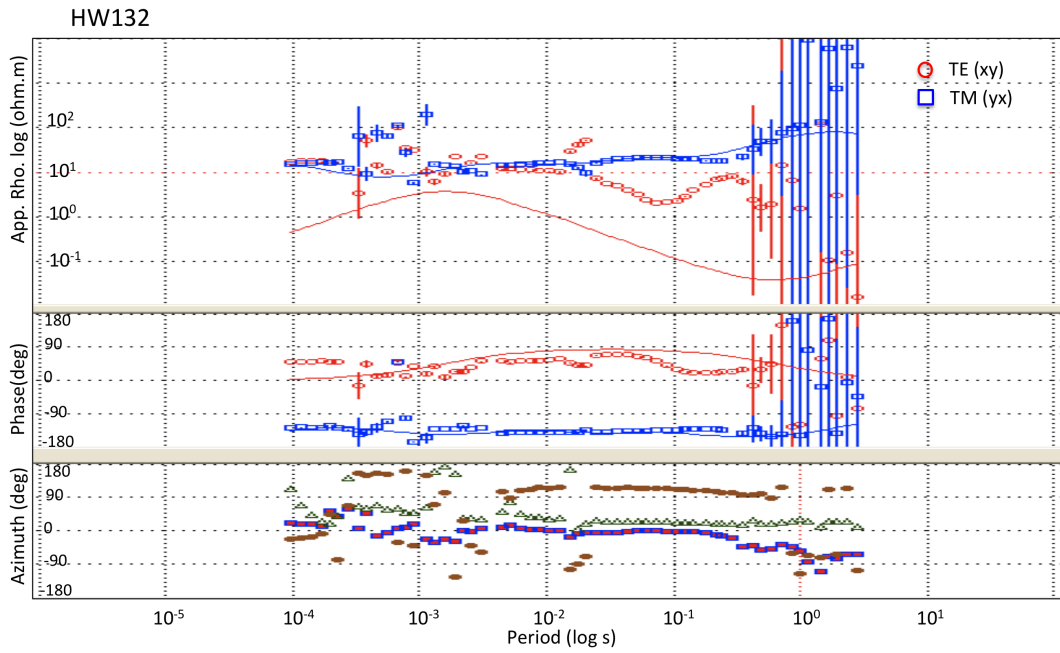


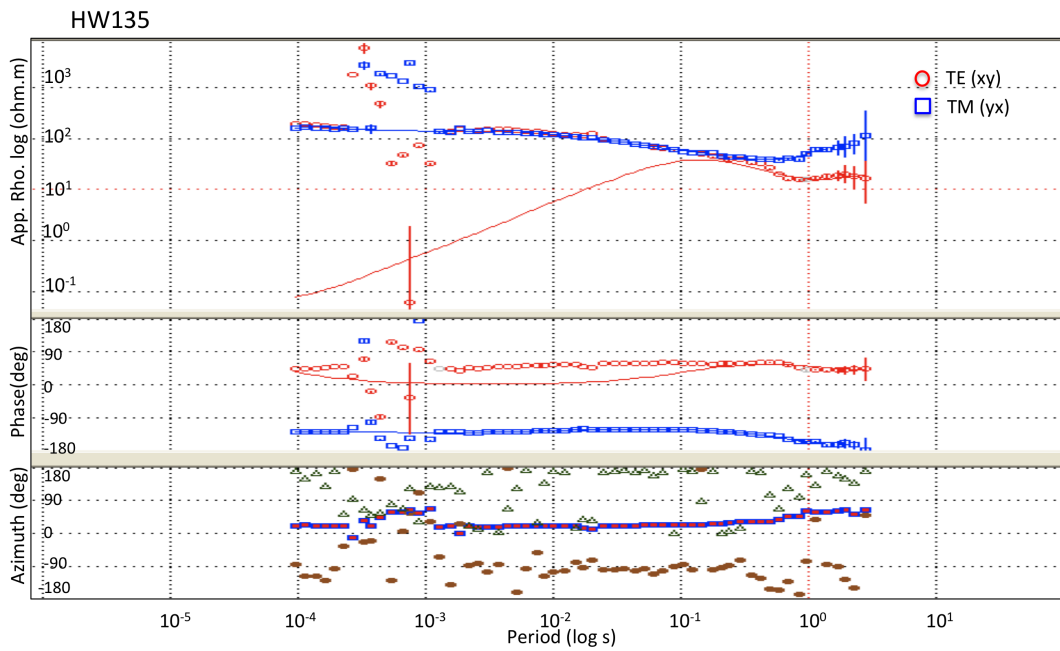
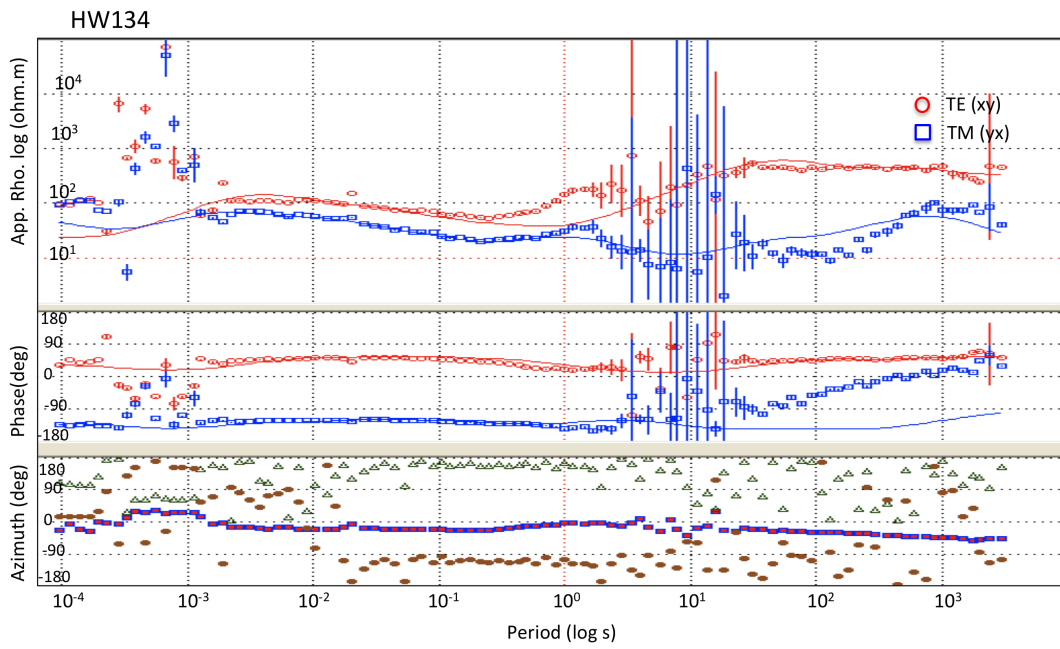


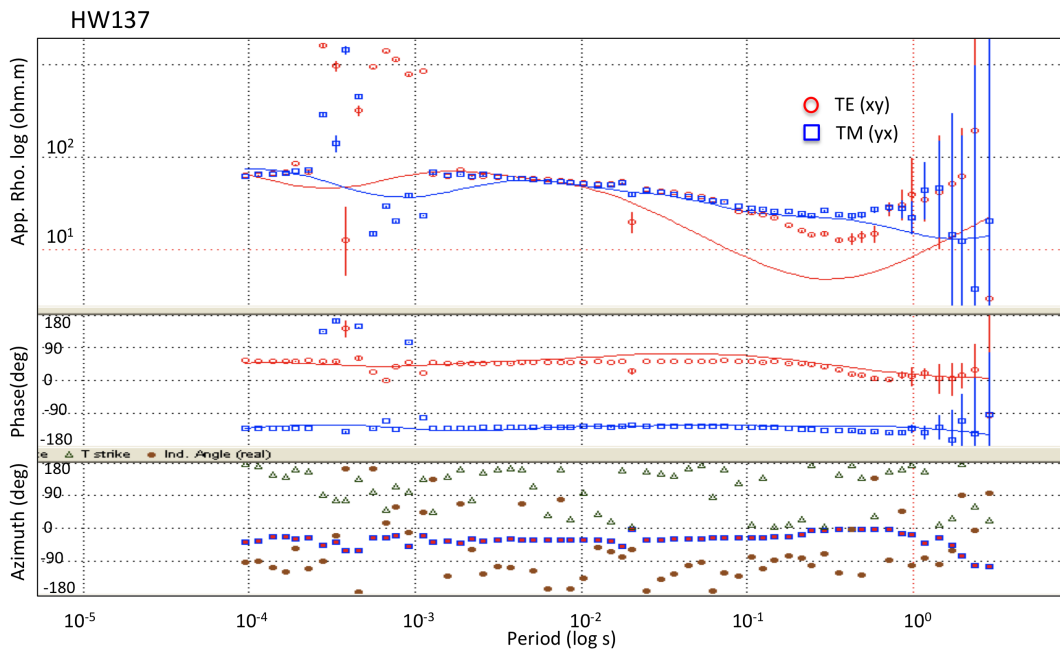
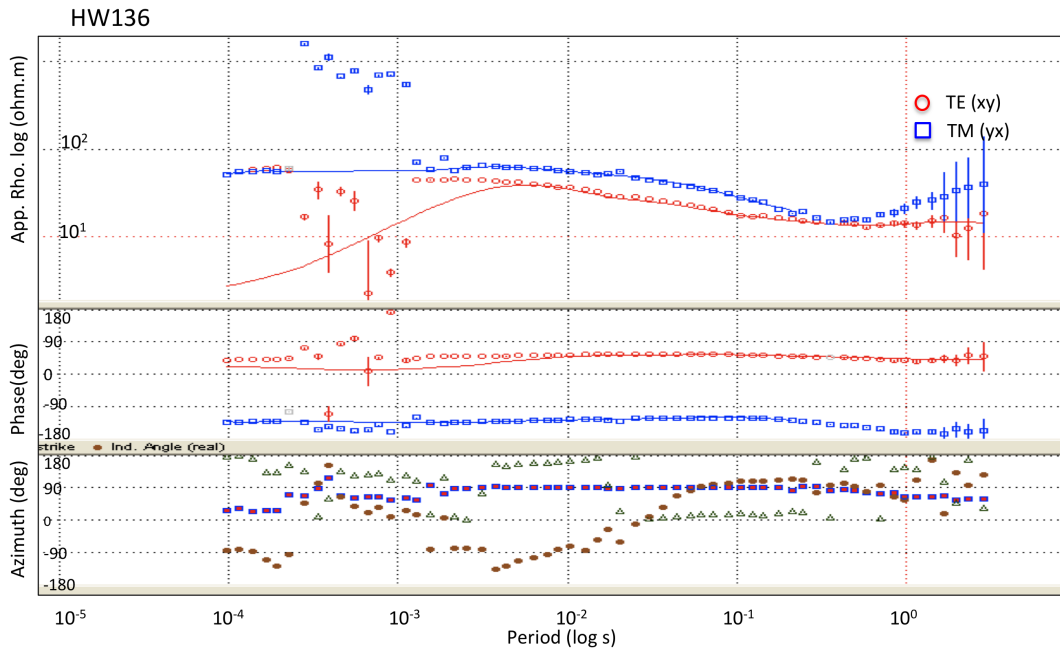


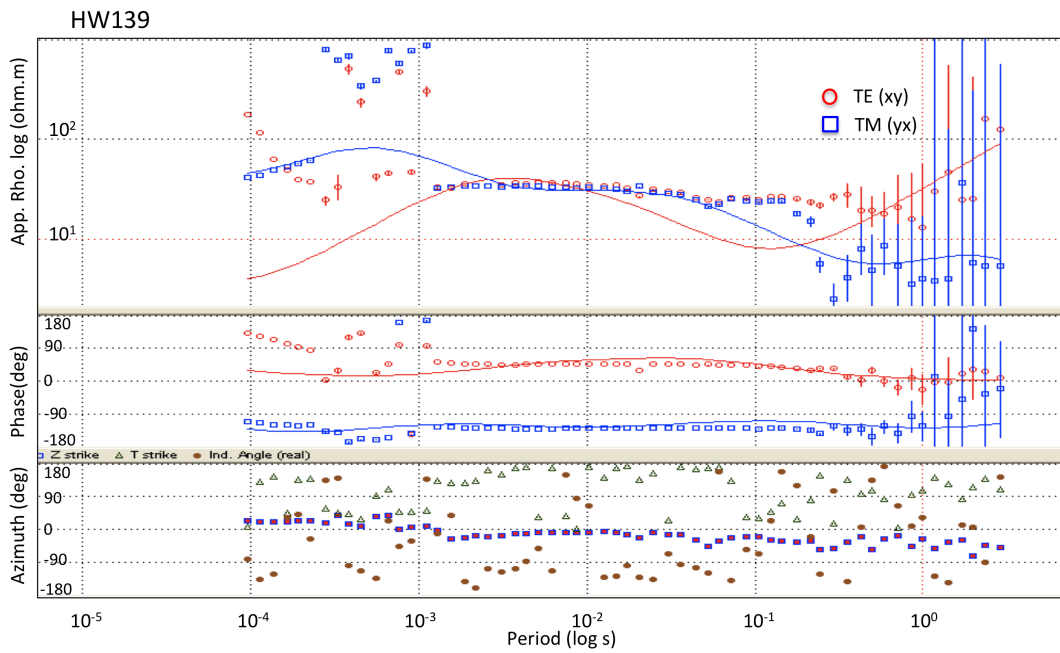
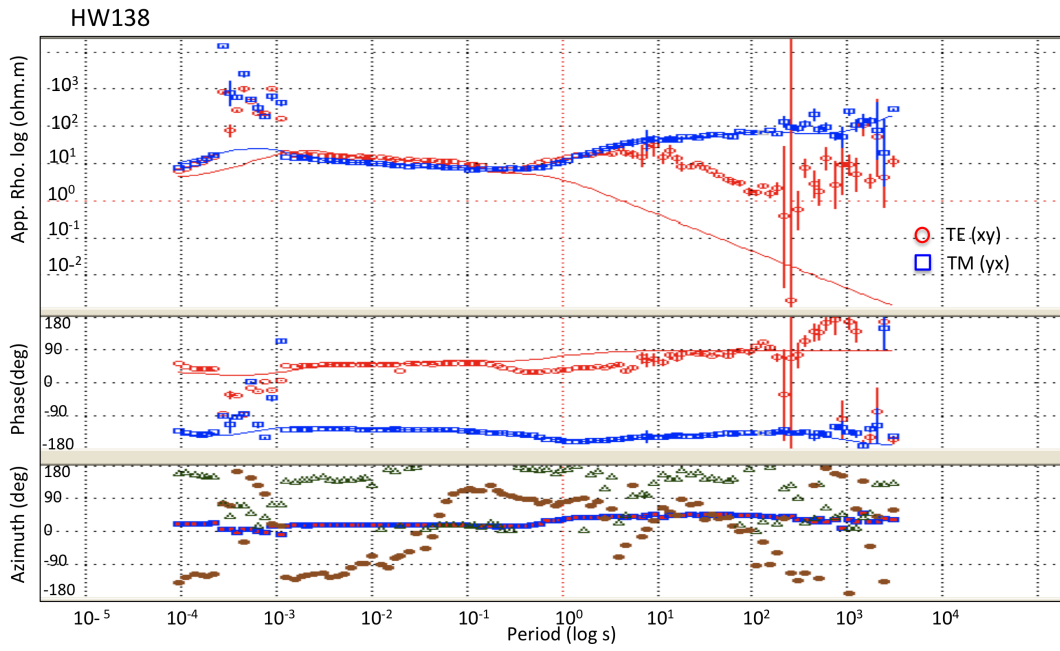




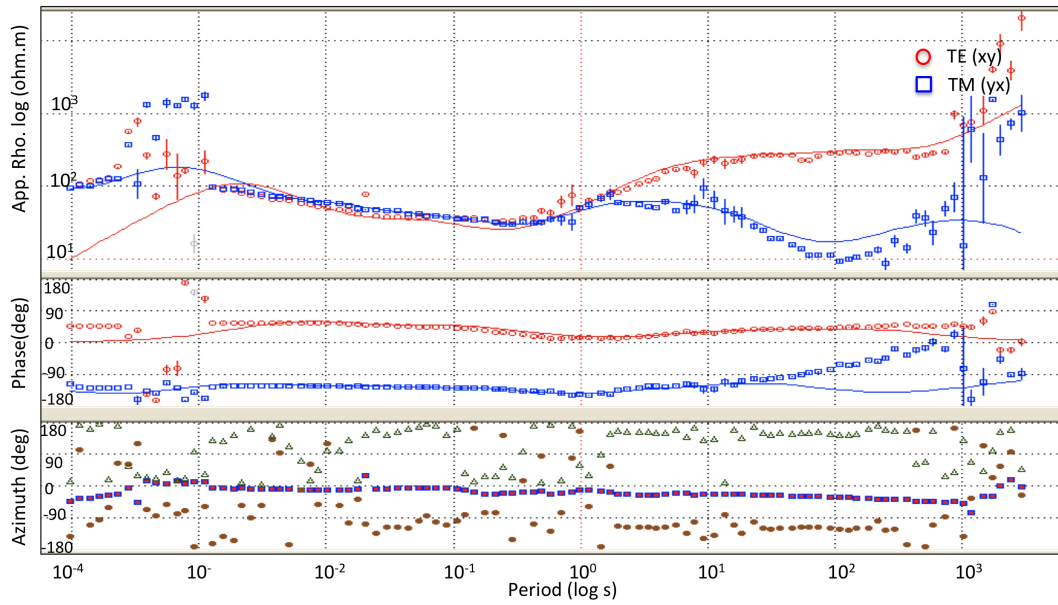




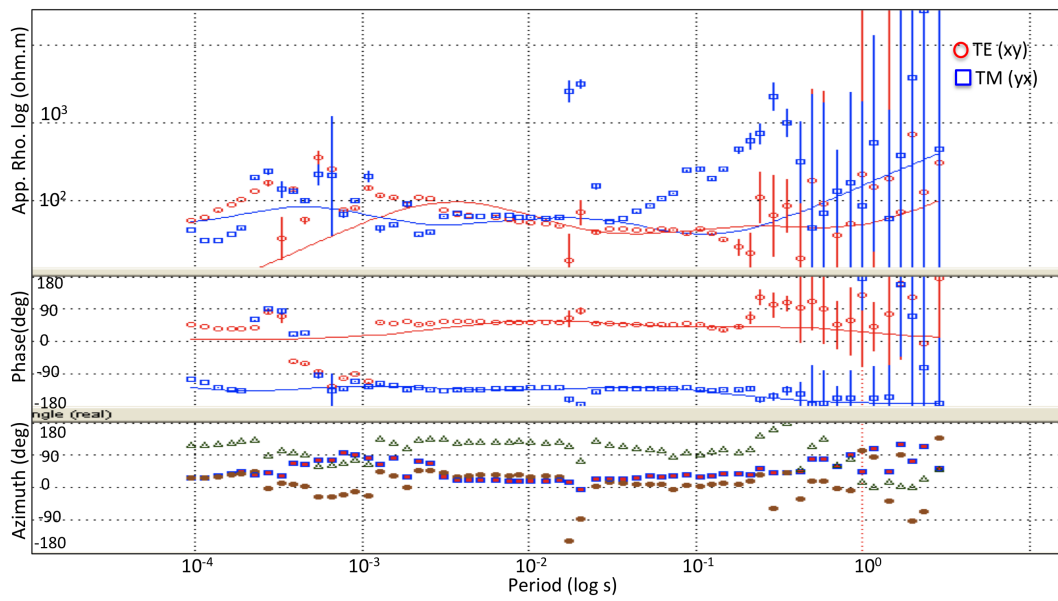




HW140

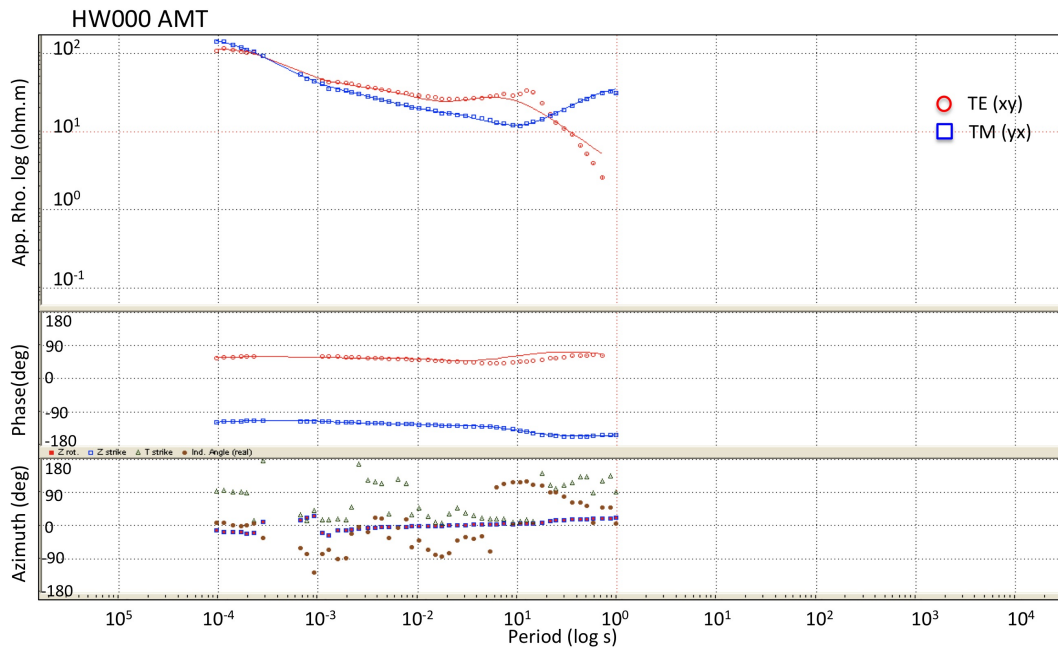


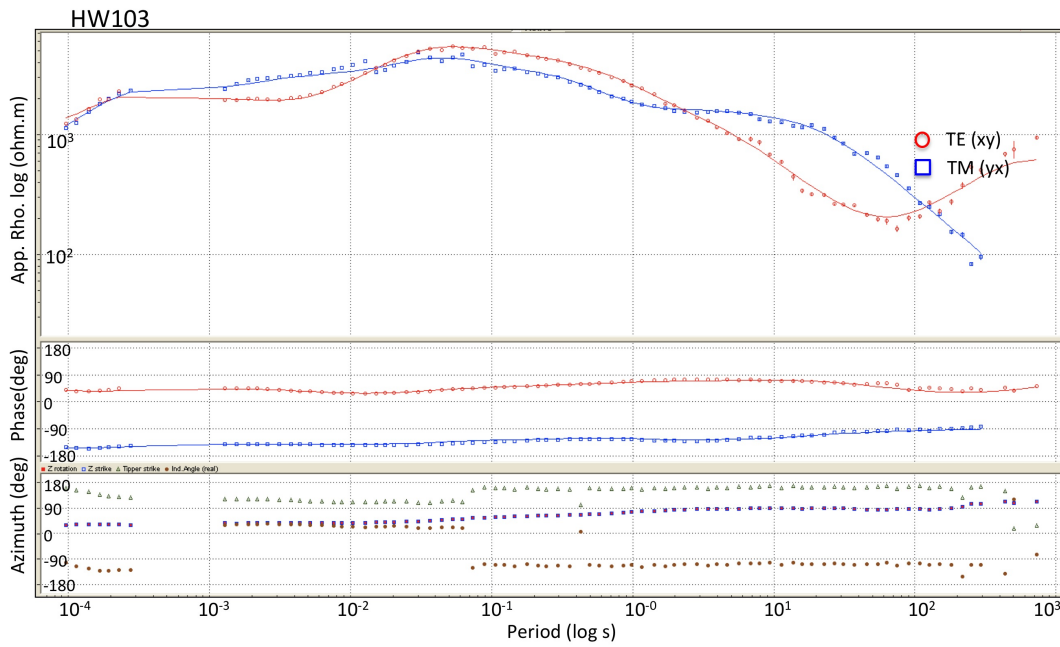
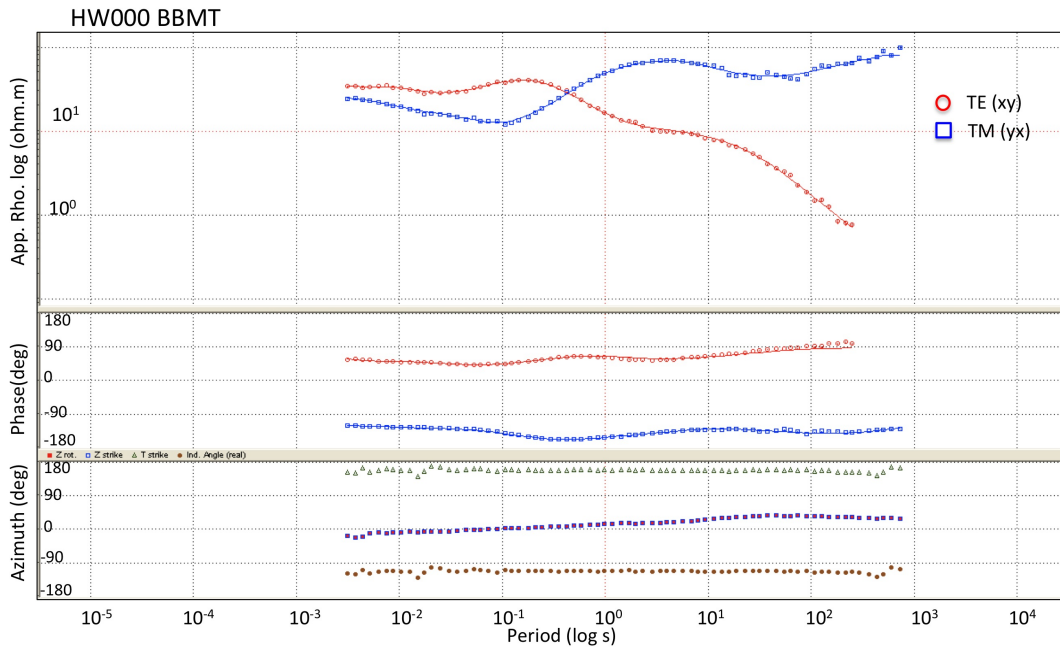
HW141

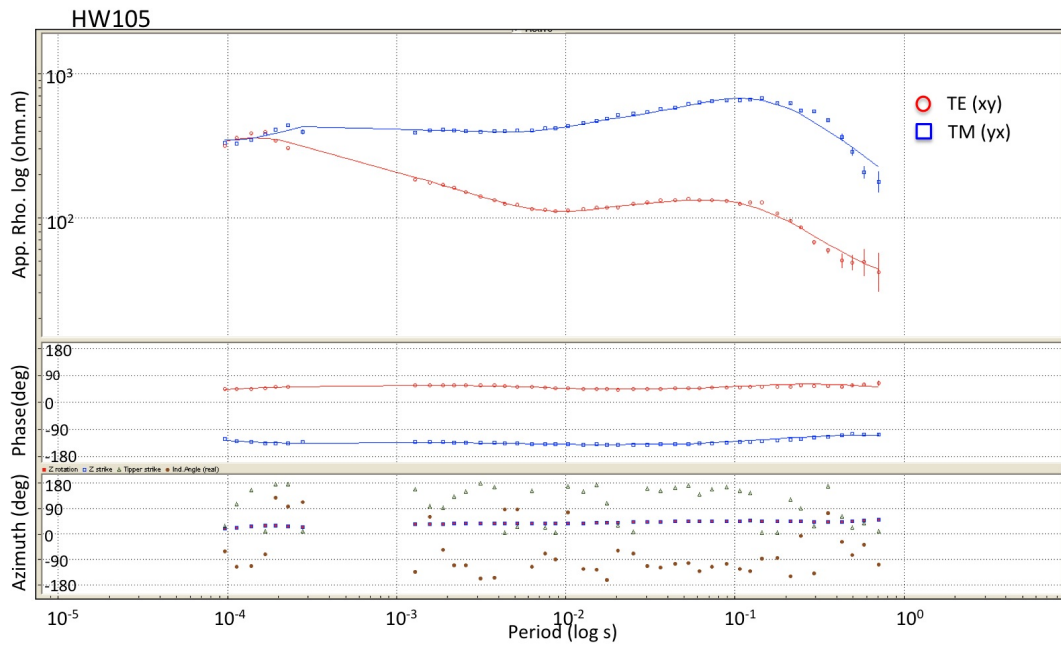
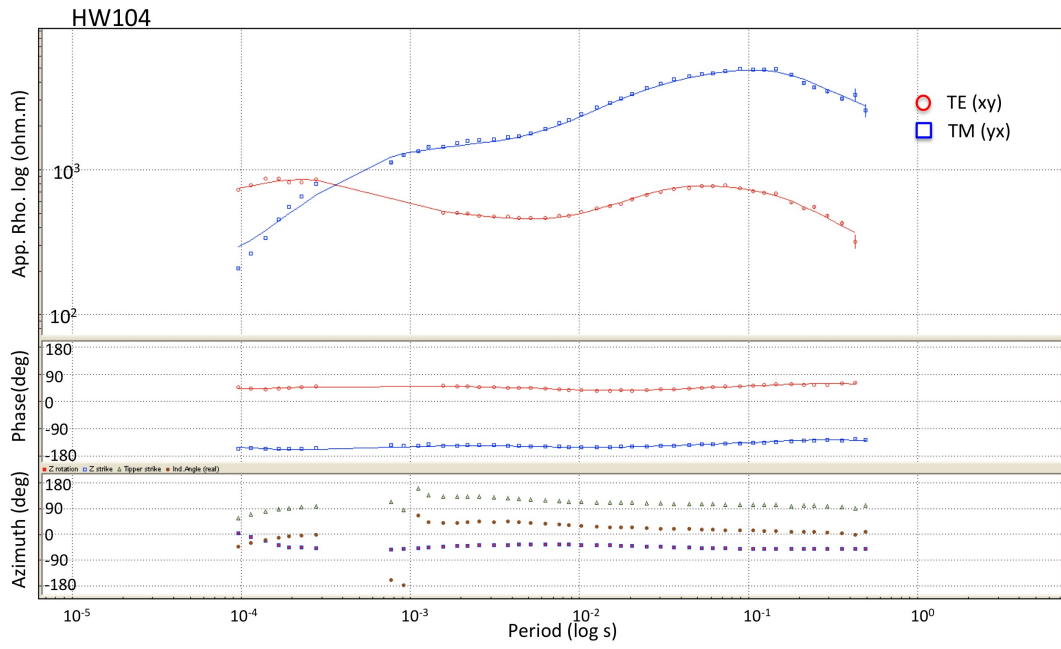


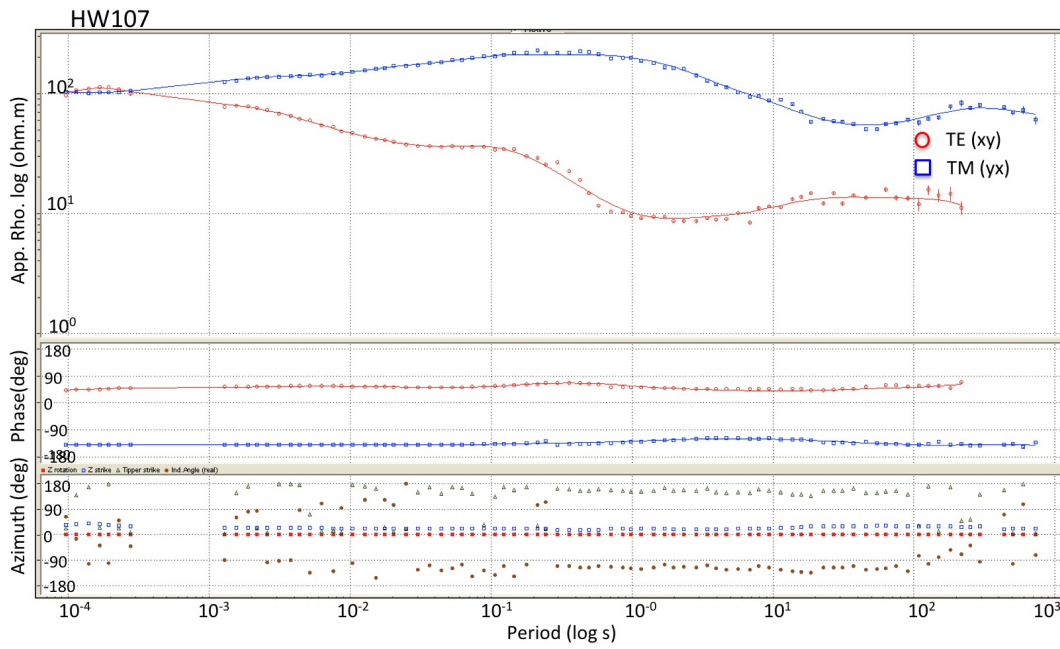
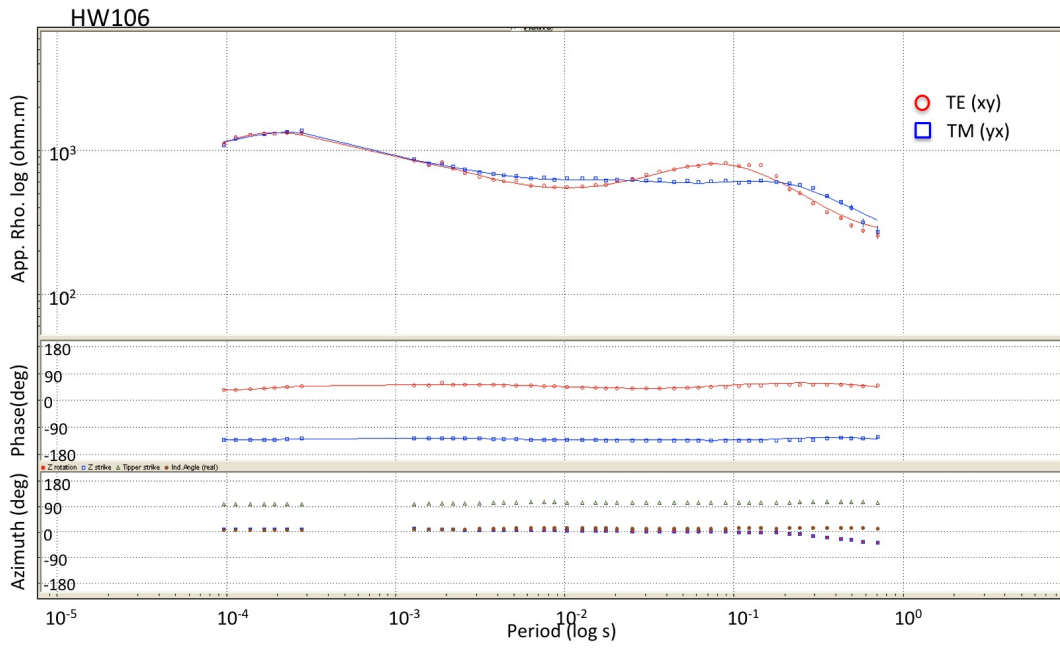
# Appendix B

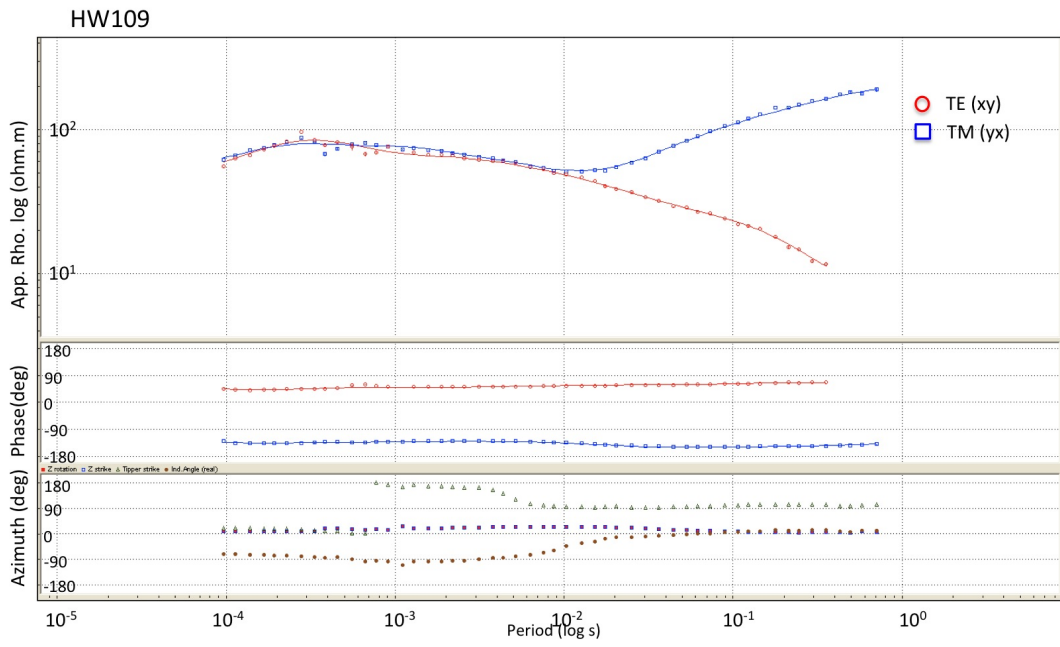
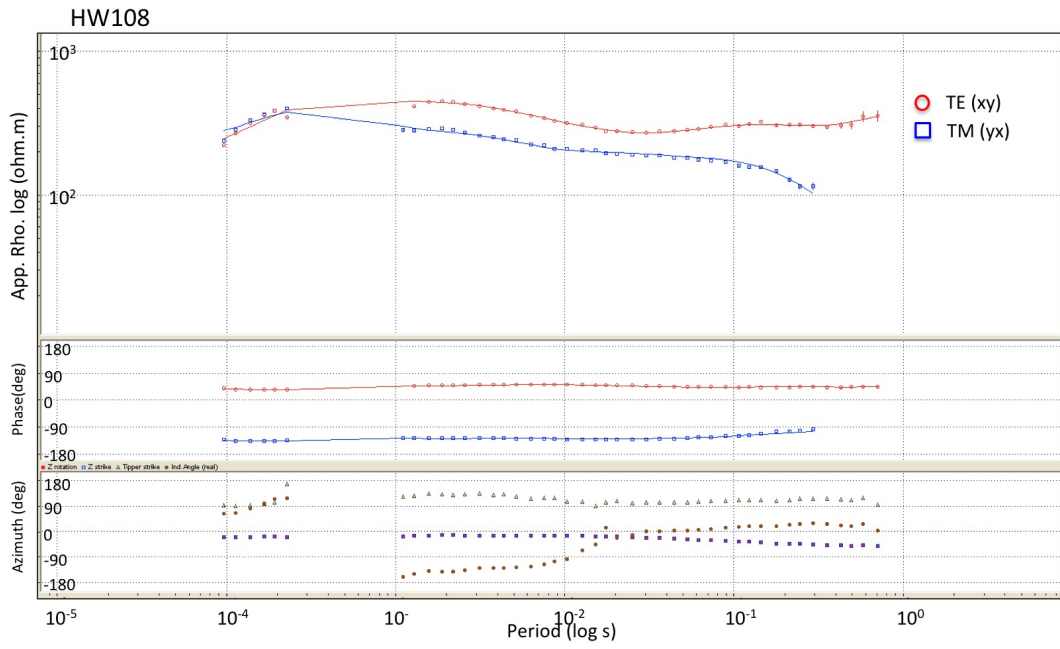
## Edited .edi files

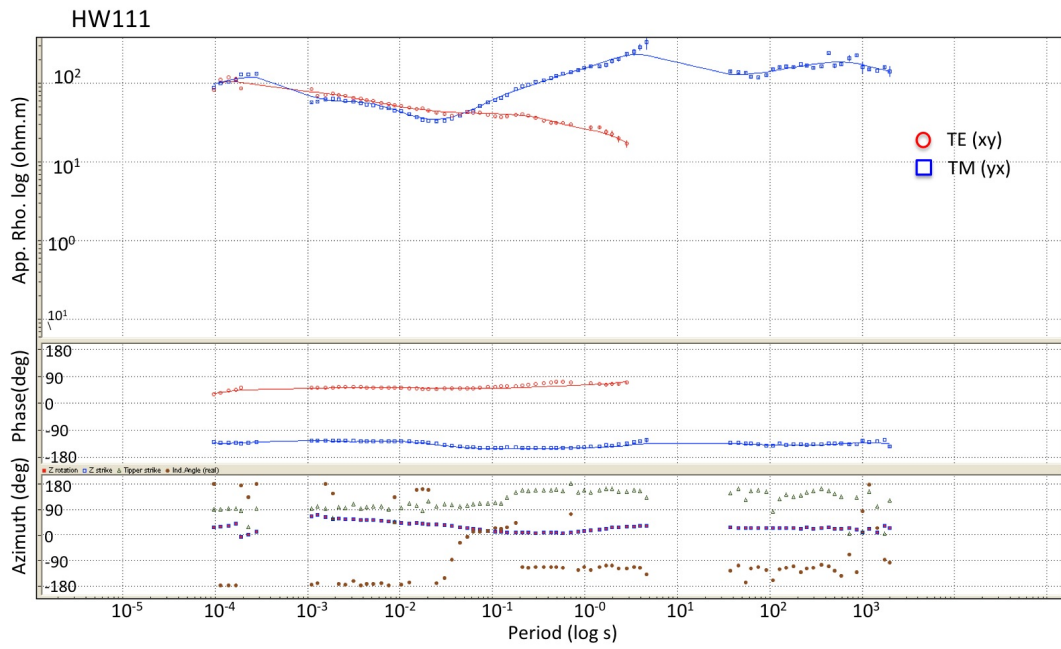
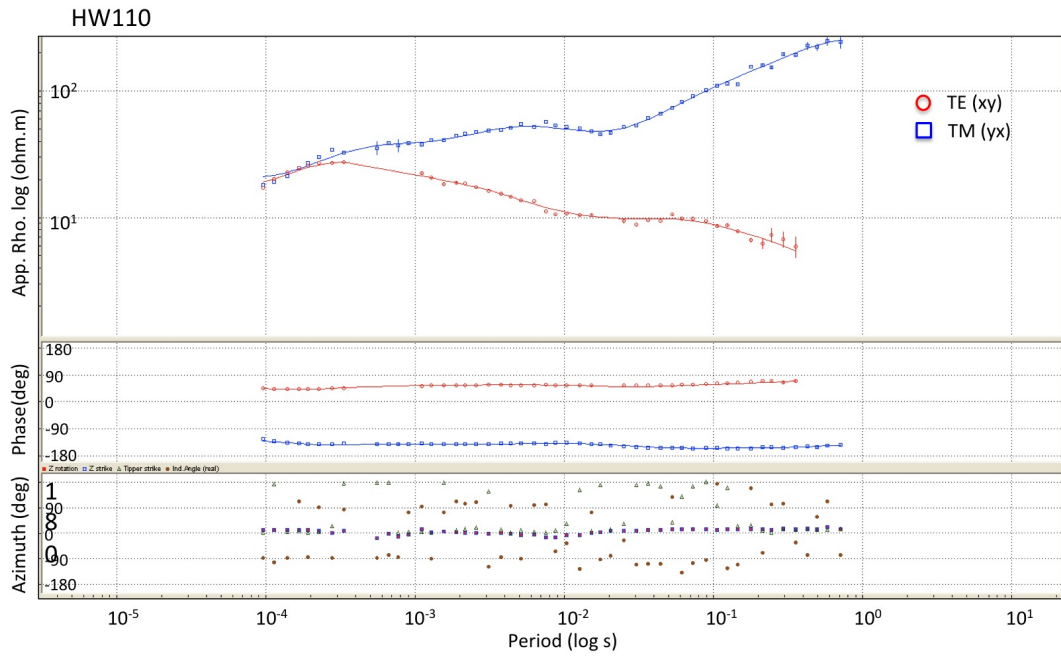


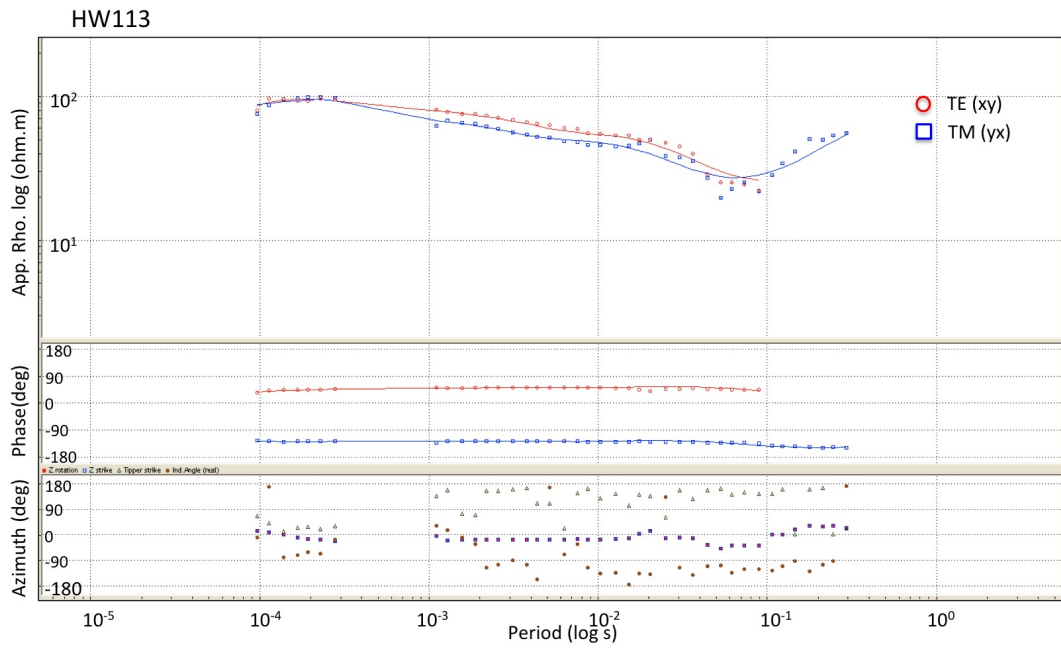
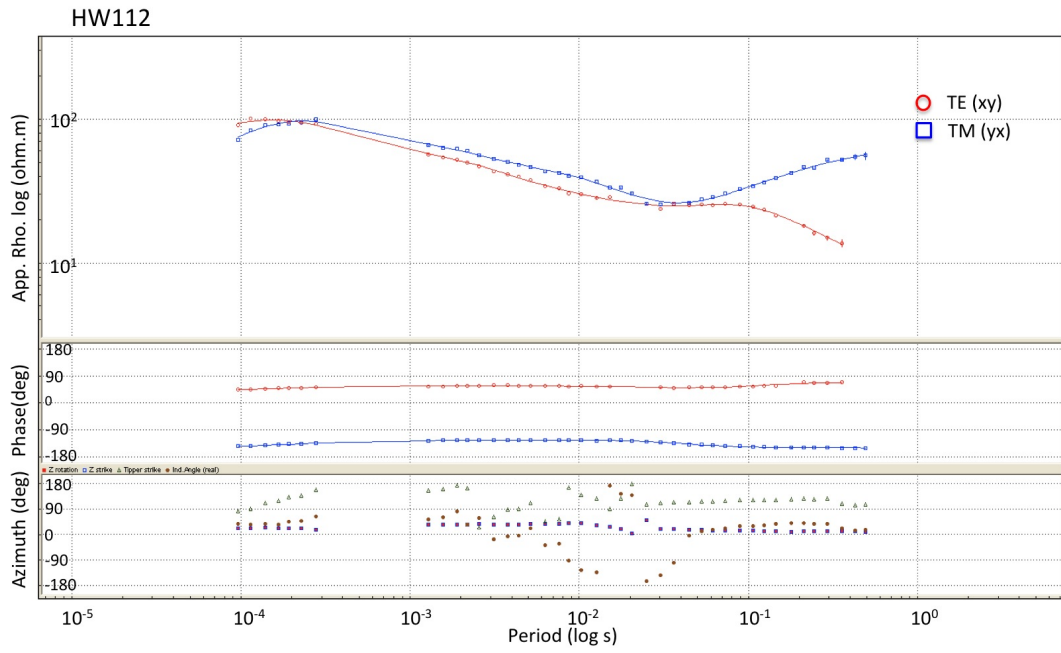


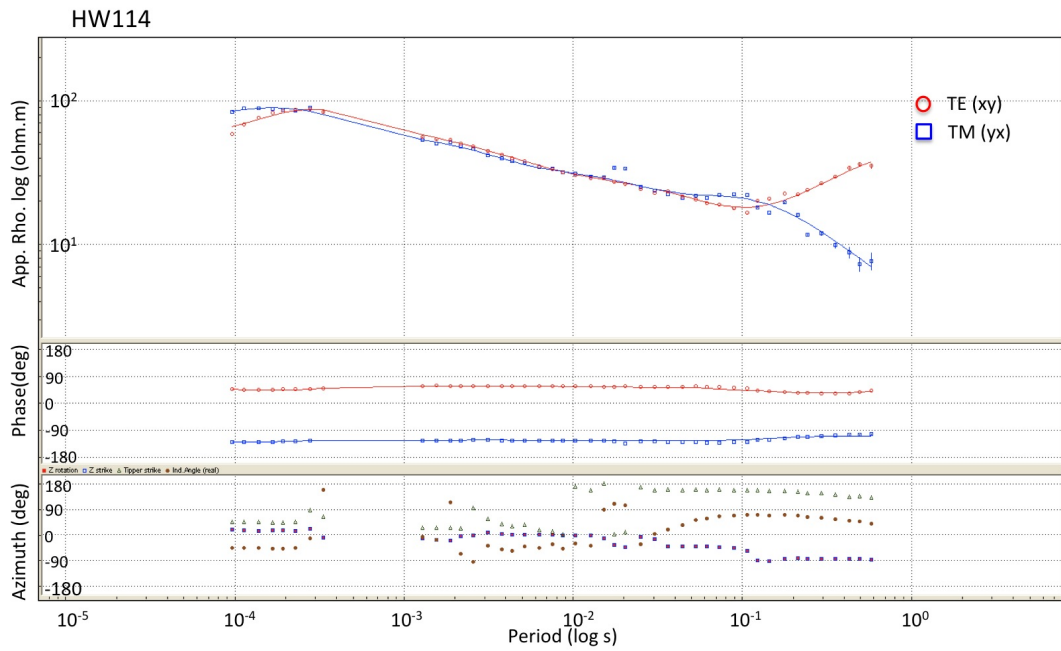
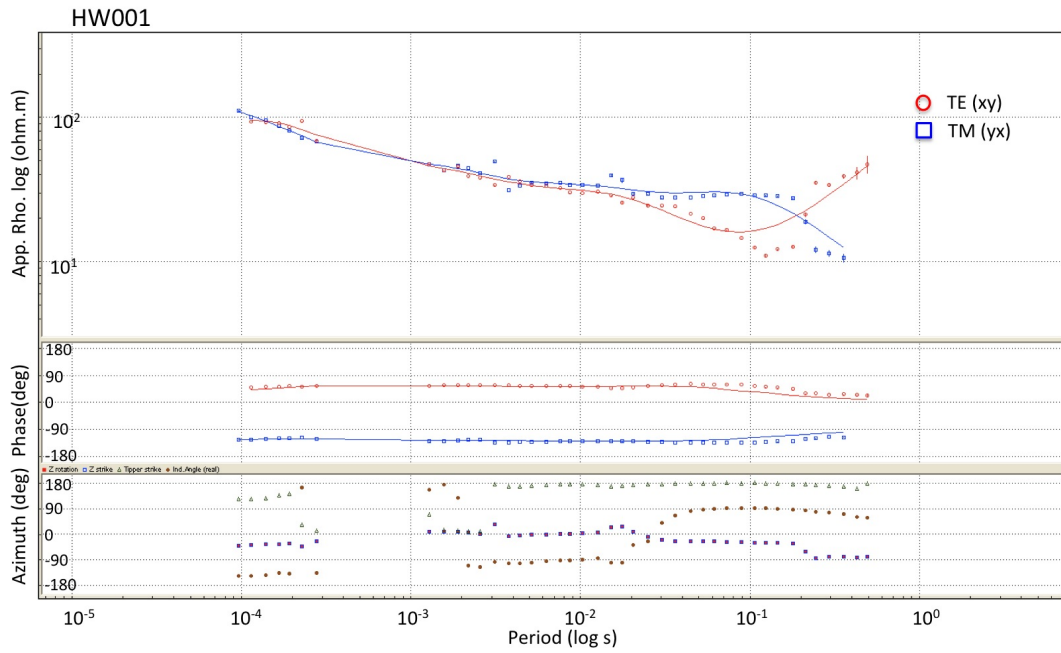


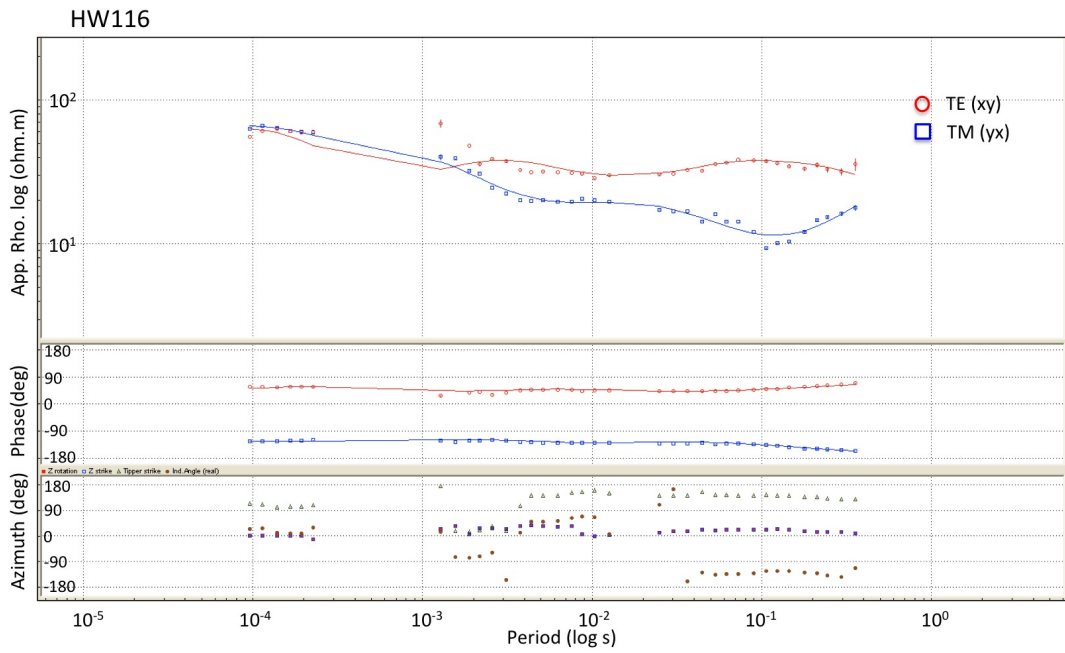
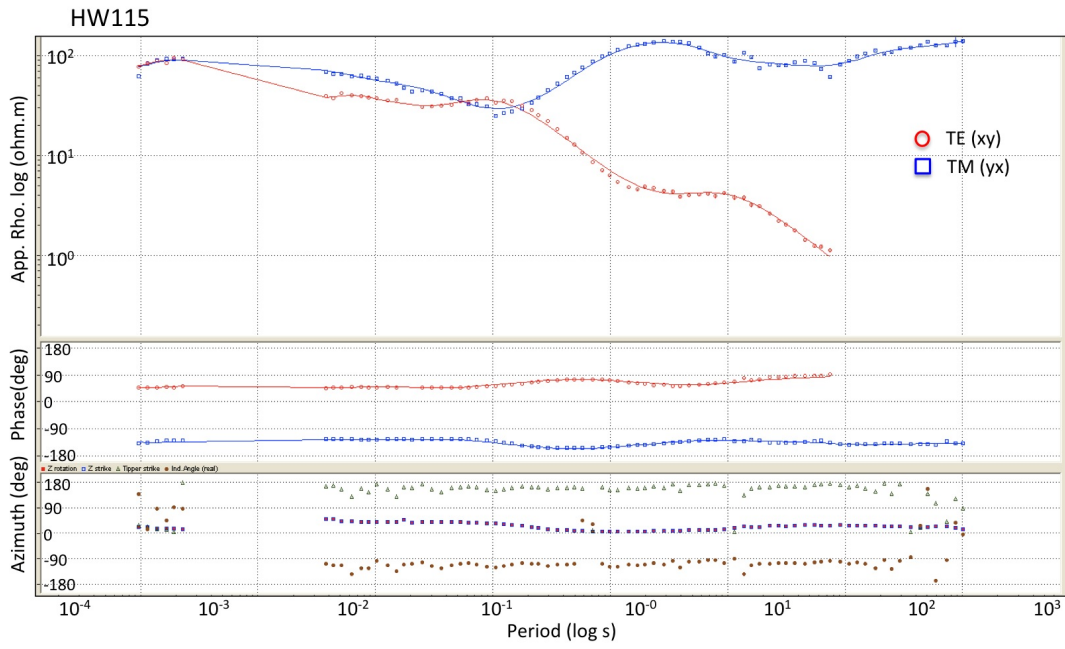


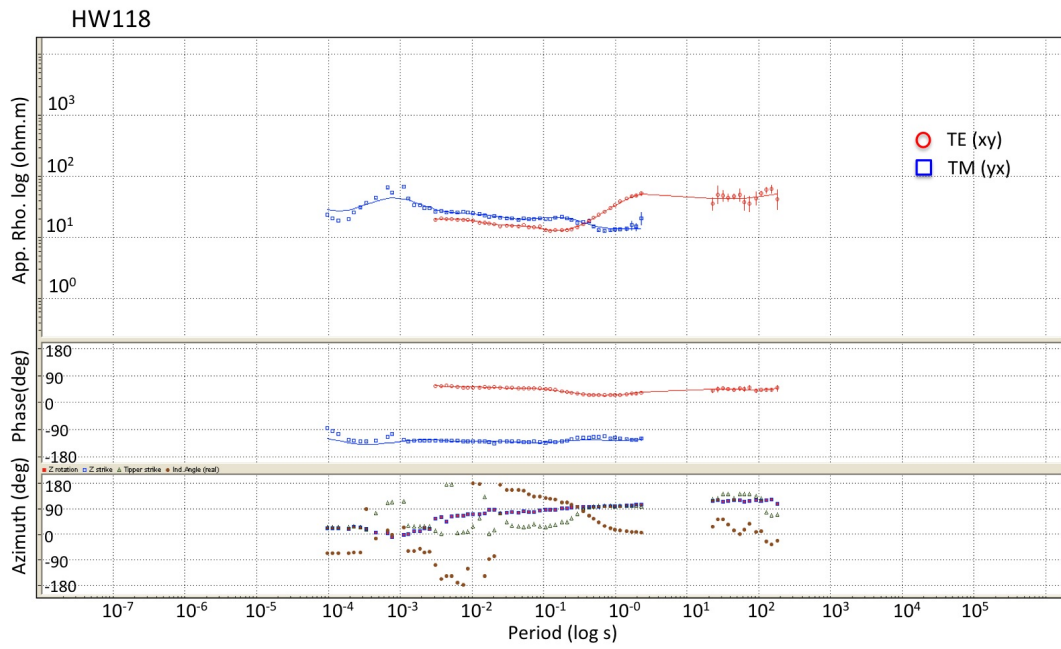
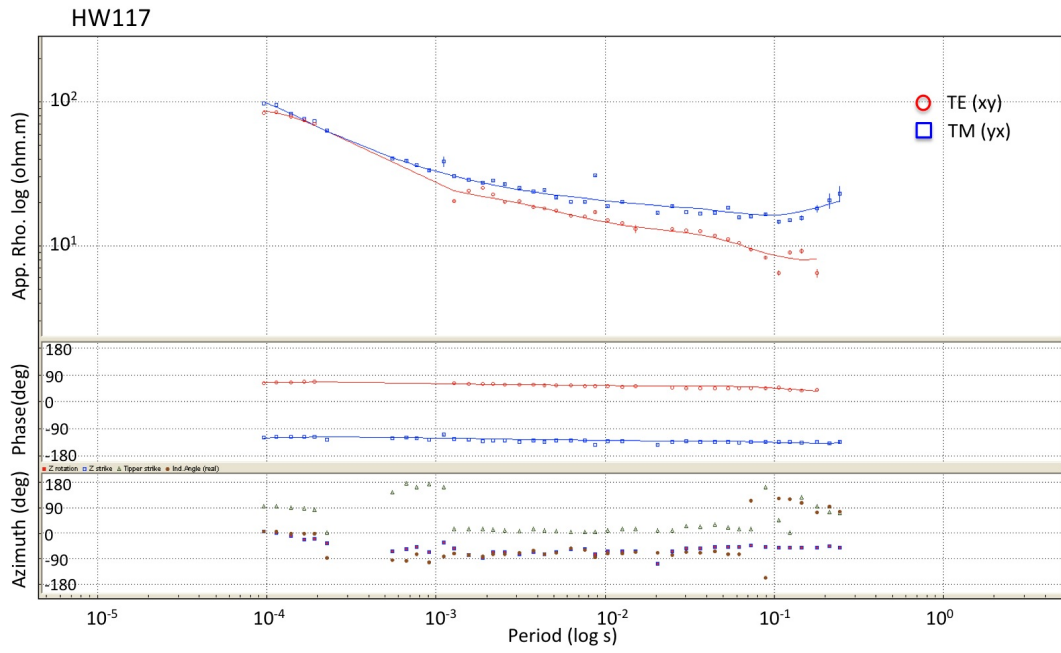


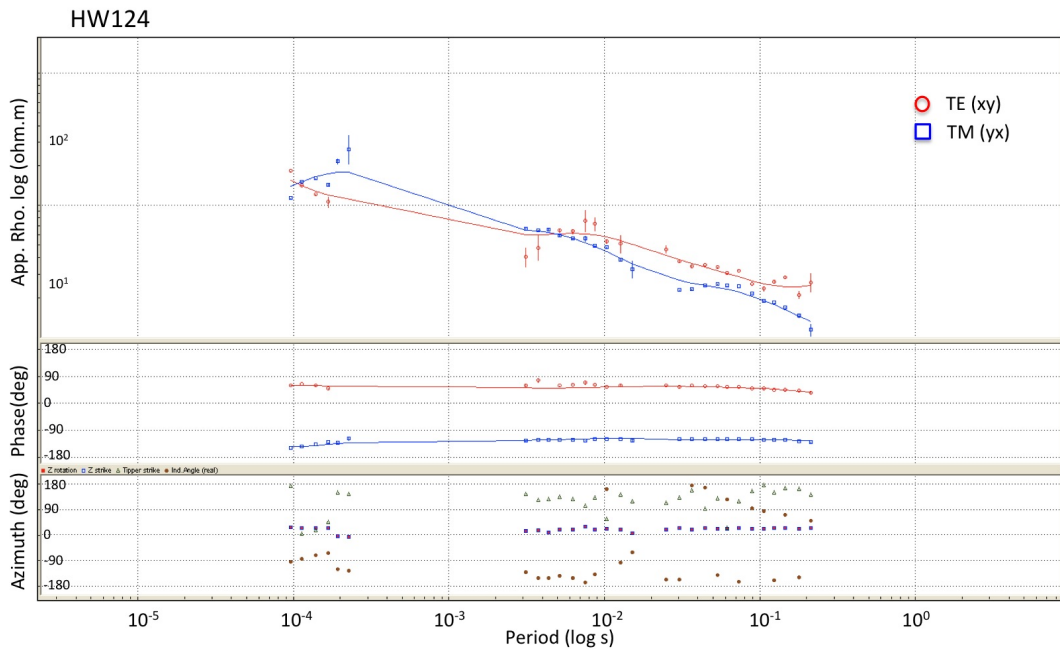
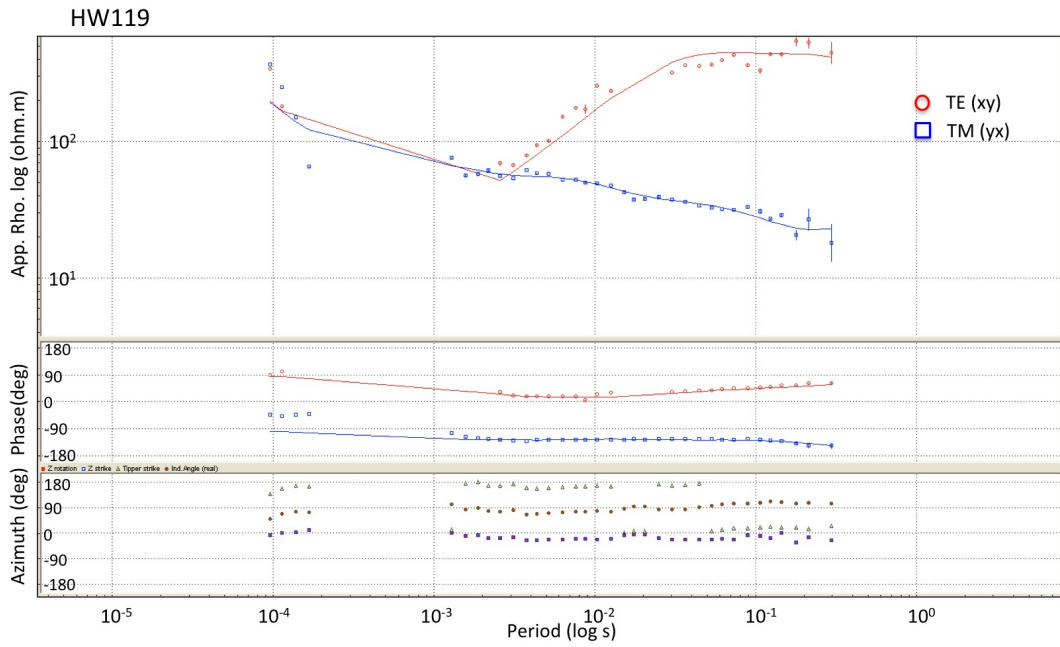


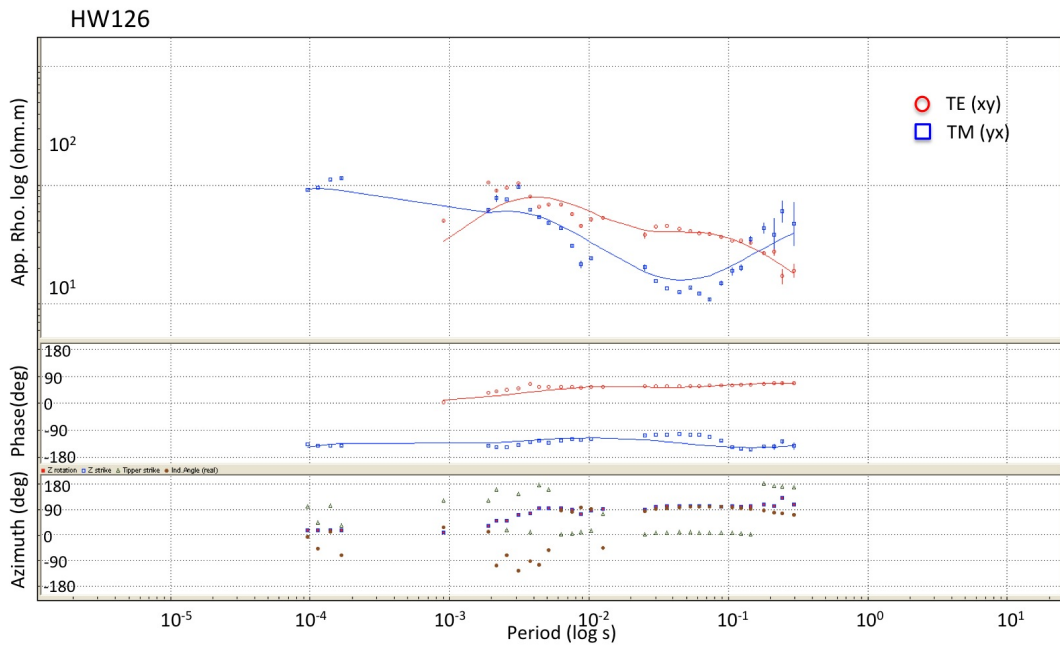
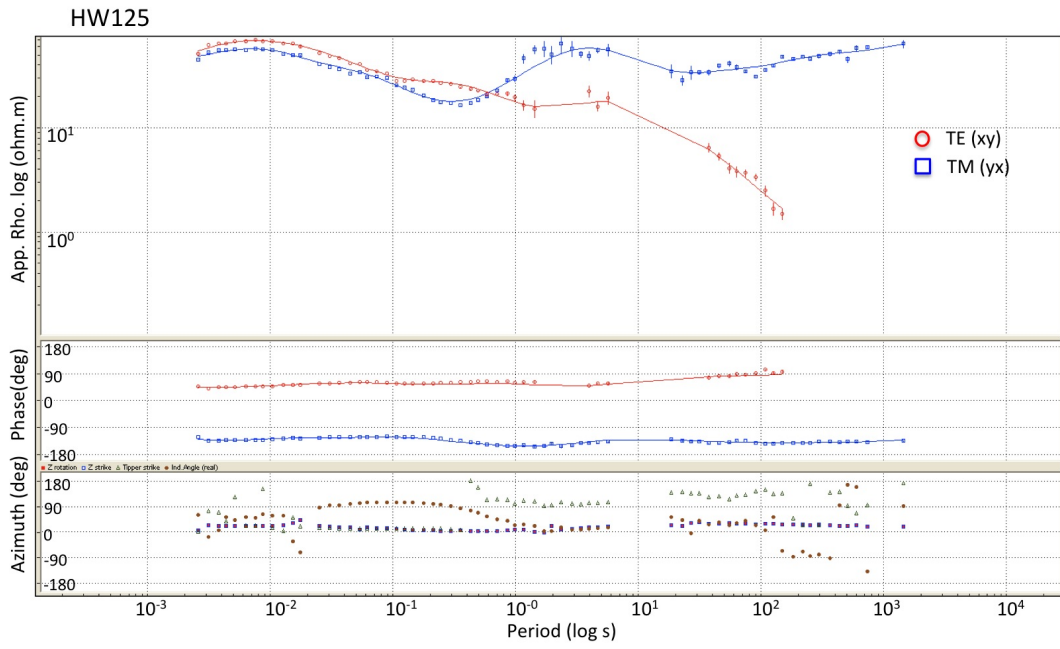


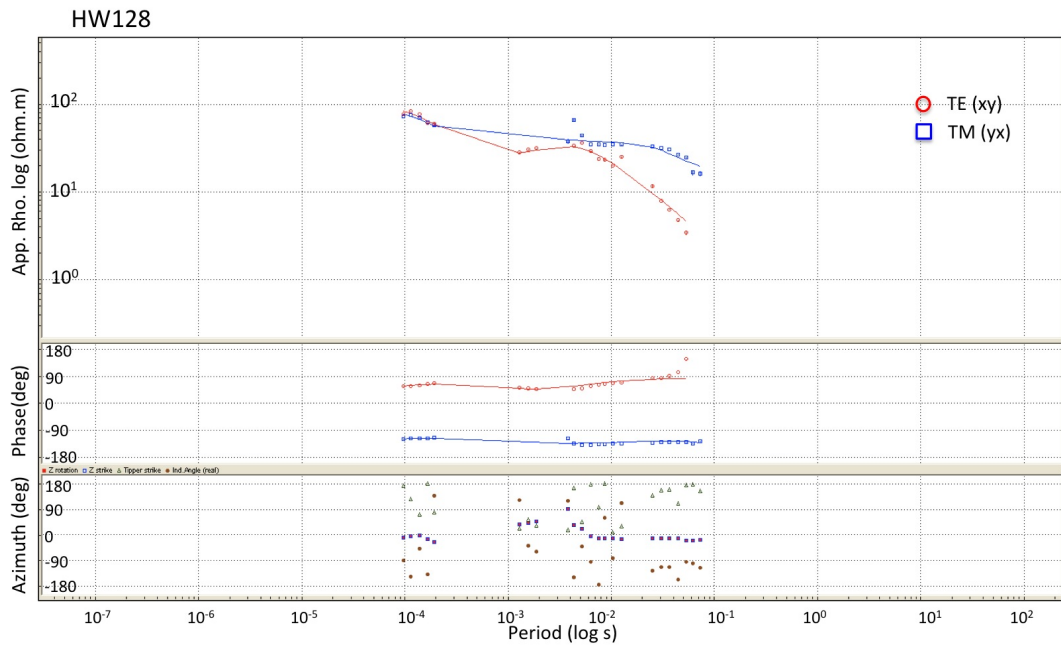
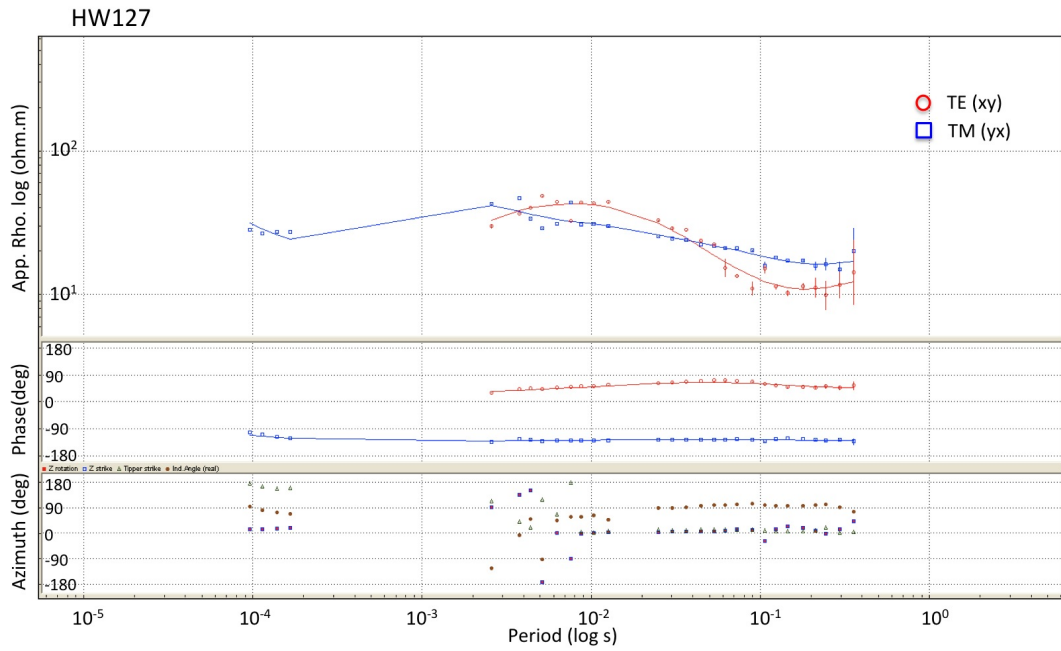


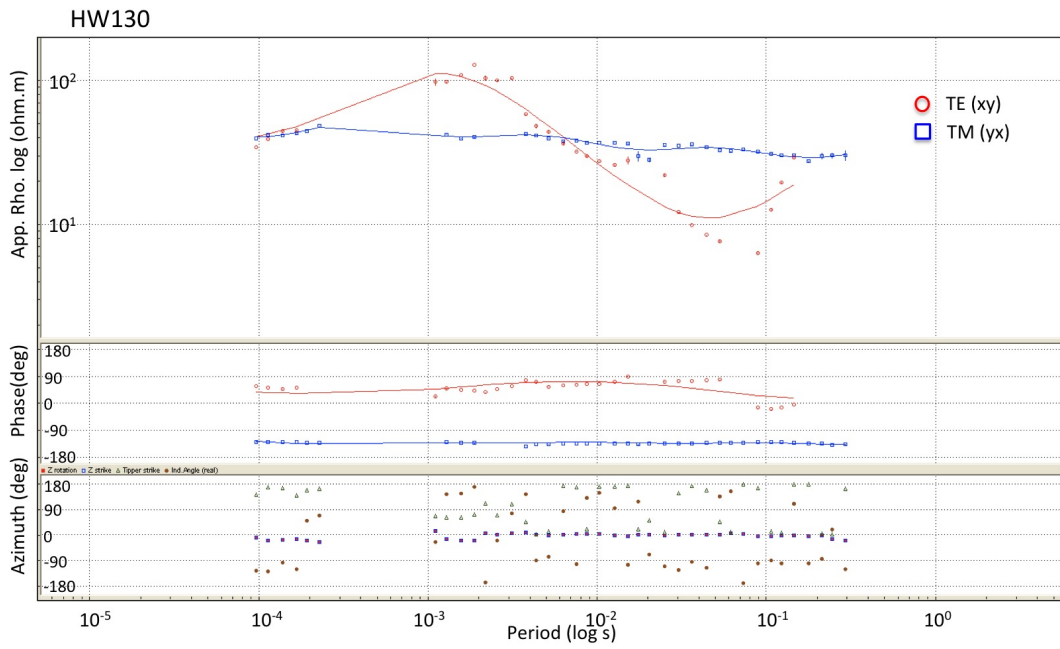
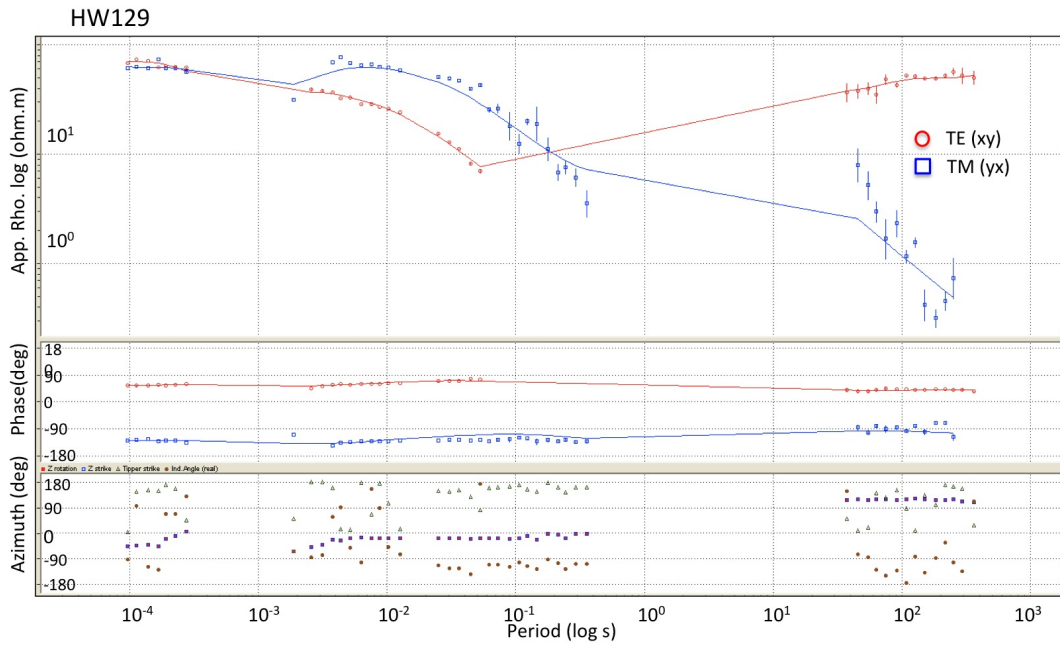


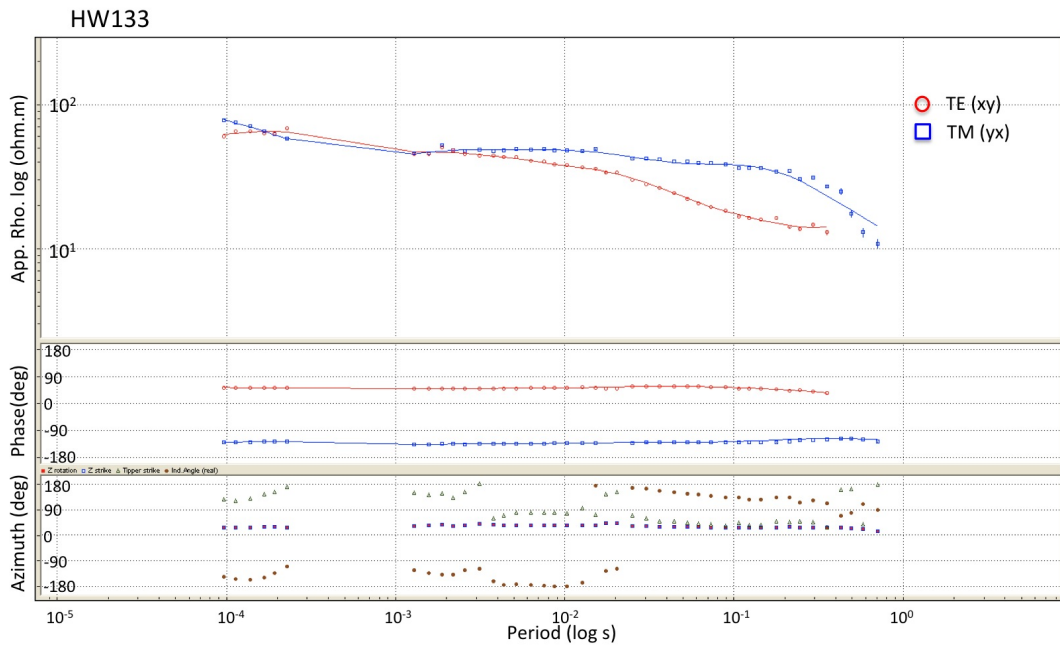
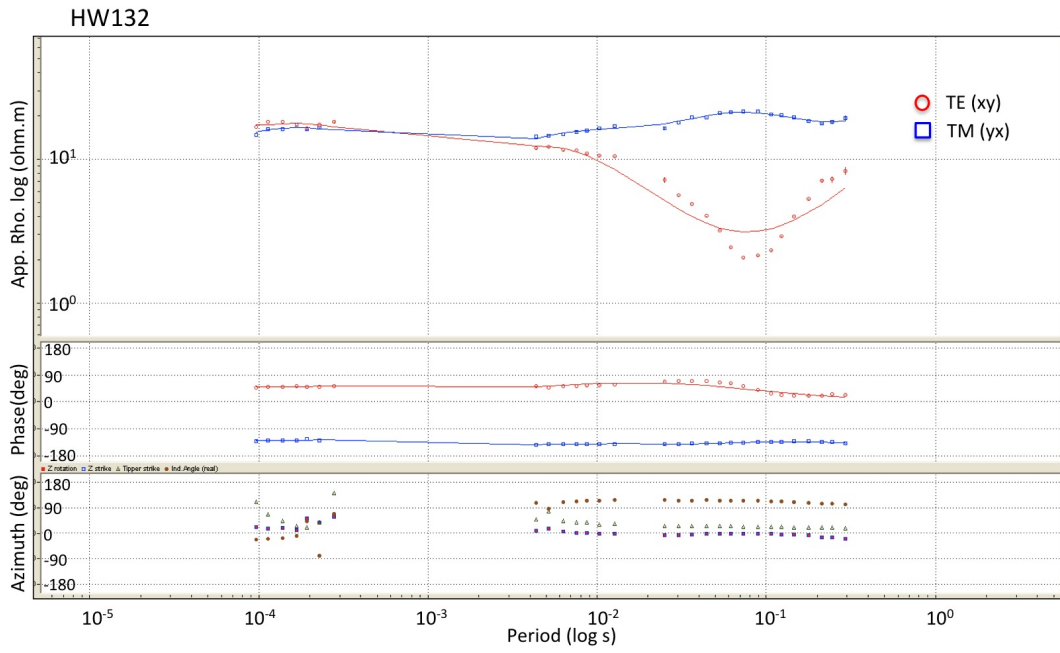


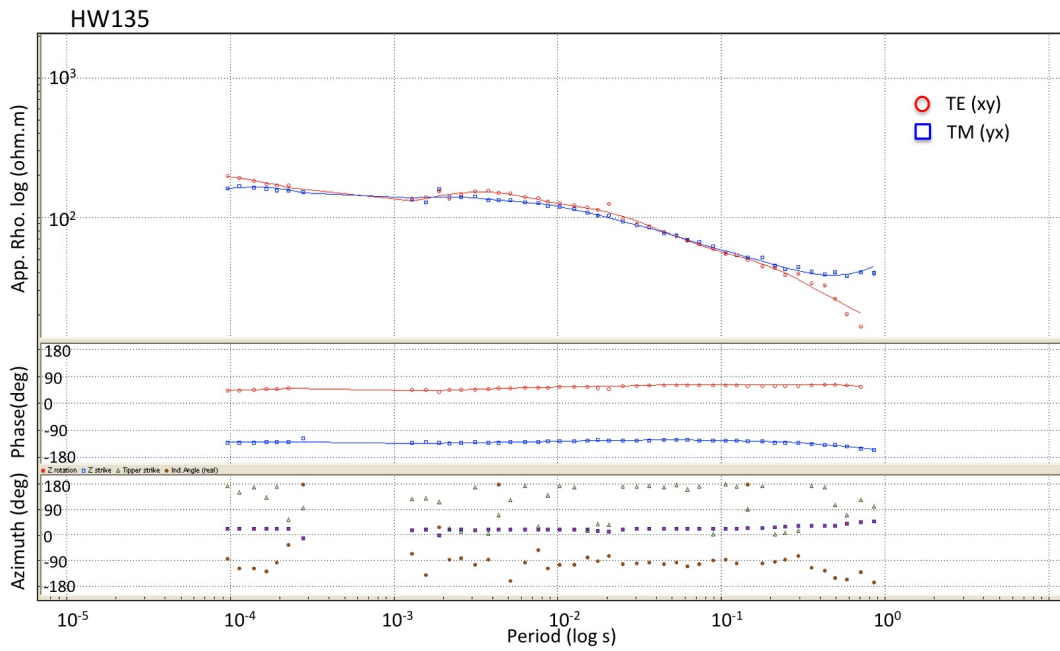
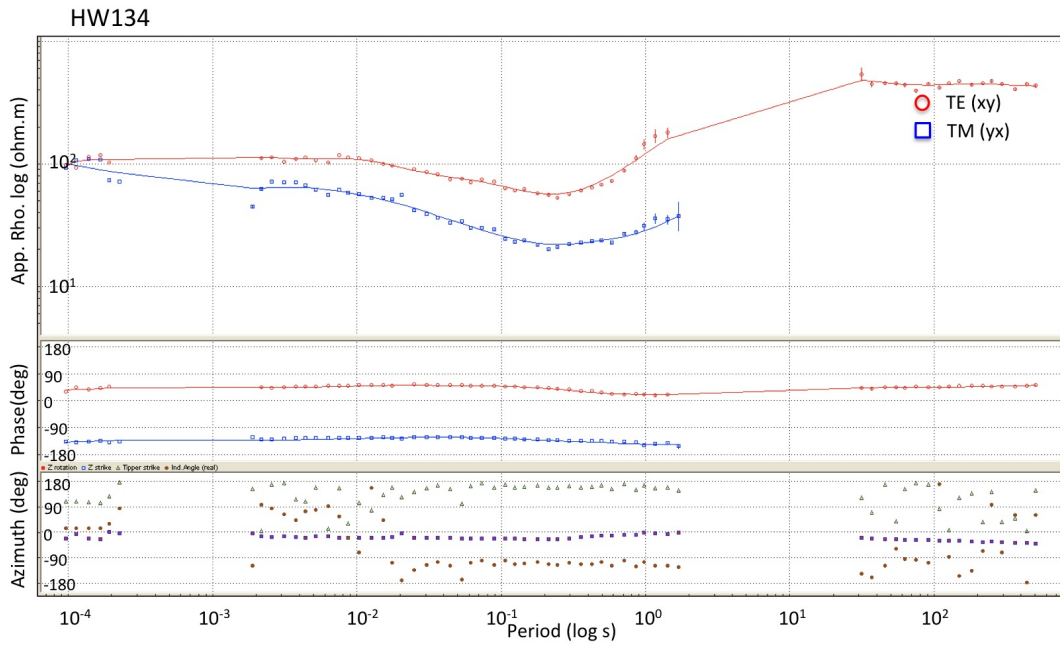




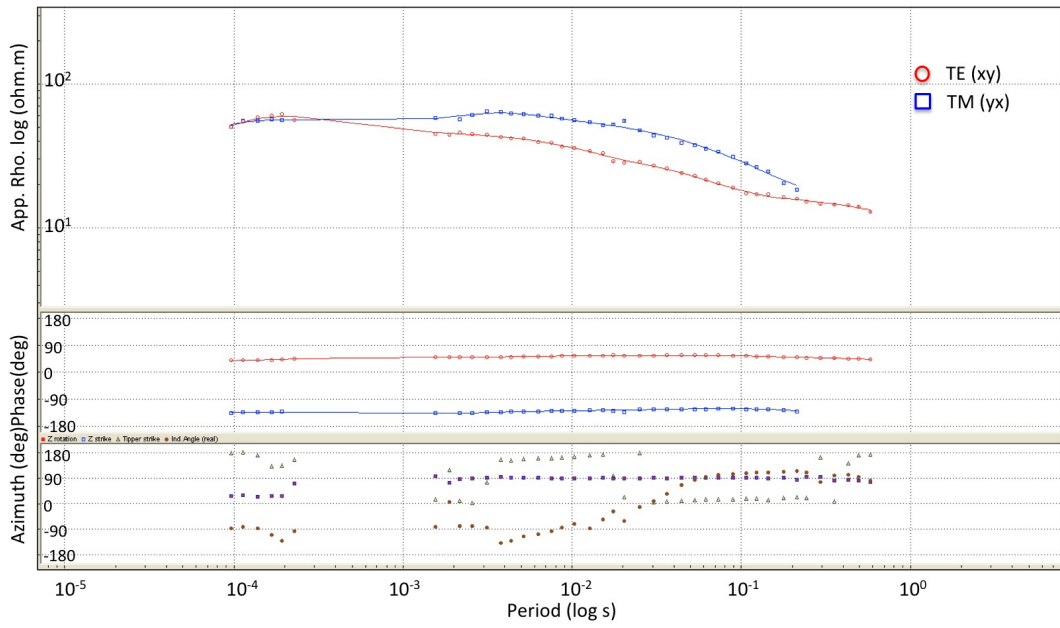




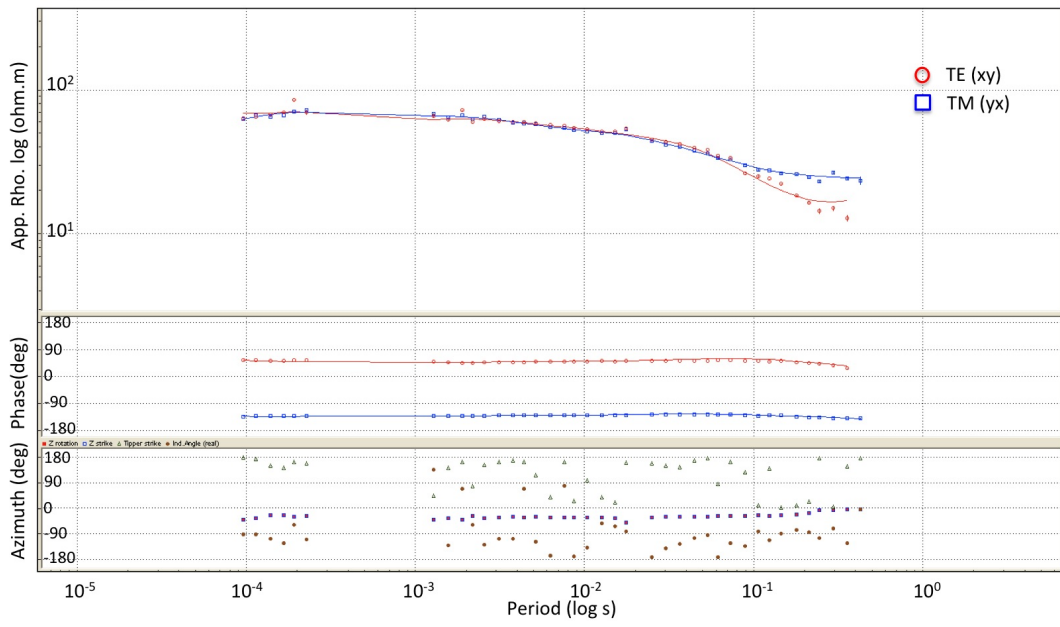


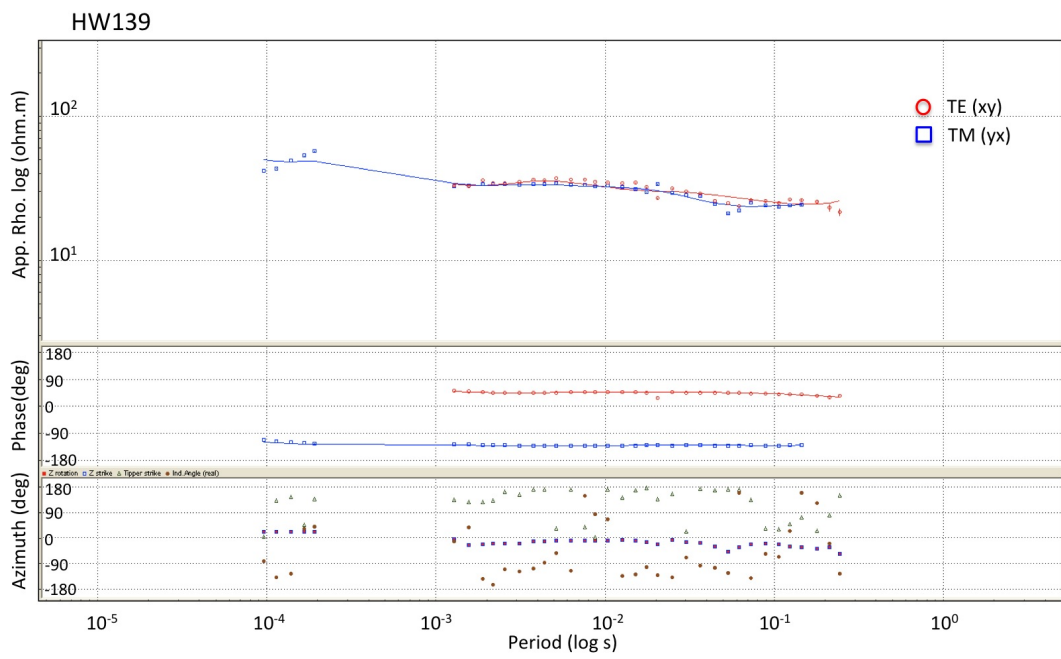
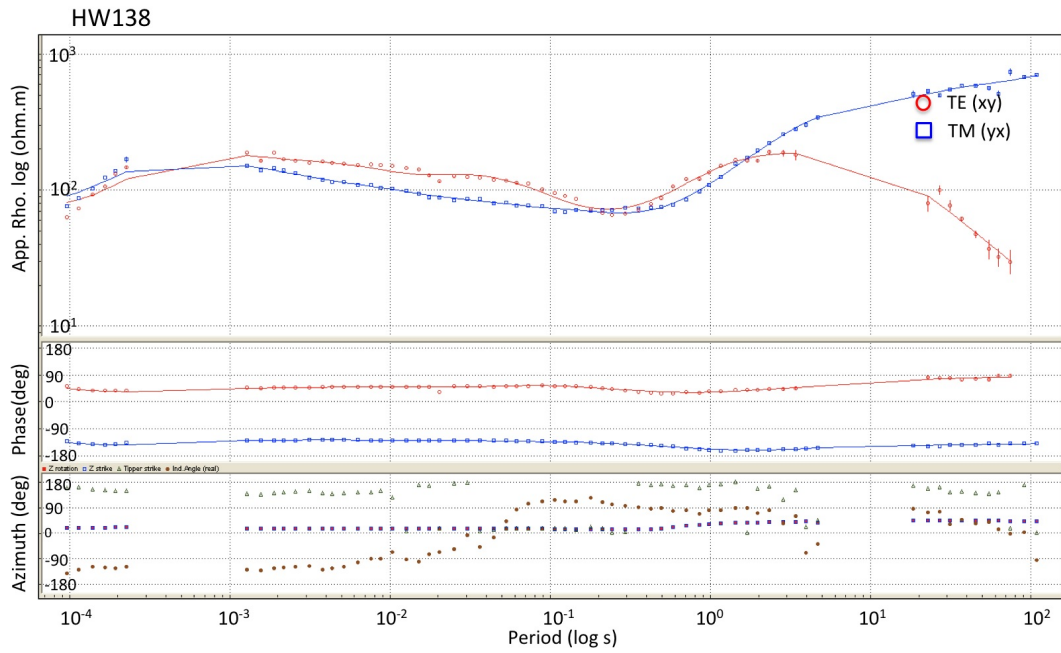


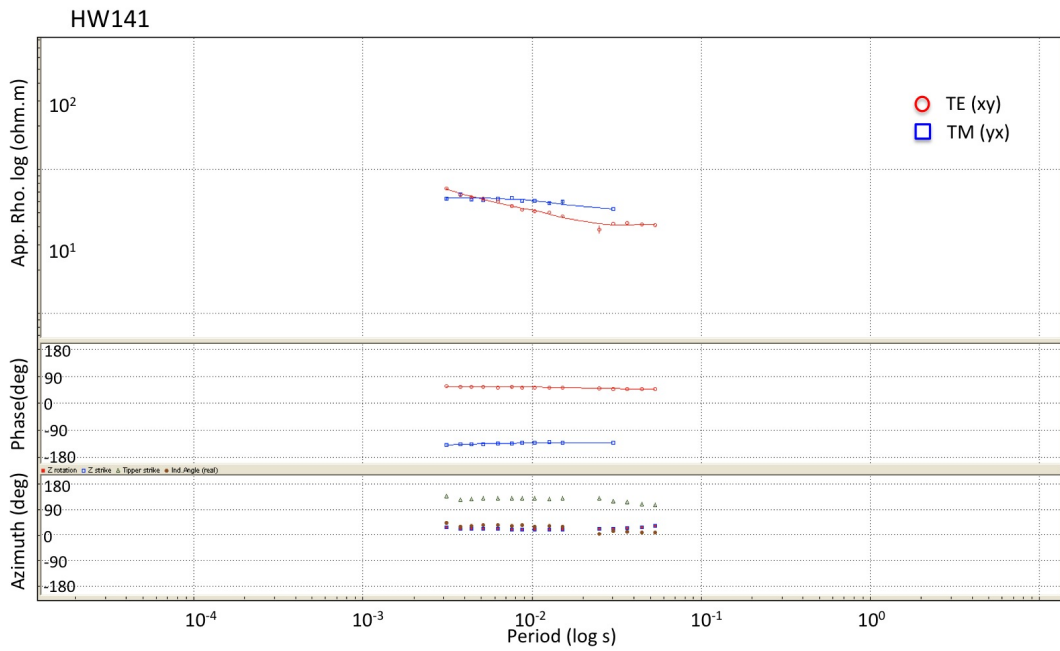
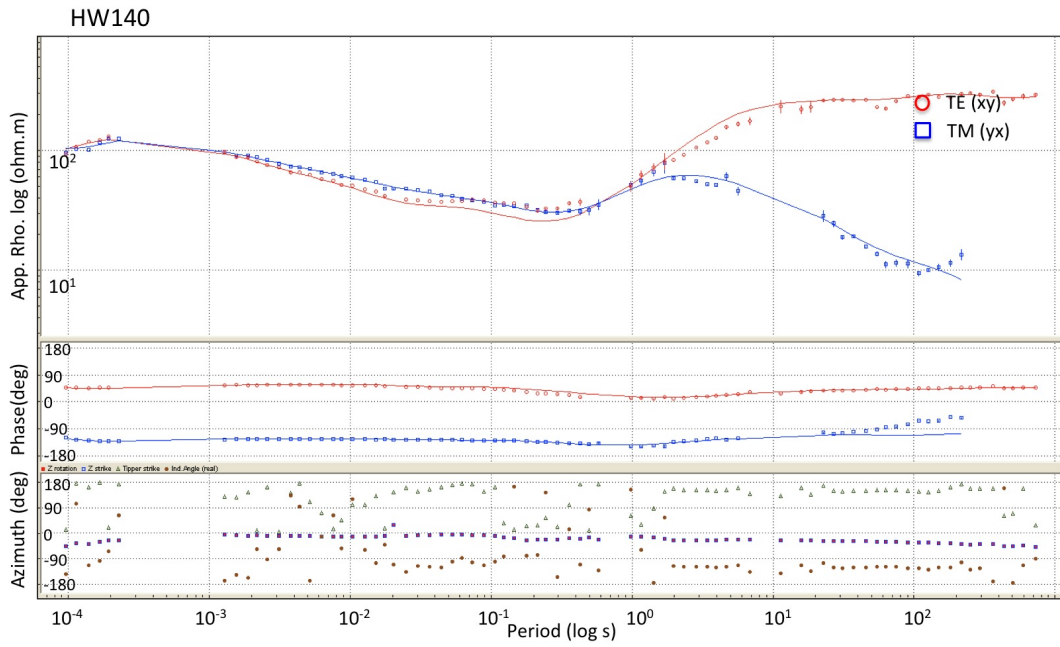
HW136



HW137





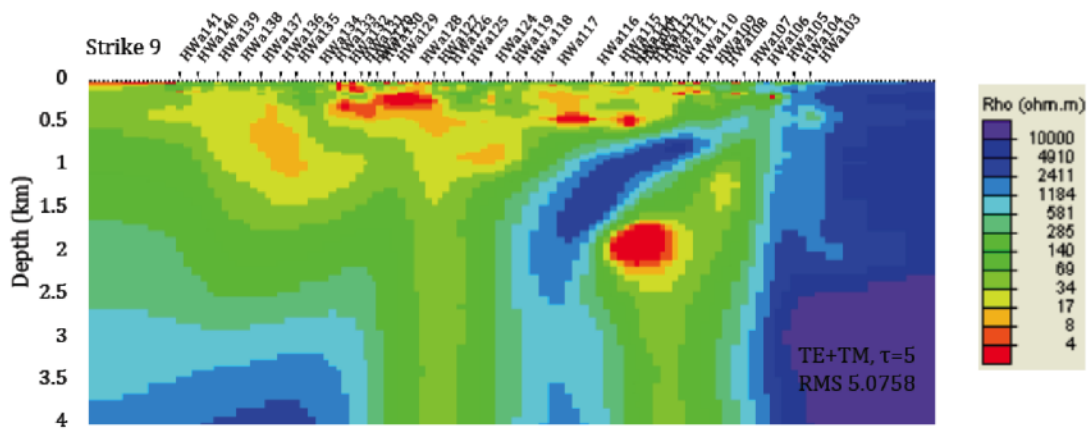
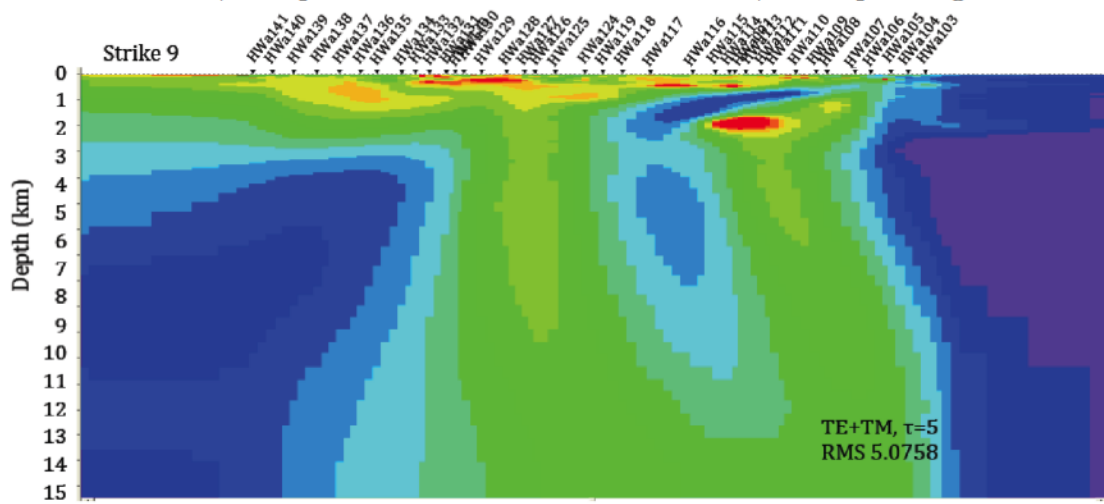


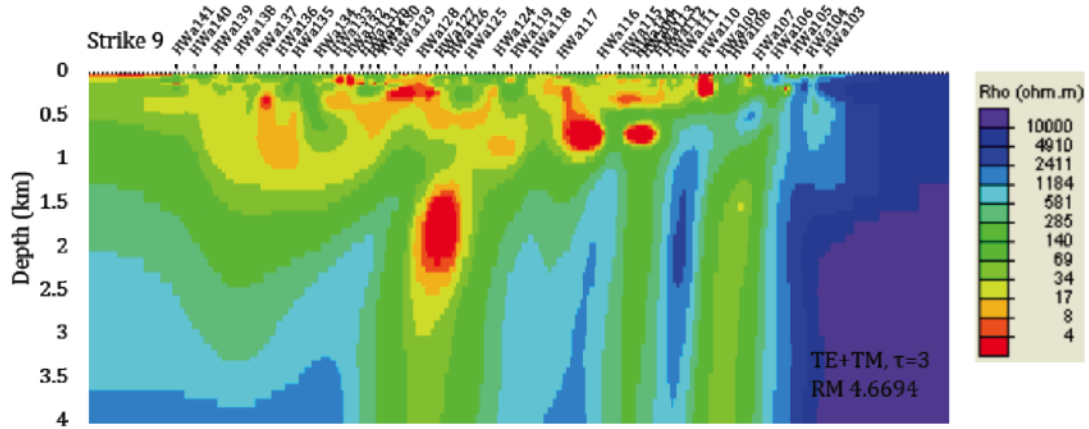
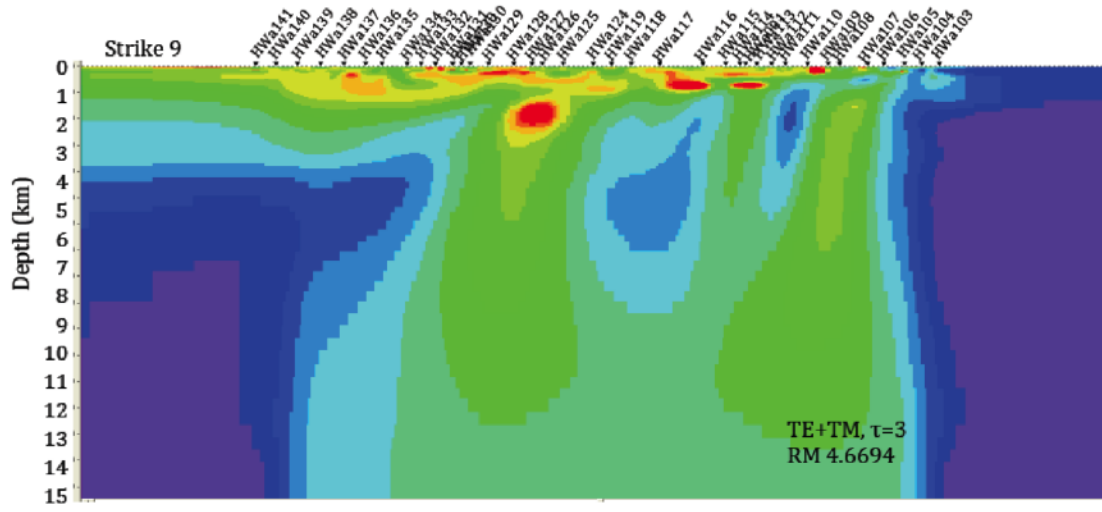


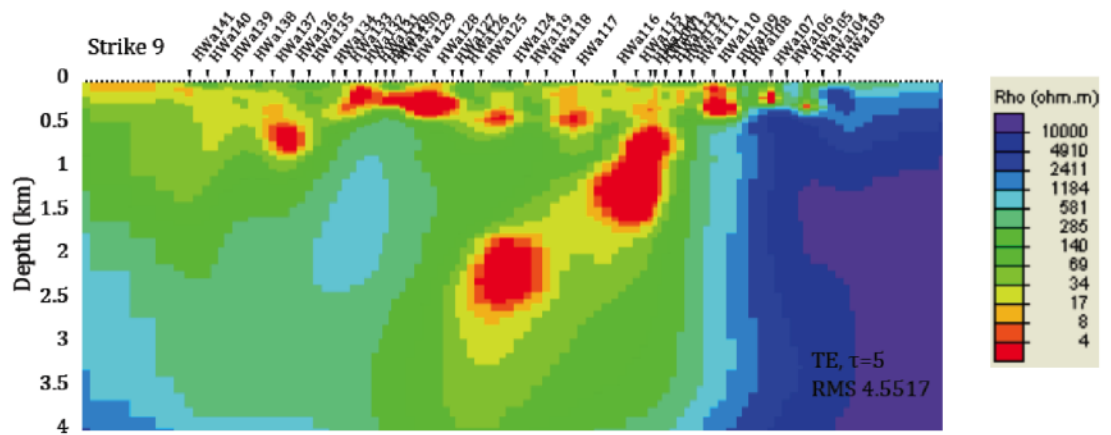
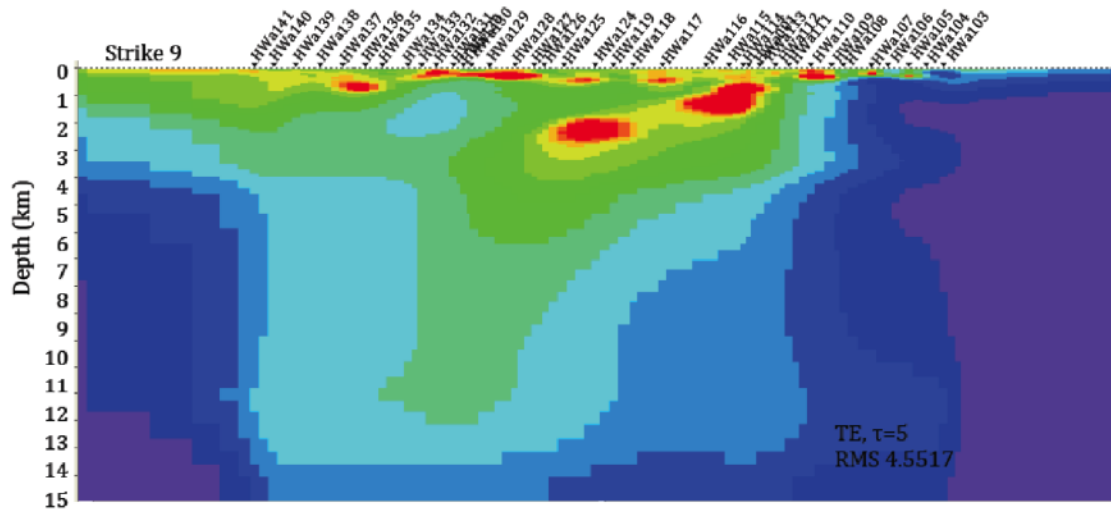
# Appendix C

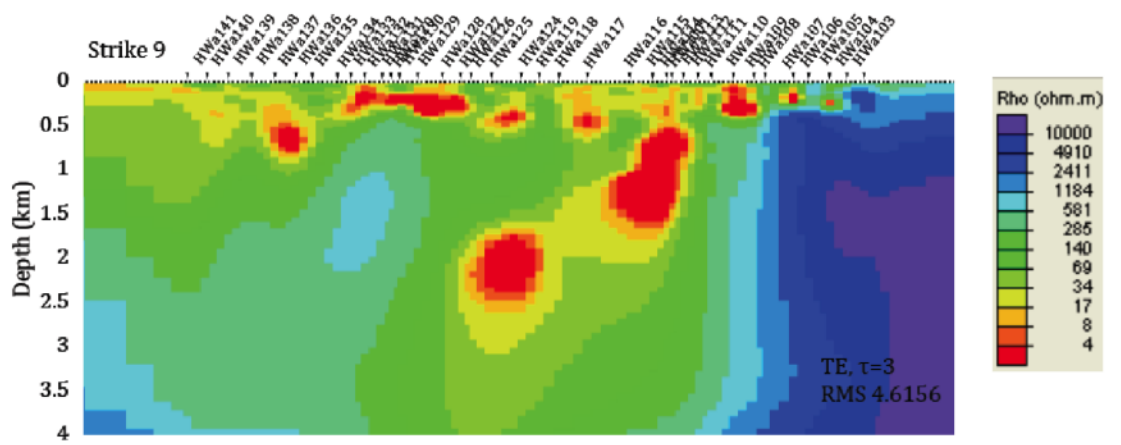
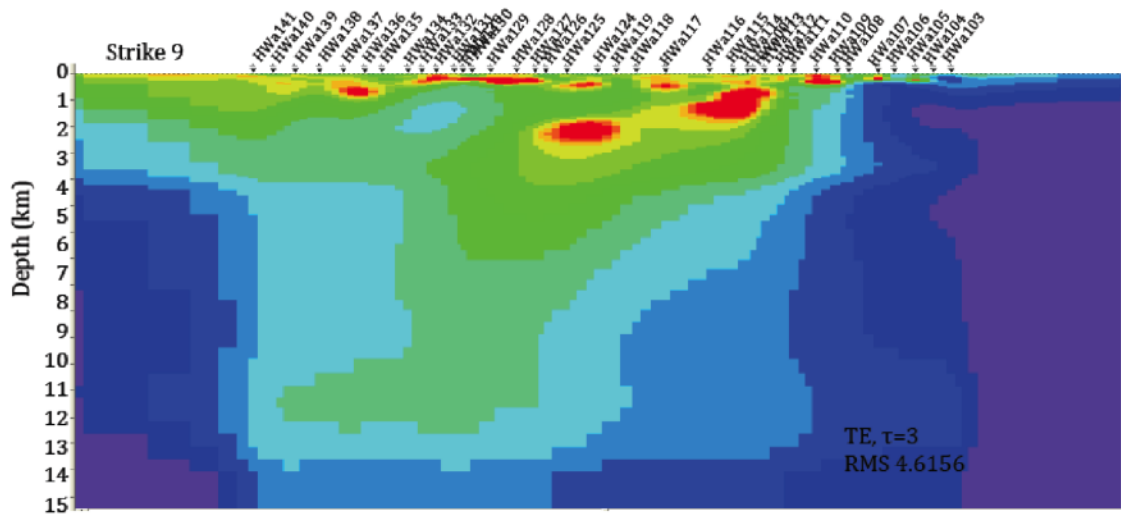
## Inversion models

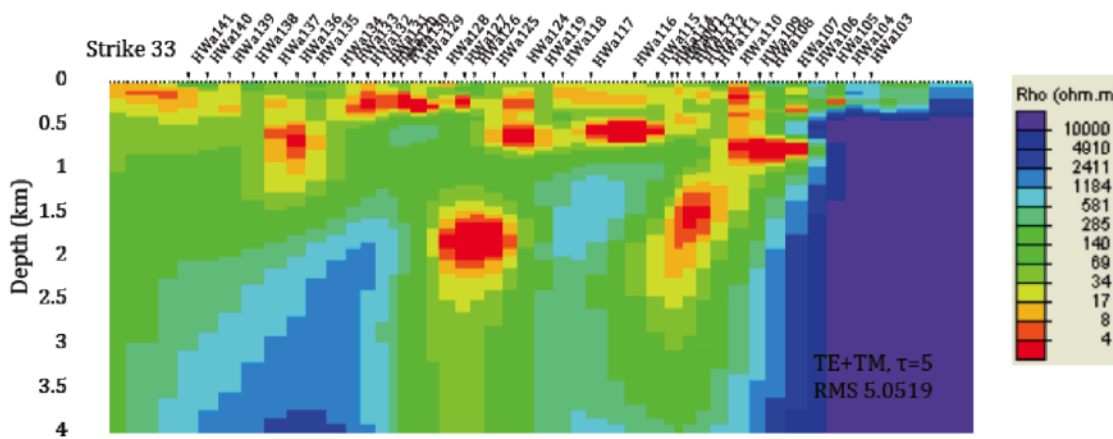
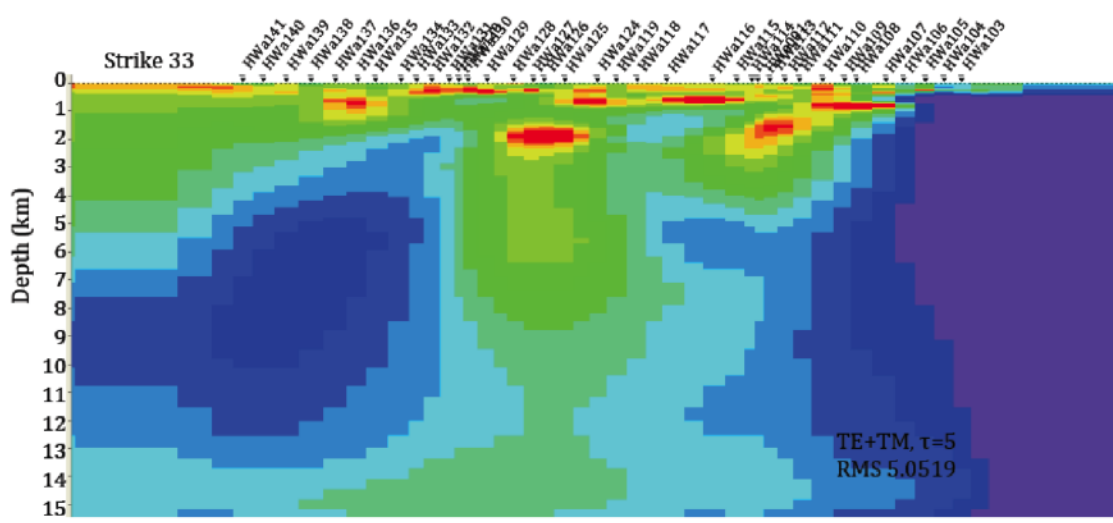
Inversion models, all apart from TM  $\tau=3$  and TM  $\tau=5$ , corresponding to Table 5.6

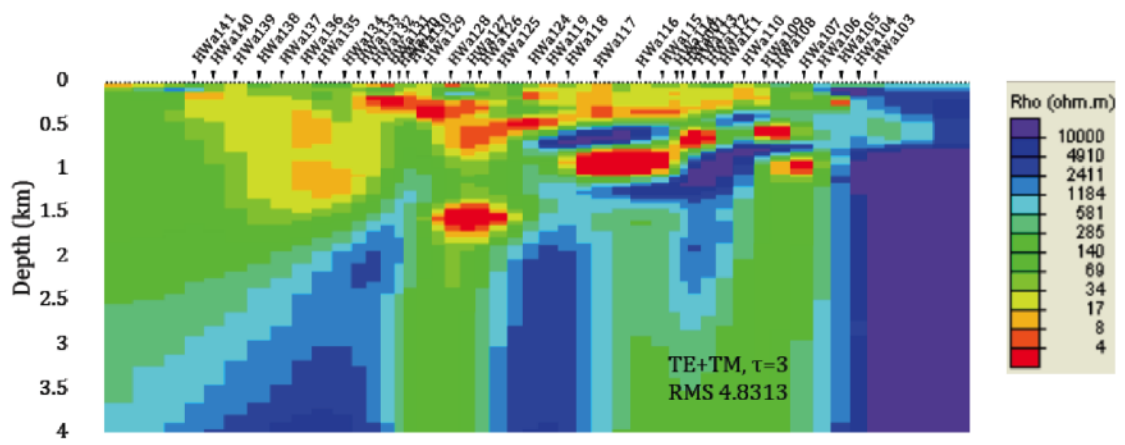
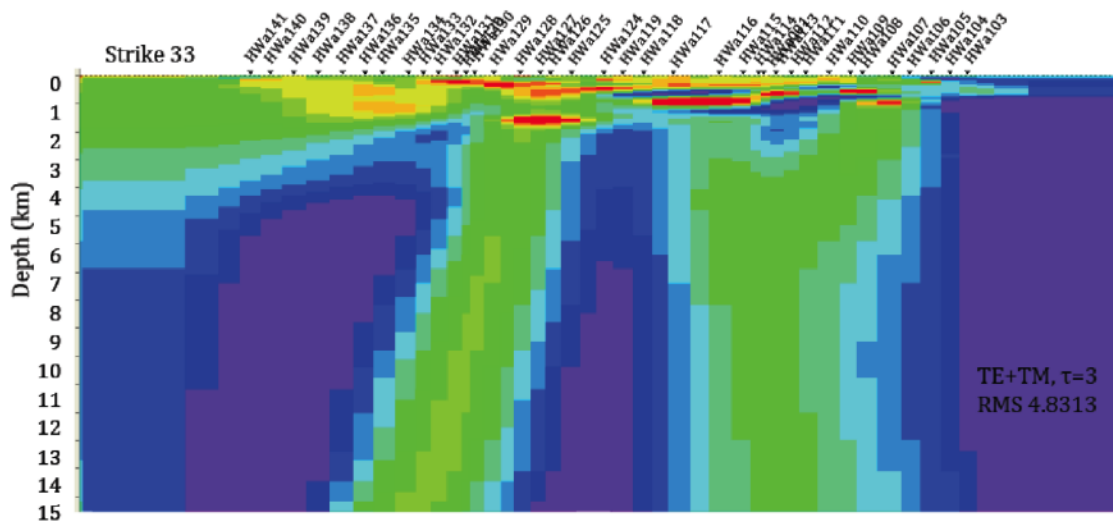


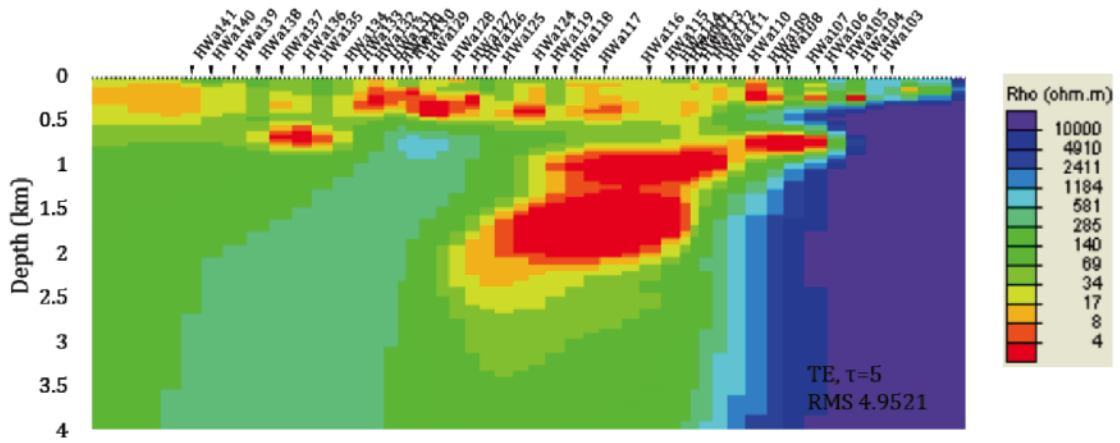
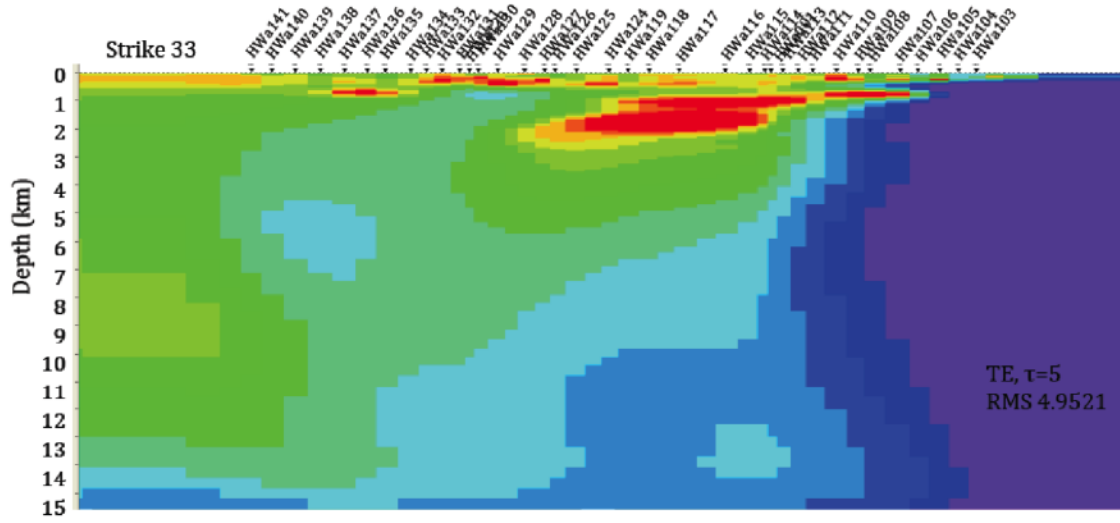


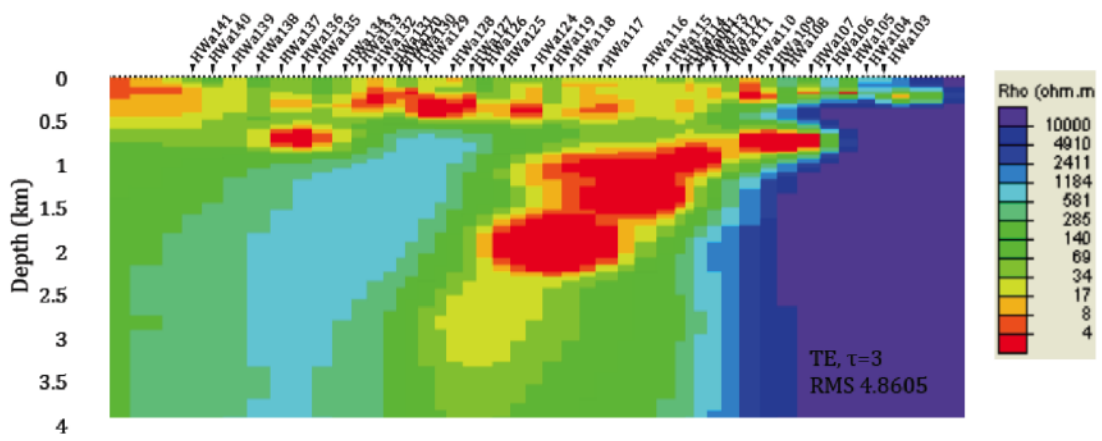
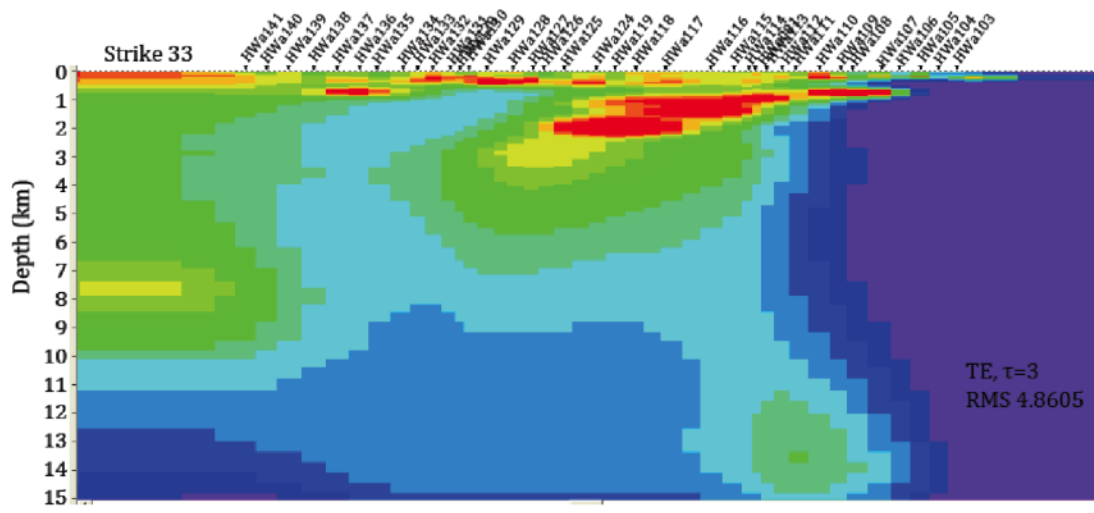










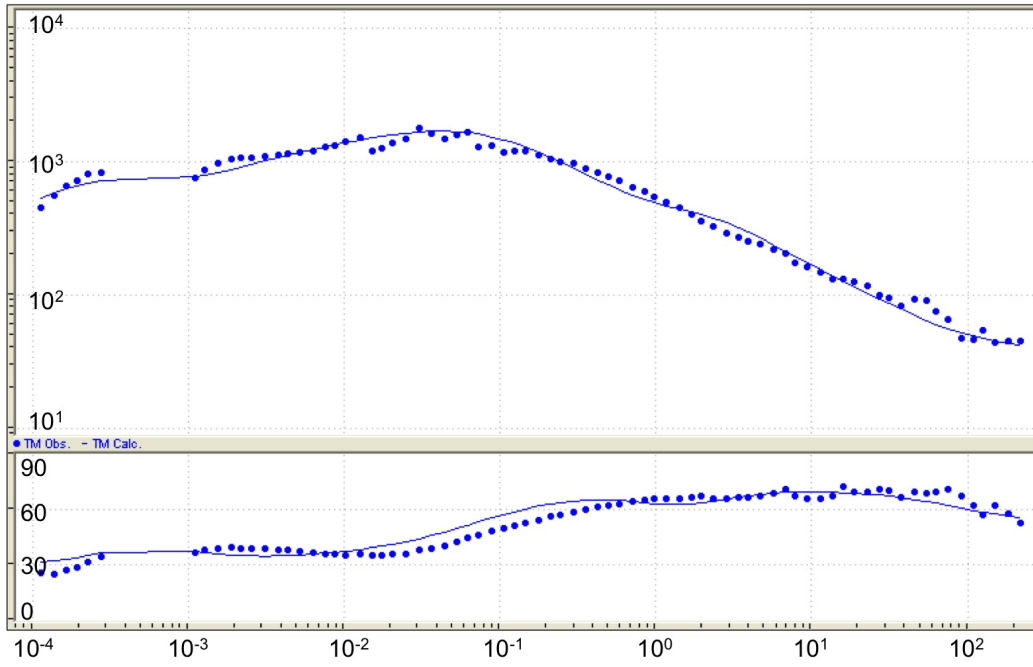


# Appendix D

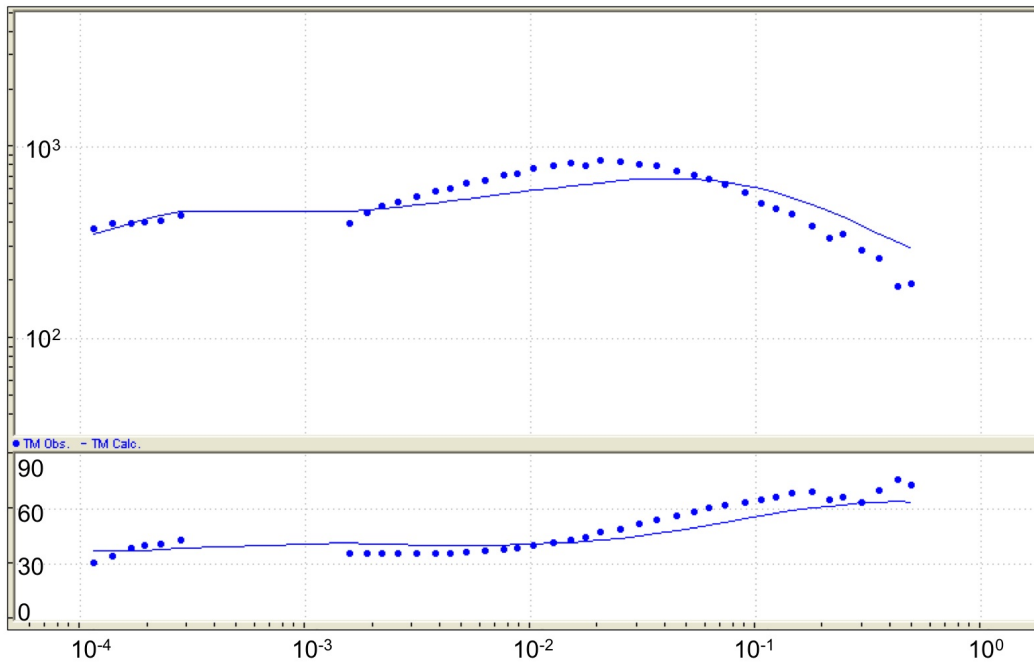
## Inversion data

Calculated data, and corresponding observed (processed) data, for the inversion model with the lowest RMS value, i.e., TM mode only,  $\tau=5$ , and a geo-electric strike of  $33^\circ$ .

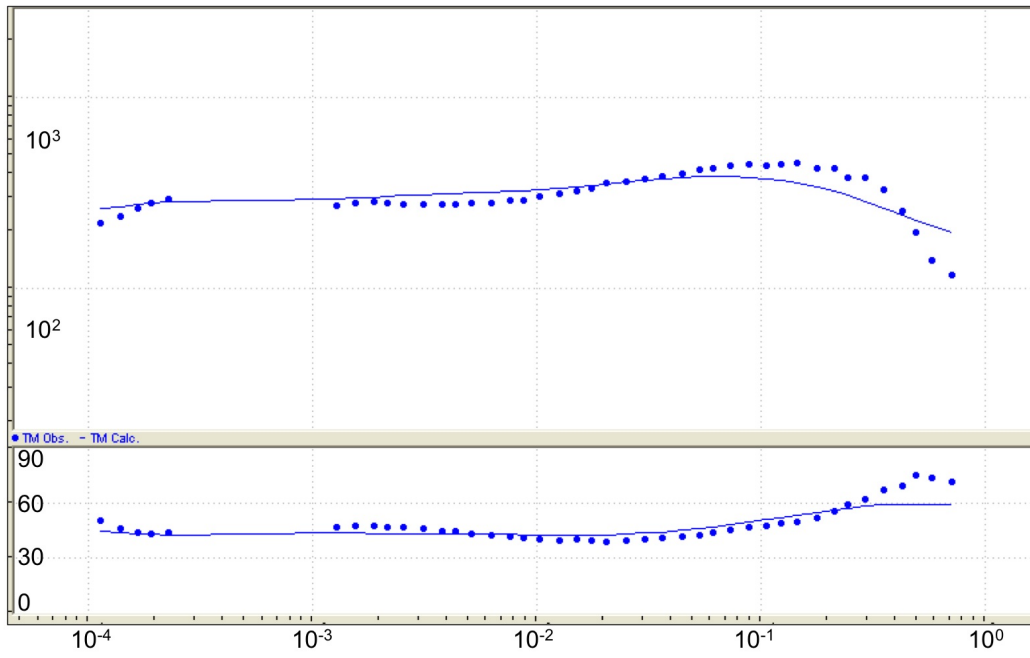
HW103



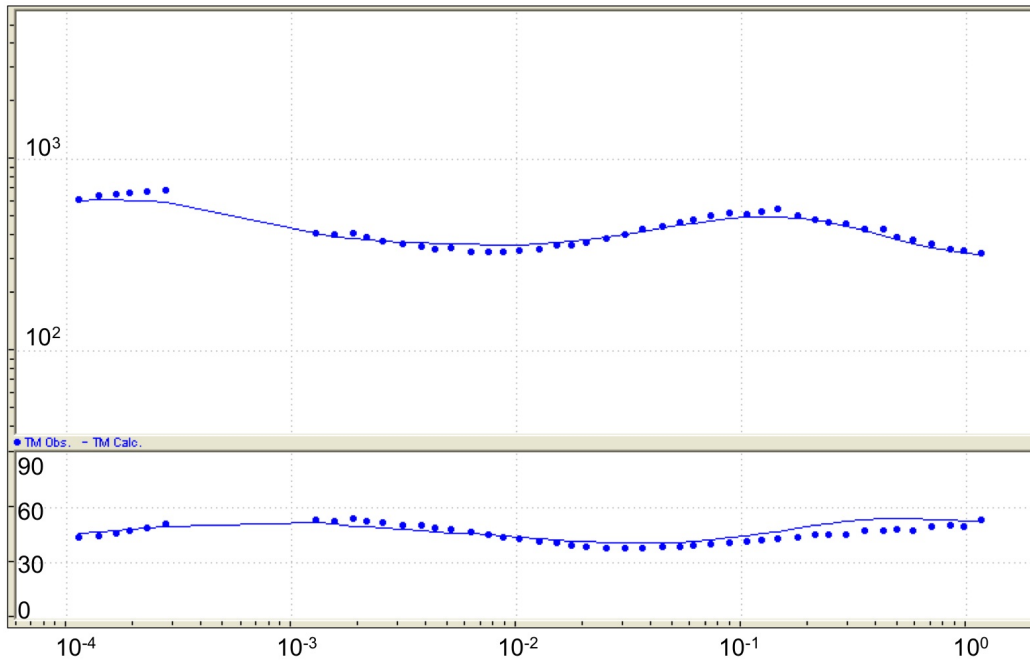
HW104



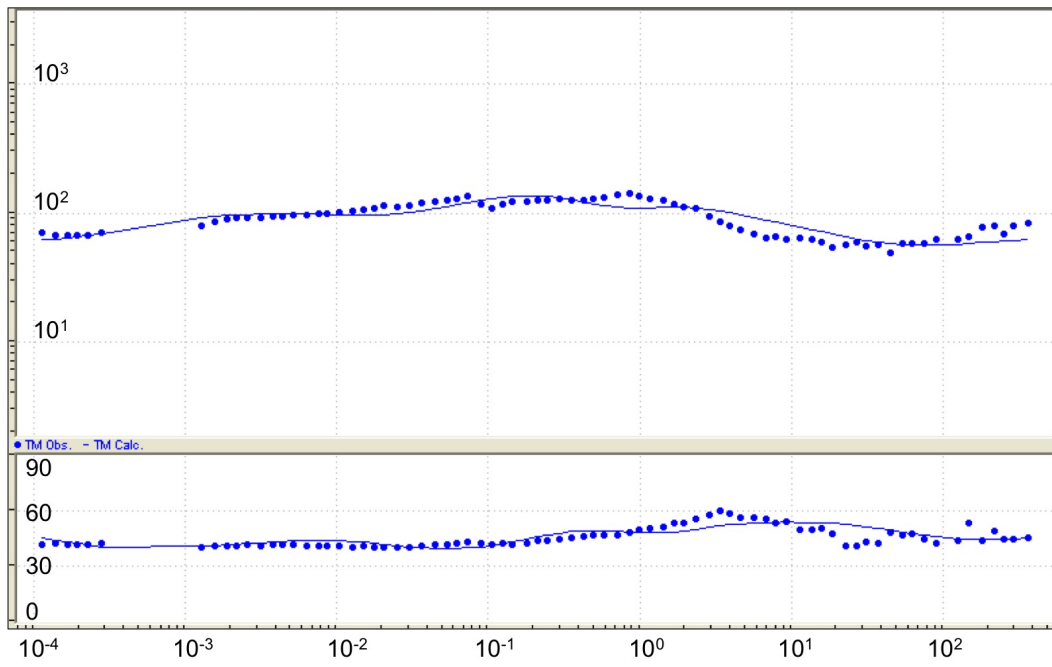
HW105



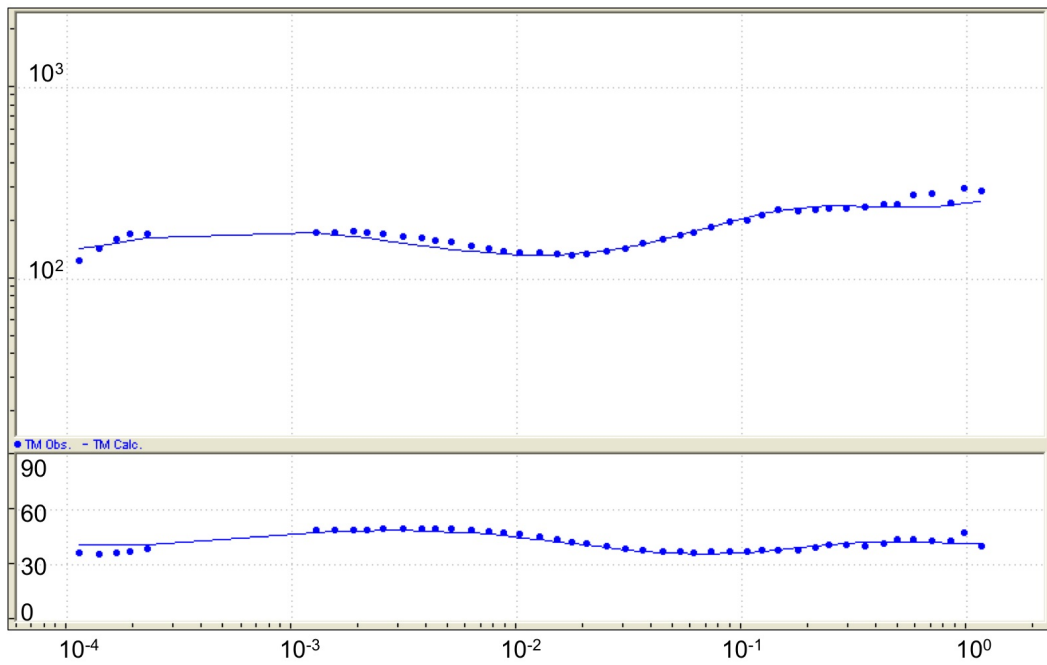
HW106



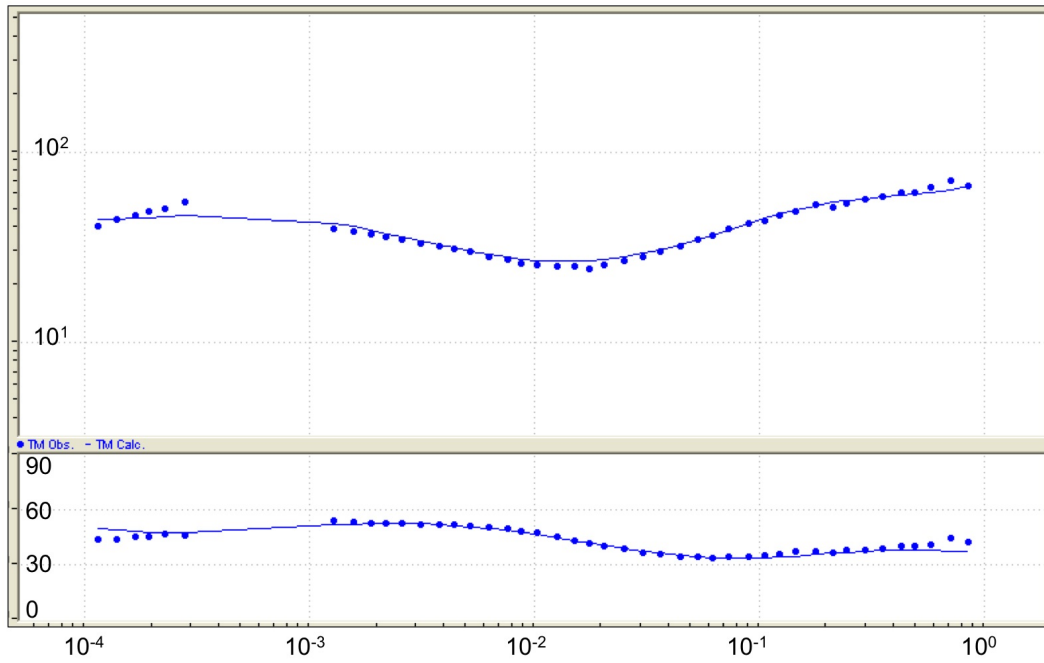
HW107



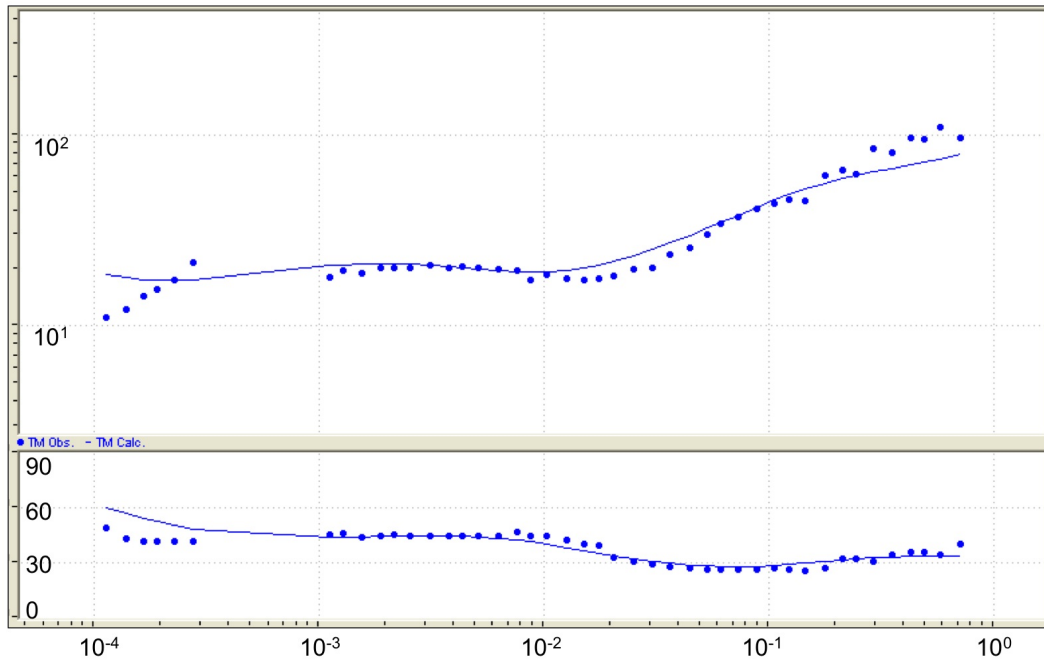
HW108



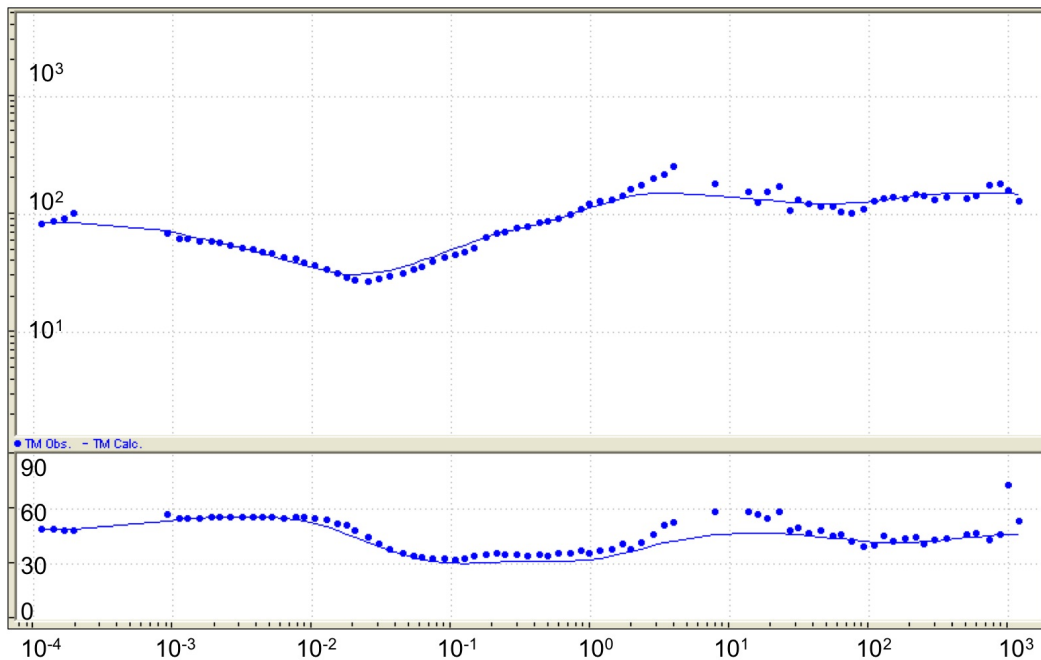
HW109



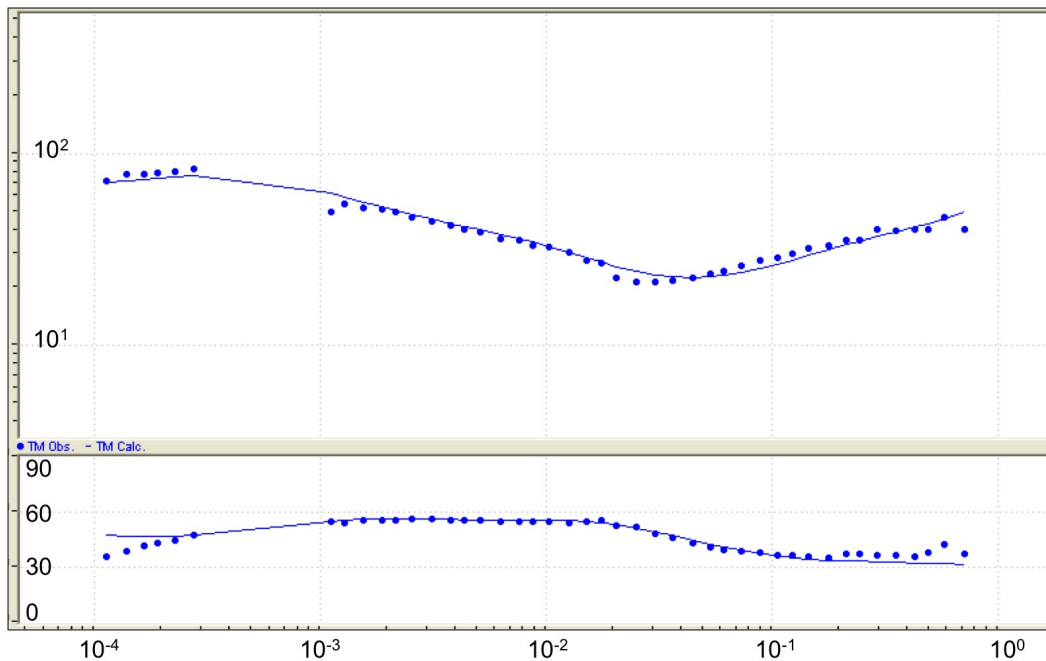
HW110



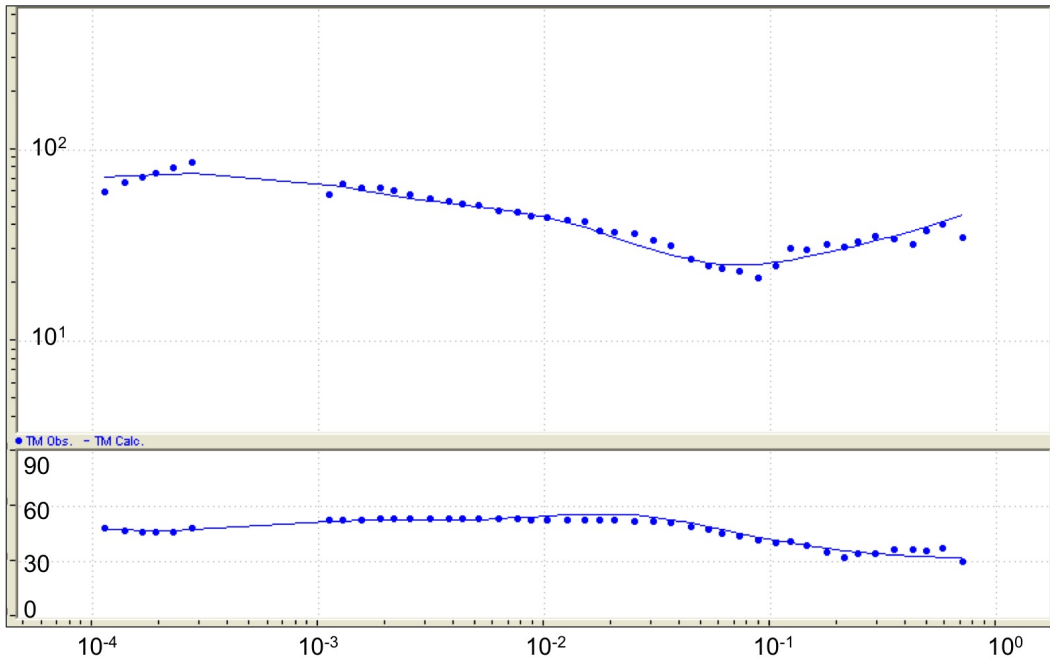
HW111



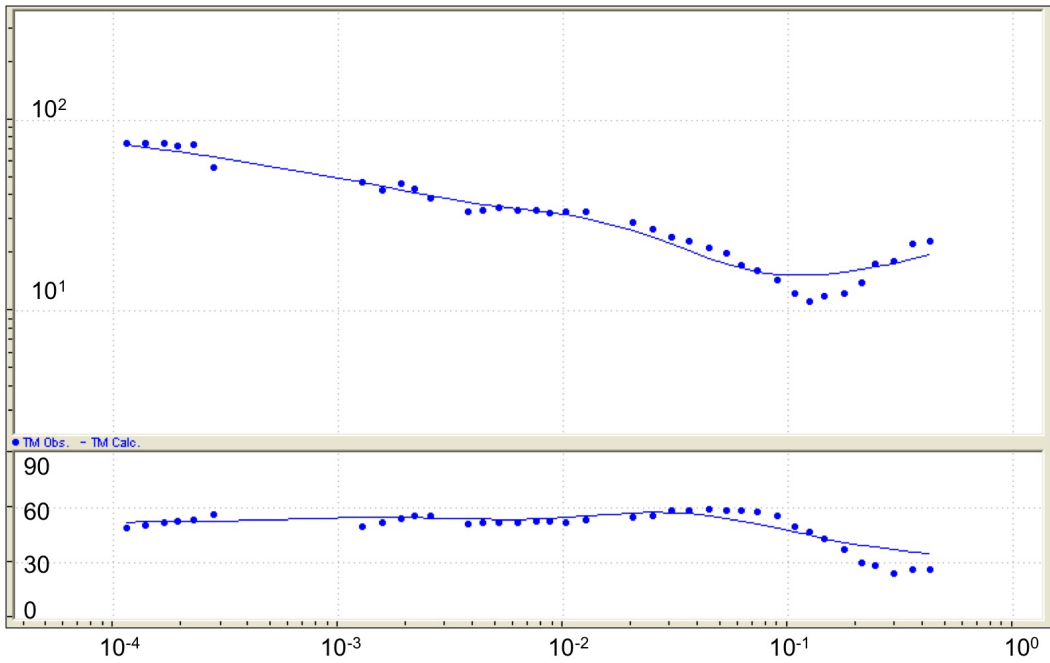
HW112



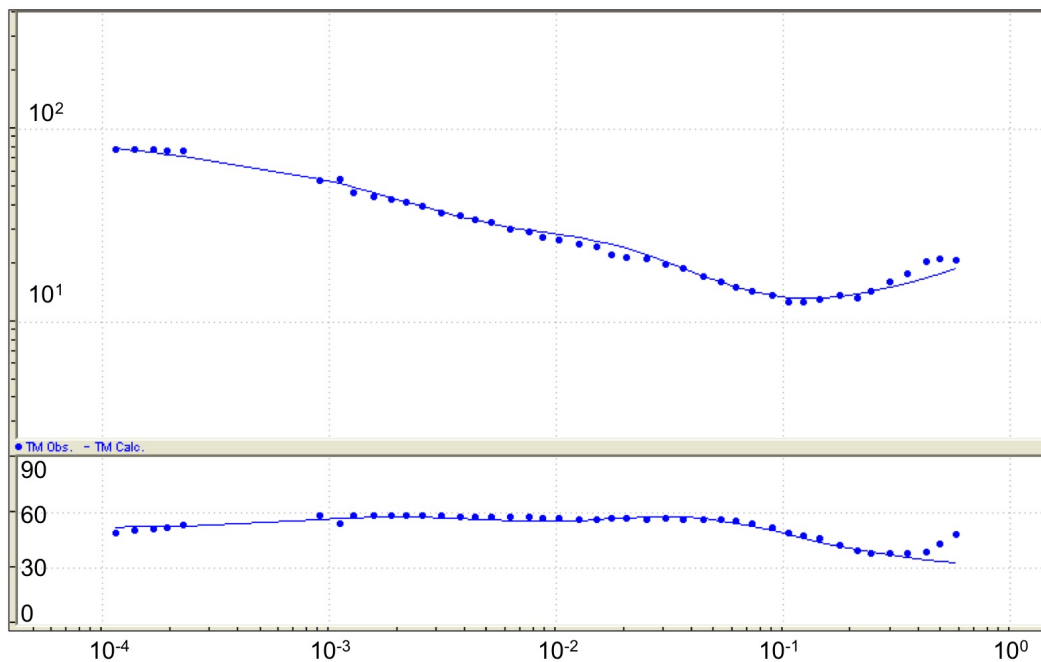
HW113



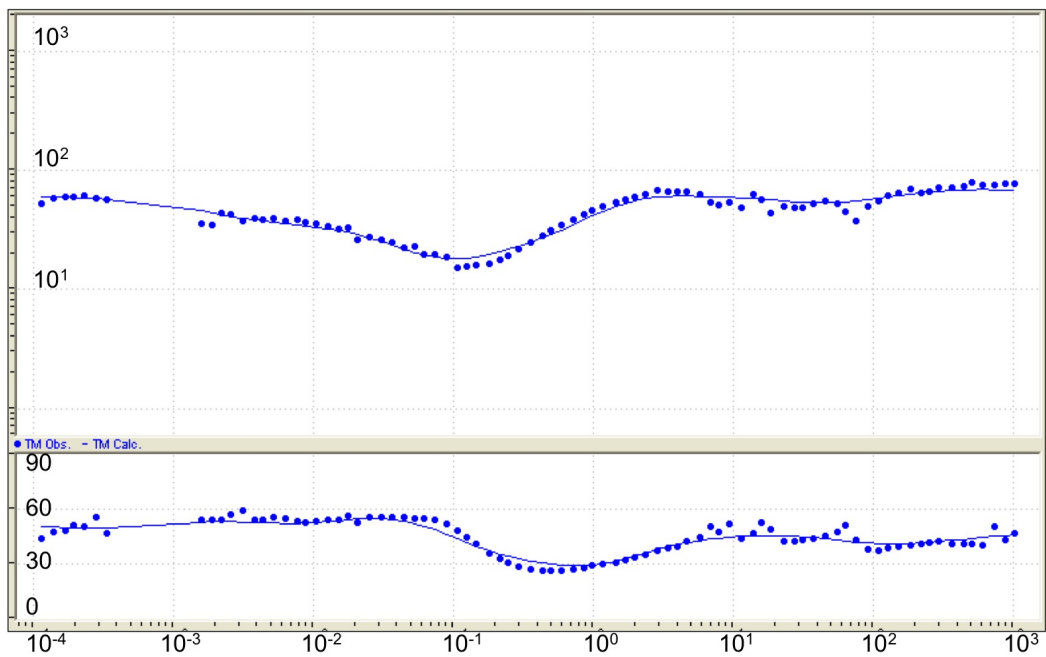
HW001



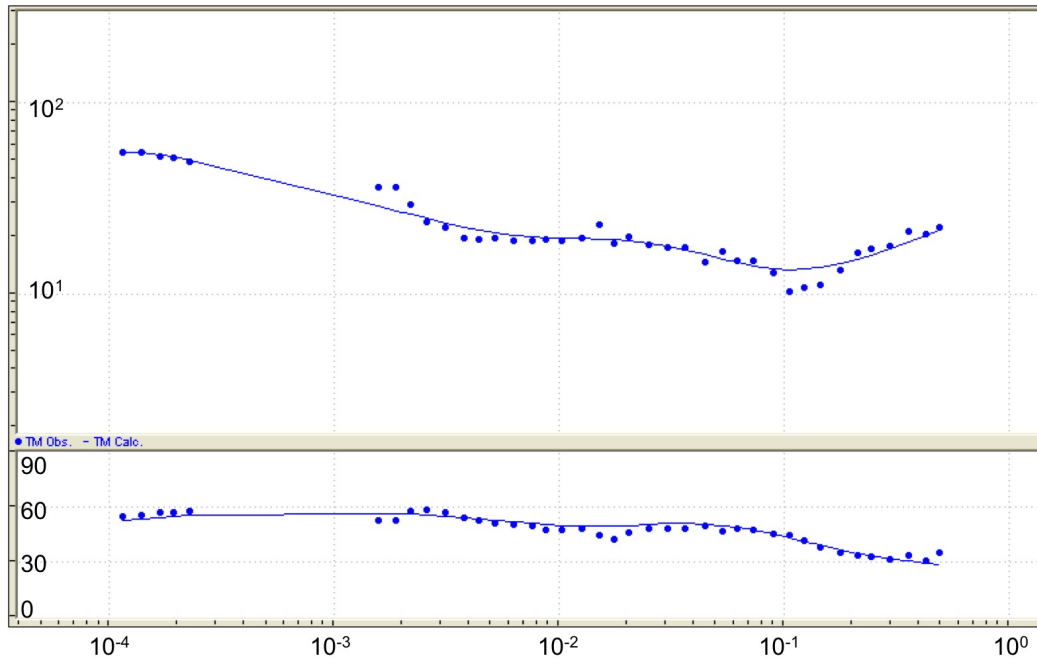
HW114



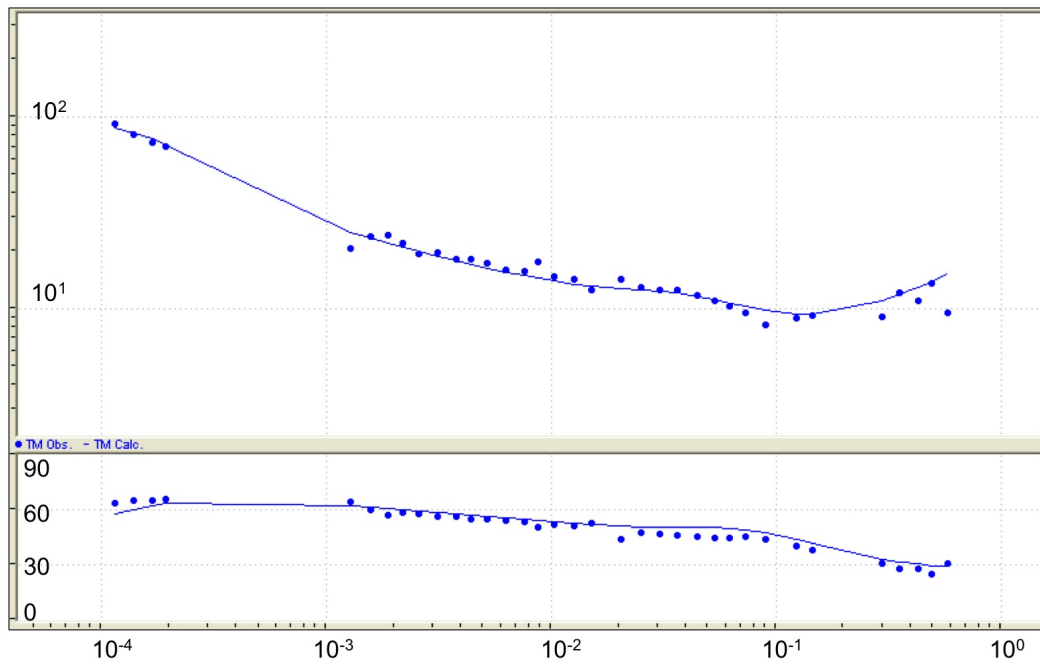
HW115



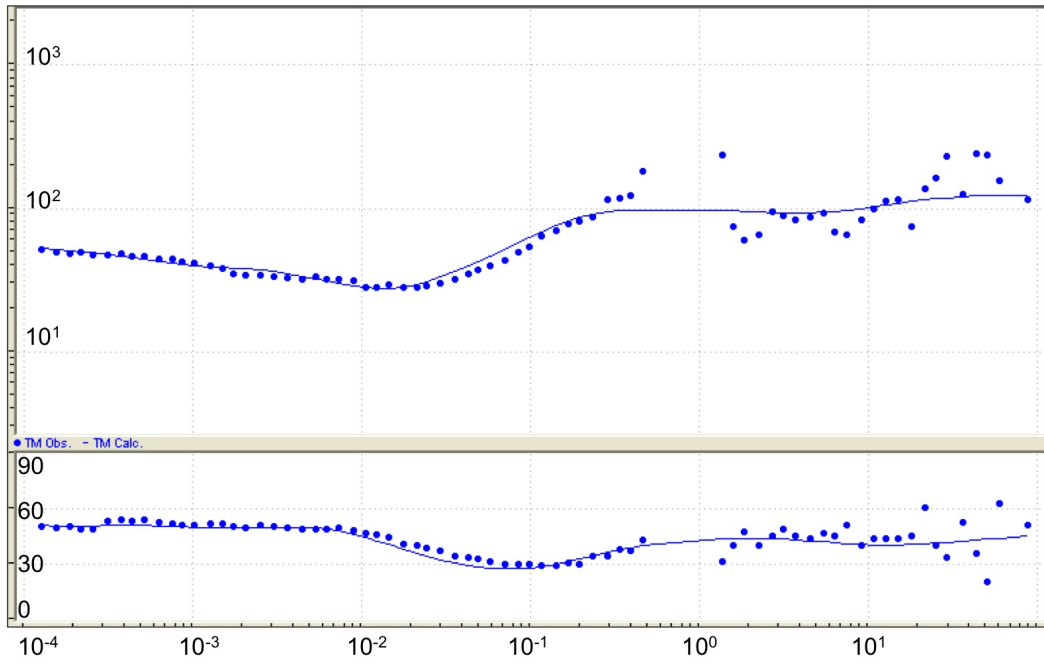
HW116



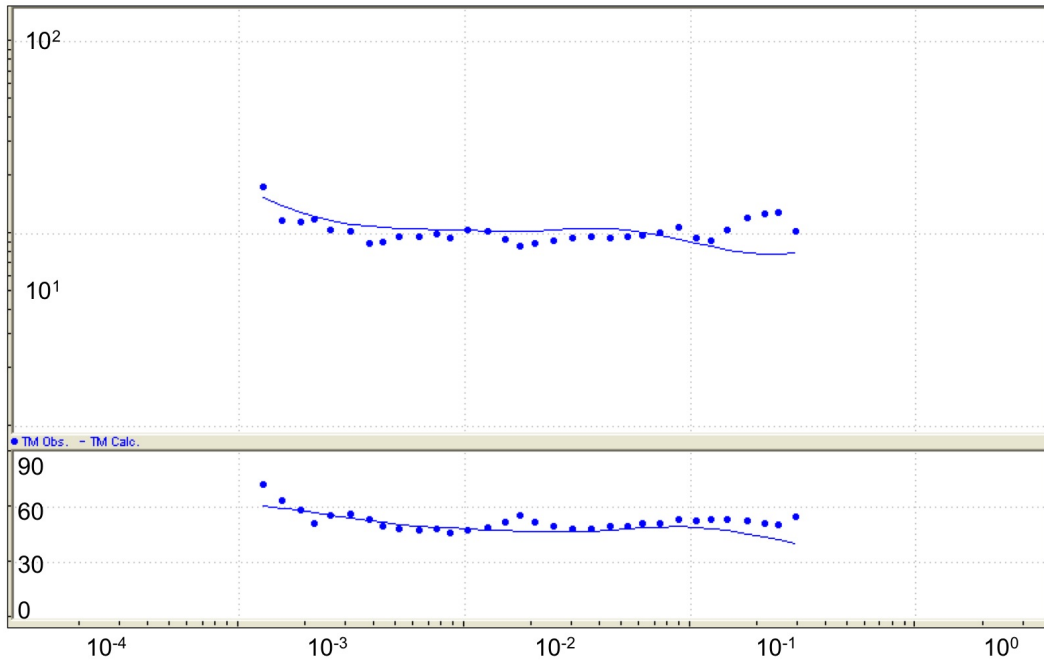
HW117



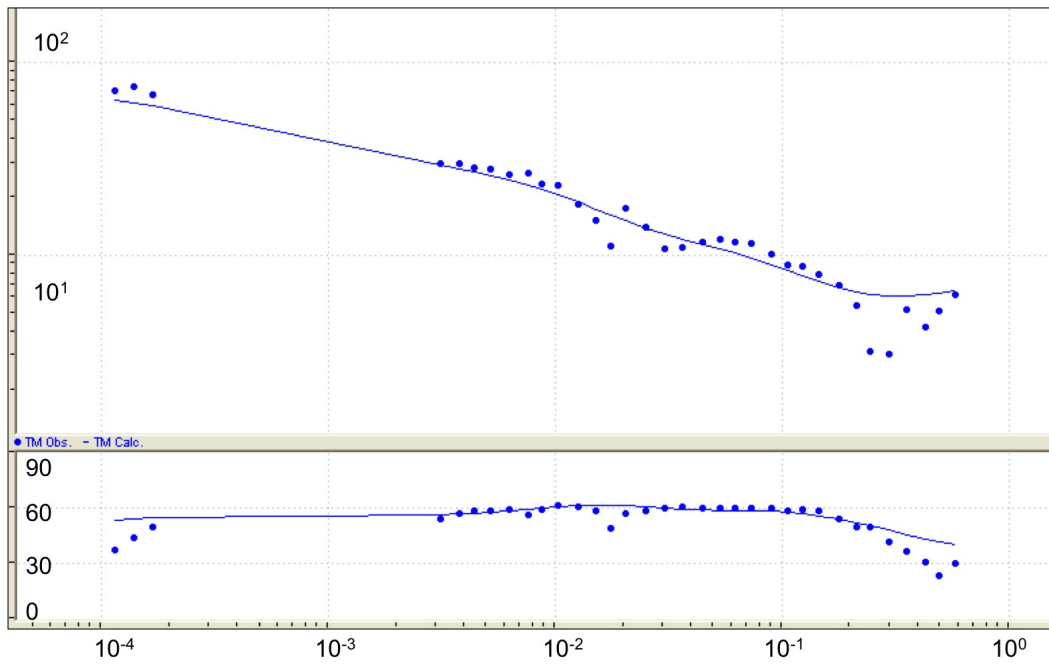
HW118



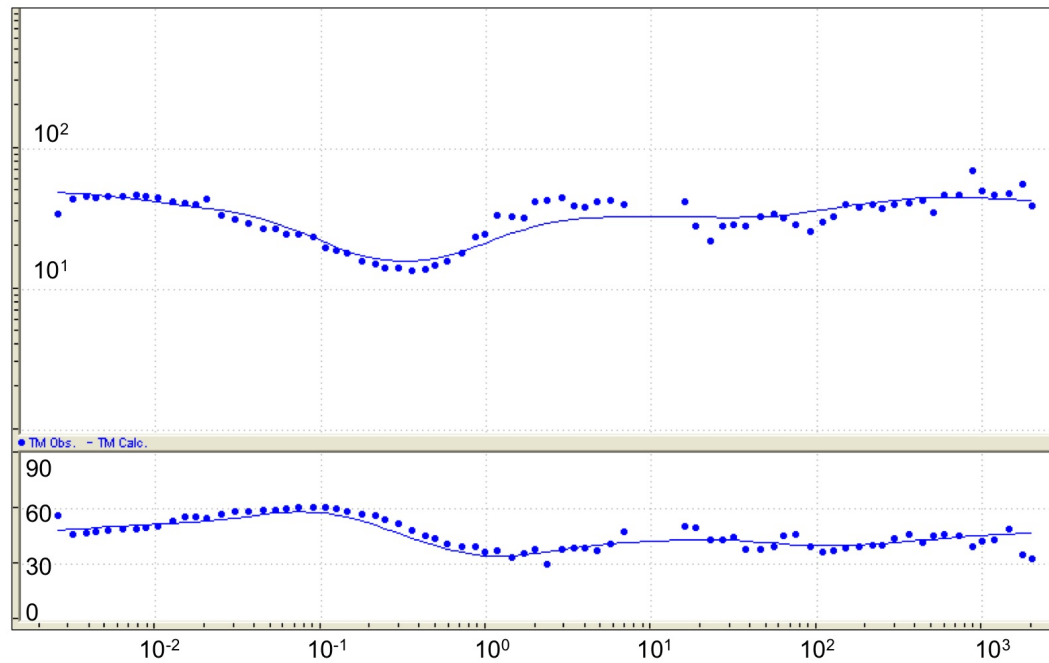
HW119



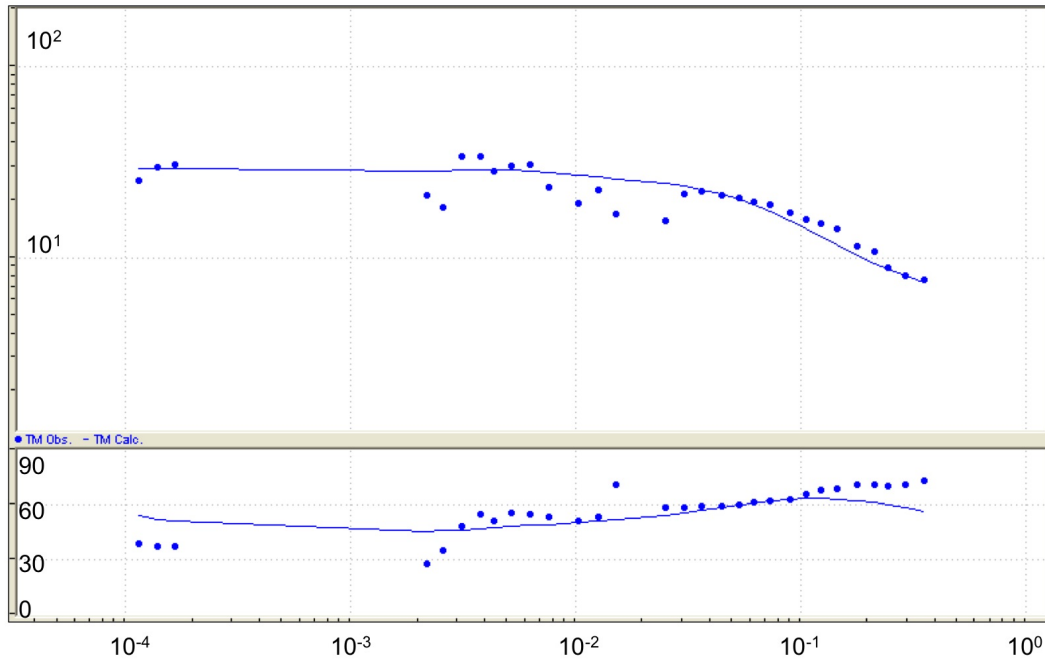
HW124



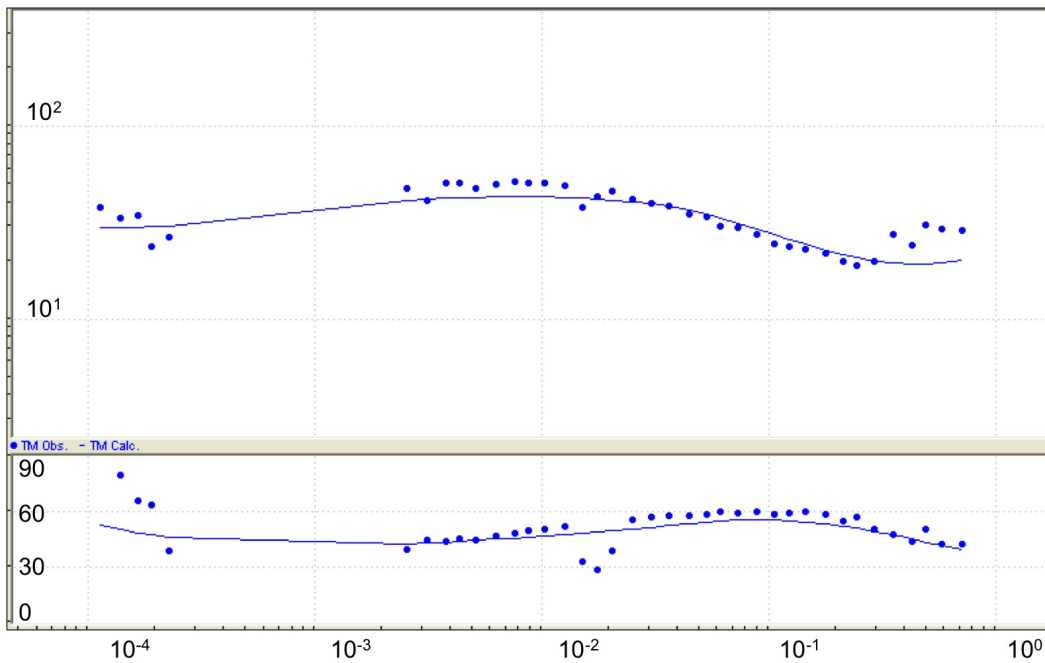
HW125



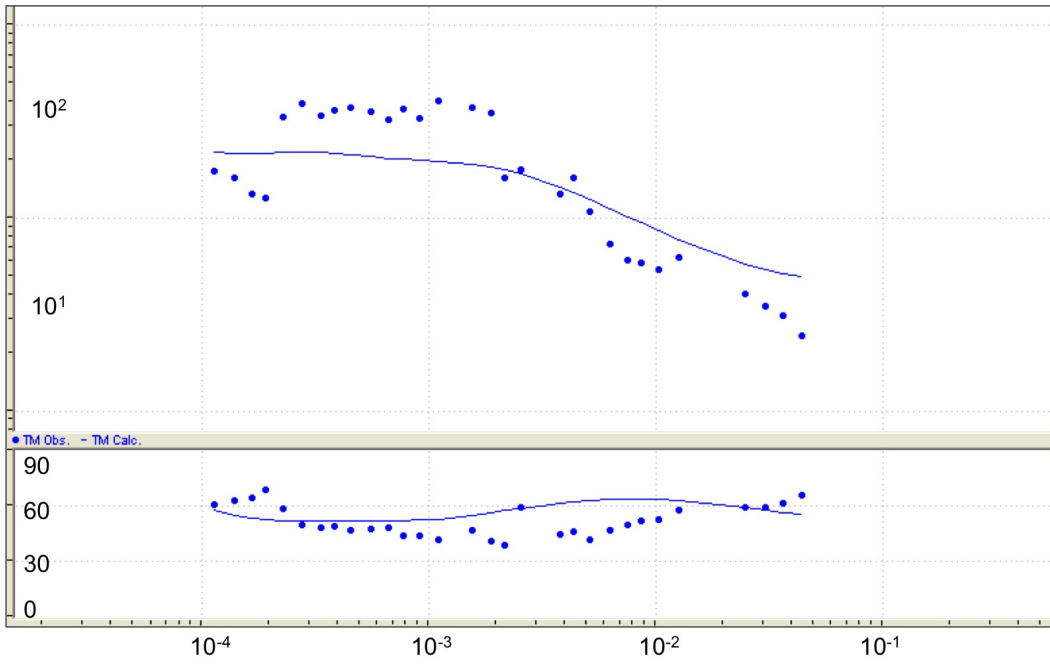
HW126



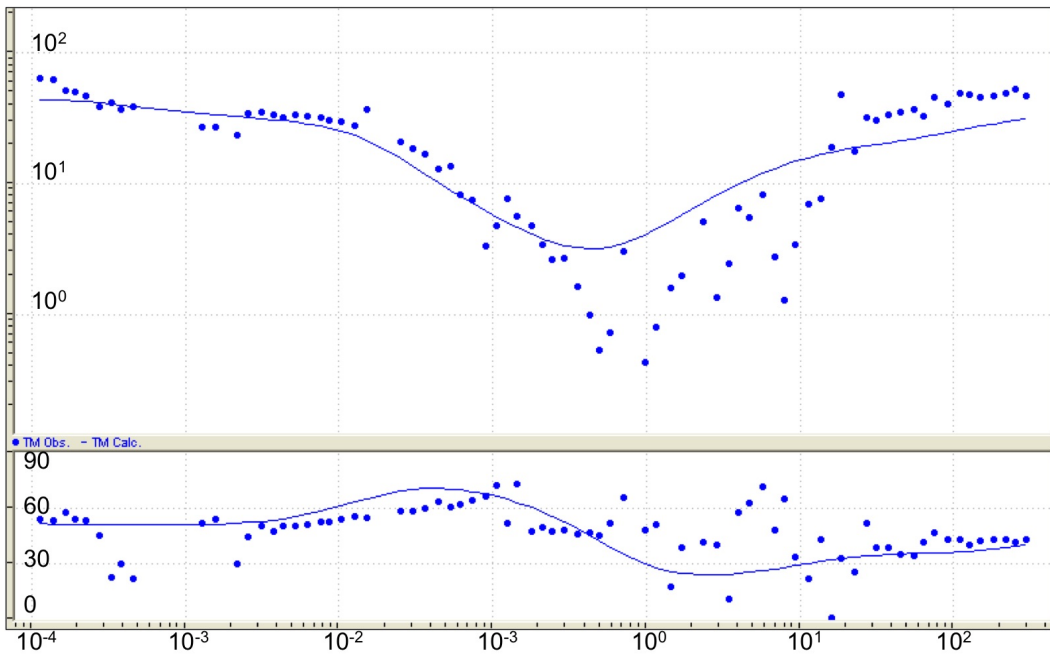
HW127



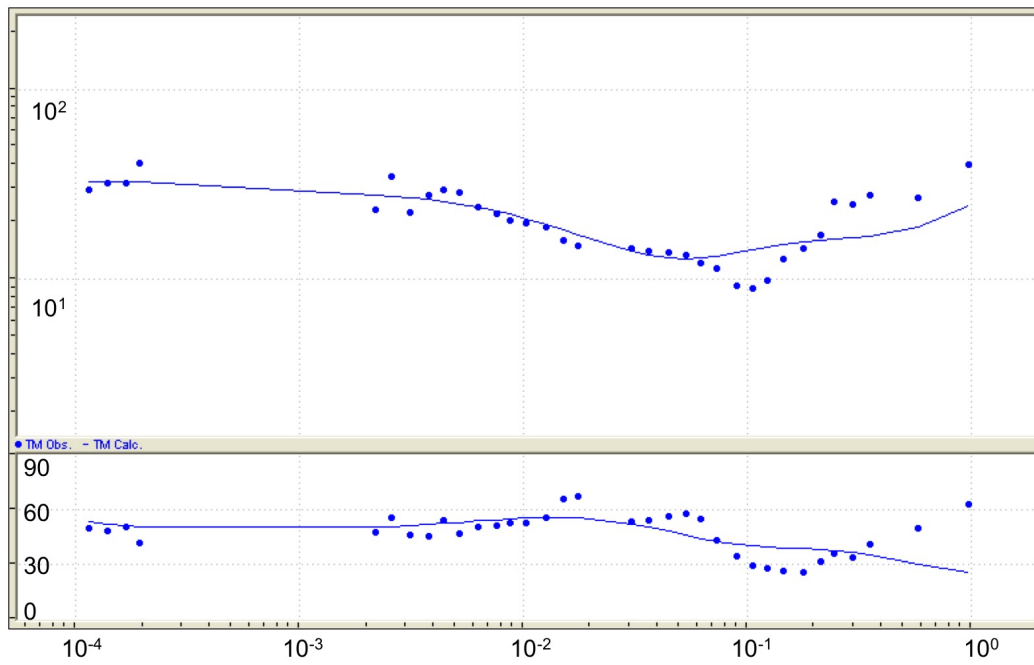
HW128



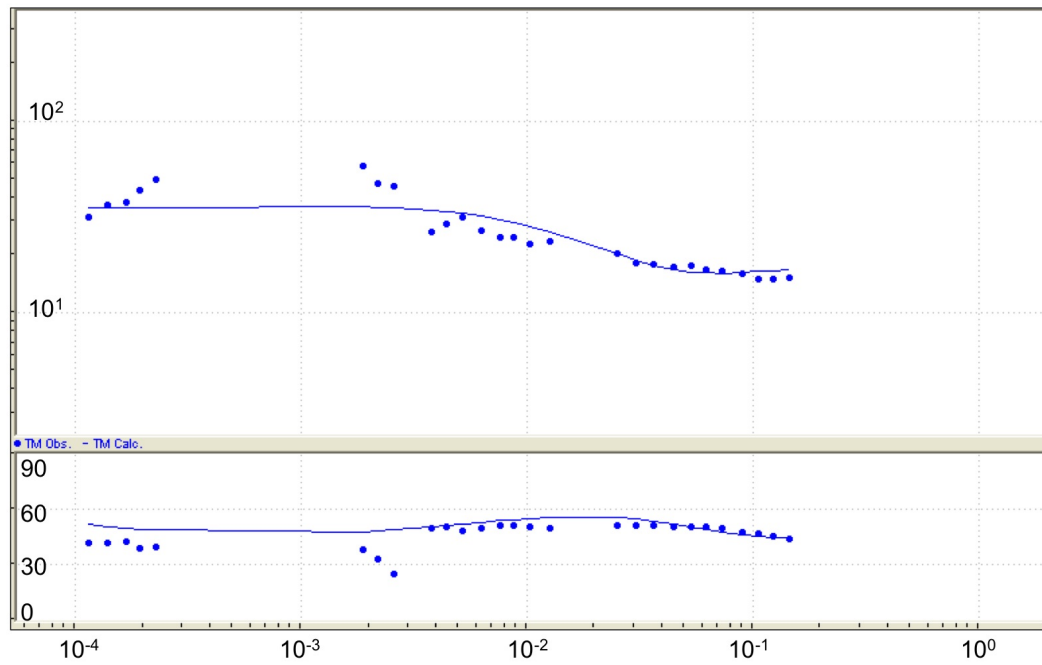
HW129



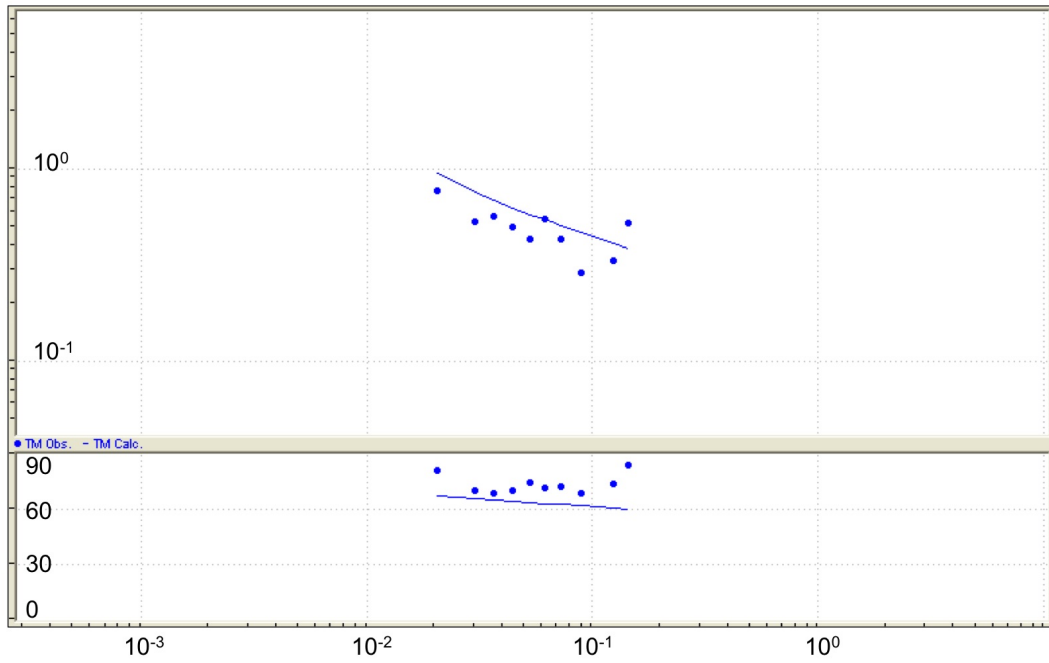
HW130



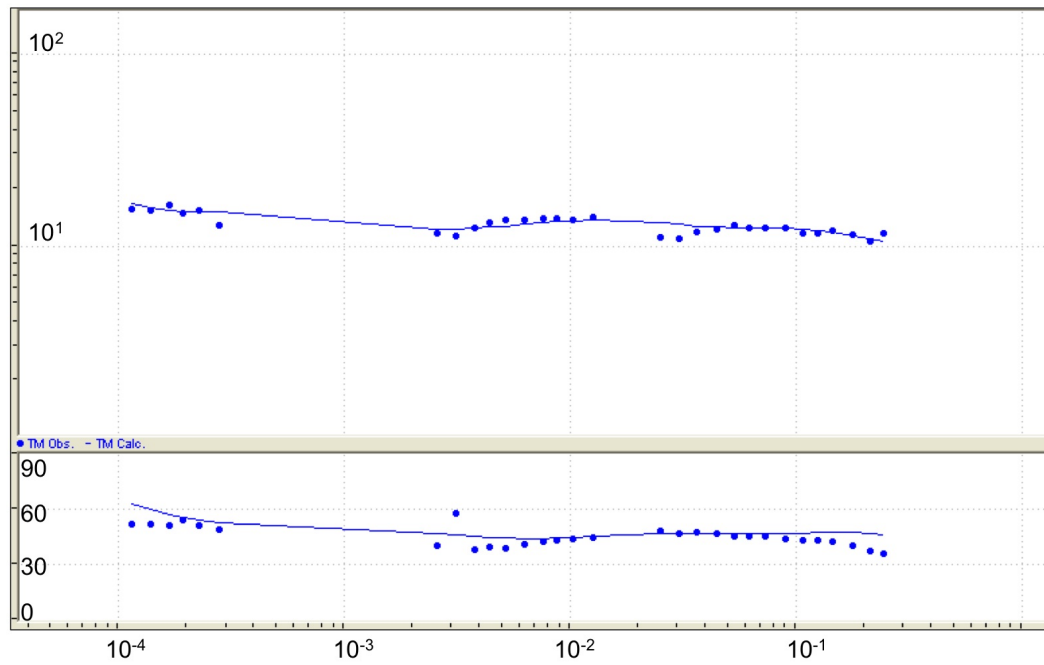
HW120



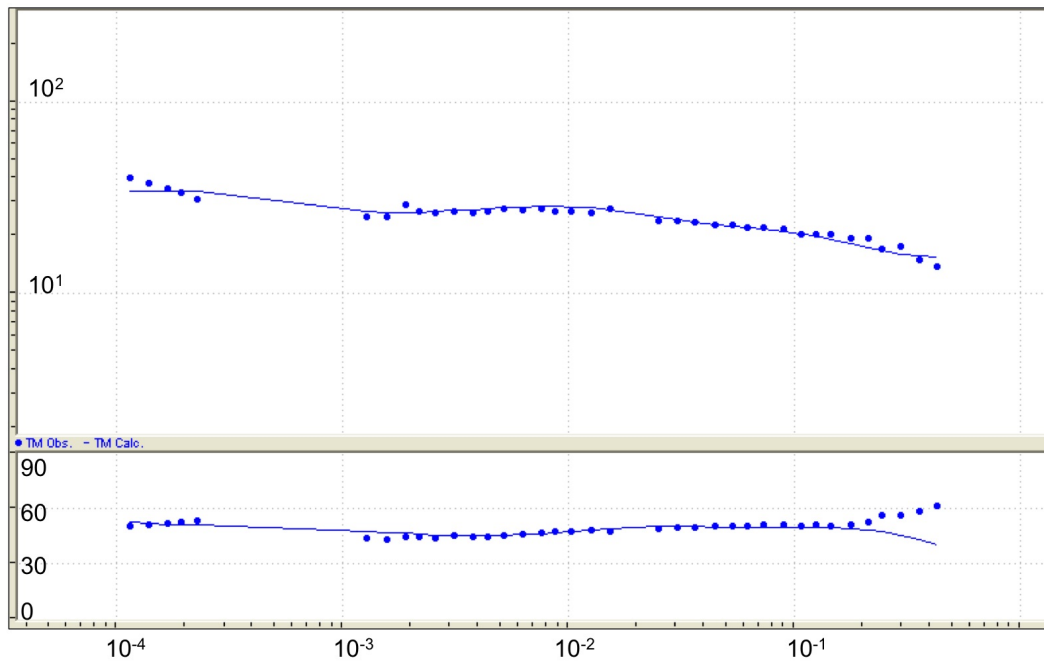
HW131



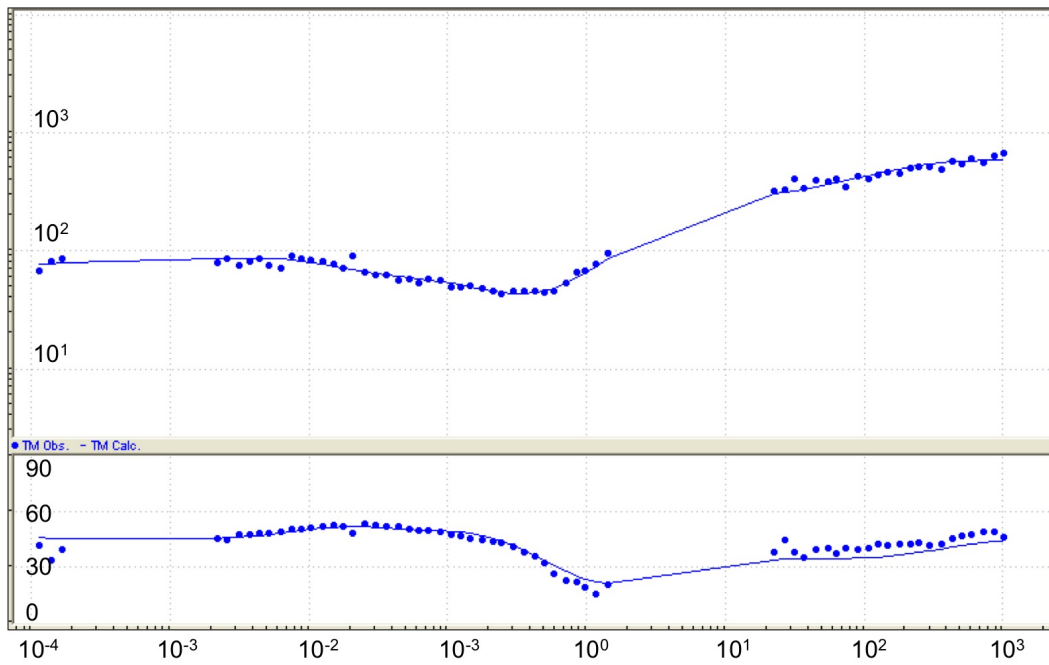
HW132



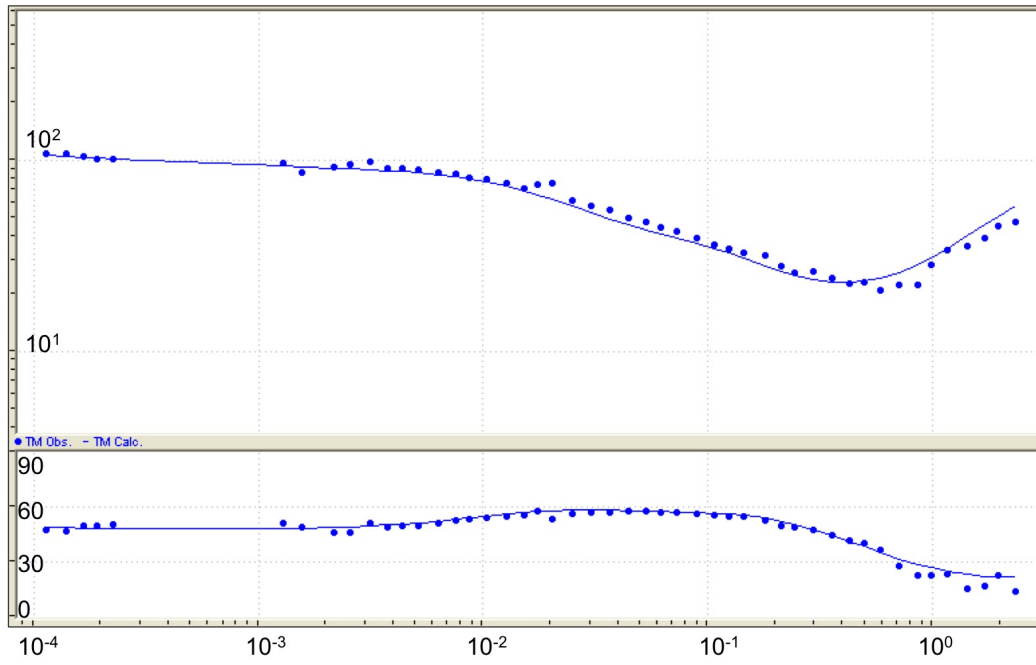
HW133



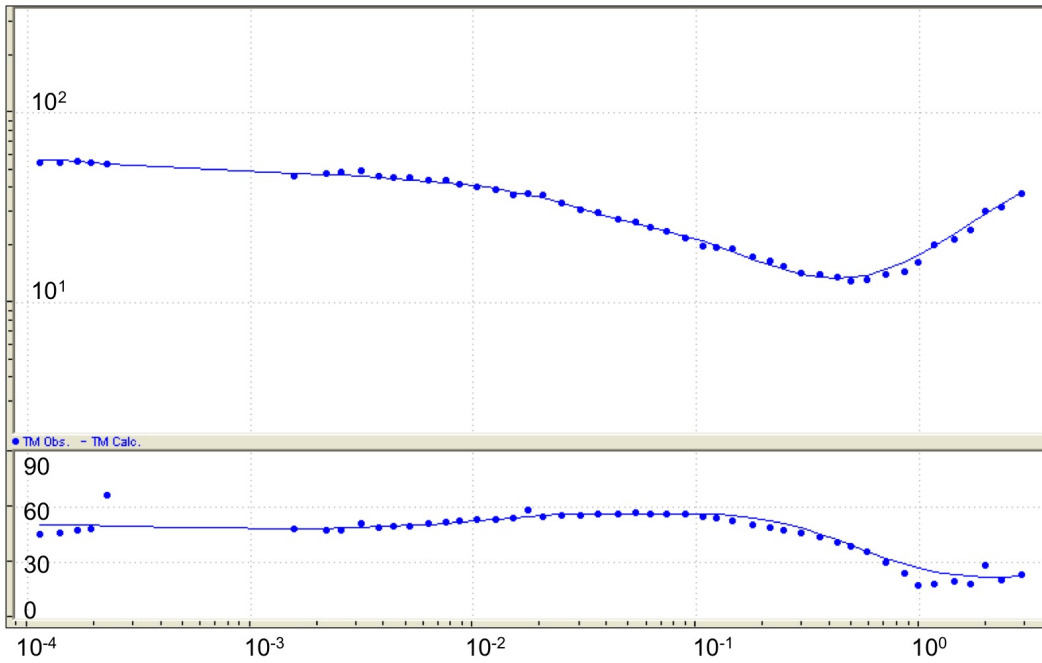
HW134



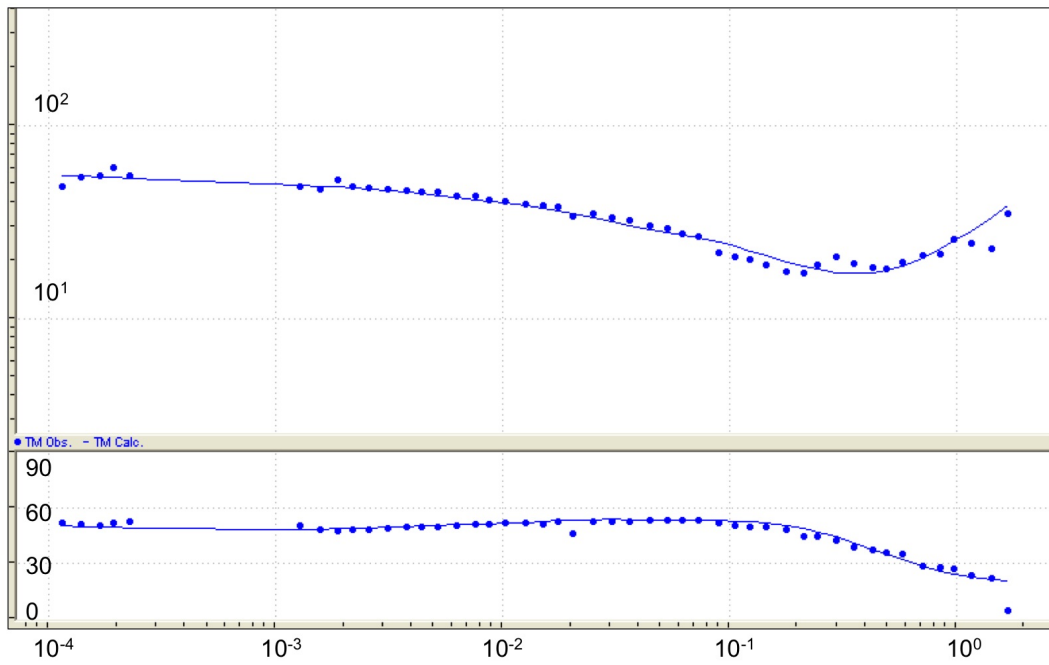
HW135



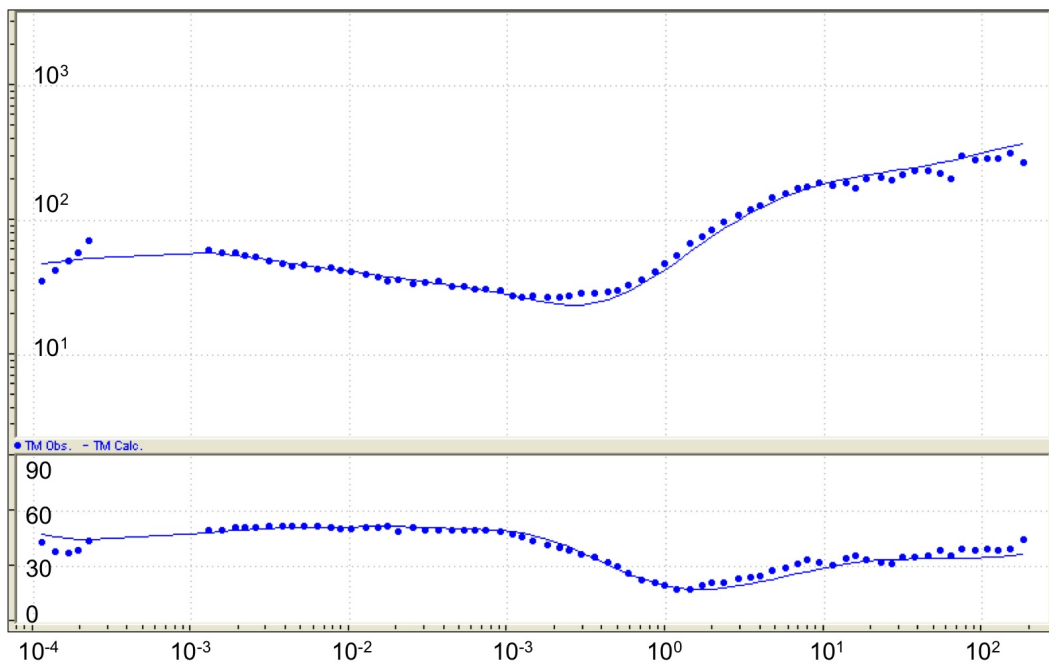
HW136



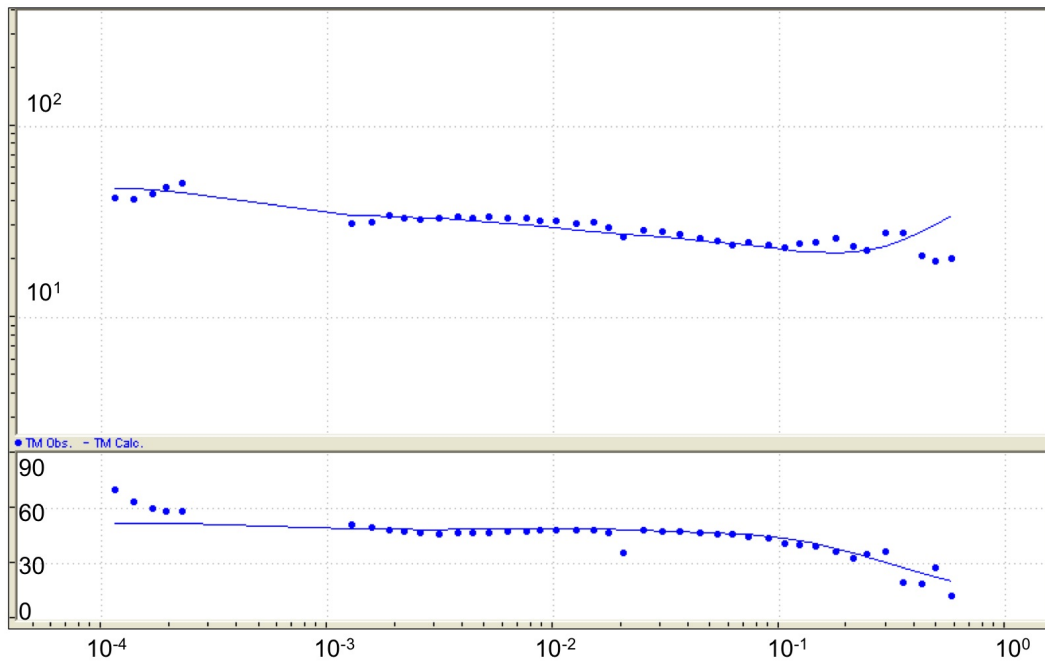
HW137



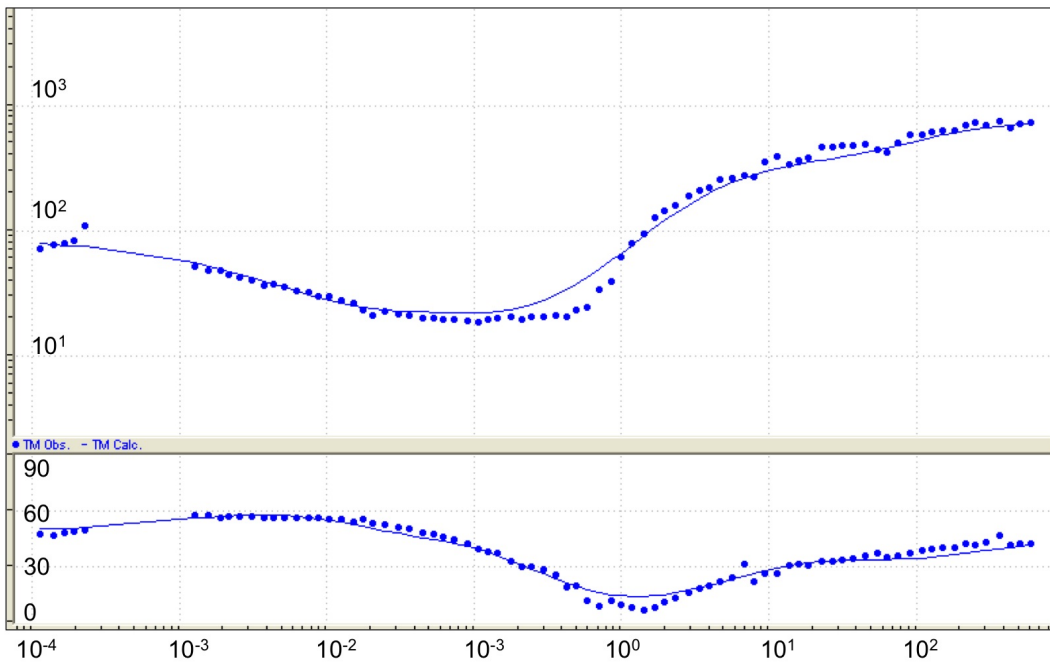
HW138



HW139



HW140



HW141

